From the holdings of the Department of Special Collections , Princeton University Library, Princeton, NJ

These documents are either in the public domain, or can only be used for educational and research purposes (Fair use) as per U.S. Copyright law (text below). By accessing this file, all users agree that their use falls in the public domain or within fair use as defined by the copyrightlaw. We do not charge any permission or usage fees for the publication of images of material inour collections, including those provided by Princeton University Library, via our website, catalog, or directly from staff.For more information regarding copyright, credit, and citation please review the information onthe Copyright, Credit and Citation Guidelines page of our website.
https://library.princeton.edu/special-collections/policies/copyright-credit-and-citation-guidelines. If you have any questions, including how to order higher-quality images from the collection, contact Special Collections Public Services via our Ask Us! Form. https://library.princeton.edu/special-collections/ask-us

---

Doctoral Dissertations, 2011-2026 Atmospheric and Oceanic Sciences

2025

Sea Salt Aerosols in Global Climate Models: Emissions, Transport, and Geoengineering Implications

Wang, Cindy

Princeton, NJ : Princeton University

---

http://arks.princeton.edu/ark:/88435/dsp01tm70mz652

U.S. Copyright law: The copyright law of the United States (Title 17, §108, United States Code) governs the making of photocopies or other reproductions of copyrighted material. Under certain conditions specified in the law, libraries and archives are authorized to furnish a photocopy or other reproduction. One of these specified conditions is that the photocopy or reproduction is not to be used for any purpose other than private study, scholarship, or research. If a user makes a request for, or later uses, a photocopy or reproduction for purposes in excess of fair use that user may be liable for copyright infringement. This institution reserves the right to refuse to accept a copying order if, in its judgment, fulfillment of the order would involve a violation of copyright law. https://www.copyright.gov/title17/title17.pdf

Sea Salt Aerosols in Global Climate Models: Emissions, Transport, and geoengineering implications

Cindy Wang

A Dissertation
Presented to the Faculty
of Princeton University
in Candidacy for the Degree
of Doctor of Philosophy

Recommended for Acceptance
by the Program in
Atmospheric & Oceanic Sciences
Adviser: Leo J. Donner

September 2025

© Copyright by Cindy Wang, 2025.

All rights reserved.

Abstract

Sea salt aerosols (SSA) play a vital role in Earth's climate system by influencing radiative balance and cloud formation. However, discrepancies between observed and modeled SSA concentrations create uncertainties in climate projections. This dissertation examines SSA emissions, radiative effects, and interactions with the global climate, focusing on their role in atmospheric processes, climate modeling, and geoengineering.

Chapter 1 identifies emission errors, vertical transport errors, and subgrid variability as key sources of discrepancies between modeled and observed SSA concentrations. By combining in situ measurements from NOAA PMEL cruise expeditions with GEOS-Chem model simulations, this chapter highlights the need for integrated approaches to improve SSA representation in global climate models (GCMs). Chapter 2 evaluates the performance of various sea spray generation functions in representing SSA emissions and aerosol optical depth (AOD). Comparisons of four sea spray generation functions in a NOAA GFDL atmosphere model reveal that simulations using the mechanistic formulation by Deike et al. (2022) achieve the highest correlation with global AOD observations. This chapter emphasizes the regional variability in SSA emission simulations and the challenges of reconciling AOD retrieval methodologies with model outputs.

Chapter 3 explores the climatic impacts of geoengineering scenarios by examining the rapid adjustments and atmospheric circulation responses to increased tropical SSA emissions under the G4sea-salt protocol in a NOAA GFDL coupled model. Enhanced tropical SSA emissions induce cooling, reducing equator-to-midlatitude temperature gradients and weakening surface westerlies, which in turn partially offset increased emissions. The analysis reveals significant differences in climate responses to zonally uniform versus regionally targeted SSA geoengineering scenarios, providing critical insights for marine cloud brightening strategies. Chapter 4 assesses radiative forcing and climate feedback parameters in the context of SSA geoengineering, comparing G4sea-salt simulations with the SSP2-4.5 baseline. By isolating the effects of SSA geoengineering, this chapter demonstrates that geo-

engineered forcings and feedbacks can be analyzed similarly to traditional climate forcings, though nonlinearities in Earth's energy imbalance (EEI) complicate attribution.

Collectively, this dissertation advances the understanding of SSA dynamics, their representation in climate models, and their potential role in geoengineering, providing critical insights for future climate mitigation and adaptation strategies.

Acknowledgements

The path to my Ph.D. has been an intense and rewarding scientific journey. This work was carried out during the challenging period of the COVID-19 pandemic, with more than half of my graduate studies conducted virtually. GFDL reopened near the end of my third year, marking a return to in-person collaboration. Earning a Ph.D. truly takes a village, and I am deeply grateful to the many individuals and mentors who have supported me along the way.

I would first like to thank my advisor, Leo Donner, and my dissertation committee members, Larry Horowitz, Luc Deike, and V. Ramaswamy, for their invaluable guidance and support throughout my Ph.D. It has been a profound honor to learn from and work alongside each of you. I am especially grateful for the time you consistently made for committee meetings and for your insightful feedback, which has been instrumental in shaping this work. I have particularly appreciated my weekly meetings with Leo, whose mentorship has taught me to approach my research with greater precision and critical thinking.

I would like to thank Pu-Lin, Huan Guo, and Larry Horowitz for their generous help in setting up the model and for patiently answering my many questions about the intricacies of the GFDL modeling system. I would like to acknowledge Paul Ginoux and Fabien Paulot for their important work on implementing the sea-salt emission and gravitational settling schemes in the GFDL model. I am also grateful for the outstanding administrative support provided by Anna, Kit, Laura, and Sammi in AOS; Dale and Latoyia at GFDL; and Sheryl, Mary Rose, and Danielle in GEO. Finally, I gratefully acknowledge the financial support of CIMES and the HMEI-PECS program.

I am deeply grateful to the brilliant scientists and postdocs I have had the privilege of working with at NOAA GFDL and at Princeton. I especially want to acknowledge the wonderful postdoctoral researchers and early-career scientists whose support and mentorship have meant so much to me throughout this journey. In particular, I would like to thank Bor-ting Jong and Zack Labe for their unwavering belief in me–even during times when I struggled to believe in myself. I want to thank Naser Mahfouz, whom I met during his time

as a postdoc at GFDL and who is now at PNNL, for his continued support, kindness, and academic mentorship. Additionally, I would like to express my sincere appreciation to my undergraduate advisor, Zhengzhao (Johnny) Luo, for his steadfast mentorship and support throughout my Ph.D.

My cohort has played an instrumental role in helping me stay grounded through the more contentious and stressful moments of my Ph.D. Entering this program as the only woman and the only person from a public undergraduate institution in my cohort was daunting, but Chenggong Wang, Ben Johnson, and Glen Chua always made me feel welcomed and supported. Thank you for being my day ones. Glen, it has been an honor to witness you embrace and take pride in your identity.

I would also like to thank the AOS students who came before me and those who have followed–leaving this remarkable community of young scientists, many of whom I consider close friends, is truly bittersweet. Lynn Hirose, I'm excited to see all that you will accomplish. Thank you for being not only a wonderful mentee but also a cherished friend. I am especially grateful to Jane and Priyam for their guidance during my early years and for their continued support even after graduating.

I have been incredibly fortunate to form lasting friendships during my time here and to maintain those that began earlier in life. There are far too many to name—across Princeton, New York, and beyond—and I would be remiss to leave anyone out. To all of you, thank you sincerely for your friendship and unwavering support throughout these years.

I want to especially thank my former coworkers, Qahtan Al Jammali and Tin Tun Naing, for joining me on countless impromptu hiking adventures that brought both joy and balance to these years. And to Christy Enama, my very first friend in college, thank you for a friendship that has endured and grown through the years. I am especially grateful to the first friends I made in graduate school–Daniel Zhou, Hannah Rabb, Michael May, and Michael Zhang–who stood by me through it all, from a difficult breakup and recovering from a scooter accident to the final stretch of completing this degree. Thank you Tianyu Gao and Sadhika

Malladi for always being a joy to see and talk to at events. I'm also thankful to the friends I met through the Princeton Math Department–Warren Li, Doug Stryker, Katie Woo, and many others–who welcomed me warmly into their community, whether at social gatherings or the occasional free food event.

I also want to thank my former roommates—Kurtland Chua, Poorvi Bellur, and Xinyi Wei—who kept me grounded during the isolating moments of the pandemic and helped me embrace and take pride in my Chinese American heritage. I will always treasure our Sunday brunches, late-night conversations, annual apple-picking trips to Terhune, and the countless other memories we created together. A special shoutout to Kurtland Chua and Sherry Li–you were the best classmates I could have asked for in our heritage Chinese class. Thank you for giving me the space to heal from the complexities and trauma of being a first-generation Chinese American, and for doing so with humor, compassion, and solidarity.

I feel incredibly fortunate to have met my partner, Serban, during my Ph.D. Serban, you are one of the greatest gifts to come out of my time at Princeton. I cannot thank you enough for your unwavering support and the sense of stability you have provided through moments of turmoil and hardship. I truly could not have done this without you.

Last, but certainly not least, I want to express my deepest and most enduring gratitude to my family—especially my parents and my brother—for their unwavering support throughout my doctoral journey. To my beloved grandmother, who passed away two years ago: though you are no longer here to witness this day, I like to believe you always knew I could achieve this. I must also acknowledge the immense sacrifices and hardships my parents faced as Chinese immigrants–starting from nothing and working tirelessly to build a better life for me and my brother. Because of their resilience and dedication, I have been able to pursue this path and become the first in my family's history to (hopefully!) earn a doctoral degree.

This thesis is for all of you–with love and endless gratitude.

To 我的父母 (my parents).

Contents

Abstract iii

Acknowledgements v

Introduction **1**

0.1 Prior presentation & publication 5

1 Integrating in-situ measurements and models to understand errors in sea salt aerosol emissions, transport, and sub-grid processes **6**

1.1 Abstract 6

1.2 Introduction 7

1.3 Methodology 11

1.3.1 In situ observations of SSA concentration 11

1.3.2 Convective precipitation data from ERA5 14

1.3.3 GEOS-Chem model simulations of SSA concentration 15

1.3.4 Calculating SSA emission 16

1.4 Governing framework 20

1.4.1 Applying Reynolds decomposition 25

1.4.2 Eddy transport 25

1.4.3 Apply to a well-mixed boundary layer 30

1.5 Q1 - Can SSA emission errors explain the differences between modeled and observed SSA concentration? 33

1.5.1 Evaluating emissions using estimates of SSA concentration 36
1.6 Q2 - Can errors in vertical transport explain the differences between modeled and observed SSA concentration? 39
1.7 Q3 - Can subgrid variability, sampling error or nonzero $\overline{D}$ explain the differences between modeled and observed SSA concentration? 47
1.7.1 Errors in sampling 47
1.7.2 Estimating $\overline{D}_{\mathrm{X}}$ 49
1.8 Conclusion 53

2 Evaluating the performance of different sea-spray aerosol emission formulations in simulating aerosol optical depth (AOD) 56
2.1 Abstract 56
2.2 Introduction 57
2.3 Methodology 61
2.3.1 AM4 61
2.3.2 SSA emissions 63
2.3.3 AOD (550 nm) validation 66
2.4 SSA emission and concentration in AM4 - 2000-2019 67
2.5 AOD validation 71
2.5.1 MODIS and MISR: 2000–2014 73
2.5.2 AERONET: 2000–2019 81
2.5.3 Maritime (MAN) AERONET: 2004-2019 88
2.6 Conclusion 91

3 Circulation responses to Sea Salt Aerosol Engineering in a GFDL Coupled Model 95
3.1 Abstract 95
3.2 Introduction 96

3.3 Background 97
3.4 Methods 100
3.4.1 Model Description 100
3.4.2 Simulation Protocol 101
3.5 Response to SSA emission increase 102
3.5.1 Sensitivity of SSA emissions to wind speed and temperature changes 106
3.5.2 Relating emission changes to rapid adjustments and circulation changes 107
3.5.3 The equatorial Pacific temperature gradient 113
3.6 Conclusion 116

4 The Radiative Feedback to Sea Salt Aerosol Engineering in a GFDL Coupled Model 119

4.1 Introduction 119
4.2 Background 120
4.3 Methods 124
4.3.1 Model Description 124
4.3.2 Simulation Protocol 124
4.4 Comparing Earth's Energy Imbalance (EEI) in Geoengineering and Abrupt-4xCO2 Scenarios 126
4.4.1 Decomposing the total feedback 132
4.5 Conclusion 138

Conclusions 142

A Integrating density flux 149

B Calculations for global and regional averages 151

B.1 Geoengineered ocean-averaged SSA emission 151
B.1.1 Geoengineered global averaged SSA emission 152

B.1.2 Geoengineered SSA emissions averaged over the global oceans 152
B.2 Globally and regionally averaged SSA emissions (land+ocean) 153
B.2.1 Global averaged SSA emission 153
B.2.2 Tropical average SSA emission 154
B.2.3 NH extratropics average SSA emission 155
B.2.4 SH extratropics average SSA emission 156
B.2.5 Globally averaged SSA emission from regional components 157
B.3 Globally and regionally averaged SSA emissions (ocean-only) 157
B.3.1 Global ocean-averaged SSA emission 158
B.3.2 Ocean-averaged SSA emissions over the tropics 159
B.3.3 Ocean-only averaged SSA emissions over the NH extratropics 160
B.3.4 Ocean-only averaged SSA emissions over the SH extratropics 161
B.3.5 Global ocean-averaged SSA emission using the regional ocean-averages 162
B.4 Converting from ocean-averaged to ocean-integrated values 162
B.5 Circulation-induced changes in SSA emission 163
B.5.1 Circulation-induced changes in ocean-integrated SSA emission 163
B.5.2 Circulation-induced changes in ocean-averaged SSA emission 164

C The sensitivity of MartMon emissions 165
C.1 Temperature sensitivity 166
C.2 Wind speed sensitivity 167

D Calculating components of the total feedback 168
D.0.1 Decomposing EEI due to feedback-related state changes 170

References 173

Introduction

On December 17, 1956, Carl-Gustaf Rossby appeared on the cover of Time magazine. The accompanying article highlighted not only his ongoing research on atmospheric circulation but also his strong interest in atmospheric chemistry, particularly during his time at Stockholm. Rossby was especially intrigued by the heterogeneous chemical composition of the atmosphere—focusing on sea-salt particles that contribute to certain types of rainfall. Although these particles may influence global climate, much about them remains unknown. For example, the chemical composition of airborne sea salts differs from that of oceanic salts. "No one knows why," the article states, "and Rossby wants to find out."

Rossby passed away shortly after this article was published, and it is striking that more than half a century later, many of the questions he raised remain largely unanswered. Sea-salt particles, or sea salt aerosols (SSA), are one of the most abundant aerosols over the global oceans, and present over 70% of the Earth's surface (Chen et al., 2020). When newly formed, SSA have a composition similar to that of seawater, primarily consisting of sodium, chloride, magnesium, sulfur, calcium, bromine, and potassium (Adachi & Buseck, 2015). During their atmospheric lifetime, SSA undergo transport, deposition and dispersion processes. They may also interact with anthropogenic emissions. Chen et al. (2020) postulates that such interactions can enhance the formation of particulate nitrate, which in turn alters the size distribution of aerosols and shortens their atmospheric lifetime. This redistribution effectively reduces the climate forcing associated with anthropogenic nitrate, highlighting the complex and often indirect role SSA play in modulating aerosol–climate interactions.

In the atmosphere, SSA can impact the climate directly through cooling by scattering solar radiation (Pachauri et al., 2014), and indirectly by acting as a source of marine cloud condensation nuclei (CCN) which affects cloud formation (O'Dowd & Smith, 1993). As one of the main sources of CCN over the oceans, SSA affects the radiative properties, amount, and lifetime of shallow marine clouds (Salter et al., 2014; Pierce & Adams, 2006). However, quantifying both the direct and indirect radiative effect of SSA on the climate remains a challenge due to uncertainties in how sea salt emissions are represented in climate models and the scarcity of comprehensive global observations of SSA concentration.

While the emissions and atmospheric burden of certain aerosols are expected to respond to climate change, there is no clear consensus on the future trends of major natural aerosols (Solomon, 2007; Stocker, 2014). It remains uncertain whether changes in cloud-aerosol interactions will dampen or amplify anthropogenic warming. Because natural aerosols like SSA are intrinsic to the climate system, they are not considered radiative forcing agents when the base state is at equilibrium. However, as climate change alters key parameters that influence aerosol production– such as wind and temperature – both the abundance of these aerosols and the contributions of their indirect and direct effects to the global energy budget are likely to change.

Most parameterizations of sea-spray production flux in global climate models assume that the primary driver of SSA production is surface 10-meter oceanic wind speed (Gong, 2003; Monahan et al., 1986; Nair et al., 2005; Vignati et al., 2001). Projected changes in surface wind speed under climate change scenarios vary regionally and seasonally, but the overall trend is either relatively modest (Eichelberger et al., 2008), or weak (J. Ma et al., 2016; McInnes et al., 2011; Paulot et al., 2020; Tegen & Schepanski, 2018; Yue et al., 2011). Recent developments in SSA studies have suggested that sea surface temperature (SST) has a significant effect on SSA production (Jaeglé et al., 2011; Mårtensson et al., 2003). Deike et al. (2022) has introduced a mechanistic sea spray generation function based on the physics of bubble bursting, which accounts for the influence of wind and waves through the breaking

distribution and entrained air flux, as well as temperature sensitivity via individual bubble-bursting mechanisms. However, the temperature dependence predicted by this mechanistic framework is not only weaker but also opposite in sign compared to the empirical relationship inferred by Jaeglé et al. (2011). Overall, the prospective temperature dependency makes SSA potentially responsible for climate feedback, although the sign and magnitude of this effect in a warmer climate remains a source of active debate.

In order to constrain the direct and indirect radiative effect of SSA on the climate, sources of errors between modeled and observed concentration of SSA must be adequately addressed. This requires improvement of SSA representation in climate models that further requires better understanding of the physical mechanisms that impact SSA production. To this end, we construct a framework for SSA within the planetary boundary layer (PBL) and then formulate and assess three key questions aimed at understanding the discrepancies between simulated and observed SSA concentrations in Chapter 1. We compare in situ measurements of SSA from NOAA PMEL cruises to model simulations of SSA from the GEOS-Chem global chemical transport model. The three limiting cases that provide possible sources of errors contributing to errors between modeled and observed SSA concentration are as follows: 1) errors in SSA emission, 2) errors in the vertical transport of SSA concentration, and 3) subgrid variability, sampling discrepancies, and/or temporal dependencies arising from the horizontal transport of SSA.

To further explore the physical mechanisms influencing SSA production, we assess the performance of various sea spray generation functions in Chapter 2, including their sensitivity to sea surface temperature (SST) and wind speed. We include the new SSA emission formula developed in Deike et al. (2022), which was developed based on the physics of bubble bursting and does not require tuning parameters to obtain a particular wind or temperature dependence. This formula has also not been implemented in climate model since its inception. We run the model with the four different sea-spray generation formulations and observe how different representations of sea-spray generation affects the geographic distribution of

SSA emission and concentration through changes in aerosol optical depth (AOD). This allows us to explore how changes in the representation of SSA emissions may influence the coherence between modeled and observed AOD, though the conclusions are constrained by the limited scope of the experiments and the use of model tunings optimized for MartMon.

SSA emissions have gained attention as one of the primary aerosols used for geoengineering via marine cloud brightening (MCB) due to its ability to cool the atmosphere. Latham (1990, 2002) first proposed spraying sea salt aerosols in the tropical marine boundary layer to offset global warming. Doing so would reduce temperatures by reflecting sunlight directly (Partanen et al., 2012), increase cloud albedo (Twomey, 1977), and extend cloud lifetimes by altering cloud microphysical properties (Albrecht, 1989). In Chapters 3 and 4, we deploy a Geoengineering Model Intercomparison Project (GeoMIP) protocol, G4sea-salt, where SSA emission is increased uniformly over the marine tropics to reduce the top-of-atmosphere (TOA) earth's energy imbalance by 2 W m^{-2}, in the GFDL AM4 and coupled model (CM4; Held et al. (2019)). In Chapter 3, we analyze the rapid adjustments and circulation responses occurring from this geoengineered increase in SSA emissions and compare changes in the equatorial Pacific temperature gradient from G4sea-salt to that of a quadrupling of CO_2. Ahlm et al. (2017); Alterskjær et al. (2012); Kravitz et al. (2013) and others have looked at the radiative forcing from MCB following GeoMIP. However, geoengineered increases in SSA emissions have not been analyzed as an external forcing applied to the climate system. In Chapter 4, we attempt to isolate and quantify feedbacks resulting from geoengineered increase in SSA emission, which is treated as a forcing on the climate system, by applying a forcing analysis similar to that for abrupt-4xCO2.

Overall, this thesis aims to fill three knowledge gaps): 1) what are the physical processes that are relevant for discerning why modeled SSA concentration differ from observations, 2) what are the limitations of improving the physical representation of SSA production and 3) what are the circulation feedbacks and radiative effects of regionally enhancing SSA in

the context of geoengineering. We address these questions in this order. Lastly, we present conclusions and a discussion of these results.

0.1 Prior presentation & publication

Parts of this work has been previously presented as conferences and workshops. Chapter 1 has been presented at the American Geophysical Union (AGU) 2021 Fall meeting in the session Aerosols, Clouds, Convection, and Precipitation III and as a guest speaker at the Department of Earth & Atmospheric Sciences (EAS) seminars at the City College of New York (CCNY). Chapter 3 and 4 have been presented at the 2023 Graduate Climate Conference at Massachusetts Institute of Technology/Woods Hole Oceanographic Institution, and AGU 2023 Fall meeting in the session titled Solar Radiation Modification for Climate Intervention, and the American Meteorological Society's (AMS) 16th Symposium on Aerosol Cloud Climate Interventions. Presentations of Chapter 3 and 4 received the Outstanding Student Presentation Award (OSPA) from AGU and the Best Student Presentation and Poster Award from the American Meteorological Society's (AMS) 16th Symposium on Aerosol Cloud Climate Interventions. The contents of Chapter 3 have been prepared as a manuscript intended for submission to Geophysical Research Letters and is currently undergoing internal review at GFDL at the time of this thesis submission.

Chapter 1

Integrating in-situ measurements and models to understand errors in sea salt aerosol emissions, transport, and sub-grid processes

1.1 Abstract

Sea salt aerosols (SSA) affect the climate radiative balance directly by reflecting incoming solar radiation and indirectly as a source of marine cloud condensation nuclei which affect cloud formation. However, differences between observations and model estimates of SSA concentration have long plagued assessments of the magnitude and scale of the potential cooling effect SSA has on the climate. This in turn translates into variabilities in global climate model (GCM) estimates of climate sensitivity. To examine the possible sources of errors between simulated and observed SSA, we combine in situ SSA measurements retrieved from NOAA PMEL cruise expeditions and simulations of SSA concentration from the GEOS-Chem global chemical transport model to constrain the production of SSA using an idealized model. We explore whether the discrepancies between modeled and observed SSA concentration can be attributed to: 1) emission errors, 2) vertical transport errors, or 3) subgrid variability, sampling errors, and/or time dependence. Our analysis shows the viability of our three alternative explanations, but it is likely that the differences between

the model and the observed SSA concentration result from a combination of all three explanations. Therefore, efforts to accurately model SSA in the atmosphere must account for a variation of these three explanations.

1.2 Introduction

Globally, the source of sea salt aerosols (SSA) is estimated to be about 0.3-30$\times 10^{12}$ kg/yr, which is a significant component of the total natural aerosol production (Lewis et al., 2004). SSA concentration is relatively smaller than that of anthropogenic aerosols (Schulz et al., 2004), but their role is significant because of their broad geographic distribution and role in cooling the atmosphere. Despite their abundance over the marine boundary layer (MBL), the impact of SSA on climate is not fully understood and the mechanisms of SSA production in SSA source functions are relatively underdeveloped (Lewis et al., 2004).

Based on a synthesis of estimations, the negative direct radiative effect of SSA ranges from -0.3 to -1.2 W m^{-2} (Heald et al., 2014a; Paulot et al., 2020; Grini et al., 2002). Although the indirect radiative effects of SSA resulting from SSA altering cloud properties remain a poorly constrained process with estimates ranging from -2.9 to +0.3 W m^{-2} (X. Ma et al., 2008). Ultimately, the wide range of the radiative effects of SSA reflects the uncertainties in the magnitude of the cooling effect SSA has on the climate, which arises from uncertainties in the modeling of sea salt emissions and the formulation of emission functions (Ayash et al., 2008; H. M. Horowitz et al., 2020).

The most prominent mechanism relevant for the production of SSA is the release of entrained air bubbles that burst during whitecap formations. Early research attempts to constrain the source function of the SSA were conducted through laboratory and field experiments ranging from whitecap simulation tanks to photographic observations of whitecaps (Callaghan, 2013; Monahan et al., 1986; M. Smith et al., 1993). However, because of limited direct SSA flux measurements at the sea–atmosphere interface, it is difficult to evaluate SSA

production at a global scale. In initial modeling efforts, the formulation of SSA emission flux was constrained by relating the production of SSA to the whitecap fraction expressed as a function of particle size and surface wind speed (10 meters) (Gong et al., 1997; Gong, 2003; Monahan et al., 1986; Nair et al., 2005; Parameswaran et al., 1995; Woodcock, 1953; Vignati et al., 2001). The source functions for SSA vary in the magnitude of their dependence on wind speed, the range of SSA radii included in global mass flux estimates, and the methodology used to generate the formulation (Andreas et al., 1995).

Wind speed is widely accepted to be a significant driver of SSA production, but the extent to which it influences SSA concentrations and discrepancies between models and observations can vary depending on the specific conditions and the location being studied. Furthermore, there may be a possibility of horizontal transport of SSA in areas with high wind speeds (Gong et al., 1997; Gong, 2003; Kinne et al., 2003). The possibility of horizontal transport of SSA in areas with high wind speed leads to poor correlations between local wind speeds and observed sea salt mass concentrations (Satheesh & Moorthy, 2005; P. Quinn et al., 2000). In the context of large climate perturbations, global SSA emissions will change depending on the response of the surface wind speed. Potential changes in surface wind speed due to climate change vary geographically and seasonally; Expected changes in wind speed in a warmer climate are estimated to be relatively modest (Eichelberger et al., 2008) or weak (J. Ma et al., 2016; McInnes et al., 2011; Paulot et al., 2020; Tegen & Schepanski, 2018; Yue et al., 2011).

However, recent developments in SSA studies have suggested that sea surface temperature (SST) has a significant effect on SSA emission by modifying the physical properties of surface ocean water (Forestieri et al., 2018; Jaeglé et al., 2011; S. Norris et al., 2008; Mårtensson et al., 2003; Sellegri et al., 2006). This prospective temperature dependency makes SSA potentially responsible for negative climate feedback, resulting in a more negative radiative effect in a warmer climate (Forestieri et al., 2018; Jaeglé et al., 2011; Struthers et al., 2013). Through direct and indirect effects, the increased quantity of SSA in the atmosphere leads

to more reflection of solar radiation from SSA. This culminates in cooling the atmosphere, potentially damping the warming from climate change. Simulations adding the temperature dependence to the SSA emission found a negative radiative feedback and a lower climate sensitivity (Dunne et al., 2020; Paulot et al., 2020). Furthermore, incorporating the SST dependency on the source function increases the correlation between the simulated and observed SSA concentration, as shown in Barthel et al. (2019), Jaeglé et al. (2011), and S. Liu et al. (2021).

Possible mechanisms to describe how SST affects SSA production refer to the rate of gas exchange between the bubble and surrounding fluids and have been observed in laboratory experiments in Mårtensson et al. (2003) and Sellegri et al. (2006). Mårtensson et al. (2003) is noted for presenting a formulation of the SSA flux that includes an explicit SST dependency, determined by laboratory measurements of the flux of particles produced from a whitecap area.

However, Jaeglé et al. (2011) is best known for modifying the wind-speed-dependent SSA source function from Gong (2003) into one that considers a potential SST dependency. Jaeglé et al. (2011) compared in-situ observations of SSA concentration retrieved from the 6 NOAA Pacific Marine Environmental Laboratory (PMEL) cruises with model output from the Goddard Earth Observing System (GEOS-Chem) global chemical transport model using Gong's wind speed-dependent SSA formulation. Jaeglé et al. (2011) then assumed that the production of SSA particles in a given time and location is balanced by removal at the same time and location and that small-scale advective properties of the atmosphere do not affect the local production of SSA. Fitting a relationship between the mass concentration of the PMEL observations and GEOS-Chem outputs to SST with a third-order polynomial function, Jaeglé et al. (2011) presents an attempt to address the differences between the model and observations by attempting to correct the modeled emissions.

Studies observe that high emissions of coarse-mode particles are caused by warm SST, while the opposite is true for ulta-fine particles (Struthers et al., 2013). However, there

remains active discourse on the SST dependency of SSA emissions: whether SSA production is independent of (Gong, 2003), suppressed by (Christiansen et al., 2019), or enhanced by SST (Jaeglé et al., 2011; S. Liu et al., 2021; Mårtensson et al., 2003; Sellegri et al., 2006). For example, Forestieri et al. (2018) reported an increase (2.1-4.1%/°C) in SSA production with an increase in temperature over 2-25°C, while Christiansen et al. (2019) reported that total particle production reaches a minimum at around 6-10°C and then asymptotes as temperature increases up to 35°C. The disparate reported effects of SST on SSA production demonstrates that the impacts of SST on SSA production remain unclear. Recent work from Deike et al. (2022) developed a mechanistic sea spray generation function that is based on the physics of bubble bursting. The physical mechanism of bubble bursting integrates the role of wind and waves via the breaking distribution and entrained air flux, and sensitivity to temperature via individual bubble-bursting mechanisms. However, they noted that the temperature sensitivity coming from their proposed scalings is weaker than that empirically derived by Jaeglé et al. (2011).

To explore the possible sources of errors between the modeled and observed concentrations of SSA, we construct an idealized model to address the differences between the SSA concentrations recovered from NOAA Pacific Marine Environmental Laboratory (PMEL) cruise expeditions and modeled from the GEOS-Chem global chemical transport model to constrain the production of SSA. The modeled and observed SSA concentrations used in this study are identical to those employed by Jaeglé et al. (2011) to derive the SST dependency on SSA production. Moreover, these concentrations have been shown to exhibit significant discrepancies between the modeled and observed SSA values.

To explore the possible sources of errors between modeled and observed SSA concentrations, we constructed a framework for SSA within the planetary boundary layer (PBL), subsequently proposing and evaluating three inquiries intended to elucidate the discrepancies between simulated and observed SSA concentrations. The initial inquiry examines prevailing interpretations of addressing the disparities between the modeled and observed SSA concen-

trations by altering the SSA emission formulation, while presuming horizontal homogeneity and the absence of the time rate of change for the mean quantities of the particles. The second inquiry also has similar assumptions for mean quantities, but scrutinizes the treatment of the vertical transport of SSA in the model and observations. The third inquiry considers the implications of subgrid variations, sampling errors, and/or temporal dependencies arising from the horizontal transport of SSA. We argue that these three limiting cases play an important role in explaining the differences between the model and the observed SSA concentration. These limiting cases likely co-occur, and the magnitude of their impacts could vary depending on the specific situations. However, here we will consider each of these cases independently to explore their plausibility and as a foundation for our future analysis exploring potential alternatives.

1.3 Methodology

1.3.1 In situ observations of SSA concentration

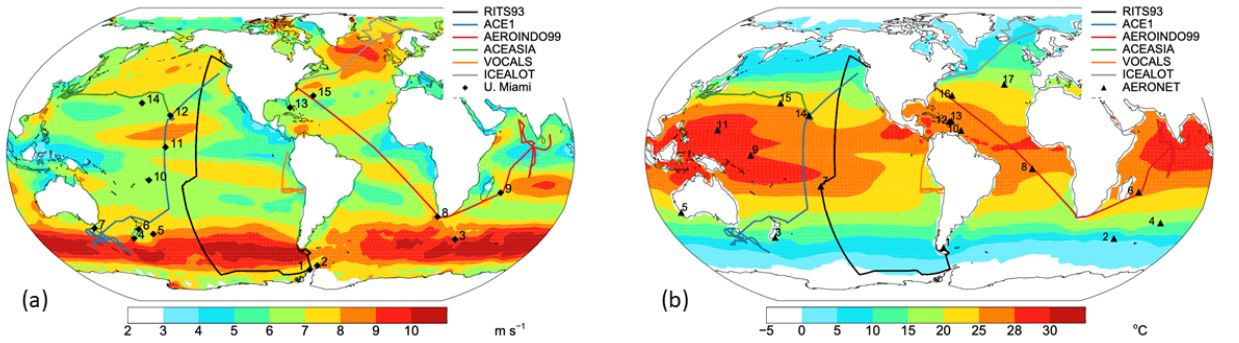


Figure 1.1: Fig. 1 from Jaeglé et al. (2011) showing the location of the observations. The 6 PMEL cruise tracks are indicated by the color lines and plotted against (a) the mean surface (10-m) wind speeds from QuikSCAT for 2008 for reference and (b) the annual mean sea surface temperature from GEOS-5 for 2008. This study does not include observations from the University of Miami-based sites (black diamonds).

We retrieve ocean observations of the SSA concentration from cruise expeditions conducted by the https://saga.pmel.noaa.gov/data/PMEL between 1993 and 2008 (Table 1.1).

The SSA concentration observations were collected on six PMEL cruises: the First Aerosol Characterization Experiment (ACE1) cruise, Indian Ocean Experiment (AEROINDO99, hereafter AERO), the Radiatively Important Trace Species cruise (RITS93), the Asian Pacific Regional Aerosol Characterization Experiment (ACEAsia), the VAMOS Ocean-Cloud, Atmosphere-Land Study (VOCALS), and the International Chemistry Experiment in the Arctic LOwer Troposphere (ICEALOT). These observations were chosen because the ship tracks cover a wide geographical range as shown in Fig. 1.1.

Table 1.1: The PMEL cruises, the date of their expedition, range of sampling time (hr), average SSA concentration ($\mu g/m^3$), range of observed wind speed (m/s) and SST (°C) retrieved during the duration of the cruise.

Cruise	**Date**	**Sampling time range (hr)**	**Average Coarse mode SSA ($\mu g/m^3$)**	**Wind Speed range (m/s)**	**SST (°C)**
AERO	Jan-Mar 1990	2.58-11.85	6.62	0.96-10.85	20.51-30.23
ACE	Oct-Dec 1995	1.90-36.14	5.50	3.61-11.94	7.29-28.49
RITS93	Mar-Apr 1993	8.11-47.16	6.86	2.78-17.43	0.21-29.25
ACEASIA	Mar-Apr 2001	2.52-22.17	5.88	1.99-13.29	9.87-22.43
ICEALOT	Mar-Apr 2008	5.18-23.32	5.86	2.13-16.27	-0.08-12.09
VOCALS	Oct-Dec 2008	5.48-35.03	5.32	3.44-10.35	17.18-20.51

SSA mass concentration is derived from the concentrations of Na^+ and Cl^- recovered by ion chromatography from PMEL cruises and averaged over the impacter sampling period ranging from 2 to almost 48 hours. Observations are retrieved from air drawn in at an average of 18 meters above the sea surface through a heated mast 5 meters above the aerosol measurement container. There, two-stage multijet cascade impacters are used to determine the concentration of Na^+ and Cl^-. However, RITS93 used a seven-stage impacter. Air drawn into the instrument inlet is kept at constant relative humidity (RH): RITS93 → RH=30%, ACE1 → RH=30–45%, ACE-ASIA, AERO and VOCALS → RH=55%, and ICEALOT → RH = <25%. RITS93 samples particles with dry geometric radii of 0.3 to 3.05 μm while ICEALOT samples between 0.4 and 3.8 μm. In GEOS-Chem, 0.01-0.4 μm is used for the

accumulation mode and 0.4 to 3.8 μm for the coarse mode. For all other cruises, bin sizes 0.01 to 0.3 μm are used for the accumulation mode and 0.3 to 3 μm for the coarse mode.

The SSA concentration (C_{SSA}) is calculated as P. K. Quinn and Bates (2005):

$$C_{\mathrm{SSA}} = \mathrm{Cl}^- + 1.47 \times \mathrm{Na}^+ \tag{1.1}$$

where Cl^- and Na^+ are expressed in mass concentrations (kg m^{-3}) and the factor of 1.47 is the mass ratio of (Na^+ + K^+ + Mg^{+2}+Ca^{+2}+SO_4 +HCO3$^-$)/Na^+ (Holland, 2020). This assumes that all measured Na^+ and Cl− are derived from seawater.

We convert units of PMEL SSA mass concentration from μg m^{-3} to kg m^{-3} (hereafter, $\overline{C}_{\mathrm{obs}}$) and are provided as duration averaged observations.

PMEL anemometer records wind speed observations as one-minute averages. The filtered 1 minute data are then averaged into 30-minute periods. Wind speed measurements are taken from a mast at heights ranging from 10-20 m above sea level. The wind speed is then converted to a wind speed at 10 m using the power law wind profile exponent in Hsu et al. (1994). Wind speed data are taken in instantaneous 1-minute sets, averaged into 30-minute bins and then averaged over the duration of the ship's sampling time (Fig. 1.2). Note that 1-minute instantaneous observations of wind speed are not provided for ACE and RITS93.

The seawater temperature is measured using a thermosalinograph (Seabird SBE-21 serial number 843) and recorded in the Scientific Computer System (SCS) system. Temperature data were stored as 30-minute averages for all ships and then averaged over the duration of the sampling period. This duration-averaging process smoothens large variances in wind speed measurements and/or SST during these sampling durations, as illustrated in the inset for ICE in Fig. 1.2.

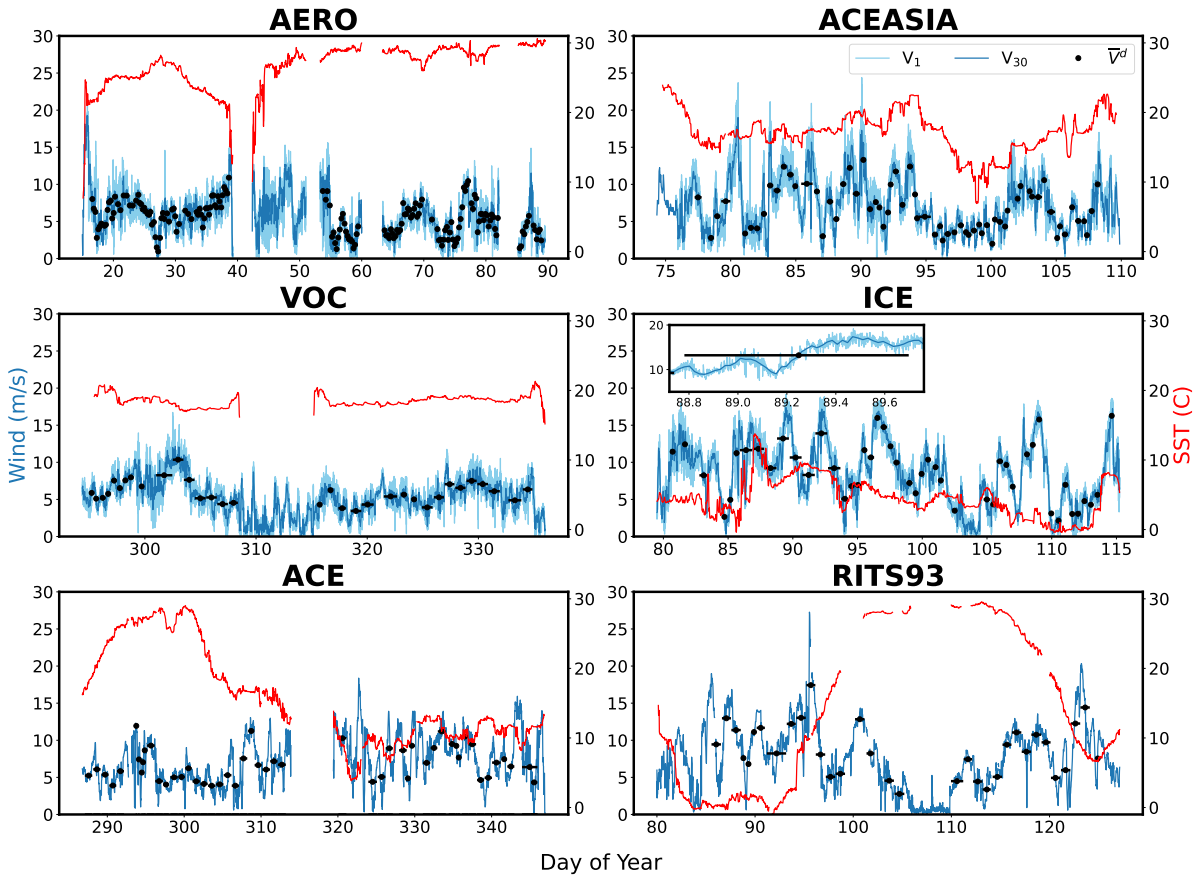


Figure 1.2: One-minute observations of wind speed ($\mathbb{V}_1$; sky blue), thirty-minute observations of wind speed ($\mathbb{V}_{30}$, dark blue), the average of the thirty-minute wind speed over the duration of the sampling period ($\overline{\mathbb{V}}^d$; black) and SST (red) observed during the duration of the cruise. An inset figure provides a zoomed-in view of averaged and high frequency (30-minute and duration averaged) wind speed over a single sampling period for ICE.

1.3.2 Convective precipitation data from ERA5

The ERA5 reanalysis for global climate and weather combines model data with observations to provide a globally complete and consistent data set of hourly estimates for a large number of atmospheric, ocean waves, and land surface quantities (Hersbach et al., 2018). The ERA5 reanalysis has been regridded to a regular lat-lon grid of 0.25 degrees for the reanalysis and 0.5 degrees for the uncertainty estimate (0.5 and 1 degree, respectively, for ocean waves). We use single pressure level (pressure at 2m) hourly products. Convective precipitation retrieved from ERA5 refers to the accumulated precipitation that falls to the Earth's surface over hourly intervals, as determined by the closest available hourly time step in the dataset. This

is generated by the convection scheme in the European Center for Medium-Range Weather Forecasts (ECMWF) Integrated Forecasting System (IFS). Units for convective precipitation (centimeters of water depth) represent the depth of the water if it were evenly spread over a grid box.

1.3.3 GEOS-Chem model simulations of SSA concentration

We compare PMEL cruise observations with GEOS-Chem simulations of SSA concentration using the Gong (2003) SSA formulation. We use the GEOS-Chem results reported and described by Jaeglé et al. (2011), using GEOS-Chem version v8-02-04 (http://acmg.seas.harvard.edu/geos/). For GEOS-Chem simulations, the native field is degraded to a horizontal resolution of $2^\circ \times 2.5^\circ$. SSA concentration is modeled at 30-minute intervals at the closest time and location along the cruise track and then averaged to match the PMEL cruise ship sampling duration. We use a subscript of $'geos'$ to refer to the GEOS-Chem simulations of the SSA concentration ($\overline{C}_{\mathrm{geos}}$).

In GEOS-Chem, the Slinn and Slinn (1980) deposition model is used over the ocean. The marine boundary layer is divided into a viscous sublayer with a surface layer above. In the viscous sublayer, brownian diffusion, impaction, and gravitational sedimentation are taken into account for aerosol deposition. In the surface layer, turbulent diffusion and gravitational settling are taken into account. Furthermore, scavenging SSA in convective updrafts, rain and washout are accounted for in the wet deposition of SSA (H. Liu et al., 2001).

GEOS-Chem incorporates assimilated meterological observations from NASA's Goddard Earth Observing System (GEOS). When the wind speed modeled in GEOS-Chem is compared with the observed wind speeds in Jaeglé et al. (2011) (Fig. 1.3), it generally captures the observed wind speed quite well, with a mean model/obs ratio of 0.99 and a correlation of r = 0.84, although there are quite a few points for which the model and observation differ by $> 25\%$. Therefore, any mismatch in SSA concentration between model and observations is likely not due to errors in modeled wind speed.

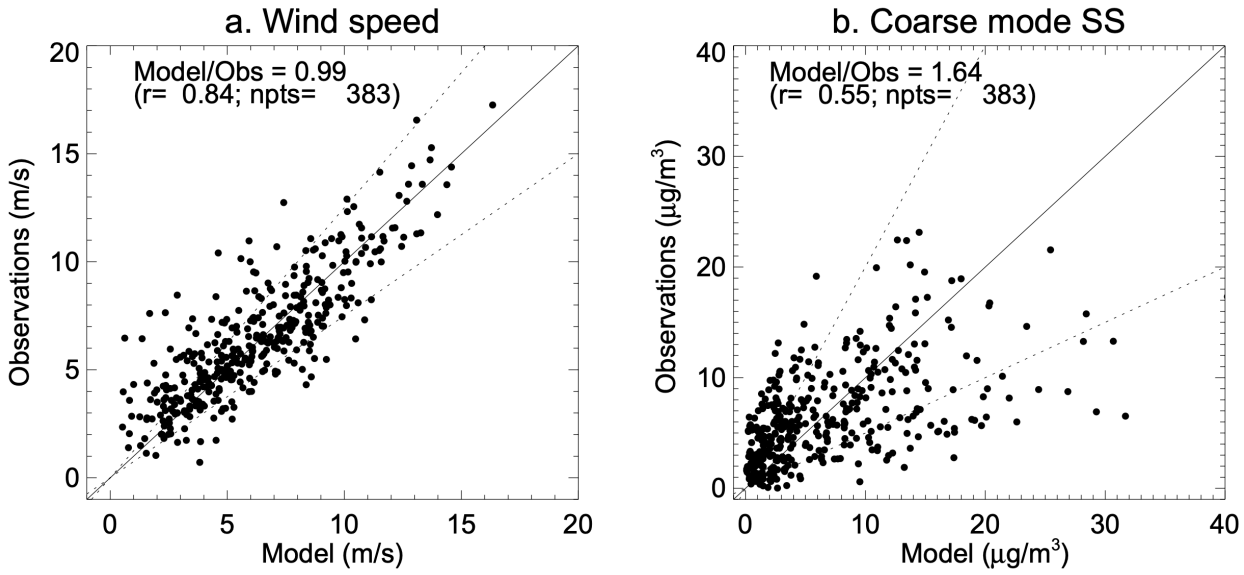


Figure 1.3: Comparing model and observations for the 6 PMEL cruises: (a) the 10-m wind speed, (b) coarse SSA mass concentrations modified from Fig. 4 from Jaeglé et al. (2011)

.

1.3.4 Calculating SSA emission

In this study, we used four emission formulation configurations: 1) MartMon (Mårtensson et al. (2003) and Monahan et al. (1986)), 2) Gong (Gong, 2003), 3) Jaegle (Jaeglé et al., 2011), and 4) Deike (Deike et al., 2022).

Martensson et al., 2003 & Monahan et al., 1986

The standard setup for AM4 uses the Mårtensson et al. (2003) for particles less than 1.4 μm radius) and Monahan et al. (1986) for particles greater than 1.4 μm).

Mårtensson et al. (2003) found a temperature dependence in the particle number emission flux. This formulation was developed using observations of the size distribution of the bubbles and aerosols produced retrieved from experiments conducted in a closed chamber and is presented as follows:

$$\frac{\mathrm{d}F_{\mathrm{mart}}}{\mathrm{d}\log D_p} = \Big(A_k T + B_k\Big) \times W \tag{1.2}$$

where A_k and B_k are size-dependent polynomials fitted to coefficients (following Mårtensson et al. (2003)), T is the sea surface temperature (K), D_p is the dry diameter, and W is the percent of the area covered by whitecap presented as a function of wind speed (m/s) from Monahan et al. (1986).

$$A_k = c_4 D_p^4 + c_3 D_p^3 + c_2 D_p^2 + c_1 D_p + c_0$$
$$B_k = d_4 D_p^4 + d_3 D_p^3 + d_2 D_p^2 + d_1 D_p + d_0$$
$$W = 3.84 \times 10^{-4} u_{10\text{ m}}^{3.41}$$

Although the Martensson formulation has both wind speed and temperature dependence, the temperature dependence is much weaker than that present in Jaeglé et al. (2011) (Paulot et al., 2020).

For supermicron particles, the Monahan et al. (1986) formulation is used to calculate emissions. This formulation is derived from laboratory measurements of aerosol fluxes and does not include any temperature dependence. The Monahan et al. (1986) emission flux is defined as:

$$\frac{\mathrm{d}F_{\text{mon}}}{\mathrm{d}r_{80}} = 1.373 \times u_{10\text{ m}}^{3.41} \times r_{80}^{-3} \times (1 + 0.057 \times r_{80}^{1.05}) \times (10^{1.19e^{-B^2}}) \tag{1.3}$$

where r_{80} is the particle radius at 80% humidity and $B = (0.380 - \log(r_{80}))/0.650$.

A combination of the Martensson formulation for smaller submicron particles and Monahan formulation for larger particles will be referred to as MartMon.

Gong et al., 2004

Based on the semi-empirical formulation of SSA derived by Monahan et al. (1986), Gong (2003) extended the range of the original equation to below 0.2 μm:

$$\frac{\mathrm{d}F_{\text{gong}}}{\mathrm{d}r_{80}} = 1.373 \times u_{10\text{ m}}^{3.41} \times r_{80}^{-A}(1 + 0.057 \times r_{80}^{3.45}) \times 10^{1.607e^{-B^2}} \tag{1.4}$$

where $A = 4.7(1 + \theta \times r_{80})^{-0.017 \times r_{80}^{1.44}}$, $B = (0.433 - \log(r_{80}))/0.433$, θ is an adjustable parameter which controls the size distribution of the submicron aerosols and is set to 30, and $\frac{\mathrm{d}F_{\mathrm{gong}}}{\mathrm{d}r}$ is the density function in units of particles m^{-2} s^{-1} $\mu\mathrm{m}^{-1}$. When evaluated against observations for submicron SSA concentrations reported by O'Dowd et al. (1997), the Gong equation captured the peak in submicron SSA concentration around $r_{80} = 0.2$ μm and increase going from $r_{80} = 0.05$ to 0.2 μm. This indicates significant improvement in the applicability of this formulation to a wider size range to simulate both the number and mass distribution of SSA down to 0.03 μm.

Jaegle et al., 2011

Jaeglé et al. (2011) investigated the possibility that emissions of SSA depend not only on the wind speed but also on other environmental variables, in particular SST. As discussed above, SSA emissions may be affected by SST as a result of the dependency of the kinematic viscosity of water and the bubble behavior with temperature (Forestieri et al., 2018; Jaeglé et al., 2011; S. J. Norris et al., 2013).

Jaeglé et al. (2011) compared in-situ observations of SSA concentration retrieved from the 6 NOAA Pacific Marine Environmental Laboratory (PMEL) cruises with model outputs from the GEOS-Chem global chemical transport model using Gong's wind speed dependent SSA formulation. Compared to the typical lifetime of SSA particles in the range of 1 to 10 μm, which is about 3 days (O'Dowd & Smith, 1993; Junge, 1972), the average atmospheric residence time of coarse SSA particles with $r_{80} = 0.6$-9 μm in GEOS-Chem is 6 hours (Jaeglé et al., 2011). Using GEOS-Chem, Jaeglé et al. (2011) found that dry deposition accounts for 70% of the total deposition for PMEL cruise observations and is therefore a dominant removal mechanism of SSA particles.

Jaegle assumes proportionality between SSA concentration and emission. For coarse SSA particles ($r_{80} = 0.6$–8 μm) and observations with wind speeds greater than 6 m/s to focus on regions with moderate to high wind speeds with locally generated SSA, Jaegle

derived a relationship between concentration biases between modeled and observations with SST. Fitting this relationship to a third-order polynomial function, they modified the source function in Eq. 1.4 to derive an empirically derived temperature- and wind-speed-dependent SSA source function. We consider the emission formulation derived in Jaeglé et al. (2011), which is currently implemented in the Earth System Model Version 4 (ESM-4) configuration used by Geophysical Fluid Dynamics Laboratory (GFDL):

$$\begin{aligned}\frac{\mathrm{d}F_{\text{jaegle}}}{\mathrm{d}r_{80}} = (0.3 + 0.1 \times T - 0.0076 \times T^2 + 0.00021 \times T^3) \\ 1.373 \times u_{10\text{ m}}^{3.41} \times r^{-A}(1 + 0.057 \times r_{80}^{3.45}) \times 10^{1.607e^{-B^2}}\end{aligned} \tag{1.5}$$

where T is the SST expressed in °C and the coefficients A and B are the same as referenced for Eq. 1.4.

Deike et al., 2022

The SSA formulation from Deike et al. (2022) is a mechanistic sea spray generation function that is based on the physics of bubble bursting. Deike et al. (2022) considers sea state effects through breaking distribution, number flux of bubbles, and air entrainment. The sum of these three mechanisms for SSA production is represented as:

$$F_{\text{deike}}(r_d) = \sum F_d(r_d) \tag{1.6}$$

Where F_d refers to the bursting mechanism, the air entrainment from the spectral model and the bubble production by the breaking wave and is defined as the number of drops per unit of surface ocean area per unit time and r_d refers to the mean drop radius. The resulting SSA source is a function of the volume of air entrained (V_A). V_A (m/s) can also be recovered as a function of 10-m wind speed (Deike et al., 2022) using the following equation:

$$V_A = 1.5 \cdot 10^{-7}(U_{10\text{ m}} - 2.5)^{2.5} \tag{1.7}$$

Note that there is a limiting case at $U_{10\ \mathrm{m}} < 2.5$ where V_A is zero. We refer to the emission calculated with the volume of air entrained recovered as a function of the 10-m wind speed as E_{Deike}.

Comparison of the 4 emission configurations

Figure 1.4 presents SSA emissions calculated using four parameterization configurations, with 30-minute averaged wind speed and SST as inputs. The nonlinear relationship between wind speed, SST, and SSA production flux implies that the averaging method used for meteorological parameters can impact emission estimates. In particular, averaging emissions calculated from high frequency wind speed data yields larger emission magnitudes compared to emissions calculated using duration-averaged wind speed.

For AERO, which sampled over warm waters, Jaegle has the highest averaged emission over the whole length of the ship, followed by Deike, Gong, and MartMon. For ACEASIA, ACE, VOC, and RITS93, which also sampled at relatively warm temperatures, Deike has the largest averaged emission, followed by Gong, Jaegle, and MartMon. In contrast, ICE, which was sampled at cold temperatures, exhibits a different pattern, with Gong having the highest average emission, followed by Deike, MartMon, and Jaegle.

In GEOS-Chem, SSA concentrations and emissions are output at 30-minute intervals. To match the PMEL sampling period, these outputs are then averaged over the sampling duration. For consistency, our subsequent analysis will use SSA emissions calculated using 30-minute average wind speeds, averaged up to the PMEL sampling period.

1.4 Governing framework

Breaking wave crests generate SSA emissions and are the main source of SSA production (Fig. 1.5). SSA can be transported by vertical and horizontal advection, turbulent mixing, and convective mass fluxes. SSA can be removed from the atmosphere by wet deposition and

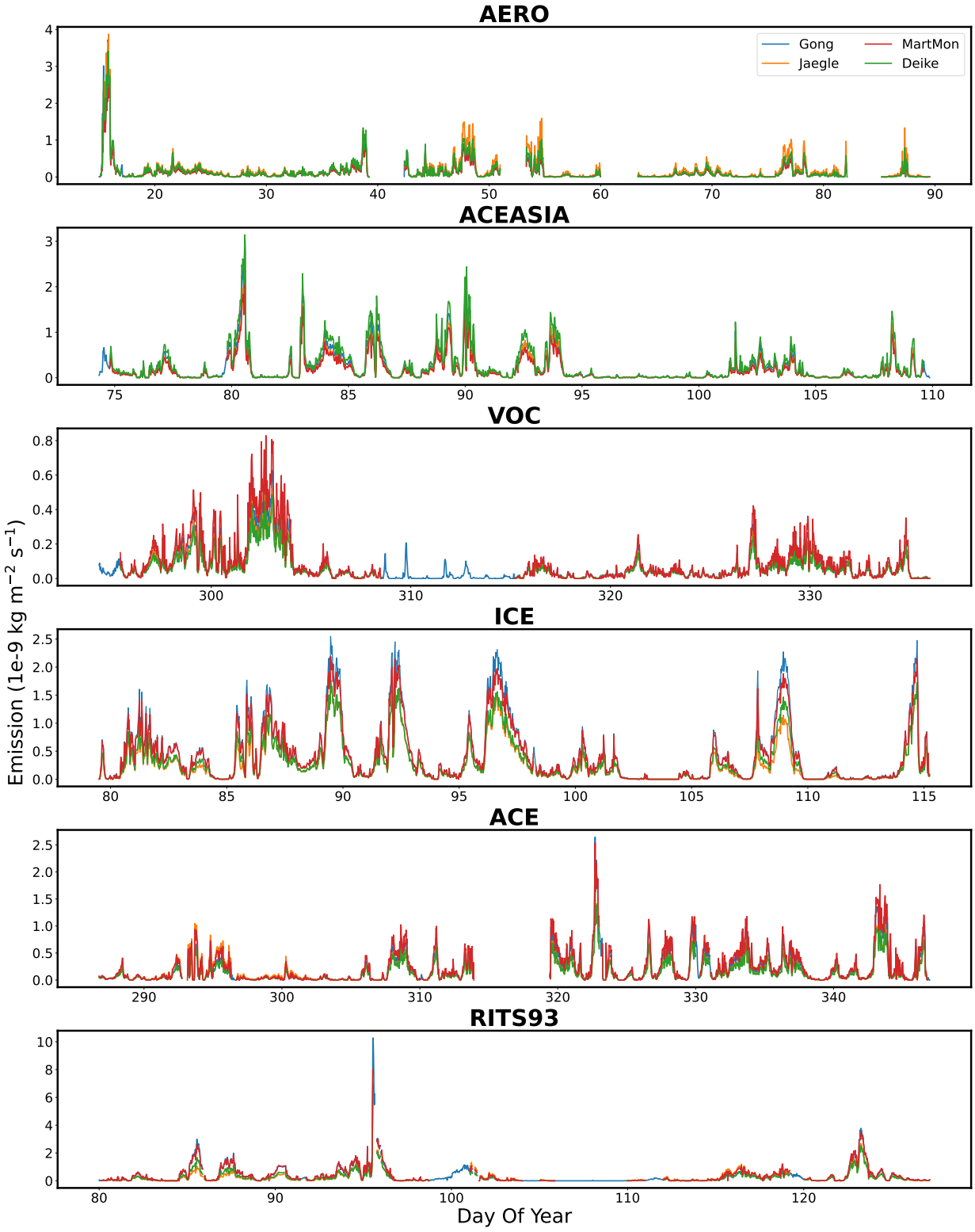


Figure 1.4: Calculations of emissions using Gong, Jaegle, MartMon and Deike for each thirty-minute observation of wind speed.

gravitational settling (to the surface at z=0). SSA particles can be scavenged by other particles or larger droplets (hence, coagulation scavenging), they could coagulate amongst themselves or with other aerosol particles to form bigger particles (hence, coagulation growth), or they could have water vapor (or other vapors) condense onto them to make them grow in size (hence, hygroscopic growth).

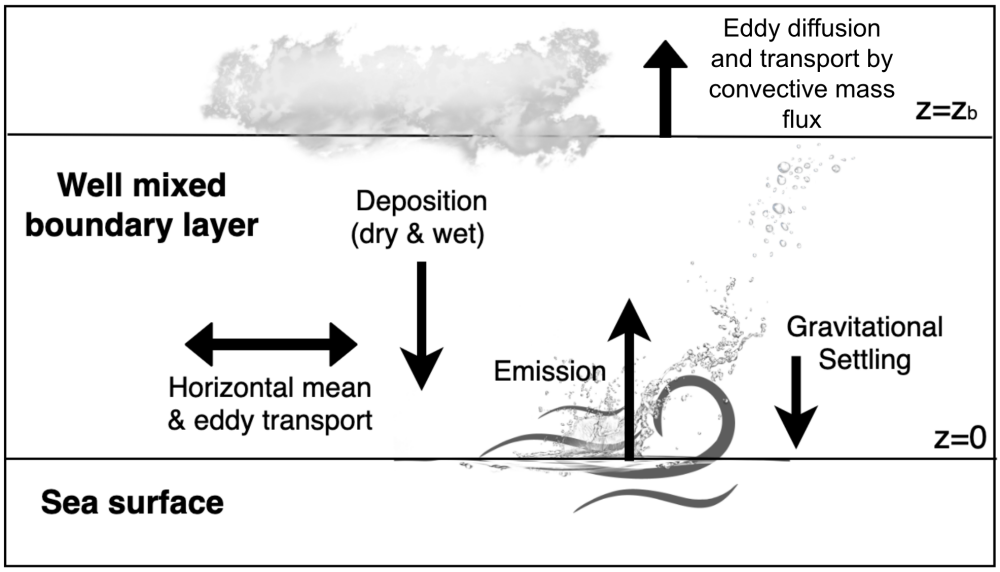


Figure 1.5: A diagram of sea salt aerosols (SSA) and their production, deposition, and transport in the atmosphere.

We begin with a general dynamic equation of aerosols, which offers a governing equation for the time evolution of atmospheric aerosol particles. This equation applies to both coarse and fine SSA particles ranging from 0.055 to 10 μm in diameter and shows the mass conservation of SSA and captures the physical processes shown in Fig. 1.5. However, focusing only on coarse SSA particles, the change in distribution function resulting from particle growth due to condensation of the vapor phase materials, collision of particles, or clustering of gas molecules that act as condensation sites is negligible (Lewis et al., 2004; van den Berg et al., 2000). Eq. 1.8 postulates that the local trend in SSA concentration is equal to the difference between the emission of SSA and the deposition and transport (flux divergence

and convergence) of SSA. This form is in height (z) coordinates.

$$\frac{\partial X}{\partial t} = P_x - L_x - \Bigg(\underbrace{u\frac{\partial X}{\partial x} + v\frac{\partial X}{\partial y} + w\frac{\partial X}{\partial z}}_{\vec{u}\cdot\nabla X} \Bigg) \tag{1.8}$$

where the flux is positive directed upwards, X refers to the SSA mass mixing ratio (kg of salt / kg of air), P_x (kg of salt/kg of air/s) refers to the production of SSA, L_x (kg of salt/kg of air/s) refers to the loss of SSA, and $\vec{u} \cdot \nabla X$ reflects the horizontal and vertical transport of SSA ($\vec{u} \cdot \nabla X = (u\frac{\partial X}{\partial x} + v\frac{\partial X}{\partial y} + w\frac{\partial X}{\partial z})$. The advective terms ($\vec{u} \cdot \nabla X$) describe the change in SSA concentration due to the bulk flow of SSA.

We can also expand the terms of production (P_x) and loss (L_x). It is important to note that we integrate this equation across all size bins for SSA. We get:

$$P_x - L_x = -\frac{1}{\rho}\frac{\partial F_{\text{depo,emis}}}{\partial z}$$

where $\frac{\partial F_{\text{depo,emis}}}{\partial z}$ refers to the emissions/deposition of SSA in units of kg/m^3/s and ρ is the density in units of kg/m^3. Using the definition of the advective derivative given by $\frac{dX}{dt} = \frac{\partial X}{\partial t} + \vec{u} \cdot \nabla X$ and substituting $\frac{\partial F_{\text{depo,emis}}}{\partial z}$ into Eq. 1.8, we get the following:

$$\frac{dX}{dt} = -\frac{1}{\rho}\frac{\partial F_{\text{depo,emis}}}{\partial z} \tag{1.9}$$

To get Eq. 1.9 in the form of SSA concentration, we multiply Eq. 1.9 by ρ to get:

$$\rho\left(\frac{dX}{dt}\right) = \rho\left(-\frac{1}{\rho}\frac{\partial F_{\text{depo,emis}}}{\partial z}\right) \tag{1.10}$$

We apply the product rule to the left-hand side (LHS) of Eq. 1.10, and rearrange to get:

$$\rho\left(\frac{dX}{dt}\right) = \underbrace{\frac{d(\rho X)}{\partial t}}_{\frac{dC}{dt}} - X\left(\frac{d\rho}{dt}\right) \tag{1.11}$$

The mass concentration of SSA can be represented as the product of the density of NaCl (ρ) and the mixing ratio (X); $C = \rho X$. For dry particles, we assume a density of 2200 kg m^{-3} (Hess et al., 1998). Then the first term of the RHS of Eq. 1.11 ($\frac{d\rho X}{\partial t}$) can be written as $\frac{dC}{dt}$. Substituting Eq. 1.11 into Eq. 1.10, we get:

$$\frac{dC}{dt} - X\left(\frac{d\rho}{dt}\right) = -\frac{\partial F_{\text{depo,emis}}}{\partial z} \tag{1.12}$$

We can expand $\frac{dC}{dt}$ and $\frac{d\rho}{dt}$ where $\frac{d\rho}{dt} = \frac{\partial \rho}{\partial t} + \vec{u} \cdot \nabla \rho$ and $\frac{dC}{dt} = \frac{\partial C}{\partial t} + \vec{u} \cdot \nabla C$, so the expression simplifies to:

$$\frac{\partial C}{\partial t} + \vec{u} \cdot \nabla C - X\left(\frac{\partial \rho}{\partial t} + \vec{u} \cdot \nabla \rho\right) = -\frac{\partial F_{\text{depo,emis}}}{\partial z} \tag{1.13}$$

Using the Leibniz product rule, we can express the last term in the LHS of Eq. 1.13 ($\vec{u} \cdot \nabla \rho$) as $\nabla \cdot (\rho \vec{u}) - \rho \nabla \cdot \vec{u}$. We apply the mass continuity equation where $\frac{\partial \rho}{\partial t} + \nabla \cdot (\rho \vec{u}) = 0$:

$$\frac{\partial C}{\partial t} + \vec{u} \cdot \nabla C + C \nabla \cdot (\vec{u}) = -\frac{\partial F_{\text{depo,emis}}}{\partial z}$$

We rearrange the terms and use the vector identity ($\nabla \cdot (C\vec{u}) = C \nabla \cdot \vec{u} + \vec{u} \cdot \nabla C$) to get:

$$\frac{\partial C}{\partial t} + \nabla \cdot \vec{u} C = -\frac{\partial F_{\text{depo,emis}}}{\partial z} \tag{1.14}$$

We introduce the term $\mathbb{V}$ that indicates horizontal components (i,j) of the wind. We then expand $\nabla \cdot (\vec{u} C)$ to vertical ($\frac{\partial (wC)}{\partial z}$) and horizontal components ($\vec{\nabla}_H \cdot (\mathbb{V} C)$). We simplify to get:

$$\boxed{\frac{\partial C}{\partial t} + \vec{\nabla}_H \cdot (\mathbb{V} C) = -\frac{\partial F_{\text{depo,emis}}}{\partial z} - \frac{\partial (wC)}{\partial z}} \tag{1.15}$$

In Eq. 1.15, the local trend in concentration is due to the transport (flux divergence) of the SSA concentration and the emission, and deposition of SSA.

1.4.1 Applying Reynolds decomposition

Recall Eq. 1.15, which shows the local rate of change of SSA concentration. We introduce the quantity of $\overline{C}$ that represents the space (area) and the time average of C ($\overline{C} = \frac{1}{\Delta x \Delta y \Delta z \Delta t} \int_t \int_z \int_y \int_x C dx dy dz dt$). We introduce the decomposition $C(x, y, z, t) = \overline{C} + C'(x, y, z, t)$, where SSA can be represented as the sum of the space and time average of C and the fluctuating component of C. We first substitute the notation to get:

$$\frac{\partial(\overline{C} + C')}{\partial t} + \vec{\nabla}_H \cdot (\overline{\mathbb{V}} + \mathbb{V}')(\overline{C} + C') = -\frac{\partial(\overline{F}_{\text{depo,emis}} + F'_{\text{depo,emis}})}{\partial z} - \frac{\partial(\overline{w} + w')(\overline{C} + C')}{\partial z}$$

Wind speed (u, v and w), deposition, emission flux ($F_{\text{depo,emis}}$), and SSA concentration (C) are variables. The fluctuating component (denoted prime; C') is defined as the departure from the mean, so the average of the fluctuating component is zero ($\overline{C'} = 0$). However, if the two fluctuations are correlated, then the average of their product is not zero. If the two fluctuating terms are not correlated, then the average of their product is zero. The equation simplifies to be:

$$\frac{\partial \overline{C}}{\partial t} + \vec{\nabla}_H \cdot (\overline{\mathbb{V}}\,\overline{C}) + \vec{\nabla}_H \cdot (\overline{\mathbb{V}'C'}) = -\frac{\partial \overline{F}_{\text{depo,emis}}}{\partial z} - \frac{\partial(\overline{w}\overline{C})}{\partial z} - \frac{\partial(\overline{w'C'})}{\partial z} \tag{1.16}$$

1.4.2 Eddy transport

Reynolds decomposition gives us a relationship between the expected value of a product and its fluctuations:

$$\overline{wC} = \overline{w}\overline{C} + \overline{w'C'} \tag{1.17}$$

where the overbar represents the average over a period of time. The left-hand side refers to the space and time average of the product of the flux of SSA (vertical velocity and SSA concentration). The $\overline{w}$ denotes the mean value (averaged in time) of w, and w' refers to the deviation from the expected value (fluctuations). The first term on the right-hand side

refers to the flux of the mean tracer by the mean vertical velocity, or simply the product of the averaged velocity and averaged SSA concentration. The last term on the right-hand side of Eq. 1.17 refers to transport by the correlation between submean fluctuations in vertical velocity and the tracer. The fluctuating component of vertical transient transport of SSA ($\overline{w'C'}$) refers to both eddy diffusion and eddy transport by convective mass fluxes (Q. Li et al., 2021; Witek et al., 2011).

$$\overline{w'C'} = \underbrace{\overline{w'C'}^{\mathrm{ED}}}_{\text{eddy diffusion}} + \underbrace{\overline{w'C'}^{\mathrm{MF}}}_{\text{convective mass flux}} \tag{1.18}$$

This section discusses the components that make up eddy transport.

Vertical eddy transport

Eddy diffusion (vertical and horizontal, respectively) is represented as:

$$\overline{w'C'} = -\kappa_V \frac{\partial \overline{C}}{\partial z} \tag{1.19}$$

$$\overline{u'C'} = -\kappa_H \frac{\partial \overline{C}}{\partial x} \tag{1.20}$$

$$\overline{v'C'} = -\kappa_H \frac{\partial \overline{C}}{\partial y} \tag{1.21}$$

Where κ_V and κ_H refer to vertical and horizontal (respectively) eddy diffusivity coefficient in height coordinates. We again rewrite the equation using the finite difference method and apply the constraint that C_{z_b+} refers to the concentration of SSA above the well-mixed boundary layer, where there is a discontinuity. And so the equation simplifies to:

$$\begin{aligned} \overline{w'C'}^{\mathrm{ED}} &= -\kappa_V \frac{\partial \overline{C}}{\partial z} \\ &= -\kappa_V \frac{\overline{C}_{z_b+} - \overline{C}_{z_b-}}{\Delta z} \\ &= \kappa_V \frac{\overline{C}_b}{\Delta z} \end{aligned} \tag{1.22}$$

This equation is applicable at the top of the boundary layer due to the discontinuity in the boundary layer, and Δz can be defined at the boundary layer.

Eddy transport by convective mass flux

Consider eddy transport by convective mass flux ($\overline{w'C'}^{\mathrm{MF}}$). Assuming that all plumes have the same properties, let us consider an ensemble of plumes. Considering a grid box with area A, we can compose a picture of the updraft (plume) with an area a_u (see Fig. 1.6). The time averaged properties of the grid box are composed of both the plume properties (denoted by subscript u) and the surrounding environment (denoted by subscript e)

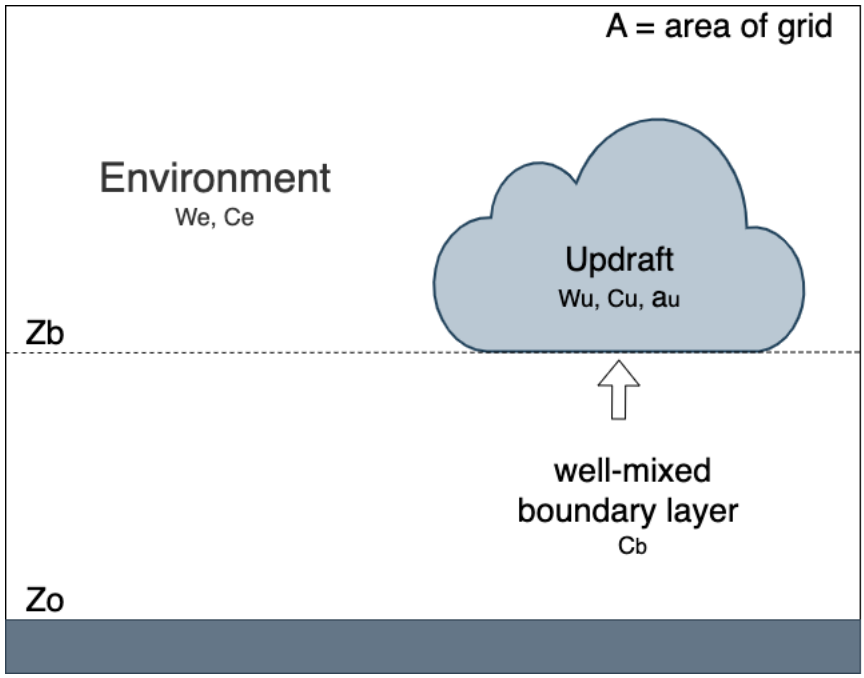


Figure 1.6: A schematic representation of an ensemble of identical plumes in a grid box with an area A.

We can derive an expression for eddy transport by convective mass fluxes by using the properties of a subgrid-scale ensemble of plumes and the environment.

$$\begin{aligned}\overline{w} &= \frac{1}{A}(a_u \cdot w_u + (A - a_u) \cdot w_e) \\ &= (a \cdot w_u) + (1 - a) \cdot w_e \end{aligned} \tag{1.23}$$

$$\overline{C} = (a \cdot C_u) + (1 - a) \cdot C_e \tag{1.24}$$

where a_u refers to the area of the updraft (plume), a refers to the fractional area of the updraft (plume) (a_u/A), subscripts of u denote properties of the plume and subscripts e refer to properties of the environment. Recall that Reynolds decomposition provides a relationship that reflects the relationship between the expected value of a quantity and its fluctuating component. We apply these relationships to derive a series of relationships for the vertical velocity of the plume (w_u) and environment (w_e) and SSA concentration of the plume (C_u) and environment (C_e):

$$w'_u = w_u - \overline{w}$$

$$C'_u = C_u - \overline{C}$$

$$C'_e = C_e - \overline{C}$$

$$w'_e = w_e - \overline{w}$$

Consider the transient flux ($\overline{w'C'}$). We can rearrange Eq. 1.23 and Eq. 1.24 to obtain an expression for the environmental propertiesccc relative to the average of the entire grid

box and plume as follows:

$$\begin{aligned}
\overline{w'C'} &= a \cdot w'_u C'_u + (1-a) \cdot (C'_e w'_e) \\
&= a \cdot (w_u - \overline{w}) \cdot (C_u - \overline{C}) + (1-a) \cdot (C_e - \overline{C}) \cdot (w_e - \overline{w}) \\
&= a \cdot (w_u C_u - w_u \overline{C} - \overline{w} C_u + \overline{w}\overline{C}) + (1-a) \cdot (w_e C_e - w_e \overline{C} - \overline{w} C_e + \overline{w}\overline{C}) \\
&= a \cdot (w_u C_u - w_u \overline{C} - \overline{w} C_u) + (1-a) \cdot (w_e C_e - w_e \overline{C} - \overline{w} C_e) + \overline{w}\overline{C}
\end{aligned}$$

We substitute (after rearranging) into Eq. 1.23 as w_e and Eq. 1.24 as C_e to further simplify the expression. Doing so, we get:

$$\begin{aligned}
\overline{w'C'} &= a \cdot (C_u) \cdot (w_u - \overline{w}) - a \cdot (w_u \overline{C}) + (1-a) \cdot (C_e) \cdot (w_e - \overline{w}) - (1-a) \cdot (w_e \overline{C}) + \overline{w}\overline{C} \\
&= a \cdot (C_u) \cdot (w_u - \overline{w}) - a \cdot (w_u \overline{C}) + \overline{w}\overline{C} + \\
&+ (1-a) \cdot \left[\left(\frac{\overline{C} - a \cdot C_u}{1-a} \right) \cdot \left(\frac{\overline{w} - a \cdot w_u}{1-a} - \overline{w} \right) - \overline{C} \cdot \left(\frac{\overline{w} - a \cdot w_u}{1-a} \right) \right] \\
&= a \cdot (C_u) \cdot (w_u - \overline{w}) - a \cdot (w_u \overline{C}) + (\overline{C} - a \cdot C_u) \cdot \left(\frac{-a \cdot (w_u - \overline{w})}{1-a} \right) - \overline{C} \cdot (\overline{w} - a w_u) + \overline{w}\overline{C} \\
&= a \cdot (C_u) \cdot (w_u - \overline{w}) + (\overline{C} - a \cdot C_u) \cdot \left(\frac{-a \cdot (w_u - \overline{w})}{1-a} \right) \\
&= a \frac{(w_u - \overline{w})(C_u - \overline{C})}{1-a}
\end{aligned} \tag{1.25}$$

We derived the preceding expression (Eq. 1.25) for the transient flux by relating the subgrid-scale processes to larger-scale quantities ($\overline{w}$ and $\overline{C}$) and plume properties. The expression applies if there are non-varying eddies in the boundary layer. Applying the

constraint of the SSA above the boundary layer as very small ($\overline{C} = \overline{C}_{z_b+} \sim 0$):

$$\begin{aligned}\overline{w'C'}^{\mathrm{MF}} &= a\frac{(w_u - \overline{w})(C_u - \overline{C})}{1-a} \\ &= a\frac{(w_u - \overline{w})(\overline{C}_b - \overline{C}_{z_b+})}{1-a} \\ &= a\frac{(w_u - \overline{w})\overline{C}_b}{1-a}\end{aligned} \tag{1.26}$$

This expression is applicable at the top of the well-mixed boundary layer where there is a discontinuity. This allows us to resolve eddy transport by convective (through updraft) mass flux using properties resolvable by dynamical cores (specifically the mean vertical velocity ($\overline{w}$), and $\overline{C}_b$) and resolved using the cumulus (convective) parameterization (a and w_u).

Recall Eq. 1.18, we can combine Eq. 1.22 and Eq. 1.26 to obtain an expression for the transient eddy ($\overline{w'C'}$):

$$\begin{aligned}\overline{w'C'} &= \kappa_V \frac{\overline{C}_b}{\Delta z} + a\frac{(w_u - \overline{w})\overline{C}_b}{1-a} \\ &= \left(\frac{\kappa_V}{\Delta z} + a\frac{(w_u - \overline{w})}{1-a}\right)\overline{C}_b\end{aligned} \tag{1.27}$$

Where Δz refers to the thin layer in which eddy diffusion occurs at the top of the boundary layer.

1.4.3 Apply to a well-mixed boundary layer

Now we consider a well-mixed boundary layer extending from the surface where $z = z_0$ to the top of the boundary layer where $z = z_b$. This assumes that the removal, sourcing, and mixing of SSA particles within the boundary layer are occurring simultaneously. This allows us to focus on the exchange between the boundary layer and the surface. We can vertically average Eq. 1.16 from $z = z_0$ to $z = z_b$ to obtain the expression that governs the

concentration of SSA within the confines of a well-mixed boundary layer.

$$\frac{1}{z_b}\int_{z_0}^{z_b}\left[\frac{\partial\overline{C}}{\partial t}+\vec{\nabla}_H\cdot\overline{\mathbb{V}}\,\overline{C}+\vec{\nabla}_H\cdot\overline{\mathbb{V}'C'}\right]dz=\frac{1}{z_b}\int_{z_0}^{z_b}\left[-\frac{\partial\overline{F}_{\text{depo,emis}}}{\partial z}-\frac{\partial\overline{w}\overline{C}}{\partial z}-\frac{\partial\overline{w'C'}}{\partial z}\right]dz \quad (1.28)$$

We use the notation $\langle\rangle$ to indicate a vertically averaged quantity. We restate the governing equation and apply specific assumptions (i.e. emission of SSA is from the surface ($z = z_0$) to get the form:

$$\frac{\partial\langle\overline{C}\rangle}{\partial t}+\vec{\nabla}_H\cdot\langle\overline{\mathbb{V}}\,\overline{C}\rangle+\vec{\nabla}_H\cdot\langle\overline{\mathbb{V}'C'}\rangle=\frac{1}{z_b}\Bigg(\overline{E}-(\overline{w}\overline{C})_{z=z_b}-(\overline{w'C'})_{z=z_b}+V_{\text{t,eff}}\overline{C}_{z>z_b} - V_{\text{t,eff}}\overline{C}\Bigg) \quad (1.29)$$

It's important to note that emission is a function of 10-meter wind speed ($E(u)$) and this relationship is nonlinear ($E(u) \propto u^{3.41}$). The term $V_{\text{t,eff}}$ accounts for mechanisms such as turbulent deposition, gravitational settling and wet deposition throughout the boundary layer. However, there is also a sink from deposition on the surface. We previously described $(wC)_{z=z_b}$ as the vertical transport of SSA evaluated at the top of the boundary layer. The term $(\overline{w}\overline{C})_{z=z_b}$ represents the transport of SSA concentration due to the mean vertical motion.

In this well-mixed boundary layer ($z_0 < z < z_b$), the SSA concentration is well mixed due to the presence of turbulent fluxes. However, at the top of the well-mixed boundary layer ($z = z_b$), there is a discontinuity. There is less turbulence causing the concentration of SSA to be lower at $z > z_b$ than the concentration of SSA in the boundary layer. There is not much sedimentation of the SSA concentration because the concentration of SSA above the boundary layer is lower than in the boundary layer ($\overline{C}_{z>z_b} < \overline{C_b}$). As a result, the vertical processes that dominate the budget of SSA in the PBL include deposition of SSA throughout the PBL, diffusion at the top of the boundary layer (z_b) and convective mass fluxes. Since $V_{\text{t,eff}}\overline{C}$ refers to the settling of SSA from within the boundary layer and because $C_{z>z_b}$ is

quite small, we can rewrite the above equation as:

$$\frac{\partial\langle\overline{C}\rangle}{\partial t}+\vec{\nabla}_H\cdot\langle\overline{\mathbb{V}}\,\overline{C}\rangle+\vec{\nabla}_H\cdot\langle\overline{\mathbb{V}'C'}\rangle=\frac{1}{z_b}\left(\overline{E}-\overline{w}\overline{C}_b-(\overline{w'C'}_b)-V_{\mathrm{t,eff}}\overline{C}_b\right) \tag{1.30}$$

Eq. 1.27 relates the fluctuating component of the vertical transient transport of SSA ($\overline{w'C'}$) to eddy diffusion and eddy transport by convective mass fluxes (Fig. 1.6). Substituting in Eq. 1.27 as $\overline{w'C'}$ evaluated at $z=z_b$, we get the following:

$$\frac{\partial\langle\overline{C}\rangle}{\partial t}+\vec{\nabla}_H\cdot\langle\overline{\mathbb{V}}\,\overline{C}\rangle+\vec{\nabla}_H\cdot\langle\overline{\mathbb{V}'C'}\rangle=\frac{1}{z_b}\left(\overline{E}-\overline{w}\overline{C_b}-\kappa_V\frac{\overline{C}_b}{\Delta z}-a\frac{(w_u-\overline{w})\overline{C}_b}{1-a}-V_{\mathrm{t,eff}}\overline{C}_b\right)$$

We can simplify the following equation by introducing the term $\overline{\alpha}$ which refers to the mean vertical velocity, the eddy diffusion, the convective mass flux (CMF) and the terminal speed (vertical deposition) of the SSA ($\overline{w}+\frac{\kappa_V}{\Delta z}+\frac{a(w_u-\overline{w})}{1-a}+V_{\mathrm{t,eff}}$). Furthermore, because this expression is integrated over all size bins, the contribution of the internal sourcing of SSA from coagulation is negligible, so the expression simplifies to:

$$\underbrace{\frac{\partial\langle\overline{C}\rangle}{\partial t}+\vec{\nabla}_H\cdot\langle\overline{\mathbb{V}}\,\overline{C}\rangle+\vec{\nabla}_H\cdot\langle\overline{\mathbb{V}'C'}\rangle}_{\overline{D}}=\frac{1}{z_b}\left(\overline{E}-(\underbrace{\overline{w}+\frac{\kappa_V}{\Delta z}+\frac{a(w_u-\overline{w})}{1-a}+V_{\mathrm{t,eff}}}_{\overline{\alpha}})\cdot\overline{C}_b\right) \tag{1.31}$$

Important quantities that are relevant to the local change in SSA concentration in this domain include the emission of SSA from the sea surface due to bubbles bursting from whitecaps (E), eddy diffusion from convective mass flux ($\frac{a(w_u-\overline{w})}{1-a}$), fluxes of SSA caused by the mean vertical wind speed ($\overline{w}$) and the deposition (dry and wet deposition and gravitational settling; $V_{\mathrm{t,eff}}$) and the divergence of any horizontal fluxes of SSA ($\vec{\nabla}_H\cdot\langle\overline{\mathbb{V}}\,\overline{C}\rangle+\vec{\nabla}_H\cdot\langle\overline{\mathbb{V}'C'}\rangle$). We can group several terms referring to the divergence of horizontal fluxes of SSA ($\vec{\nabla}_H\cdot\langle\overline{\mathbb{V}}\,\overline{C}\rangle+\vec{\nabla}_H\cdot\langle\overline{\mathbb{V}'C'}\rangle$) and the local time rate of change of SSA

($\frac{\partial\langle\overline{C}\rangle}{\partial t}$) in the LHS of the Eq. 1.31 as $\overline{D}$. Whereas the term $\overline{\alpha}$ refers to the vertical transport of SSA concentration.

Eq. 1.31 can be simply evaluated as:

$$\boxed{\overline{D} = \frac{1}{z_b}\left(\overline{E} - \overline{\alpha} \cdot \overline{C}\right)} \tag{1.32}$$

where $\overline{D}$ refers to the sum of the local time derivative of concentration and the horizontal convergence (mean and eddy), $\overline{\alpha}$ refers to vertical transport through deposition, mean vertical velocity, eddy diffusion and convective mixing (hereafter referred to as vertical transport parameter), and $\overline{E}$ is the emission.

Equation 1.32 represents the SSA budget in the PBL, which incorporates all the mechanisms of transport, production, and removal that impact the SSA particles. This theoretical framework is applied to observations of SSA concentration retrieved from the PMEL cruise and to model simulations of SSA concentration from GEOS-Chem in the following sections.

1.5 Q1 - Can SSA emission errors explain the differences between modeled and observed SSA concentration?

In this section, we investigate whether errors in emission estimates can account for the discrepancies between modeled and observed SSA concentrations in our simplified model. To facilitate this comparison, we assume that PMEL shipboard observations are representative of the larger model grid box, enabling a direct comparison between ship-based measurements and GEOS-Chem simulations.

We retrieve the vertical transport parameter using GEOS-Chem. The horizontal grid resolution of GEOS-Chem is $2^\circ \times 2.25^\circ$ with 55 vertical sigma levels for simulations driven by GEOS-4 meteorological fields (years prior to 2005) and 72 hybrid eta vertical levels for

simulations driven by GEOS-5 meteorological fields (years 2005–2008). Thus, $\overline{D}$, which refers to the sum of the local time derivative and horizontal convergence, is negligible due to smooth gradients, steady state, and due to the model not resolving small-scale advection, $\overline{D} = 0$. For GEOS-Chem, SSA concentrations ($\overline{C}_{\text{geos}}$) are modeled using Gong emissions ($\overline{E}_{\text{gong}}$) and modeled large-scale advective dynamics and convective vertical transport. Eq. 1.32 for GEOS-Chem becomes $\overline{E}_{\text{gong}} = \overline{\alpha} \cdot \overline{C}_{\text{geos}}$, which we use to estimate the vertical transport parameter as $\overline{\alpha} = \frac{\overline{E}_{\text{gong}}}{\overline{C}_{\text{geos}}}$.

Next, we assume that the emission of SSA in the MBL is balanced by the removal of SSA at the same time and location, an assumption that is consistent with previous interpretations of SSA production in GCMs (De Leeuw et al., 2011; Jaeglé et al., 2011; Lewis et al., 2004; M. Smith et al., 1993). Neighboring and local advective and turbulent processes are deemed negligible. Furthermore, we assume that there is no local rate of change and no horizontal advection, which implies that the $\overline{D} = 0$.

Combining the following assumptions of $\overline{D} = 0$, use of observed SSA concentration ($\overline{C}_{\text{obs}}$) and the vertical transport parameter calculated from GEOS-Chem ($\overline{\alpha} = \frac{\overline{E}_{\text{gong}}}{\overline{C}_{\text{geos}}}$), we get the following form of the simplified model, Eq. 1.32:

$$\overline{E} = \frac{\overline{E}_{\text{gong}}}{\overline{C}_{\text{geos}}} \times \overline{C}_{\text{obs}} \tag{1.33}$$

Applying these assumptions yields an expression that implies that there is a value of emission ($\overline{E}$) that will produce the observed concentration. We compare the emissions calculated in Eq. 1.33 with a suite of SSA emission schemes (Deike, MartMon, Jaegle and Gong) to compare various treatments of SSA emissions in Fig. 1.7. Although this comparison yields various estimates of emissions, none of the parameterizations perfectly captures the emissions calculated in Eq. 1.33. Next, we evaluate the different emission approaches by generating estimates of the SSA concentration.

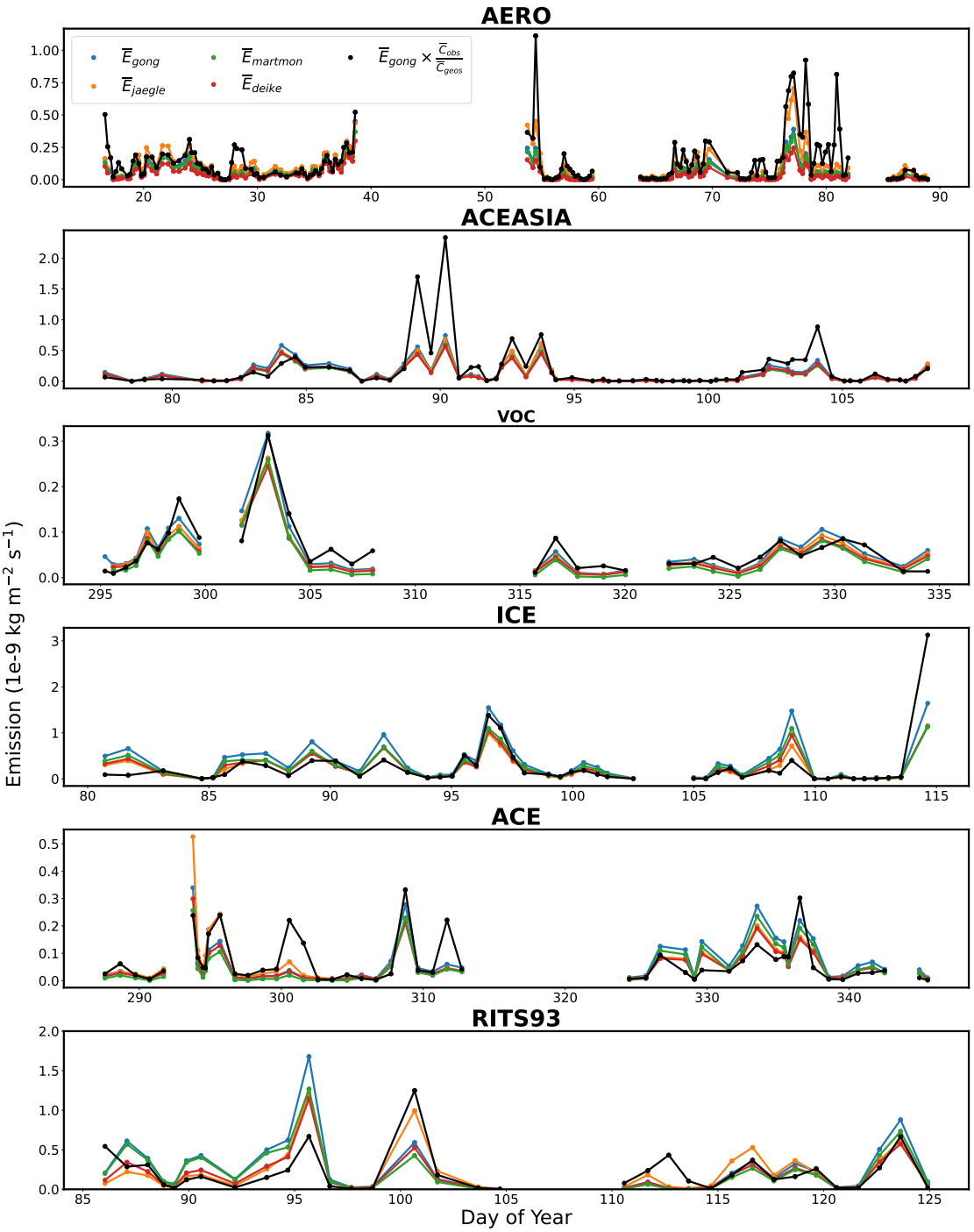


Figure 1.7: The time series of duration-averaged SSA emissions were calculated using PMEL observed wind speeds and SSTs, applying four different parameterizations: $\overline{E}_{\text{gong}}$ from Gong (2003), $\overline{E}_{\text{jaegle}}$ from Jaeglé et al. (2011), $\overline{E}_{\text{martmon}}$ from Mårtensson et al. (2003) and Monahan et al. (1986), $\overline{E}_{\text{deike}}$ from Deike et al. (2022). The results were compared with emissions calculated using Eq. 1.33.

1.5.1 Evaluating emissions using estimates of SSA concentration

SSA concentration from the simple model in Eq. 1.32 can be written as a function of $\overline{D}$, $\overline{\alpha}$ and $\overline{E}_{\mathrm{X}}$:

$$\overline{C}_{\mathrm{X}} = \overline{C}_{\mathrm{X}}\left(\overline{E}_{\mathrm{X}}, \overline{\alpha}, \overline{D}\right) \tag{1.34}$$

We generate estimates of the concentration using various emission schemes (Jaegle, MartMon and Deike) to assess what the estimated SSA concentration would be under the assumptions made in this framework and if these estimates are close to observed concentration. Assuming $\overline{D} = 0$ and using emission scheme X and the vertical transport parameter calculated from GEOS-Chem ($\overline{\alpha} = \frac{\overline{E}_{\mathrm{gong}}}{\overline{C}_{\mathrm{geos}}}$), the expressions for the estimated concentration for each emission configuration X are derived as follows:

$$\overline{C}_{\mathrm{gong}} = \overline{C}_{\mathrm{gong}}\left(\overline{E}_{\mathrm{gong}}, \overline{\alpha} = \frac{\overline{E}_{\mathrm{gong}}}{\overline{C}_{\mathrm{geos}}}, \overline{D} = 0\right) = \overline{C}_{\mathrm{geos}} \tag{1.35}$$

$$\overline{C}_{\mathrm{jaegle}} = \overline{C}_{\mathrm{jaegle}}\left(\overline{E}_{\mathrm{jaegle}}, \overline{\alpha} = \frac{\overline{E}_{\mathrm{gong}}}{\overline{C}_{\mathrm{geos}}}, \overline{D} = 0\right) \tag{1.36}$$

$$\overline{C}_{\mathrm{martmon}} = \overline{C}_{\mathrm{martmon}}\left(\overline{E}_{\mathrm{martmon}}, \overline{\alpha} = \frac{\overline{E}_{\mathrm{gong}}}{\overline{C}_{\mathrm{geos}}}, \overline{D} = 0\right) \tag{1.37}$$

$$\overline{C}_{\mathrm{deike}} = \overline{C}_{\mathrm{deike}}\left(\overline{E}_{\mathrm{deike}}, \overline{\alpha} = \frac{\overline{E}_{\mathrm{gong}}}{\overline{C}_{\mathrm{geos}}}, \overline{D} = 0\right) \tag{1.38}$$

In Fig. 1.8 we compare estimates of SSA concentration using various emission schemes with PMEL observations of SSA concentration. The concentrations calculated using the four SSA emission configurations show minimal differences overall. However, in AERO, concentrations calculated using Jaegle emission parameterization are consistently higher than those from the other three configurations. AERO was sampled over relatively warmer waters, significantly increasing emissions and subsequently estimated concentrations when using Jaegle's SSA production flux as a result of its strong temperature dependence. In contrast, ICE was sampling over cooler waters, resulting in suppressed SSA emissions and concentrations when using temperature-dependent production fluxes from MartMon and Jaegle. As a

result, the concentrations calculated using the Gong emission parameterization for ICE are greater than those in the other three configurations. Thus, demonstrating the impact of the meteorological conditions on the calculated emissions and concentrations.

We compare the RMSE, correlation coefficient and bias between the emission-adjusted concentration and the observed concentration in Table 1.2. Under the assumptions of this limiting case, $\overline{C}_{\text{Jaegle}}$ exhibits the highest correlation to the majority of the observations, while MartMon has the lowest RMSE for the majority of the cruises. Our analysis reveals that the concentration estimates from Jaegle, Deike, and MartMon exhibit the highest correlation coefficient, lowest Root Mean Square Error (RMSE), or lowest bias compared to observed concentrations for at least one of the cruises. In contrast, Gong's wind speed-dependent emission scheme does not outperform the other parameterizations in any of the cruises across the evaluated metrics. Thus, incorporating a temperature dependence in Gong's formulation, as in Jaegle's emission formula, yields improved concentration estimates. However, the temperature-dependent fit to SSA emission (Jaegle) only partially reconciles the discrepancies with observed SSA concentrations, leaving 36-81% of the variations unexplained (based on the square of the correlation coefficient).

In this case, we assume $\overline{D} = 0$, ship-based observations are representative of coarse-grid box averages, and vertical transport errors in the model are negligible. This framework allows us to isolate and investigate whether emission errors are responsible for the discrepancies between modeled and observed SSA concentrations. Our analysis compares four emission schemes and uses the simple model to calculate the concentration for each scheme under the assumptions made in this limiting case. We find that overall none of the emissions can generate estimates of concentrations that completely match all of the observed concentrations.

Deike presents a more physically derived SSA formulation, but does not perform well in generating estimates of concentration that match observed concentration. However, the merits of improving the physical representation of SSA production processes may not be fully disclosed in this analysis, since severe assumptions regarding observed SSA concentrations,

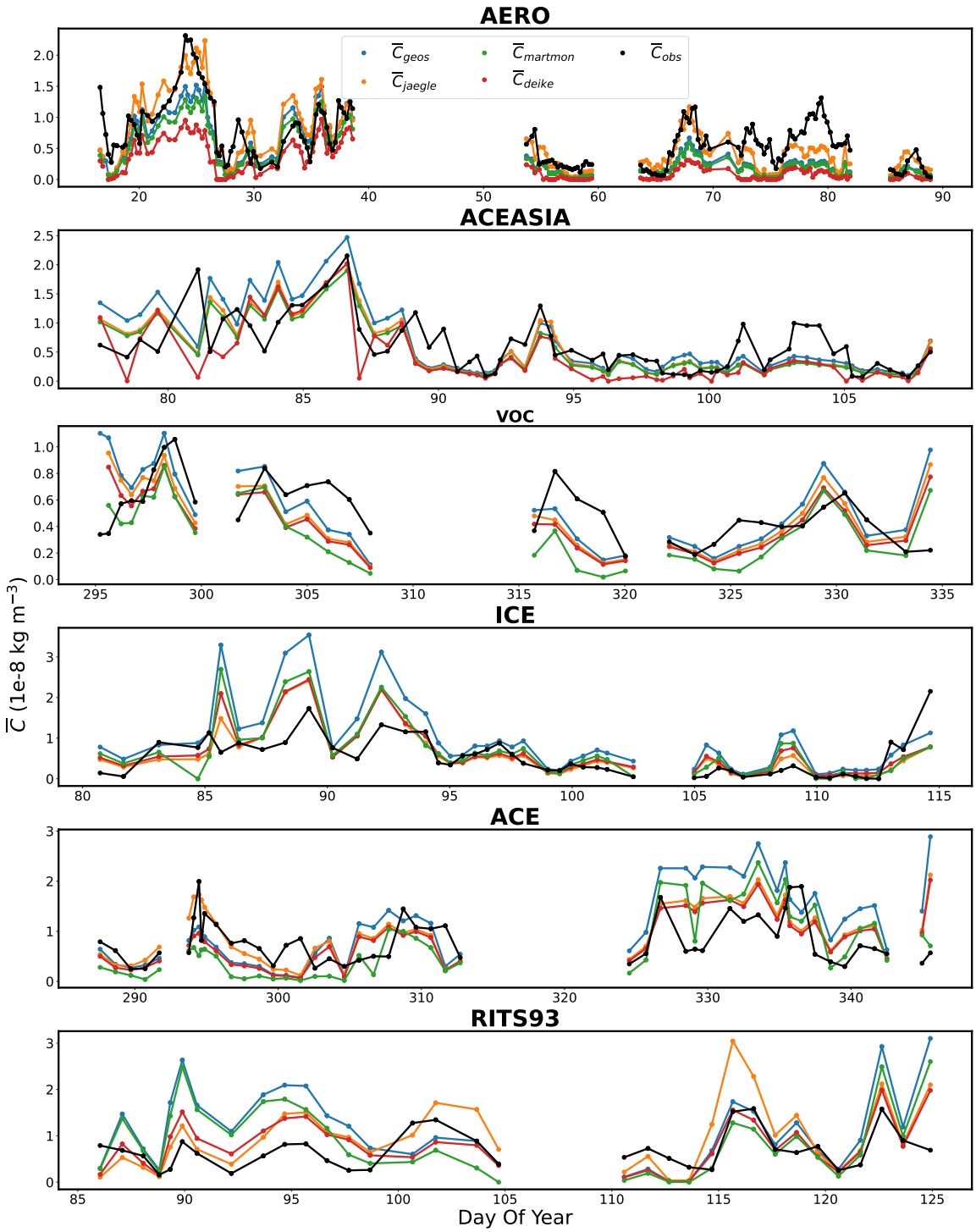


Figure 1.8: SSA concentration for Jaegle, MartMon and Deike are calculated using $\overline{\alpha}_{\text{geos}}$ and are compared to observed and modeled (GEOS-Chem) SSA concentration.

$\overline{D}$, and the vertical transport parameter of GEOS-Chem were made. As a result, remaining discrepancies can be attributed to errors in the treatment of emission, in addition to errors

		AERO	ACEASIA	VOC	ICE	ACE	RITS93
Gong ($\overline{C}_{\text{geos}}$)	Corrcoef	0.78	0.64	0.38	0.66	0.37	0.40
	RMSE	3.78	4.50	2.94	7.46	7.76	8.69
	Bias	−0.33	0.34	0.22	4.81	0.62	1.00
Jaegle ($\overline{C}_{\text{Jaegle}}$)	Corrcoef	*0.81*	*0.65*	0.43	*0.69*	*0.49*	*0.72*
	RMSE	*3.06*	3.90	2.61	*4.10*	5.28	5.81
	Bias	*0.07*	0.09	*0.01*	*1.62*	0.40	0.55
MartMon ($\overline{C}_{\text{MartMon}}$)	Corrcoef	0.79	*0.65*	0.45	0.67	0.40	0.53
	RMSE	4.13	*3.85*	*2.55*	4.45	*5.22*	*4.70*
	Bias	−0.41	*0.01*	−0.09	2.73	0.19	*0.37*
Deike ($\overline{C}_{\text{Deike}}$)	Corrcoef	0.78	0.64	*0.52*	0.60	0.48	0.38
	RMSE	5.42	4.33	2.85	5.44	5.86	7.23
	Bias	−0.73	−0.35	−0.29	1.74	*−0.06*	0.52

Table 1.2: The correlation coefficient, root mean squared error (RMSE) and bias between the calculated SSA concentration (using Jaegle, Deike and MartMon emission and vertical transport parameter from GEOS-Chem) and observed SSA concentration ($\overline{C}_{\text{obs}}$). The values that have highest correlation coefficient or lowest RMSE and bias are italicized.

in modeled vertical transport mechanisms, sampling, and sub-grid variability. For these reasons, in the next two sections we will explore an alternative set of assumptions.

1.6 Q2 - Can errors in vertical transport explain the differences between modeled and observed SSA concentration?

In the previous section, we explored the potential impact of emission errors on the discrepancies between modeled and observed SSA concentrations. Here we explore the possibility of errors in the representation of vertical transport in GEOS-Chem and its potential role in driving these differences. For comparison purposes, we treat PMEL shipboard observations as spatially representative of the larger GEOS-Chem grid box, allowing for a direct comparison between ship-based measurements and the larger-scale GEOS-Chem simulations.

In the atmosphere, SSA is transported vertically by processes including large-scale advection, convection, mixing, turbulence, and gravitational settling. With SSA concentrations changing by a factor of 10–100 from the surface to the upper troposphere (Yu et al., 2019), variations in vertical transport of SSA likely contribute to these variations of vertical profiles of SSA concentration.

Amongst existing efforts to constrain SSA emission, there are few considerations of how SSA varies with altitude due to the errors in modeled vertical transport mechanisms. SSA removal is more efficient in liquid water clouds than in ice clouds; however, Murphy et al. (2019) found that the GEOS-5 model may be removing aerosol too slowly in ice clouds, leading to an overestimation of SSA. Furthermore, this overestimation may also be traced to the improper removal of SSA from air transported in the subgrid convective parameterization. S. Li et al. (2013); Kim et al. (2015); Xu et al. (2013) compared aerosol optical depth (AOD) profiles of SSA from GEOS-Chem simulations and flight measurements and found that GEOS-Chem underestimates AOD in the boundary layer, which indicates errors in modeling the vertical distribution of SSA.

In general, vertical aerosol transport is widely regarded as a source of error in SSA simulation in various chemical transport models. Recall Eq. 1.32, $\overline{\alpha}$ refers to the deposition of SSA from the boundary layer ($V_{\mathrm{t,eff}}$), and the vertical transport of SSA by mean vertical velocity ($\overline{w}$) eddy diffusion ($\frac{\kappa_V}{\Delta z}$) and convective mixing ($\frac{a(w_u-\overline{w})}{1-a}$):

$$\boxed{\overline{\alpha} = \overline{w} + \frac{\kappa_V}{\Delta z} + \frac{a(w_u - \overline{w})}{1-a} + V_{\mathrm{t,eff}}} \tag{1.39}$$

This section investigates the hypothesis that discrepancies between observed and modeled SSA concentrations may originate from inaccuracies in the representation of vertical transport within the GEOS-Chem model. In contrast to our previous analysis, we do not take the GEOS-Chem vertical transport parameter as given, but instead examine its validity. We explore how the vertical transport parameter varies when we use different emission

formulations. The vertical transport parameter from Eq. 1.32 can be written as a function of $\overline{E}_{\mathrm{X}}$, $\overline{C}$ and $\overline{D}$:

$$\overline{\alpha}_{\mathrm{X}} = \overline{\alpha}_{\mathrm{X}}\left(\overline{E}_{\mathrm{X}}, \overline{C}, \overline{D}\right) \tag{1.40}$$

We assume $\overline{D}$=0, and use various emission schemes X to generate estimates of vertical transport that will produce the observed concentration ($\overline{C}_{\mathrm{obs}}$).:

$$\overline{\alpha}_{\mathrm{gong}} = \overline{\alpha}_{\mathrm{gong}}\left(\overline{E}_{\mathrm{gong}}, \overline{C}_{\mathrm{obs}}, \overline{D} = 0\right) \tag{1.41}$$

$$\overline{\alpha}_{\mathrm{jaegle}} = \overline{\alpha}_{\mathrm{jaegle}}\left(\overline{E}_{\mathrm{jaegle}}, \overline{C}_{\mathrm{obs}}, \overline{D} = 0\right) \tag{1.42}$$

$$\overline{\alpha}_{\mathrm{martmon}} = \overline{\alpha}_{\mathrm{martmon}}\left(\overline{E}_{\mathrm{martmon}}, \overline{C}_{\mathrm{obs}}, \overline{D} = 0\right) \tag{1.43}$$

$$\overline{\alpha}_{\mathrm{deike}} = \overline{\alpha}_{\mathrm{deike}}\left(\overline{E}_{\mathrm{deike}}, \overline{C}_{\mathrm{obs}}, \overline{D} = 0\right) \tag{1.44}$$

We generate estimates of $\overline{\alpha}$ using Eq. 1.41, 1.42, 1.43, and 1.44 needed to reconcile the discrepancies between observed and modeled SSA concentrations using different emission schemes shown in Fig. 1.9. We compare our estimates of the vertical transport parameter with the vertical transport parameter retrieved from GEOS-Chem ($\frac{\overline{E}_{\mathrm{gong}}}{\overline{C}_{\mathrm{geos}}}$).

Estimates of $\overline{\alpha}$ in Fig. 1.9 seem to mirror the variability in emissions in Fig. 1.7. This can be attributed to the fact that when the same observed concentration data are used in evaluating $\overline{\alpha}$, any differences in estimates will be solely due to variations in emission schemes. This implies that within this framework, the vertical transport required to reconcile the observed and modeled SSA concentrations is constrained by the emission schemes.

Deike et al. (2022) presents a mechanistic SSA formulation that is based on the physics of bubble bursting. We privilege it as the SSA emission parameterization with a higher degree of physical accuracy. In Table 1.3, we calculate the correlation coefficient, RMSE and bias between $\overline{\alpha}_{\mathrm{deike}}$ and alternative estimates of $\overline{\alpha}$ to evaluate differences among the emission formulations via estimates of the vertical transport under the assumptions pertaining to this limiting case. For AERO, ACEASIA, ACE and RIT93, $\overline{\alpha}_{\mathrm{deike}}$ has the highest correlation

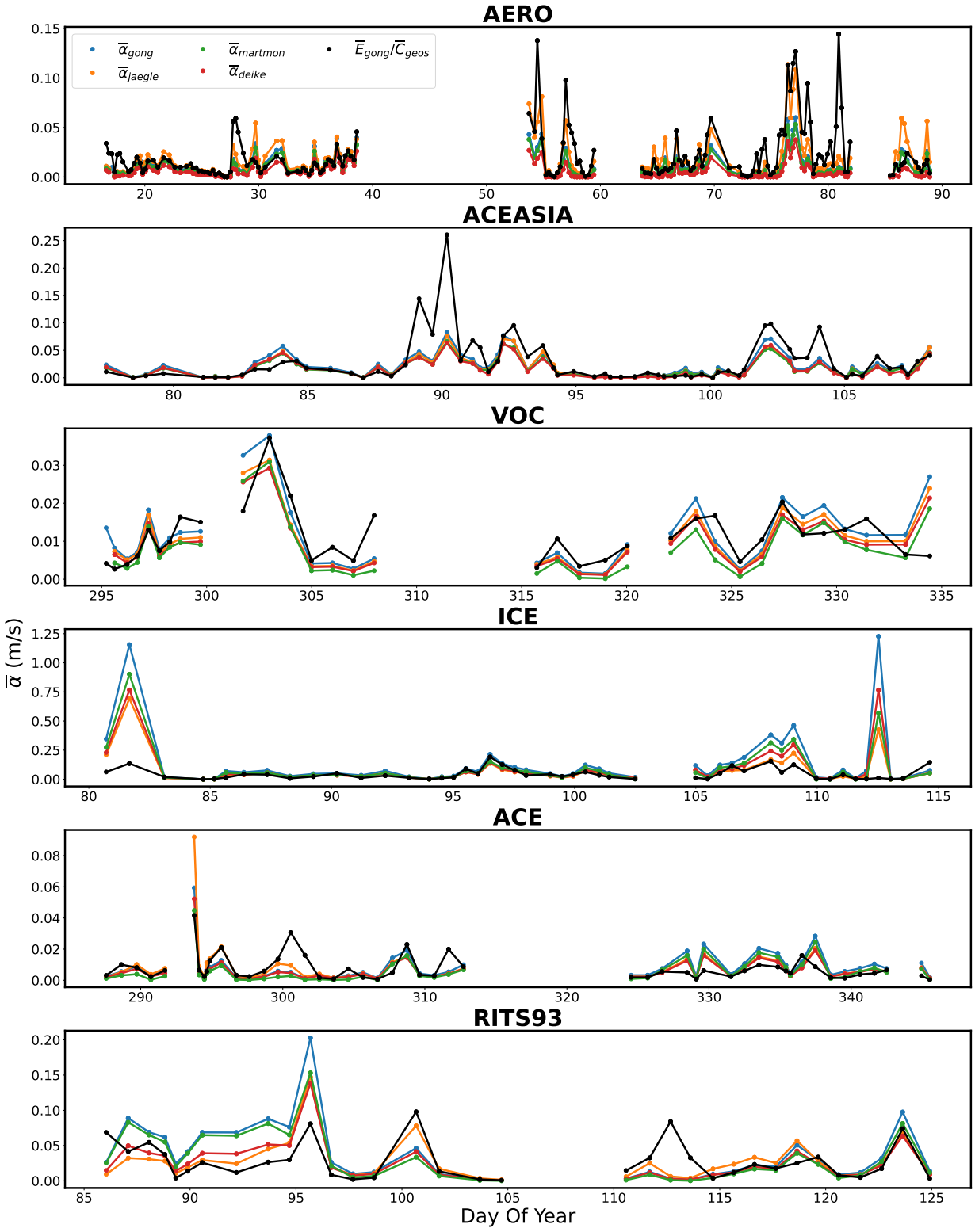


Figure 1.9: Estimates of calculated vertical transport rates ($\overline{\alpha}_{\text{gong}}$, $\overline{\alpha}_{\text{jaegle}}$, $\overline{\alpha}_{\text{martmon}}$, $\overline{\alpha}_{\text{deike}}$) and $\overline{\alpha}_{\text{geos}}$ from GEOS-Chem. Note that the limits are different for the figures.

coefficient, lowest RMSE and bias magnitude with $\overline{\alpha}_{\text{gong}}$ and/or $\overline{\alpha}_{\text{martmon}}$. For VOC, the correlation coefficient of $\overline{\alpha}_{\text{deike}}$ with $\overline{\alpha}_{\text{jaegle}}$ is tied to those of $\overline{\alpha}_{\text{gong}}$ and $\overline{\alpha}_{\text{martmon}}$. For ICE alone, $\overline{\alpha}_{\text{deike}}$ has the highest correlation coefficient with $\overline{\alpha}_{\text{jaegle}}$.

In contrast to the empirically based formulation derived by Jaeglé, the production formulations proposed by MartMon and Gong adopt a more physically based approach, aiming to represent the fundamental processes governing SSA emissions (Mårtensson et al., 2003; Monahan et al., 1986; Gong, 2003). The vertical transport parameters estimated using MartMon and Gong show higher correlation coefficients and lower bias and RMSE to the vertical transport parameter estimated using the physically derived Deike emission scheme. In comparison, Jaegle exhibits a lower correlation and higher bias magnitude to Deike. This highlights the advantages of formulations based on physical models in capturing the underlying processes that govern SSA emissions and their impact on the vertical transport parameter. Furthermore, $\overline{\alpha}_{\text{deike}}$ shows a poor correlation with vertical transport retrieved from GEOS-Chem. This suggests that, under the given assumptions, the vertical transport modeled in GEOS-Chem may not accurately capture the underlying physical processes that govern the vertical transport of SSA and may consequently lead to errors in the modeled SSA concentrations.

We further explore the systematic behavior of the estimated vertical transport parameters under the assumptions of this case. Recall that by assuming $\overline{D} = 0$ in Eq. 1.32, we get a linear relationship between emissions and concentration in the form of: $\overline{E} = \overline{\alpha} \cdot \overline{C}$. In cases where modeled concentrations underestimate observations, this bias can be addressed by either increasing emissions or decreasing $\overline{\alpha}$. Similarly, if the modeled concentrations overestimate observations, this bias can be addressed by either decreasing emissions or increasing $\overline{\alpha}$. In this study, we focus on correcting the concentration biases by changing $\overline{\alpha}$ while utilizing a suite of emission schemes. The biases between the modeled and observed concentrations are correlated with temperature, with models tending to underestimate the concentrations at higher temperatures and overestimating at lower temperatures (Jaeglé et al., 2011). In Fig.

		AERO	ACEASIA	VOC	ICE	ACE	RITS93
Gong ($\overline{\alpha}_{\text{gong}}$)	Corrcoef	*0.97*	*0.99*	*0.99*	0.96	*0.99*	*0.99*
	RMSE	*0.01*	*0.01*	*0.01*	0.11	*0.01*	*0.01*
	Bias	0.97	0.38	0.48	0.45	0.38	0.20
Jaegle ($\overline{\alpha}_{\text{jaegle}}$)	Corrcoef	0.88	0.98	*0.99*	*0.99*	0.86	0.82
	RMSE	0.02	*0.01*	*0.01*	0.05	*0.01*	0.02
	Bias	2.20	0.17	0.27	−0.25	0.35	*−0.13*
MartMon ($\overline{\alpha}_{\text{martmon}}$)	Corrcoef	0.96	*0.99*	*0.99*	0.97	0.96	0.96
	RMSE	*0.01*	*0.01*	*0.01*	*0.04*	*0.01*	*0.01*
	Bias	*0.72*	*0.06*	*0.16*	*−0.06*	*0.04*	−0.20
GEOS-Chem ($\frac{\overline{E}_{\text{gong}}}{\overline{C}_{\text{geos}}}$)	Corrcoef	0.65	0.78	0.76	0.50	0.61	0.51
	RMSE	0.03	0.03	*0.01*	0.15	*0.01*	0.03
	Bias	2.89	0.79	0.36	−0.53	0.17	*−0.13*

Table 1.3: The correlation coefficient, root mean squared error (RMSE) and bias between the vertical transport estimates ($\overline{\alpha}_{\text{gong}}$, $\overline{\alpha}_{\text{jaegle}}$, $\overline{\alpha}_{\text{martmon}}$ and GEOS-Chem modeled vertical transport parameter ($\frac{\overline{E}_{\text{gong}}}{\overline{C}_{\text{geos}}}$)) and vertical transport parameter estimated using Deike emission ($\overline{\alpha}_{\text{deike}}$). The values that have highest correlation coefficient and lowest RMSE and bias are italicized.

1.10, we normalize the estimates of the vertical transport parameter ($\overline{\alpha}$) by their average value at 20°C to highlight variations in $\overline{\alpha}$ at different temperatures. We find that for a given emission rate, $\overline{\alpha}$ decreases as a function of temperature to address the biases between the modeled and observed concentration.

Most estimates of the vertical transport parameter show an inverse relationship with temperature, except for those derived from GEOS-Chem, which display little to no relationship. This suggests a systematic issue in the representation of $\overline{\alpha}$ and its underlying physics, which appear to be temperature dependent. Among the emission schemes, Jaegle's formulation has the strongest temperature dependence, leading to increased emissions at higher temperatures. This partially compensates for biases where the modeled concentrations underestimate the observations at elevated temperatures, thus dampening the temperature dependence of $\overline{\alpha}$. Consequently, this is reflected in the less pronounced decrease in $\overline{\alpha}_{\text{jaegle}}$ with temperature, as shown in Fig. 1.10. In contrast, emission schemes with weaker or no temperature dependency (i.e., MartMon, Deike, and Gong) require a stronger temperature-

dependent adjustment to $\overline{\alpha}$ to address concentration biases, leading to a more pronounced decrease in $\overline{\alpha}$ with temperature in Fig. 1.10.

An alternative approach to correcting concentration biases is by modifying the emissions. In this context, Jaeglé et al. (2011) derived a temperature-dependent fit for emissions, assuming no errors in the vertical transport parameter modeled in GEOS-Chem and setting $\overline{D} = 0$. This fit results in increased emissions with increasing temperatures to address biases between modeled and observed concentrations. This positive temperature dependence of emissions contrasts with the inverse temperature dependence observed in $\overline{\alpha}$. However, our analysis suggests potential errors in the GEOS-Chem modeled vertical transport and reveals that vertical transport parameter exhibits a temperature dependence. This indicates that the observed temperature-dependent fit for emissions might be an artifact of systematic issues in the vertical transport parameter rather than an inherent temperature dependence in SSA emissions. Errors in vertical transport physics at high temperatures could be linked to mesoscale phenomena, such as convection, cold pools, and gusts, which are absent from the model or poorly parameterized. Furthermore, warmer SSTs can create a more turbulent boundary layer, which facilitates more mixing and aerosol deposition (Parajuli et al., 2020; Waples & Klump, 2013).

In this section, we investigated the role of inaccuracies in vertical transport in explaining the discrepancies between modeled and observed SSA concentrations. By generating estimates of $\overline{\alpha}$ under the assumption of $\overline{D} = 0$, utilizing $\overline{C}_{\text{obs}}$, and applying various SSA emission schemes, we hypothesized that a specific estimate of $\overline{\alpha}$ could reconcile the observed concentrations at a given location. However, our findings indicate that while it is always possible to find a vertical transport parameter to satisfy the simple model for any single observation, doing so does not provide a clear or general solution for remedying deficiencies in vertical transport across the observational dataset.

This exposes limitations on assuming the absence of errors between modeled and large scale advective dynamics and convective mass transport. It is possible that the vertical

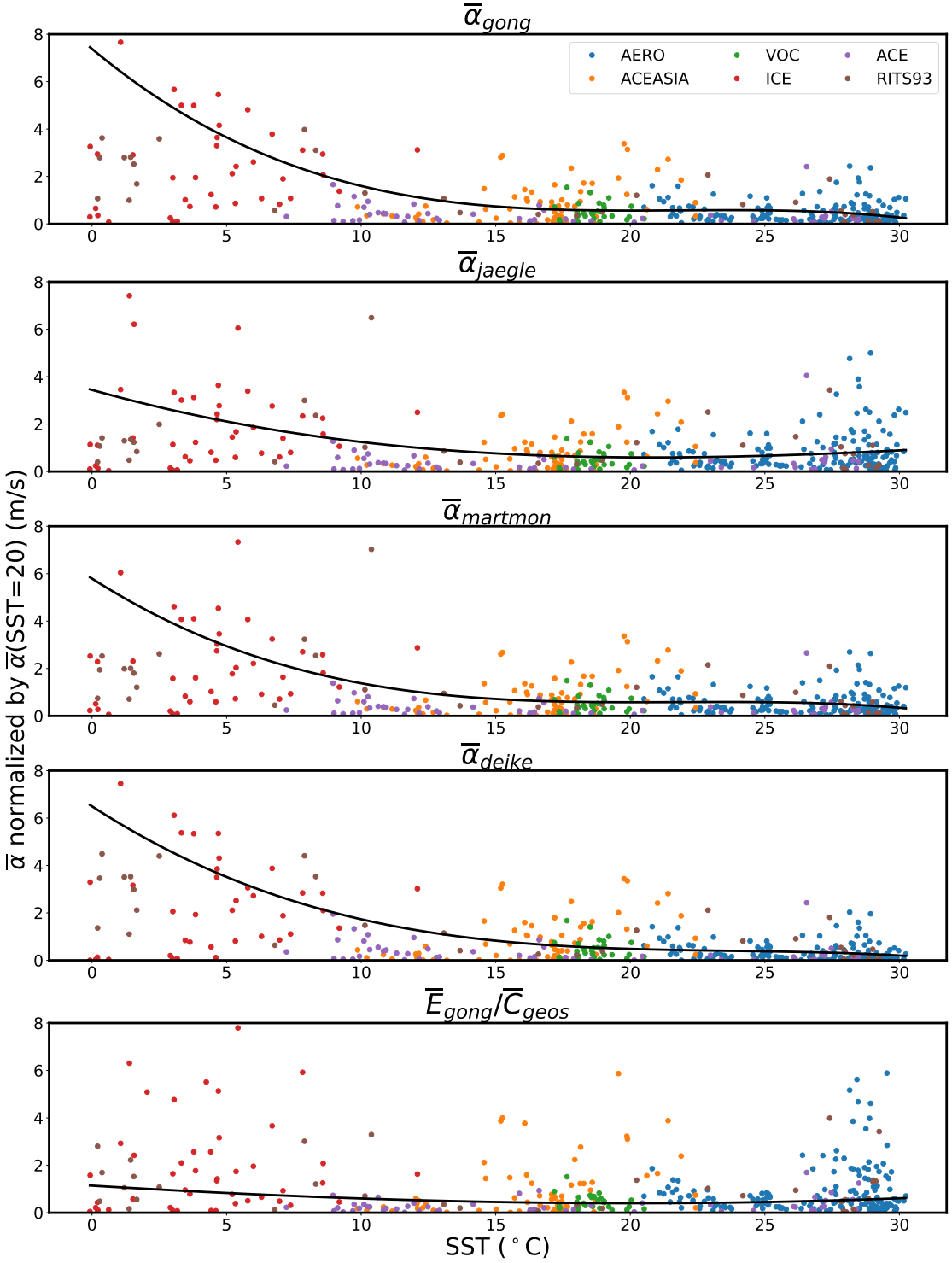


Figure 1.10: The estimates of the vertical transport parameter, normalized by its average value at an SST of 20°C, are shown as a function of SST. The black lines represent the best-fit third-order polynomial to the composite estimates.

transport flux calculated by the model differs from the actual vertical transport processes occurring during the PMEL cruise expeditions, potentially impacting comparisons between modeled and observed SSA concentrations. Discrepancies in the estimated vertical transport parameter can also result from the assumption that $\overline{D} = 0$, inconsistencies between modeled and observed concentrations, errors in the emission formulation, and mismatches between observational sampling and model domains. Furthermore, the vertical transport parameter exhibits a temperature-dependent relationship, indicating potential systematic issues in the representation of $\overline{\alpha}$ and its underlying physics. As a result, the budget equations used to formulate a relationship between observed and modeled quantities must account for possible biases in the model estimates of vertical transport.

1.7 Q3 - Can subgrid variability, sampling error or nonzero $\overline{D}$ explain the differences between modeled and observed SSA concentration?

We have thus far considered the attribution of discrepancies between the model and observed SSA concentration to errors in emissions and vertical transport. However, in both cases, we have assumed both $\overline{D} = 0$ and the observed SSA concentrations can be compared to grid-box averaged concentrations from GEOS-Chem. Here we present a case that analyzes the limitations of these assumptions and takes into account the effect of sampling discrepancies and nonzero $\overline{D}$.

1.7.1 Errors in sampling

The sampling period for the SSA concentrations on PMEL cruises ranges from 2 to 24 hours, with a mean of 11 hours. For an average ship speed of 24 km/hour, this sampling period can cover distance of approximately 50-580 km, with a mean of 265 km (Jaeglé et al., 2011).

Due to the wide area covered during the atmospheric residence time of SSA, it is plausible that events resulting in small-scale variability in SSA concentration may have occurred prior to the ship sampling along the track.

Fig. 1.11 shows the full duration of one sampling period for March 2001 during one of the PMEl cruises: the ACEASIA cruise. SSA concentration in the GEOS-Chem model is reflected in a 2D space with a grid resolution of $2° \times 2.5°$. However, the SSA concentration observed by the PMEL ship is 1D and constrained by the movement, speed, and track of the ship, which samples only part of the GEOS-chem model grid. The convective precipitation data from the ERA5 reanalysis is used here to show the presence of convective events and a proxy for local-changes in 10-meter wind speeds along the cruise track and reflect a finer grid resolution of $0.25° \times 0.25°$.

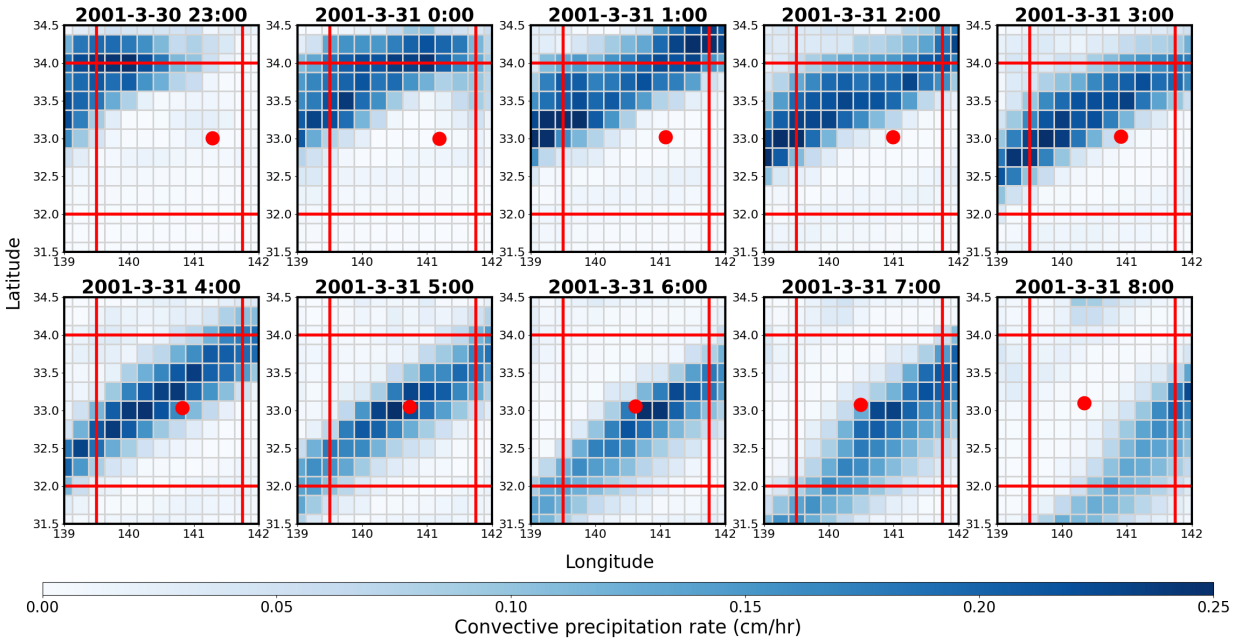


Figure 1.11: Convective precipitation rate (cm/hr) from ERA5 for every hour shown over the duration of one sampling period event for the cruise ACEASIA. The red circle represents the position of the research cruise during the hour of the sampling period. The figure displays overlapping grids: red lines represent the GEOS-Chem grid, while gray lines denote the ERA5 grid-box.

In contrast to the GEOS-Chem grid resolution, the PMEL ship samples a small portion of the full 2D domain. The environment where the ship is sampling within this grid-box

is not horizontally homogeneous, and there are certain times when the ship is sampling over this convective environment. When the ship samples during these events, the observed concentration can be substantially different from the modeled concentration. Thus, the actual SSA concentration averaged over the grid box may not match the concentrations sampled by the PMEL ships or modeled in GEOS-Chem. In conclusion, the mismatch between the GEOS-Chem resolution and the ship's sampling methodology may be a primary contributor to the discrepancies between the modeled and observed SSA concentrations. Fig. 1.11 illustrates one case where this is a problem but this is likely present elsewhere throughout the cruise expeditions.

1.7.2 Estimating $\overline{D}_{\mathrm{X}}$

Both observed and modeled SSA concentrations refer to a sum of the contribution of the SSA concentration generated in the large-scale environment and within convective plumes. The SSA concentration can be expressed in both spaces in the form of: $\overline{C}_{\mathrm{x}} = a_{\mathrm{x}} \cdot C_p + (1 - a_{\mathrm{x}}) \cdot C_e$, where x is 1D or 2D, C_p refers to the concentration within the convective updraft plume, C_e refers to the concentration in the environment, and a_x refers to the fraction of the domain that contains convective plumes.

SSA concentration variations occur on small scales; therefore, variations in the SSA concentration in the plume (C'_p) and the environment (C'_e) from the mean ($\overline{C}_x$) can be written as the difference between the contribution from the plume or environment and the total averaged SSA concentration. For 1D and 2D spaces, this is written in the form of: $C'_{p,\mathrm{x}} = C_p - \overline{C}_{\mathrm{x}}$ and $C'_{e,\mathrm{x}} = C_e - \overline{C}_{\mathrm{x}}$.

The SSA concentration observed in the trajectory of the sampling period is not the same as the SSA concentration modeled over the sampling period ($\overline{C}_{1\mathrm{D}} \neq \overline{C}_{2\mathrm{D}}$). In the model, the SSA concentration is calculated using the grid-scale average of subgrid-scale convective properties calculated in the atmospheric models GEOS-4 and GEOS-5. Consequently, $\overline{D}_{\mathrm{X}}$ of Eq. 1.31 is small for a 2D space because the model averages out the heterogeneity of

the SSA concentration over a larger area, resulting in a smoother spatial distribution. In contrast, in a 1D space, $\overline{D}_{\mathrm{X}}$ is larger due to the irregular sampling of the ship's track, which captures more of the spatial variability and extremes in SSA concentration.

In Fig. 1.11, localized convection in the form of convective precipitation is evident within the GEOS-Chem grid box. In particular, there are instances where the ship samples directly over an area with convective activity, potentially producing a plume of enhanced SSA concentration. The presence of convection has significant implications for the SSA concentrations sampled by cruise ships, as it generates a time rate of change in SSA concentrations. Therefore, the disparity between modeled and observed SSA concentration may be due to the presence of subgrid variability of meteorological processes like convective precipitation and gustiness that affects SSA concentration but is smoothened out in the coarser GEOS-Chem grid scale. Subsequently, this raises the possibility of subgrid variability and thus $\overline{D}_{\mathrm{X}} \neq 0$.

We rewrite $\overline{D}_{\mathrm{X}}$, which represents local tendency and horizontal divergence (via advection and turbulent mixing) of SSA concentration from Eq. 1.32 as a function of $\overline{E}_{\mathrm{X}}$, $\overline{\alpha}$, and $\overline{C}$:

$$\overline{D}_{\mathrm{X}} = \overline{D}_{\mathrm{X}}\left(\overline{E}_{\mathrm{X}}, \overline{\alpha}, \overline{C}\right) \tag{1.45}$$

Where X refers to emission schemes that can be used (MartMon, Deike, Gong, and Jaegle) to generate estimates of SSA emission. Using observed concentration from PMEL and the vertical transport parameter estimated from GEOS-Chem, we retrieve estimates of $\overline{D}_{\mathrm{X}}$ for observations of SSA concentration:

$$\overline{D}_{\mathrm{gong}} = \overline{D}_{\mathrm{gong}}\left(\overline{E}_{\mathrm{gong}}, \overline{\alpha} = \frac{\overline{E}_{\mathrm{gong}}}{\overline{C}_{\mathrm{geos}}}, \overline{C}_{\mathrm{obs}}\right) \tag{1.46}$$

$$\overline{D}_{\mathrm{jaegle}} = \overline{D}_{\mathrm{jaegle}}\left(\overline{E}_{\mathrm{jaegle}}, \overline{\alpha} = \frac{\overline{E}_{\mathrm{gong}}}{\overline{C}_{\mathrm{geos}}}, \overline{C}_{\mathrm{obs}}\right) \tag{1.47}$$

$$\overline{D}_{\mathrm{martmon}} = \overline{D}_{\mathrm{martmon}}\left(\overline{E}_{\mathrm{martmon}}, \overline{\alpha} = \frac{\overline{E}_{\mathrm{gong}}}{\overline{C}_{\mathrm{geos}}}, \overline{C}_{\mathrm{obs}}\right) \tag{1.48}$$

$$\overline{D}_{\mathrm{deike}} = \overline{D}_{\mathrm{deike}}\left(\overline{E}_{\mathrm{deike}}, \overline{\alpha} = \frac{\overline{E}_{\mathrm{gong}}}{\overline{C}_{\mathrm{geos}}}, \overline{C}_{\mathrm{obs}}\right) \tag{1.49}$$

These expressions recover the contribution of small scale atmospheric imbalance on SSA concentration. This also permits various estimates of $\overline{D}_{\mathrm{X}}$ for different emission schemes shown in Fig. 1.12 upon which we see a preponderance of negative values of $\overline{D}_{\mathrm{X}}$ is observed for all cruises.

In Eq. 1.45, $\overline{D}_{\mathrm{X}}$ includes the local tendency of SSA concentration, advection, and horizontal dispersion by turbulent mixing (recall Eq. 1.32). The magnitude of this term reveals the contribution of any horizontal and temporal inhomogeneities to observations of SSA concentrations and how this translates into differences between observed and modeled SSA concentration. The magnitude of $\overline{D}_{\mathrm{X}}$ is greatest for ACEASIA during the sampling period shown in Fig. 1.11 (-9.15e-13 kg m^{-3} s^{-1} for Gong, -9.52e-13 kg m^{-3} s^{-1} for Jaegle, -1.00e-12 kg m^{-3} s^{-1} for MartMon and -1.01e-12 kg m^{-3} s^{-1} for Deike), indicating the presence of significant sub-grid scale local imbalance throughout this sampling period, which contributes to the differences between modeled and observed SSA concentration.

Convective events occurring prior to the PMEL ship entering the domain where SSA concentration measurements are taken can influence the observed SSA concentration but may not be captured by the model due to a combination of mismatches between the 1D and 2D spatial sampling and the modeled SSA concentration failing to account for subgrid scale convection in this region/time. Possible disruption events include shallow cloud systems or precipitation events that cause washout or wet deposition of SSA (Junge & Gustafson, 1956). Convective wind gusts are another potential disruption event, leading to a temporary increase in SSA production and the formation of SSA particle plumes. The total residence time of the SSA particles within the radius range (r_{80} = 0.6-8 μm) of 6 hours is short in the interpretation of the budget equation of SSA (Jaeglé et al., 2011); however small-scale atmospheric perturbations can still occur within the trajectory of these particles prior to their deposition, sometimes prolonging their presence in the air or hastening their deposition. The in situ observations of SSA then include the effect of this earlier small-scale disruption event that occurred.

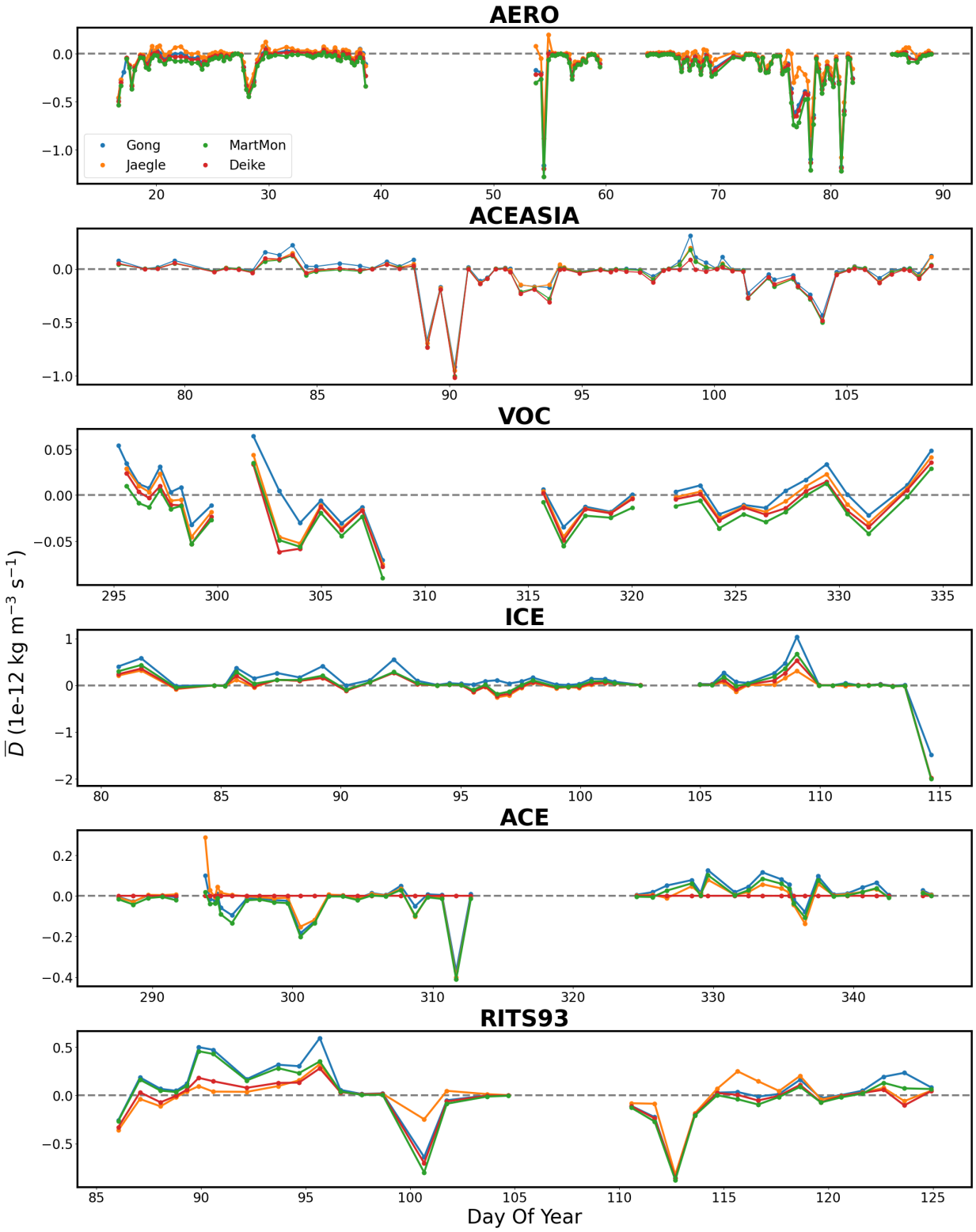


Figure 1.12: Timeseries of estimates of $\overline{D}$ calculated for the PMEL cruises using various emission schemes (Gong, Jaegle, MartMon and Deike).

We conclude that the disparity in resolution of GEOS-Chem to the sampling done by the ships contributes to the differences between modeled and observed SSA concentration. This lends itself to the presence of subgrid variability of SSA concentration that is reflected in observations but not model simulations due to their sub-grid scale nature. We present the case for considering the effect of accounting for small-scale upstream disruptive events in the form of convective gustiness or washout when modeling SSA production and the mechanisms through which they affect SSA concentration which have not been previously considered when remedying the differences between model and observations of SSA concentration. The effect of convective gustiness and precipitation covarying with temperature has implications on the strength of the climate feedback from SSA, but its magnitude is so far an unexplored area of interest for future work.

1.8 Conclusion

This study was motivated by the potential implications for climate feedback effects from SSA due to recent evidence for the SST dependency in SSA production (Jaeglé et al., 2011; Mårtensson et al., 2003). The development of the temperature dependency on SSA production means that SSA concentrations would likely increase in a warming climate, while previously SSA concentration was thought to change very little, due to the weak response of surface wind speed to climate change (IPCC (2007)). Current estimates of the negative radiative effect from SSA range from -0.3 to -1.2 W m^{-2} (Grini et al., 2002; Heald et al., 2014b; Paulot et al., 2020), and contribute to about 15% of the total cloud feedback (Gettelman et al., 2016). Prior to this development, wind speed was considered to be the main driver for SSA production, as SSA particles enter the atmosphere from bursting bubbles that form due to wind-driven whitecaps. SSA production scales with wind speed, but wind speed only accounts for a quarter of the variability between the modeled and observed SSA concentration.

This encourages consideration of other parameters relevant for SSA emission, including sea surface temperature (SST).

The explanations for the temperature dependency in SSA production are underdeveloped, which results in uncertainty on the strength of the possible feedback SSA poses in a warming climate. Furthermore, the differences between observed and model estimates of SSA concentration and emission have long plagued the accuracy of modeling the climatic impacts of aerosols, including SSA. When comparing observed SSA concentration with SST, there is no clear temperature dependence of the aerosol concentration. Chen et al. (2020) similarly observed no direct dependence of SST on SSA concentration for particles ranging from 0.07 to 0.25 μm using model simulations. This raises further issues with the temperature dependence of SSA and whether this temperature dependence is due either to another parameter or to an SSA emission mechanism covarying with temperature. To address these questions and uncertainties, we need to observe the departures between observed and modeled SSA concentrations to determine the instances when other physical processes and meteorological parameters that are currently not considered may be relevant for SSA production or loss.

We identify key bulk processes that are relevant for modifying and affecting the concentration of SSA particles in chemical transport models and generate a simple 1-D model (Eq. 1.32). To this end, we conducted three separate inquiries into explanations for the differences between observed and modeled SSA concentration that are explained by: 1) errors in emission (E_{X}), 2) errors in vertical transport ($\overline{\alpha}_{\mathrm{X}}$), and 3) subgrid variability, sampling discrepancies, and non-zero $\overline{D}_{\mathrm{X}}$. We explore alternative explanations by assuming the error lies in one term of Eq. 1.32. We then solve for the value of that term in our idealized model that would eliminate the error. It is likely that these limiting cases co-occur. For example, atmospheric convection impacts both the SSA vertical distribution and horizontal transport of SSA.

The sea spray generation function from Deike et al. (2022) is presented as a more physically derived representation of SSA emission. However, our analysis suggests that under

assumptions of $\overline{D} = 0$ and the absence of vertical transport errors in the model, Deike does not perform well in generating concentration estimates to match the observed concentration in Q1. The merits of improving the physical representation of the SSA production mechanisms are not fully disclosed in the analysis for Q1, as severe assumptions were made with respect to $\overline{D}$ and the vertical transport parameter of GEOS-Chem in this framework. We suggest that improved representation of model physics and transport relevant for SSA production, in addition to correcting SSA emission, would be relevant in resolving the discrepancy between model and observations. Ultimately, accurately modeling and capturing the full dynamics responsible for the budget of SSA in the atmosphere must account for the variation of these three mechanisms. A related approach using remote sensing observations of small-scale convective events, which are sampled at finer temporal and spatial resolutions may provide an ideal setup for a more in-depth investigation. However, we lay the foundation for future analysis to explore these potential alternatives. This work encourages the examination of errors in the modeled vertical transport mechanisms, as well as sampling errors and the local time tendency and horizontal divergence of the SSA concentration. The impact of the small-scale atmospheric imbalance is reflected in the observed SSA concentration but not in the model because of the coarser GEOS-Chem grid that smoothens out these subgrid–scale properties. Subgrid–scale processes like convection and convective wind gusts exhibit a temperature dependency and, therefore, are relevant, as it has implications for the magnitude of the climate feedback effects resulting from SSA. Recent developments indicate that the frequencies of hourly and daily wind gust events are projected to increase in a warming climate (Cheng et al., 2012; Jeong & Sushama, 2019). Although the impact of climate change on precipitation is somewhat more uncertain, many favor increased precipitation due to increased evaporation (O'Gorman & Schneider, 2009; Solomon, 2007; Tebaldi et al., 2006). The implications of these changes in a warming climate may subsequently affect SSA production and the subsequent climate feedback from SSA.

Chapter 2

Evaluating the performance of different sea-spray aerosol emission formulations in simulating aerosol optical depth (AOD)

2.1 Abstract

This study investigates the impact of various sea spray generation functions on atmospheric simulations, focusing on sea salt aerosol (SSA) emission and aerosol optical depth (AOD) representation. We compare simulations using the mechanistic sea spray generation function developed by Deike et al. (2022) with configurations employing functions from Mårtensson et al. (2003), Monahan et al. (1986), Gong (2003), and Jaeglé et al. (2011) using the GFDL AM4 model forced with observed sea surface temperature (SST). Our analysis validates model simulations of AOD against a suite of observations: satellite retrievals (MISR and MODIS), ground-site observations (AERONET), and cruise observations (MAN component of AERONET). We find that different sea-spray generation functions show varied performance across geographical regions, with Deike's formulation achieving the highest global correlation with all three groups of AOD observations globally. However, Deike exhibits an overall negative bias, potentially due to lower emissions, differences in size distribution, or variations in wind speed. Our findings highlight the complexities involved in comparing AOD

retrieval methodologies with model simulations and underscore the need for further advances in modeling SSA. Improving the representation of aerosol transport and removal processes, alongside refining SSA production mechanisms, is thus essential for achieving greater model accuracy.

2.2 Introduction

Originally sourced from the ocean, sea salt aerosol (SSA) rises to the surface as air bubbles in white caps. Air bubbles then burst, releasing seawater droplets into the atmosphere. The size of droplets vary depending on the production mechanism and are categorized into three types: film drops, jet drops, and spume drops. Film drops are generated when bubbles break at the surface of the ocean, releasing sea salt particles into the atmosphere; the film drop radii are typically less than 0.5 μm (Andreas, 1998). Jet drops are formed from the collapse of the internal cavity of bubbles, which produces a vertical jet of water, producing jet drops with moderate radii ranging from 0.5 to 4 μm. Spume droplets are generated in high-wind environments where drops are torn from wave crests into the air and are generally particles with radii greater than 4 μm. For large-scale simulations or long-range transport, the production of film drops is typically more significant than the production of jet drops or spume drops (Monahan et al., 1986).

Since there are no direct measurements of SSA flux at the sea-atmosphere interface, it is difficult to evaluate the plethora of SSA formulations, except under idealized laboratory conditions. However, methods relying on field measurements of SSA concentration face practical difficulties, as low concentrations of SSA particles can result in poor counting statistics and may require longer sampling times to accurately represent the variability and trends of SSA concentrations over time. More difficulties arise when SSA particles are in the presence of a marine atmosphere with other particles. The need to create adequate techniques to accurately relate observed concentration to emissions flux offers an opportunity

for improvements with respect to exploring SSA production. This necessitates an accurate representation of the relationship of SSA emissions to SSA concentration, for which numerical models are required for direct comparisons.

SSA emissions are commonly estimated using the whitecap fraction and are expressed solely as a function of wind speed. As a result, accurate modeling of wind speed is crucial for reliable SSA emission and concentration estimates. However, inter-model differences in the transport and deposition of SSA can also translate to significant biases in estimated SSA concentrations (X. Liu et al., 2007). These biases arise from variations in simulated transport pathways, deposition mechanisms, and interactions with other atmospheric constituents, leading to differences in the removal of SSA from the atmosphere (Athanasopoulou et al., 2008; Kelly et al., 2009; Righi et al., 2013). SSA concentrations are directly affected by air–sea interactions, such as near-surface winds, SST, sea surface salinity, precipitation, and sea surface wind stress (Chen et al., 2020; Seinfeld & Pandis, 2016). Modeling SSA emissions only as a function of wind speed neglects consideration of other properties relevant to the sea-air interface where SSA are produced. This approach leads to biases when comparing the simulated SSA concentration with in situ measurements. To remedy these biases, several research groups have directed their focus on more comprehensive estimates of the whitecap fraction through various approaches, such as using field site observations (Clarke et al., 2006; M. Smith et al., 1993), advancing parameterizations of wave formulation (Shi et al., 2009), or using a satellite-based whitecap fraction (Albert et al., 2016).

Monahan et al. (1986) used a laboratory whitecap simulation tank, designed to replicate marine aerosol production mechanisms, and whitecap observations to develop a parameterization for SSA production flux that is a function of the wind speed at 10 meters. This parameterization considers the indirect production of SSA through bubbles and includes the mechanisms of SSA production through jet drop and film drop using observational and laboratory data between the radius of the SSA particle at 80% relative humidity, r_{80}, of 0.4 to 20 μm. The limitation of the applicable size range caused an unrealistic overestimation

of SSA flux when extrapolated below r_{80} = 0.4 μm threshold. This occurred because the flux number curve exhibited a monotonic increase below 0.4 μm as particle size decreases (see Fig. 1 in Gong (2003)), contradicting field measurements (O'Dowd et al., 1997) that show submicron sea-salt aerosols peak around r = 0.2 μm and decrease as the particle size decreases to r = 0.05 μm. This inconsistency required further improvements in the SSA source production flux.

Following suit, Gong (2003) extended the range of the original equation to below 0.2 μm. Further variations of the SSA emissions formulation assuming wind speed dependency as the only driver follow the form of $\frac{dF}{dr} = f(r_{80}) \times u_{10}^{3.41}$, where f is a function of particle size (μm) at RH = 80%, u_{10} is the wind speed measured at 10 meters, which is raised to a power of 3.41 determined by whitecap laboratory experiments conducted by Monahan et al. (1986). Other flux formulations of SSA production flux are reviewed by Andreas et al. (1995) and De Leeuw et al. (2011).

Further work proposed a potential dependency of SSA production on temperature. The possible mechanisms through which sea surface temperature (SST) may affect SSA production include the rate of gas exchange between the bubble and surrounding fluids; such as temperature dependence has been observed in laboratory experiments by Mårtensson et al. (2003) and Sellegri et al. (2006). Recent field and laboratory observations suggest that SSA emissions may be affected by SST as a result of the dependency of the kinematic viscosity of water and the bubble behavior with temperature (Forestieri et al., 2018; Jaeglé et al., 2011; S. J. Norris et al., 2013). Mårtensson et al. (2003) present a formulation of the SSA production flux, including temperature dependence, determined by laboratory measurements of the flux of particles produced from a whitecap area for particle radii smaller than 1.4 μm and requires numerous coefficients for specific particle diameter ranges, a cumbersome factor to account for when implementing this formulation in large-scale models such as general circulation models (GCM). Further work integrating this dependency into a flux formulation

leads us to the formulation derived by Jaeglé et al. (2011), which has a stronger temperature dependence compared to the formulation derived by Mårtensson et al. (2003).

Recent work from Deike et al. (2022) proposed a mechanistic sea spray generation function that is based on the physics of bubble bursting. The physical mechanism of bubble bursting integrates the role of wind and waves via the breaking distribution and entrained air flux, and sensitivity to temperature via individual bubble-bursting mechanisms. Furthermore, this methodology does not require tuning of parameters to obtain a particular wind or temperature dependence. They were able to retrieve the coherence between the model and composites of various laboratory and field observations of SSA emissions, demonstrating the effectiveness of a mechanistic approach towards constraining SSA production. However, they noted that the temperature sensitivity coming from their proposed scalings is weaker than that empirically derived by Jaeglé et al. (2011). This further supports our consideration of alternative mechanisms other than a direct temperature dependence on SSA production.

In this study, we run an atmospheric chemistry-climate model with the mechanistic sea spray generation function developed by Deike et al. (2022). We then compare this simulation with configurations using other sea spray generation functions, including the standard set-up for the atmospheric model, which combines the Mårtensson et al. (2003) and Monahan et al. (1986) schemes, as well as configurations using the sea spray generation functions of Gong (2003) and Jaeglé et al. (2011). The primary objective of this study is to perform a comprehensive analysis and comparison of various sea spray generation functions, examining their sensitivities to sea surface temperature (SST) and wind speed. Model simulations are then evaluated against aerosol optical depth (AOD) observations to assess the extent to which refinements in sea salt aerosol (SSA) emission representations can enhance AOD simulation accuracy.

2.3 Methodology

2.3.1 AM4

In this study, we use the Geophysical Fluid Dynamics Laboratory (GFDL) atmosphere model (AM4) model (M. Zhao et al., 2018). AM4 has a horizontal resolution of approximately 100 km on a cubed-sphere grid with 33 layers. The model is run on a cubed-sphere grid and the results are interpolated onto a 180 latitudes x 288 longitudes grid for analysis. We conduct AMIP simulations with AM4 (1979-2014), but extended to 2019 using observed gridded sea surface temperature (SST). However, years 2000-2019 will be mainly used in this analysis because these years correspond to available aerosol optical depth (AOD) observations that will be used for validation with our simulations.

There are four simulations, each corresponding to one of the four SSA production flux configurations described in the preceding section. In this study, we retain the MartMon tuning used in the CMIP6 configuration of GFDL-CM4, which increases both fine and coarse mode SSA emissions by 33% above values MartMon generates (M. Zhao et al., 2018). This tuning is also applied to simulations using the Gong and Jaegle emission scheme. By contrast, no such scaling is applied to the simulation using the Deike scheme. Beyond SSA-specific tunings, all simulations were conducted within the GFDL AM4 framework, which includes a broader suite of model-wide tunings. For a general discussion of tunings in general circulation models (specifically AM3), see Schmidt et al. (2017). These tunings impact surface wind speed, which is important for SSA emissions. All simulations use identical scavenging efficiencies for sea salt in the wet deposition scheme, originally selected for use with MartMon.

Figure 2.1 shows the 20-year climatology (2000–2019) of Deike and the differences between Deike and the three other AMIP runs. Although SST is prescribed and identical across simulations, wind speed and land temperature are not constrained to observations and evolve over time, as highlighted by regional differences in Fig. 2.1. In particular, the AMIP run

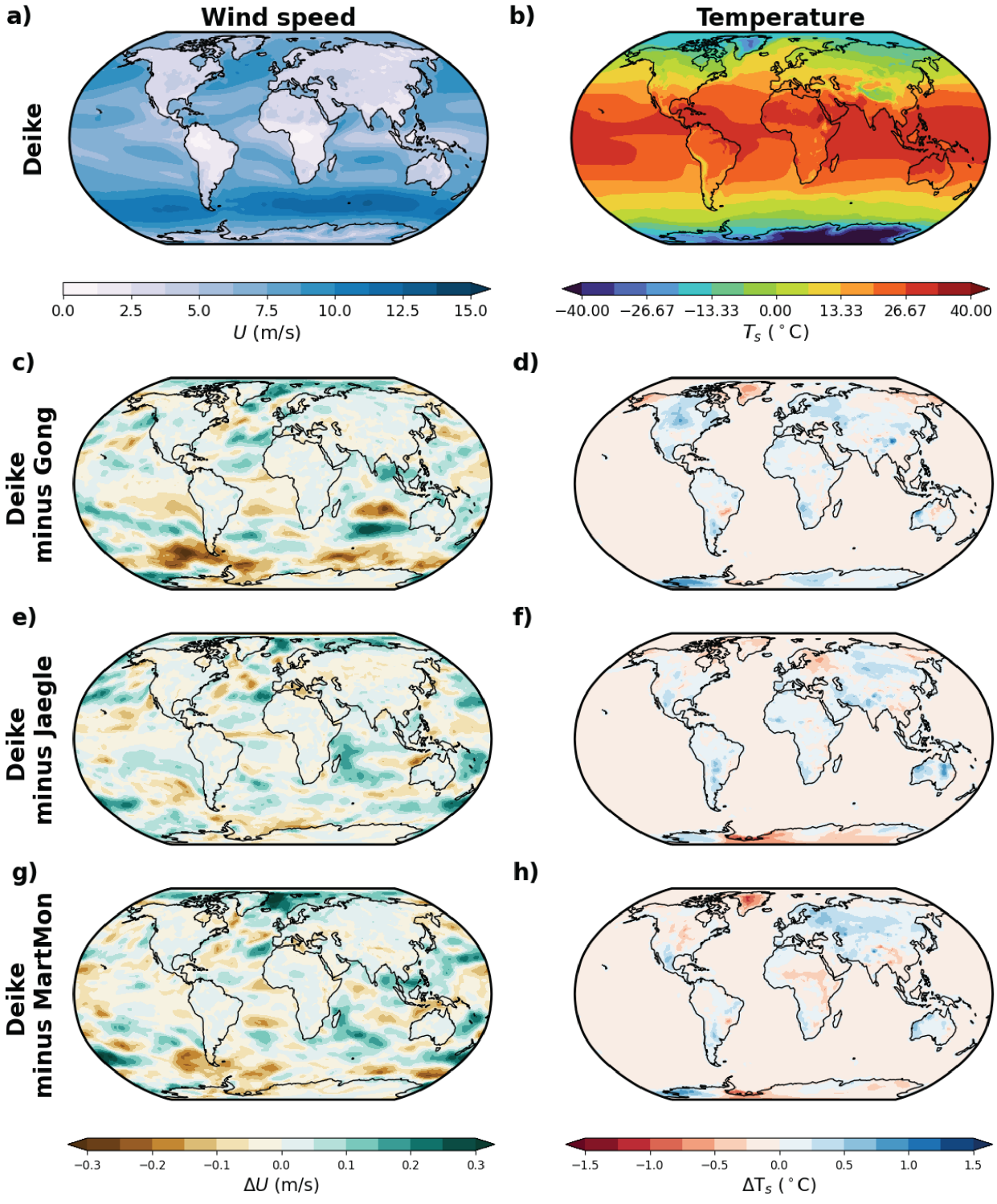


Figure 2.1: The 2000–2019 averaged (left) 10-meter wind speed and (right) surface temperature for a and b) Deike and the difference in wind speed and temperature between Deike, and the three other schemes: c and d) Gong, e and f) Jaegle and g and h) MartMon.

using Gong's emission formulation exhibits higher wind speeds than those of Deike in the Southern Ocean.

2.3.2 SSA emissions

In AM4, SSA are grouped into five size bins with dry radii ranging from 0.1 to 10 μm (Paulot et al., 2020): 0.1-0.5 μm, 0.5-1.0 μm, 1.0-2.5 μm, 2.5-5.0 μm and 5.0-10 μm. The standard setup for AM4 uses a combination of two schemes: Mårtensson et al. (2003) for particles less than 1.4 μm and Monahan et al. (1986) for particles greater than 1.4 μm, referred to as "MartMon" in this work. In addition to this standard setup, we run AM4 with three other SSA emission schemes: 1) Deike et al. (2022), 2) Gong (2003), 3) Jaeglé et al. (2011). All of these emission schemes differ in their sensitivity to SST (Table 1), with Jaeglé et al. (2011) having the strongest sensitivity to SST. However, Gong (2003), Jaeglé et al. (2011), and Monahan et al. (1986) all have the same wind speed scaling ($u^{3.41}$). More details about the four emission schemes (Deike, MartMon, Jaegle, and Gong) can be found in Chapter 1.

Name	**Description**	**Smallest sea-salt particle (μm)**	**Largest sea-salt particle (μm)**	**Emissions reference**
MartMon	Wind speed & weak temperature	0.01	1.40	Martensson et al., 2003
	Wind speed	1.40	10.00	Monahan et al., 1986
Gong	Wind speed	0.01	10.00	Gong et al., 2003
Jaegle	Wind speed & strong temperature	0.01	10.00	Jaegle et al., 2011
Deike	Wind speed & weak temperature	0.01	10.00	Deike et al., 2022

Table 2.1: A comparison of the four configurations of emission scheme that is used in the AM4 AMIP simulations. The radius sizes are given in terms of dry radius (μm).

Emission sensitivity to temperature & wind speed

In Fig. 2.2, we compare the sensitivity of each emission formulation to a range of surface temperatures and wind speeds. Among the four emission formulations, Gong's parameterization is the only one without any temperature dependency. In contrast, the Deike, Jaegle, and MartMon formulations exhibit dependencies on both temperature and wind speed, but their responses to these changes differ. Jaegle has the strongest temperature dependency, with emissions increasing almost five times as the temperature rises from 0 to 25°C (Fig. 2.2f). The dependence of wind speed is largely similar for all four emission configurations, although Deike and MartMon exhibit a slightly lower emission sensitivity to wind speed at high wind speed (>14 m/s; Fig. 2.2a and g). Furthermore, Gong's emission formulation appears to produce higher emissions than MartMon under the same wind speed and temperature conditions. Jaegle's formulation adopts Gong's wind speed dependency but produces higher SSA emissions at high wind speeds, particularly at high temperatures (Fig. 2.2e vs. Fig. 2.2c). However, Jaegle yields lower emissions than Gong at low temperatures and high wind speeds. This is likely due to the strong temperature dependence in Jaegle's parameterization, as shown in Fig. 2.2e when comparing emissions at T = 0 m/s and T = 25 m/s.

Fig. 2.3 illustrates the percentage change in emission per °C and m/s. While the parameterization of SSA in Deike et al. (2022) shows sensitivity to both temperature and wind speed, the magnitude of the SSA emissions decreases with increasing temperature (Figs. 2.2b and 2.3a). This contrasts with the positive relationship between SSA emissions and temperature observed in Jaegle and MartMon (Figs. 2.2f and h, respectively). Jaegle exhibits greater temperature sensitivity, with emissions changing from 1% to 25%/°C over a range of temperatures, whereas for MartMon, the percentage change in emissions per degree increase is less than 1% over the same temperature range.

In Fig. 2.3b, Gong, Jaegle, and MartMon show similar percentage changes in emission per change in wind speed (m/s). However, Deike's behavior deviates, with a notably larger %

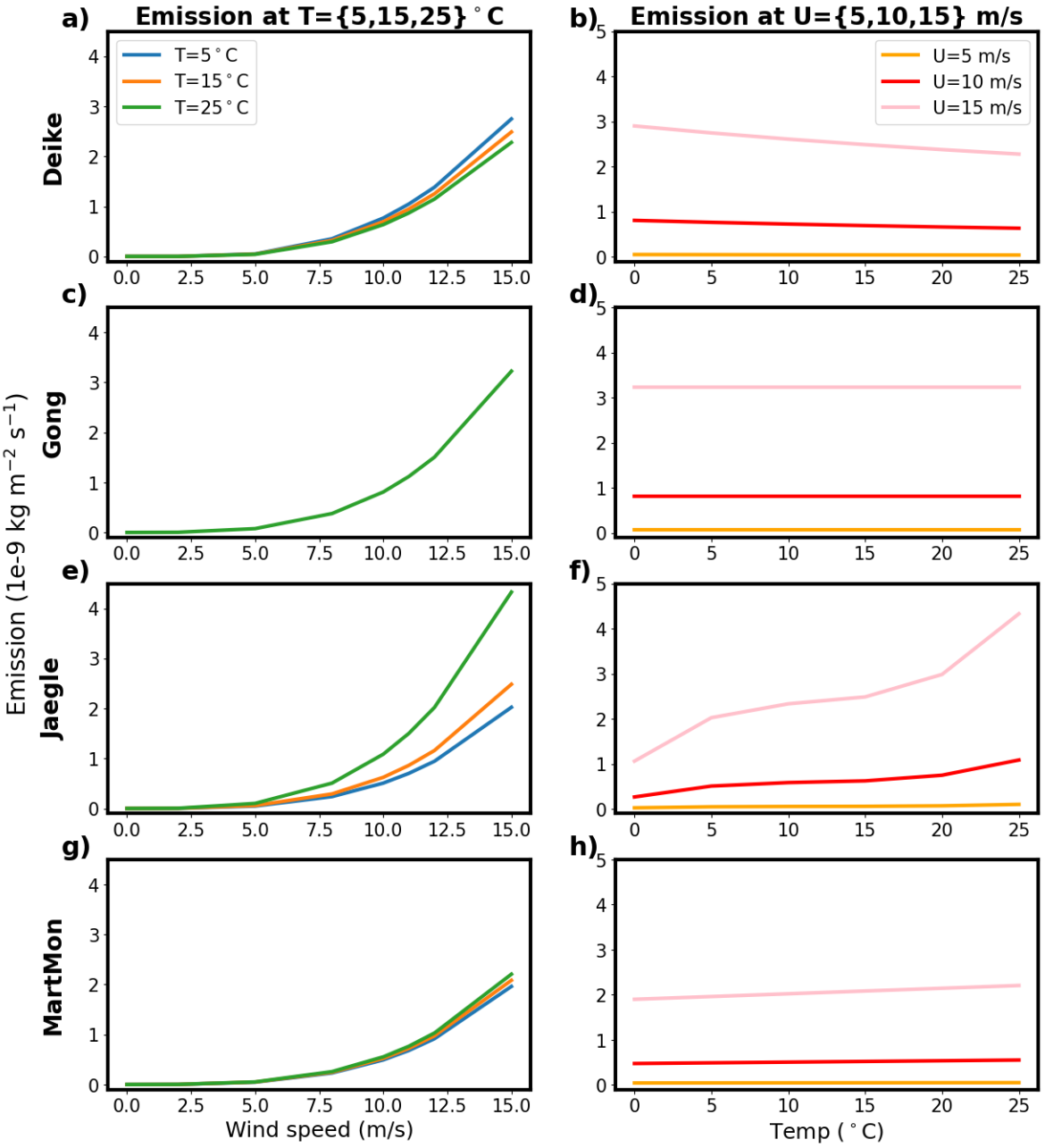


Figure 2.2: In the first column (a, c, e and g), SSA emissions are computed for the Deike, Gong, Jaegle and MartMon at a constant temperature (T = 5, 15 and 25°C) while altering the wind speed. In the second column (b, d, f and h), the wind speed remains constant (U = 5, 10 and 15 m/s) and emissions are calculated as the temperature increases.

increase in emission observed at lower wind speeds. In general, Deike appears to suggest that SSA production is perhaps suppressed at higher temperatures, consistent with the findings of Christiansen et al. (2019). In general, the disparate effects of SST on SSA production

have been well documented in previous observational and laboratory studies (Barthel et al., 2019; S. Liu et al., 2021; Anguelova & Webster, 2006; Lewis et al., 2004; Christiansen et al., 2019; Jaeglé et al., 2011; Forestieri et al., 2018; Sellegri et al., 2006), making it challenging to draw firm conclusions about the sensitivity of SSA production to SST.

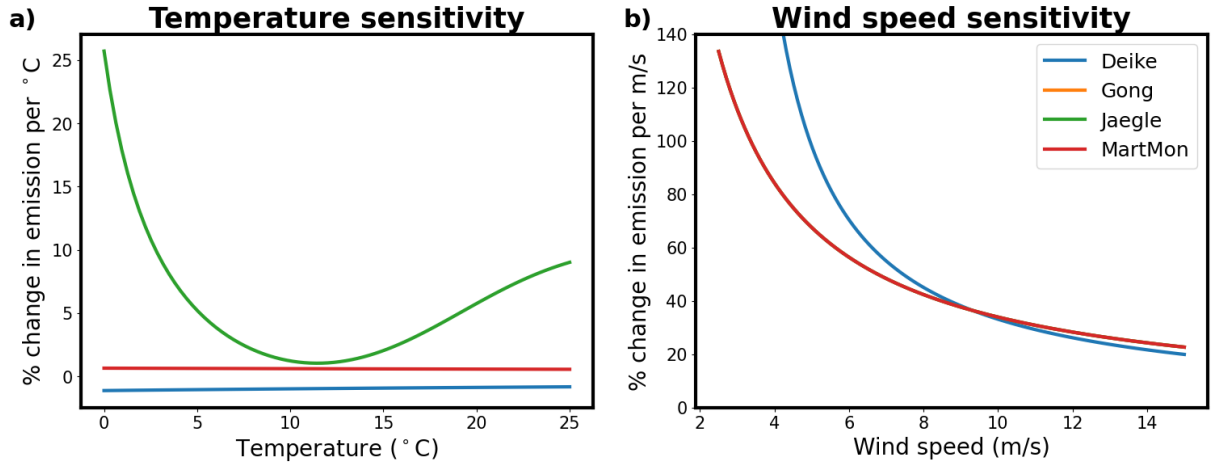


Figure 2.3: The % change in emission per unit increase in a) temperature (°C) and b) wind speed (m/s) for the four emission configurations. This is computed by calculating the emission when temperature is increased in increments of 0.5°C or when wind speed is increased by increments by 0.1 m/s. This specific increment were calculated using finite differences and verified to converge with smaller increments. Note that the curves for Gong and Jaegle in panel b are not visible because they overlap with the MartMon line.

2.3.3 AOD (550 nm) validation

We will evaluate our simulated AOD against multiple observational datasets over the 2000 to 2019 period. These datasets include

- Ground-based measurements (516) from the AERONET sunphotometer network which covers the 2000-2019 period (Holben et al., 1998)

- Regional monthly mean AOD observations from satellite instruments over the 2000-2014 period:

a) MODIS Collection 6 Deep Blue and Dark Target merged aerosol product provided monthly with a resolution of 1°×1° (Levy et al., 2007; Bilal et al., 2018; Sayer et al., 2014)

b) MISR operational (V22) Dark Blue aerosol retrievals provided monthly with a resolution of 0.5°×0.5° (Kahn et al., 2009; Kalashnikova et al., 2013)

- Maritime Aerosol Network (MAN) component of AERONET (Smirnov et al., 2011), which covers the 2004-2019 period and provides ship-based observations over global oceans.

All AOD observations and model simulations will be evaluated at a wavelength of 550 nm, allowing for consistent comparison. The four validation products offer distinct advantages. MODIS and MISR provide satellite-retrieved AOD observations with broad spatial coverage, while AERONET offers ground-site measurements from a global network of sites. Furthermore, Maritime AERONET provides a compilation of cruise observations over the global oceans, where SSA contributes to a substantial part of total AOD.

By comparing our model simulations with these diverse observational datasets, we can gain valuable insight into the strengths and limitations of different AOD retrieval methods and their geographic distributions.

2.4 SSA emission and concentration in AM4 - 2000-2019

A comparison with the four model runs reveals significant differences in SSA emissions and concentrations, particularly in the Southern Ocean and tropics (Figs. 2.4a and e). In the Southern Ocean, Deike's scheme produces higher SSA emissions and concentrations than Jaegle and MartMon, but lower than Gong. This aligns with the stronger wind speeds modeled in Gong's simulation compared to Deike's in the Southern Ocean (Fig. 2.1), which

likely drive higher emissions in this region. Additionally, differences between Deike and Gong (also Jaegle and MartMon) at a given wind speed may also contribute to the variations in emissions between the two simulations (Fig. 2.3b). In the tropics, Deike's model yields lower SSA emission and concentration than Gong and Jaegle. Notably, Deike's model shows the highest correlation with both emissions and concentrations when compared to MartMon and Gong. However, Jaegle exhibits the lowest bias magnitude relative to Deike's emissions, while MartMon shows the lowest bias magnitude and RMSE relative to Deike SSA concentration (Fig. 2.4). Overall, variations in the evolution of wind speed, along with the differing sensitivities of emission schemes to temperature and wind speed, likely drive the observed differences in SSA emission and concentration patterns across model simulations and regions.

Figure 2.5 presents a comparison of the zonally averaged distribution of SSA emission and surface mass concentration (2000-2019) simulated by AM4 using four different SSA emission formulations, summed over all SSA size bins. In the Southern Ocean, where strong winds enhance the emission of SSA (Derkani et al., 2020; Bertram et al., 2018), the amount of SSA emissions from Gong and Deike are greater than the emission obtained with Jaegle and MartMon parameterizations. Gong's emissions are the largest in this region, likely due to higher wind speeds in the Gong simulation (Fig. 2.1c) and the inherently higher emission rates produced by Gong's parameterization (Fig. 2.2d). In contrast, Jaegle yields higher emissions than Gong, Deike, and MartMon in the tropics, likely due to contributions from the stronger temperature dependence in Jaegle's formulation. In the tropics, the SSA emission calculated using Deike et al. (2022) is similar to that obtained with the combined parameterization based on laboratory experiments Mårtensson et al. (2003) and Monahan et al. (1986). Fig. 2.5b illustrates that the differences in emission among the four experiments are also reflected in the resulting SSA concentration (at 997.9 mb). In the Southern Ocean, the concentration of SSA for Deike does not appear to be proportional to emissions and appears to be lower.

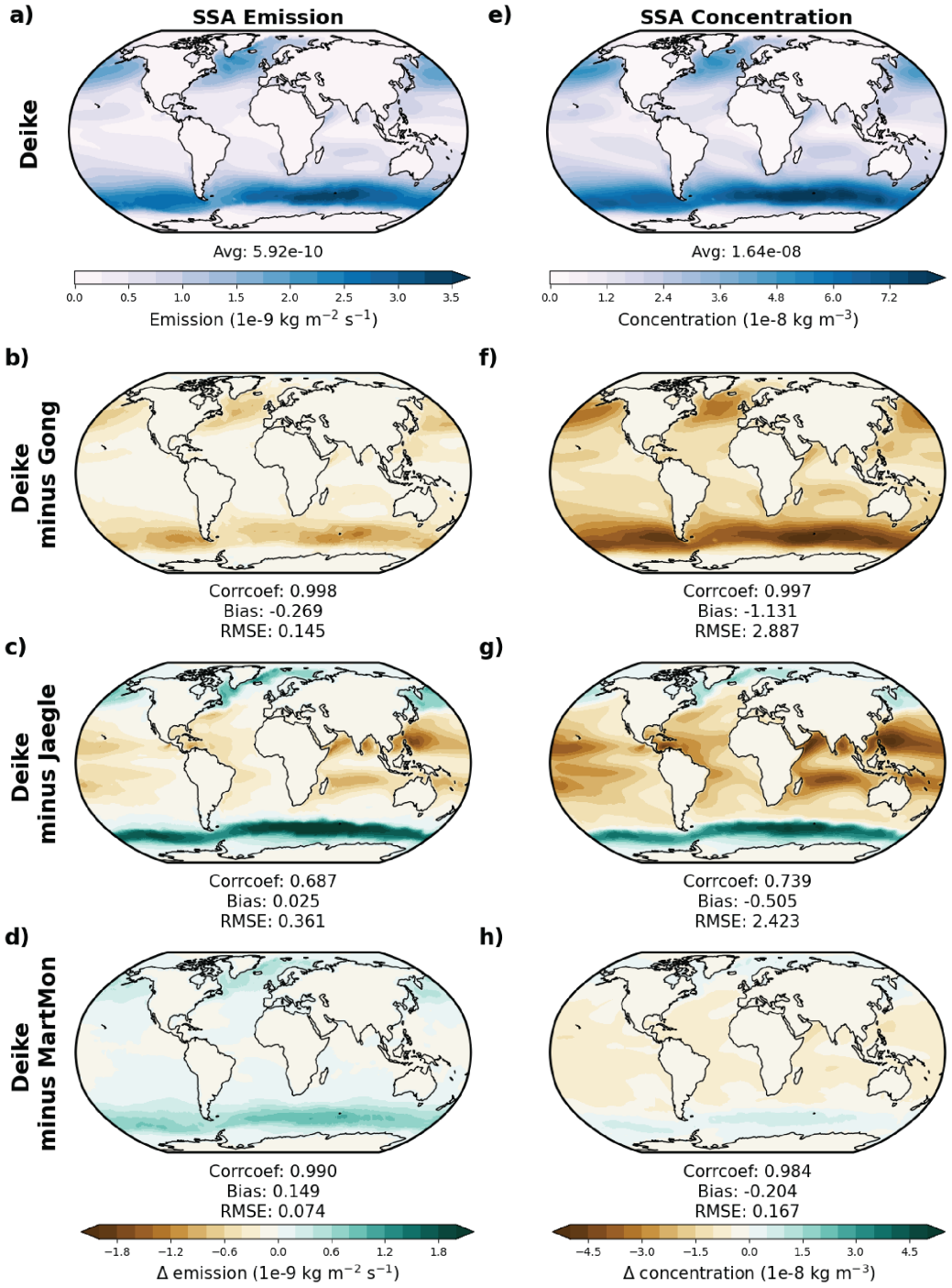


Figure 2.4: The 2000–2019 averaged SSA emission and surface concentration for Deike and the difference between the results from AMIP simulations with Deike and the other three schemes. The RMSE, bias and correlation coefficient between Gong, Jaegle and Gong relative to Deike are presented alongside.

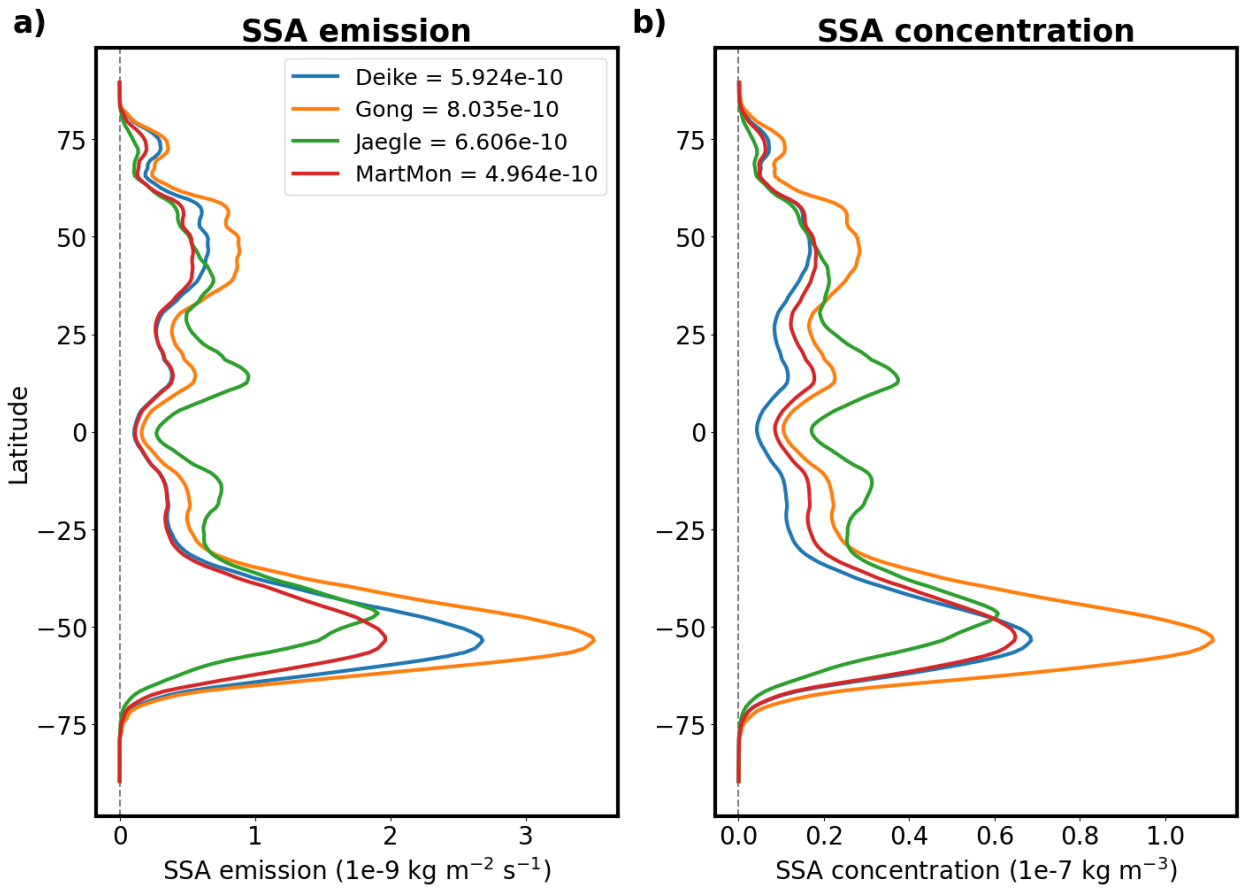


Figure 2.5: The zonal-mean SSA emissions and surface mass concentration (2000–2019) calculated using Deike (blue), Gong (orange), and Jaegle (green), and MartMon (red) in the lowest model layer. The global averaged emissions (kg m^{-2} s^{-1}) is given after the scheme name.

To better understand the emission to concentration discrepancies observed in Fig. 2.5, we look at the size distribution, as outputted by the model, in Fig. 2.6. The SSA emission from Deike et al. (2022) for film and jet droplets ranging from 0.01 to 5 μm, is smaller than that from Gong, Jaegle, and MartMon. This is consistent with the comparison of sea spray generation functions presented in Fig. 4 of Deike et al. (2022), which shows that the Deike production flux has a lower magnitude than those of Jaegle and Martenssen for smaller particles, particularly within the same range as the AM4 submicron bins (0.1 to 1 μm). Deike et al. (2022) noted an apparent underestimation in their formulation for particle radii smaller than 0.5 μm, as their model does not account for organic aerosol particles that dominate

this size range. In contrast, for larger particles, comprising spume particles ranging from 5 to 10 μm, the average SSA emission of Deike et al. (2022) exceeds that from Gong, Jaegle and MartMon in Fig. 2.6. This is consistent with Fig. 4 of Deike et al. (2022) showing that Deike's production flux is significantly higher than that of Jaegle and Gong for larger particles. Thus, the total emission is mainly comprised of larger particles. The size distribution of SSA particles has significant implications for the lifetime of SSA. In particular, larger particles have shorter atmospheric lifetimes due to size-dependent deposition rates (i.e., dry deposition and gravitational settling), which limit their spatial distribution and resulting concentrations (Gong et al., 1997; Kawakami et al., 2008; Lewis et al., 2004). This explains why the zonally averaged concentration for Deike is similar to MartMon in the Southern Ocean, despite Deike having higher emissions than MartMon in that region. The differences in net gravitational settling associated with particle size distributions thus play a key role in shaping concentration fields. As an illustrative example of how the physical characteristics of particles beyond total mass, such as shape and density, can affect gravitational settling, Ginoux (2003) emphasizes the role of non-sphericity in modifying settling velocities. Therefore, the distribution of particle properties strongly modulates their atmospheric lifetime.

2.5 AOD validation

Aerosol Optical Depth (AOD) is a measure of the extinction of solar radiation by aerosol particles in the atmosphere and quantifies how much light is prevented from reaching the Earth's surface by aerosols in the atmosphere. AOD is a dimensionless number, with higher values indicating higher aerosol concentrations or smaller particle sizes, both of which contribute to more pronounced light extinction. In essence, AOD ranges from 0 for a completely clear sky with no aerosols to values approaching or even exceeding 1 for conditions characterized by significant haze or pollution.

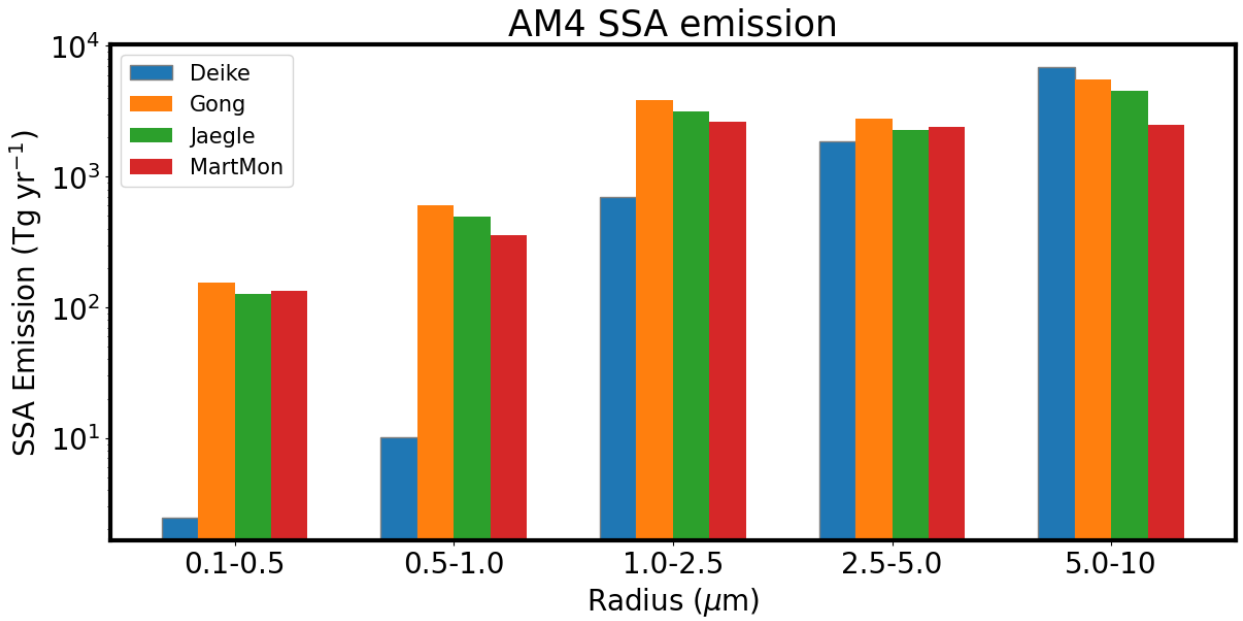


Figure 2.6: The 20 year (2000-2019) globally integrated SSA emissions (Tg yr^{-1}) partitioned into the 5 size bins used by AM4.

In AM4, aerosol optical properties are calculated based on dry mass concentration, specific extinction coefficients, and relative humidity, as described in Ginoux et al. (2006). The model simulates the optical depth of five aerosol species: sulfate, black carbon, organic carbon, sea salt, and mineral dust, with the latter two further divided into small and large particle size bins (L. W. Horowitz et al., 2020). Dust and sea salt are each partitioned into five size bins ranging from 0.1 to 10 μm. For dust, the first size bin (0.1–1 μm) is referred to as "small dust particles", while the remaining four size bins (1–10 μm) are collectively defined as "large dust particles" (Pu et al., 2020).

Fig. 2.7 shows the zonal 20-year average of optical depths for each species. Since we are only modifying the representation of SSA emissions in the four runs, we anticipate minimal changes in optical depths for the other aerosol species. The zonal distribution of the total AOD components supports this expectation, indicating that changes in SSA optical depths drive the variations in total AOD.

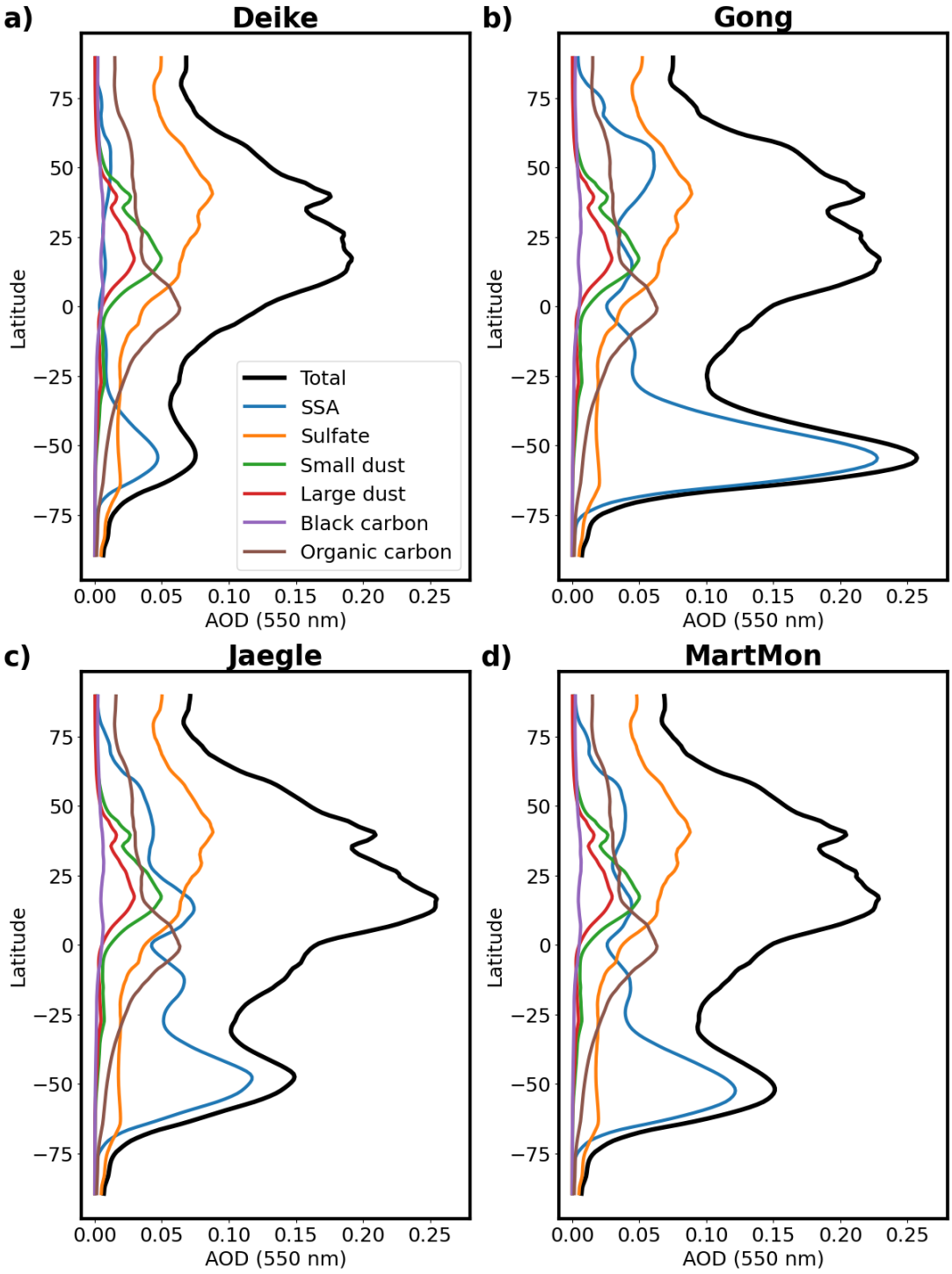


Figure 2.7: Components of the zonal mean total AOD from the AM4 model for the 4 simulations.

2.5.1 MODIS and MISR: 2000–2014

As mentioned above, the AOD observations from MODIS (Levy et al., 2007) and MISR (Kahn et al., 2009) are derived from satellite retrievals. MODIS employs separate algorithms

for retrieving AOD over land and ocean, utilizing the "Deep Blue" algorithm for land surfaces and the "Dark Target" algorithm for ocean surfaces (Bilal et al., 2018; Sayer et al., 2014). The Dark Target algorithm is not effective over bright land surfaces. The MODIS product used in this study combines Deep Blue and Dark Target AOD retrievals to provide a comprehensive global aerosol product at a high resolution of 3 km. Similarly, MISR uses two distinct algorithmic approaches for land and water surfaces, but the product used in this study includes retrievals over the ocean (dark blue) and land (light blue) (Kalashnikova et al., 2013). Using both MODIS and MISR products in our analysis enables a more comprehensive representation of satellite-retrieved AOD, enhancing spatial and temporal coverage, which is useful for constraining and verifying aerosol parameterizations in global climate models (Liu et al., 2006; Kinne et al., 2006; Ban-Weiss et al., 2014).

Fig. 2.8 presents the 15-year average AOD observations from MODIS and MISR, as well as their difference. Both MODIS and MISR capture the geographic distribution of high AOD in Saharan Africa and South Asia. The correlation coefficient between MODIS and MISR is 0.877, indicating a strong spatial similarity between the two satellite retrievals despite the different algorithms used for their retrievals. The differences between MODIS and MISR reveal that MODIS tends to retrieve higher aerosol optical depths over oceanic regions than MISR. This finding is consistent with previous work (Kahn et al., 2009) that compared MODIS and MISR AOD retrievals and found that MISR AOD observations are slightly lower than MODIS over both ocean and land for AOD values greater than 0.2, and vice versa for low AOD areas. This suggests that the algorithm used in MODIS may be more sensitive to the presence of aerosols in the oceans, leading to higher AOD retrievals compared to MISR.

The zonal distribution of MODIS and MISR observations, as shown in Figure 2.9, reveals that differences in their retrieval algorithms affect observed AOD across all latitudes. Notably, MISR AOD observations are consistently lower than MODIS AOD observations.

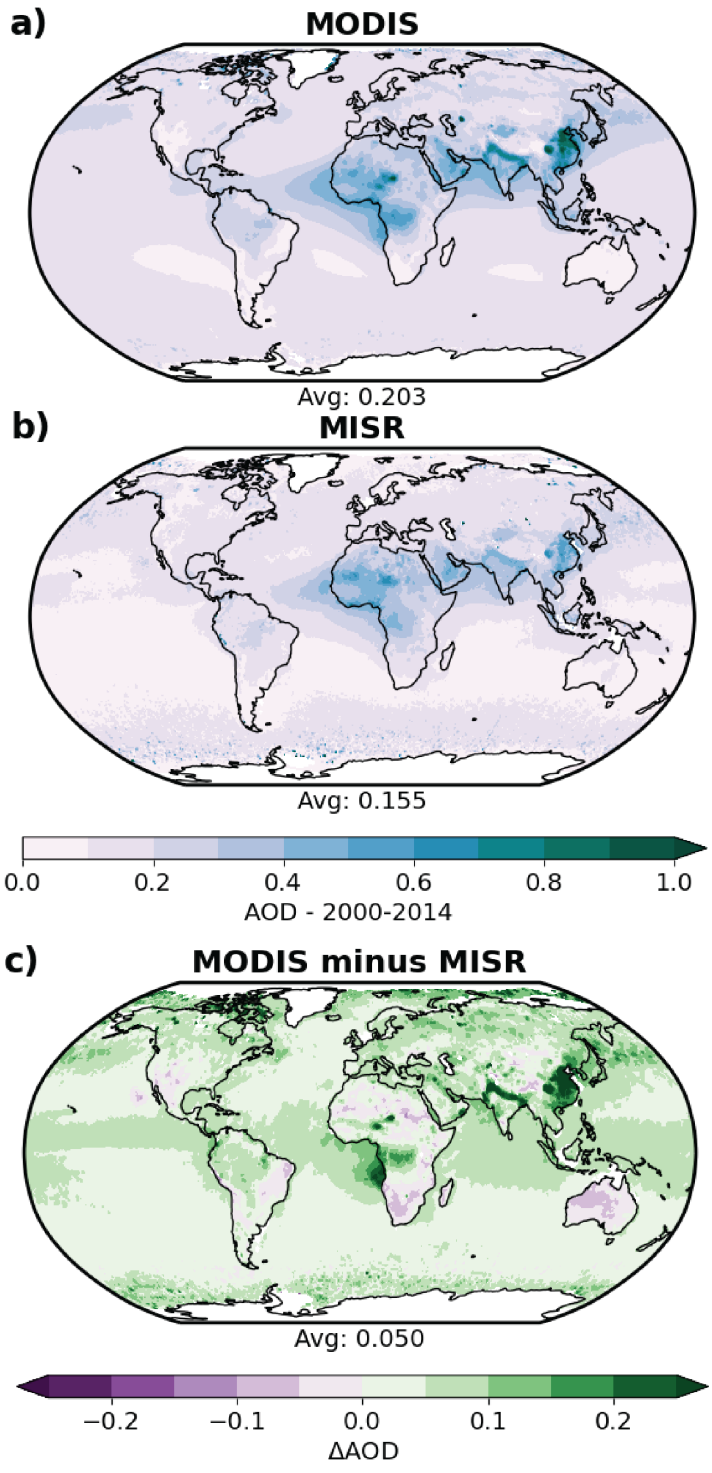


Figure 2.8: The 15-year (2000–2014) averaged AOD observation retrieved from a) MODIS and b) MISR, and their difference c) MODIS minus MISR.

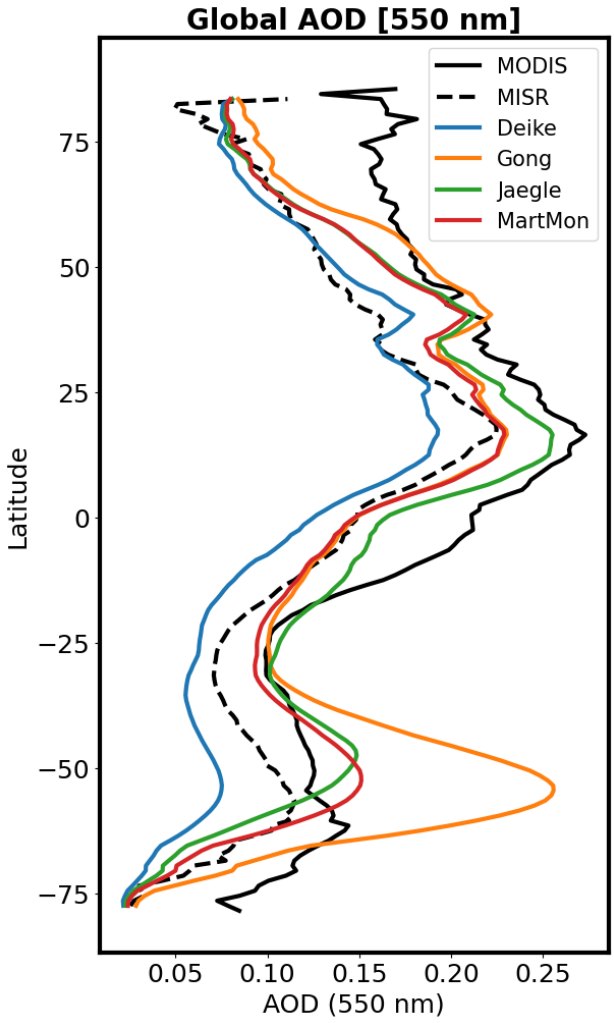


Figure 2.9: The zonal-mean AOD (2000–2014) observation retrieved from MODIS and MISR, alongside AOD modeled in Deike, Gong, Jaegle and MartMon.

To better account for these differences in our analysis, we stipple areas where the modeled AOD falls out of the range of MISR and MODIS estimates in Fig. 2.10.

Deike exhibits the highest correlation with both MISR and MODIS observations but largest RMSE and bias magnitude to MODIS observations, while Gong has the largest RMSE and bias magnitude to MISR observations. A significant portion (84.46%) of the modeled AOD in Deike falls outside the observational range. In comparison, a lower percentage of AOD estimates from Gong (65.56%), Jaegle (60.5%) and MartMon (57.93%) fall outside the range of observational uncertainty, particularly over tropical ocean regions (Fig. 2.9).

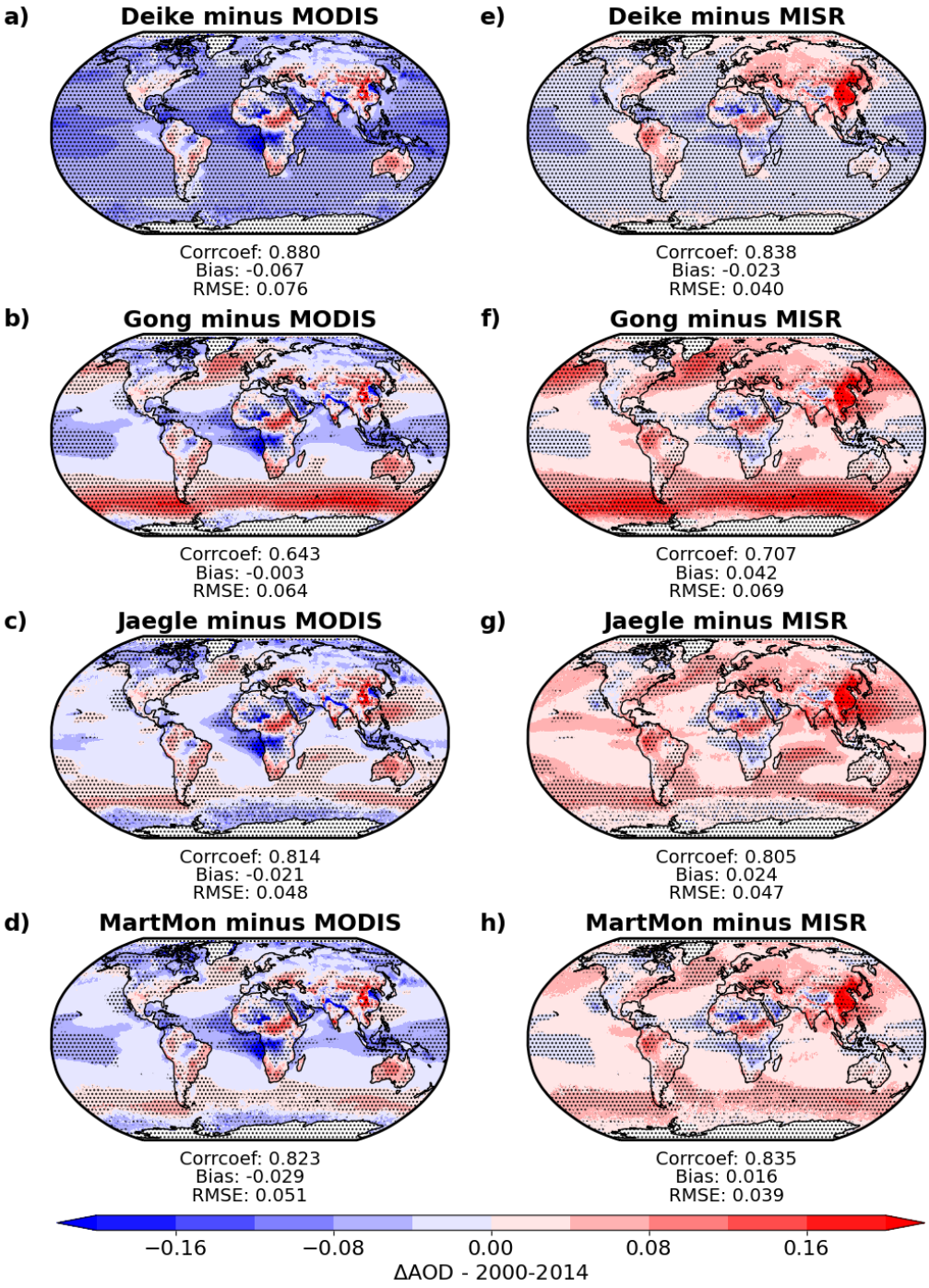


Figure 2.10: The difference between the 15-year (2000–2014) averaged AOD from the 4 AM4 runs (Deike, Gong, Jaegle and MartMon) and AOD observations from the satellite retrievals, MODIS and MISR. The ocean–only statistics for RMSE, bias (model-obs) and correlation coefficient are shown below each panel. The stipple are over areas where the modeled AOD falls outside of the range of MODIS and MISR estimates.

Although many of the AOD values modeled in Deike fall outside the range of observational uncertainty, Deike only slightly underestimates the MISR observations (Fig. 2.9). In contrast, Gong significantly overestimates AOD in certain regions, particularly the Southern Ocean (Fig. 2.9). This regional overestimation strongly skews the overall statistical performance of Gong, leading to a lower correlation coefficient and higher RMSE. Deike generally underestimates AOD globally (i.e., negative bias) compared to both MISR and MODIS observations whereas MartMon has the lowest bias magnitude for MISR. This negative bias is potentially driven by lower winds in Deike or by the underestimation noted in the Deike formulation for particle radius sizes less than 0.05 μm. Furthermore, Gong, Jaegle, and MartMon tend to underestimate MODIS AOD observations while overestimating MISR AOD observations (Fig. 2.10), highlighting differences in how each emission scheme compares with the respective satellite datasets.

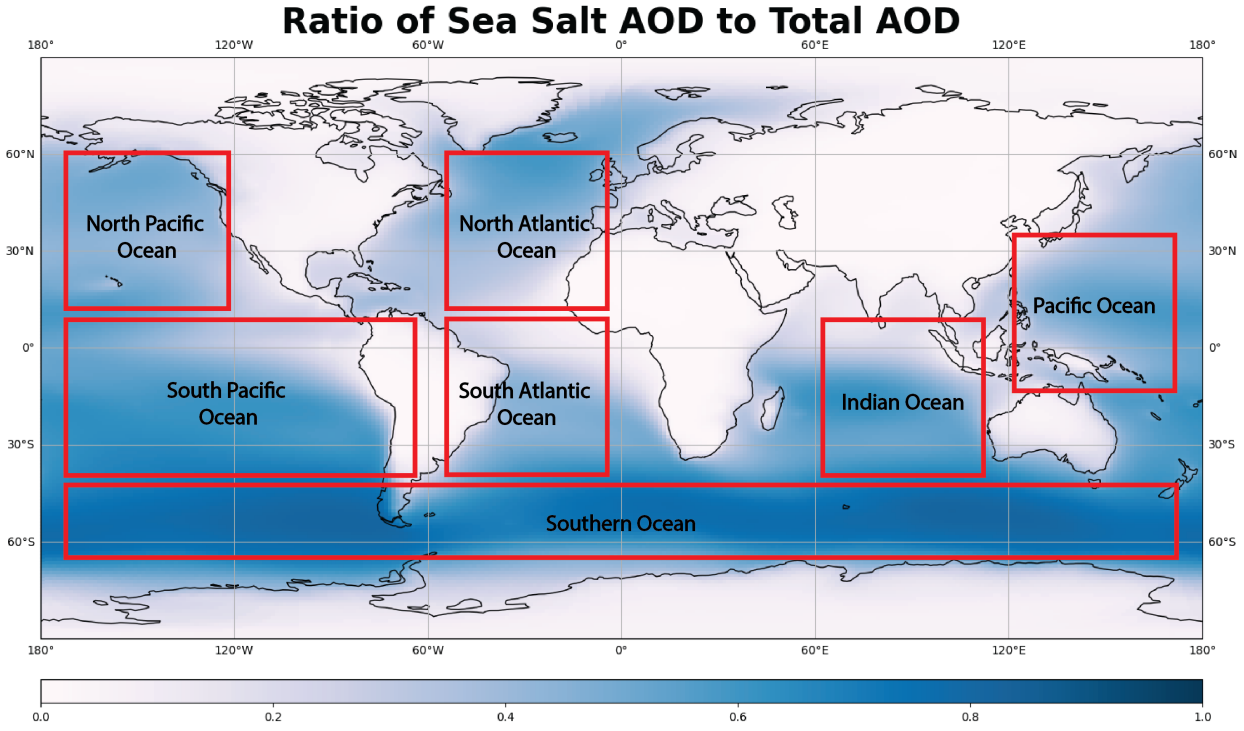


Figure 2.11: The panel–based groupings of regions of interest, superimposed on a map showing the four-run averaged ratio of SSA AOD to total AOD.

We next focus our analysis on seven geographical ocean regions where the contribution of modeled sea salt AOD to total AOD is the largest, as shown in Fig. 2.11. These regions represent aggregated spatial averages derived from the panels shown in Fig. 17 of L. W. Horowitz et al. (2020). Figure 2.12 shows the 15-year averaged seasonal cycle of AOD from MODIS, MISR, and the four AM4 simulations, spatially averaged over the seven corresponding ocean regions. The model captures seasonal variations in the Atlantic and Indian Oceans, with varying performance across all regions. The seasonal AOD cycle is reasonably well represented in all regions, though the accuracy varies by location. For example, the model captures the September AOD peak in the South Atlantic Ocean with remarkable accuracy, whereas in the North Atlantic Ocean, the timing of the AOD peak is shifted by a few months.

Table 2.2 provides statistical metrics, the correlation coefficient, the mean squared error (RMSE), and bias, comparing the AOD model simulations with the observations of MISR and MODIS in the seven ocean regions (Fig. 2.11). The simulation with the highest correlation coefficient varies by region and satellite dataset. For example, Deike shows the highest correlation coefficient with both MODIS and MISR in the North Atlantic Ocean and with MISR in the Atlantic Ocean, while Gong slightly outperforms Deike in the South Pacific Ocean for MODIS. For MISR, Deike consistently outperforms other simulations in the Southern Ocean, with the highest correlation coefficient, lowest bias magnitude, and RMSE compared to MISR observations. In contrast, Jaegle exhibits the highest RMSE in the South Pacific Ocean, South Atlantic Ocean, Indian Ocean, and Pacific Ocean. These region-specific patterns reflect broader trends seen in global comparisons: while Deike achieves the highest global correlation with satellite-retrieved AOD, most estimates still fall below the observational uncertainty range. Gong, Jaegle, and MartMon tend to underestimate AOD compared to MODIS but overestimate it relative to MISR. Collectively, these results underscore the importance of using multiple satellite datasets to evaluate model accuracy across different spatial domains.

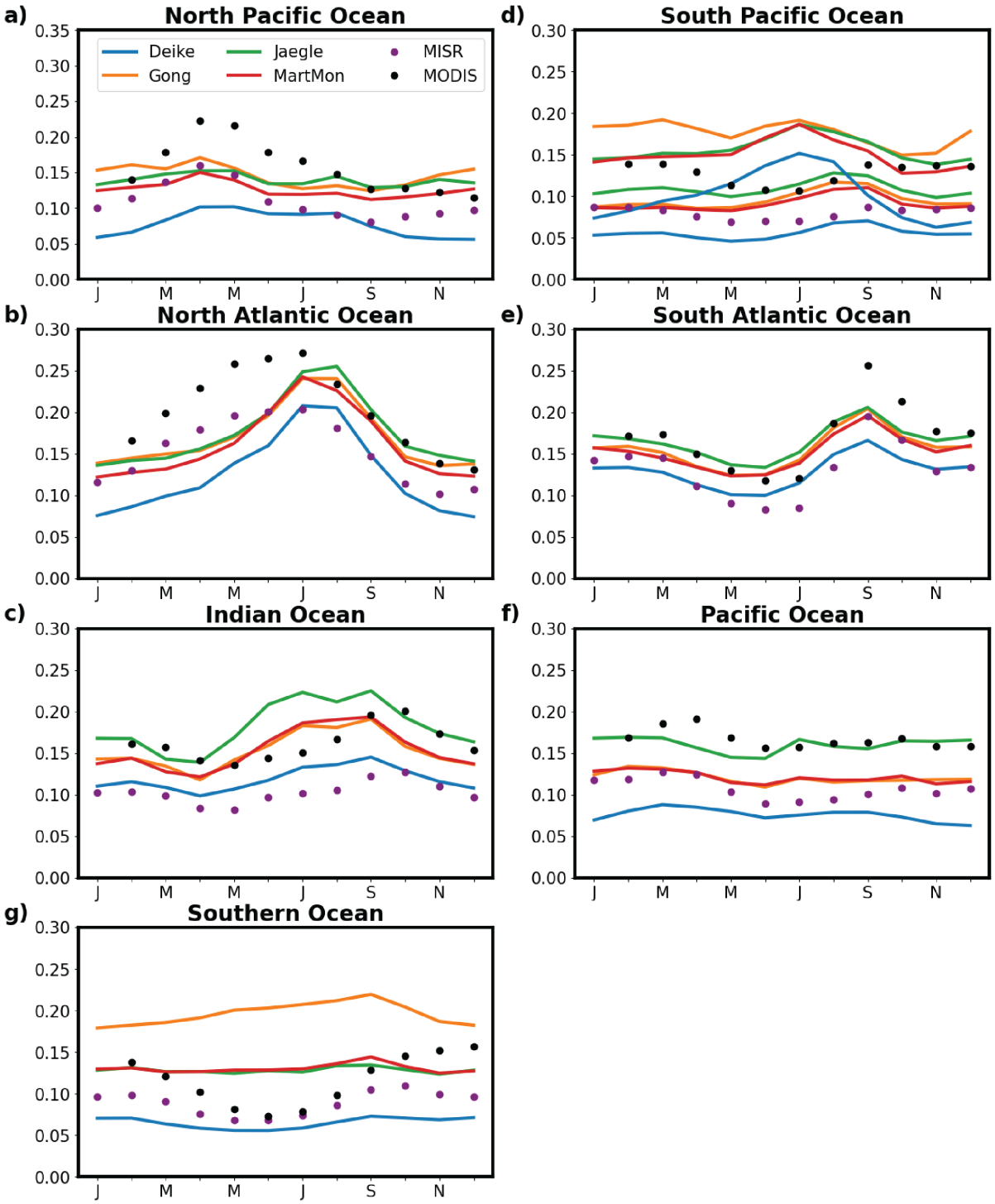


Figure 2.12: Monthly climatology (2000–2014) of AOD simulated by AM4 using Deike (blue line), Gong (orange line), Jaegle (green line), MartMon (red line) and measured by MISR (purple circle) and MODIS (black circle) satellite instruments for each geographic region.

		Corrcoef		RMSE		Bias	
		MODIS	MISR	MODIS	MISR	MODIS	MISR
North Pacific Ocean	Deike	*0.470*	0.612	*0.195*	0.037	−0.545	−0.274
	Gong	−0.083	0.757	0.208	0.040	*−0.150*	0.369
	Jaegle	0.364	0.841	0.202	0.035	−0.177	0.319
	MartMon	0.163	*0.943*	0.201	*0.022*	−0.264	*0.184*
South Pacific Ocean	Deike	0.135	*0.391*	0.185	0.025	−0.603	−0.298
	Gong	*0.236*	−0.039	*0.184*	0.020	−0.312	0.208
	Jaegle	0.200	−0.002	0.187	0.031	*−0.219*	0.377
	MartMon	0.161	0.008	*0.184*	*0.016*	−0.347	*0.152*
North Atlantic Ocean	Deike	*0.495*	*0.852*	*0.192*	0.040	−0.441	−0.209
	Gong	0.410	0.817	0.202	0.033	*−0.186*	0.182
	Jaegle	0.446	0.734	0.199	0.037	−0.188	0.171
	MartMon	0.456	0.811	0.196	*0.027*	−0.247	*0.085*
South Atlantic Ocean	Deike	0.122	*0.910*	*0.190*	*0.017*	−0.316	*0.022*
	Gong	*0.162*	0.879	0.193	0.030	−0.171	0.236
	Jaegle	0.085	0.887	0.197	0.039	*−0.118*	0.320
	MartMon	0.109	0.882	0.193	0.028	−0.190	0.212
Indian Ocean	Deike	0.110	*0.893*	0.190	*0.018*	−0.524	*−0.156*
	Gong	*0.164*	0.646	0.189	0.029	−0.280	0.270
	Jaegle	0.079	0.574	0.194	0.047	*−0.174*	0.462
	MartMon	0.223	0.672	*0.188*	0.025	−0.301	0.230
Pacific Ocean	Deike	*0.301*	0.417	*0.190*	0.033	−0.593	−0.287
	Gong	−0.104	*0.845*	*0.190*	*0.015*	−0.359	*0.135*
	Jaegle	−0.263	0.461	0.197	0.055	*−0.148*	0.514
	MartMon	−0.289	0.821	0.191	0.016	−0.360	0.138
Southern Ocean	Deike	−0.118	*0.957*	*0.180*	*0.025*	−0.475	*-0.260*
	Gong	*0.336*	−0.150	0.220	0.109	0.661	1.266
	Jaegle	0.020	0.418	0.191	0.041	*0.066*	0.476
	MartMon	0.046	0.365	0.191	0.043	0.085	0.500

Table 2.2: Correlation coefficient, RMSE and bias for regional mean AOD in the four model simulations against MODIS and MISR for seven regions of interest shown in Fig. 2.11. Bias is computed as a relative (fractional) bias. For each region, the values with the lowest RMSE, lowest absolute value of bias, and highest correlation coefficient are italicized.

2.5.2 AERONET: 2000–2019

We evaluate the simulated AOD against measurements from the AERONET sunphometer network (2000-2019; Holben et al. (1998)), which captures local changes in AOD at hundreds

of sites. Many of the sites in Fig. 2.13a are on land, where positive biases are associated with a higher dust loading and nitrate aerosols (L. W. Horowitz et al., 2020). Although SSA emissions originate over oceans, wind-driven advection can transport sea salt particles to interior parts of continents, such as the Amazon (Ikegami et al., 1994; Patterson et al., 1980; Talbot et al., 1990), the central Greenland ice sheet (Davidson et al., 1989) and the interior of the USA (Junge & Gustafson, 1956).

In Figure 2.13b and c, we compare AOD observations from AERONET with satellite-retrieved AOD from MISR and MODIS. Despite differences in the mechanisms of observation retrieval, AERONET exhibits a high correlation with both MISR and MODIS data. Over North America and oceanic regions, AOD observations from AERONET closely match those from MISR. However, MODIS shows a higher correlation coefficient, lower bias, and lower RMSE to AERONET compared to that for MISR. This is likely due to large discrepancies in AOD observations between MISR and AERONET over South Asia and southern Africa. However, despite the differing retrieval methods, the two types of AOD observational products show small discrepancies and significant similarities.

Notably, the spatial patterns and magnitudes of AOD differences for the Jaeglé, Gong, and MartMon emission schemes (Fig. 2.10) show similarities to the observed discrepancies between satellite retrievals (MODIS/MISR) and AERONET (Fig. 2.13). For example, Gong's positive ΔAOD over the Southern Ocean (Fig. 2.10b and f) mirrors the underestimation by MODIS and MISR relative to AERONET in the same region (Fig. 2.13b and c). Moreover, the sign and magnitude of the bias and RMSE between the models and MODIS/MISR are often comparable to those between MODIS/MISR and AERONET. In contrast, model and AERONET biases tend to be smaller, suggesting better agreement with ground-based observations (Fig. 2.14). The alignment in sign–and in some locations, magnitude–between model–AERONET and MODIS–MISR differences adds confidence in the fidelity of the Jaegle, Gong, and MartMon sea salt aerosol formulations. These results strongly suggest that a significant portion of the model–satellite discrepancies may arise from

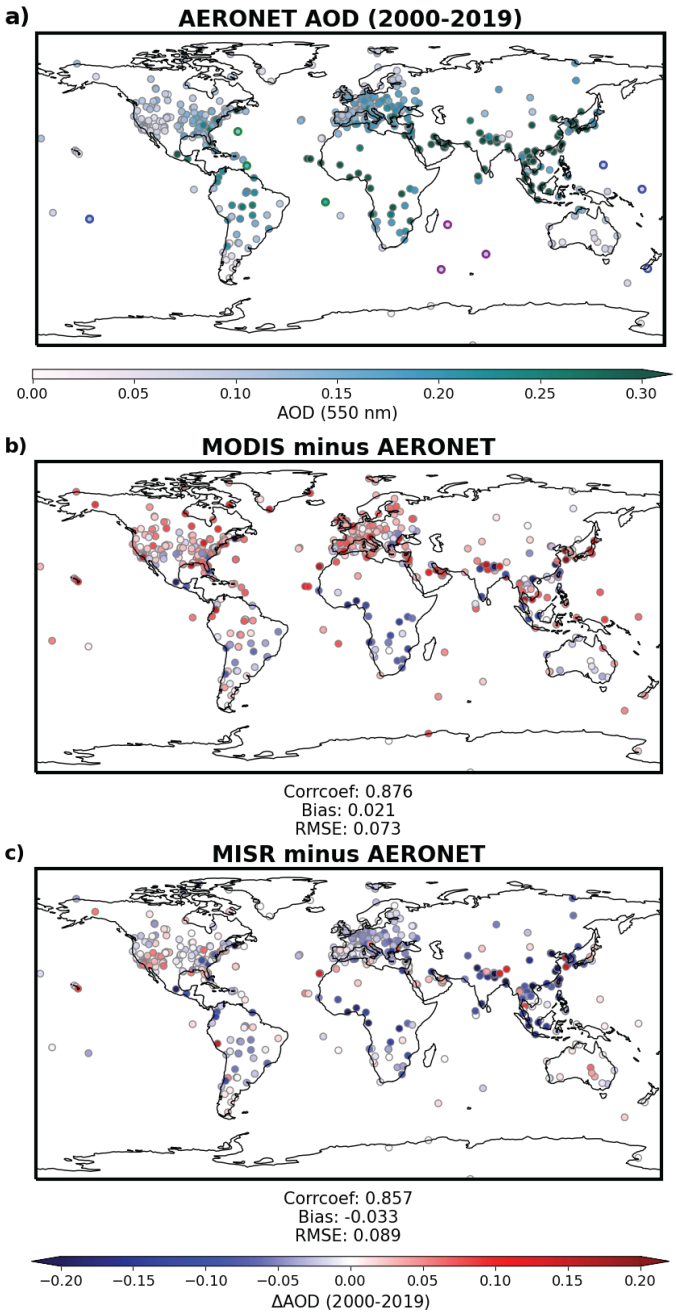


Figure 2.13: The 2000–2019 average AOD from the AERONET sun photometer network. Sites in a) Bermuda, b) Barbados and c) Ascension Island are located in the Atlantic Ocean and are highlighted in green. Sites in d) Reunion, e) Crozet Island and f) Amsterdam Island are located in the Indian Ocean and are highlighted in purple. Sites g) Guam, h) Nauru, i) Dunedin and j) Tahiti are located in the Pacific Ocean and are highlighted in blue. Panels b and c show the differences between AERONET and MODIS/MISR, respectively. Correlation coefficients, bias, and RMSE are provided below figures b and c.

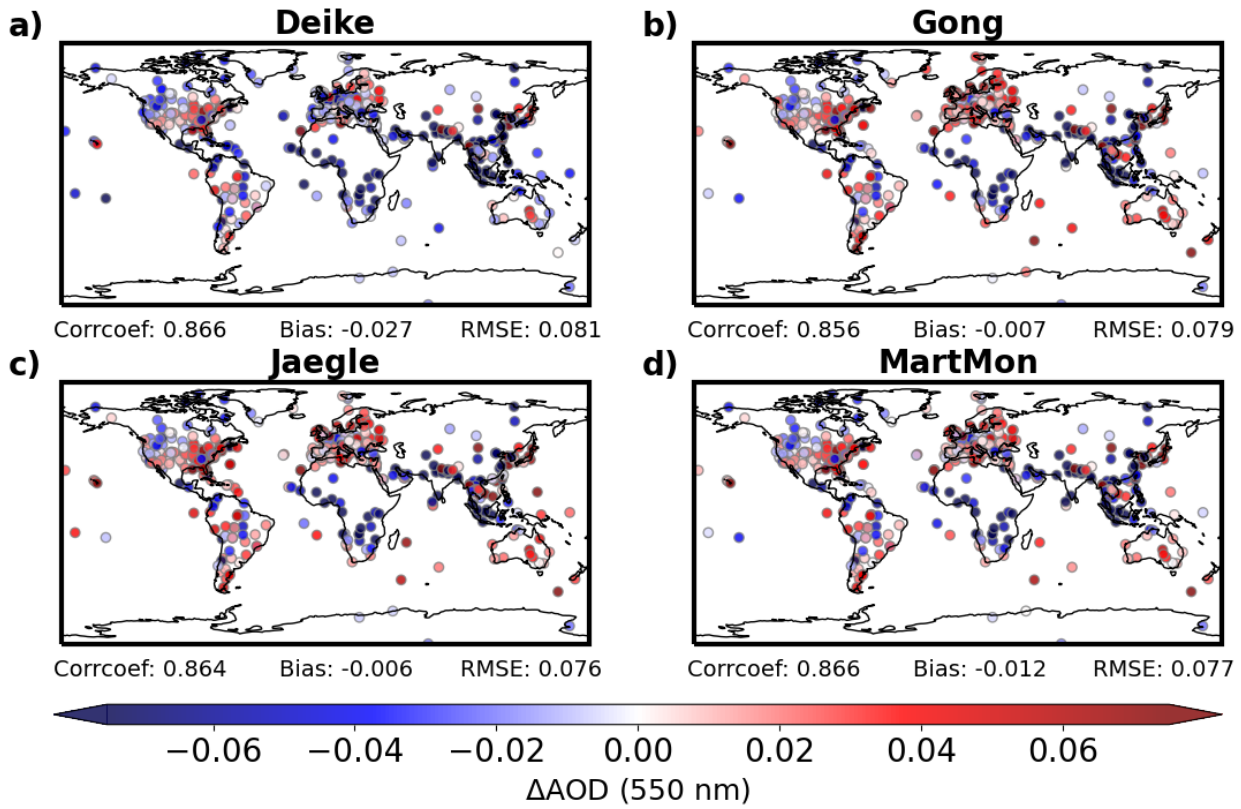


Figure 2.14: The difference between modeled AOD and AERONET observations for 2000–2019 for a) Deike, b) Gong, c) Jaegle, and d) MartMon. Correlation coefficients, bias, and RMSE are also reported for each model.

known limitations and regional biases in satellite retrievals rather than from deficiencies in the emission schemes (Sayer et al., 2014).

In Fig. 2.14, the differences between the modeled and observed AOD are similar in all 4 simulations over land. Fig. 2.11 shows that SSA aerosols contribute negligibly to the total AOD over land, suggesting that the observed biases over land are primarily attributed to non-SSA aerosols. In contrast, oceanic sites exhibit high variability across model configurations, with models underestimating or overestimating AOD depending on the simulation. For example, near the Southern coast of South Africa, the Deike simulation underestimates AOD, while Gong, Jaegle and MartMon overestimates it.

Following Fei et al. (2019), we identify 10 AERONET sites where SSA contributes more than 50% of the total AOD. Fig. 2.15 shows the seasonal cycle of AOD for these sites,

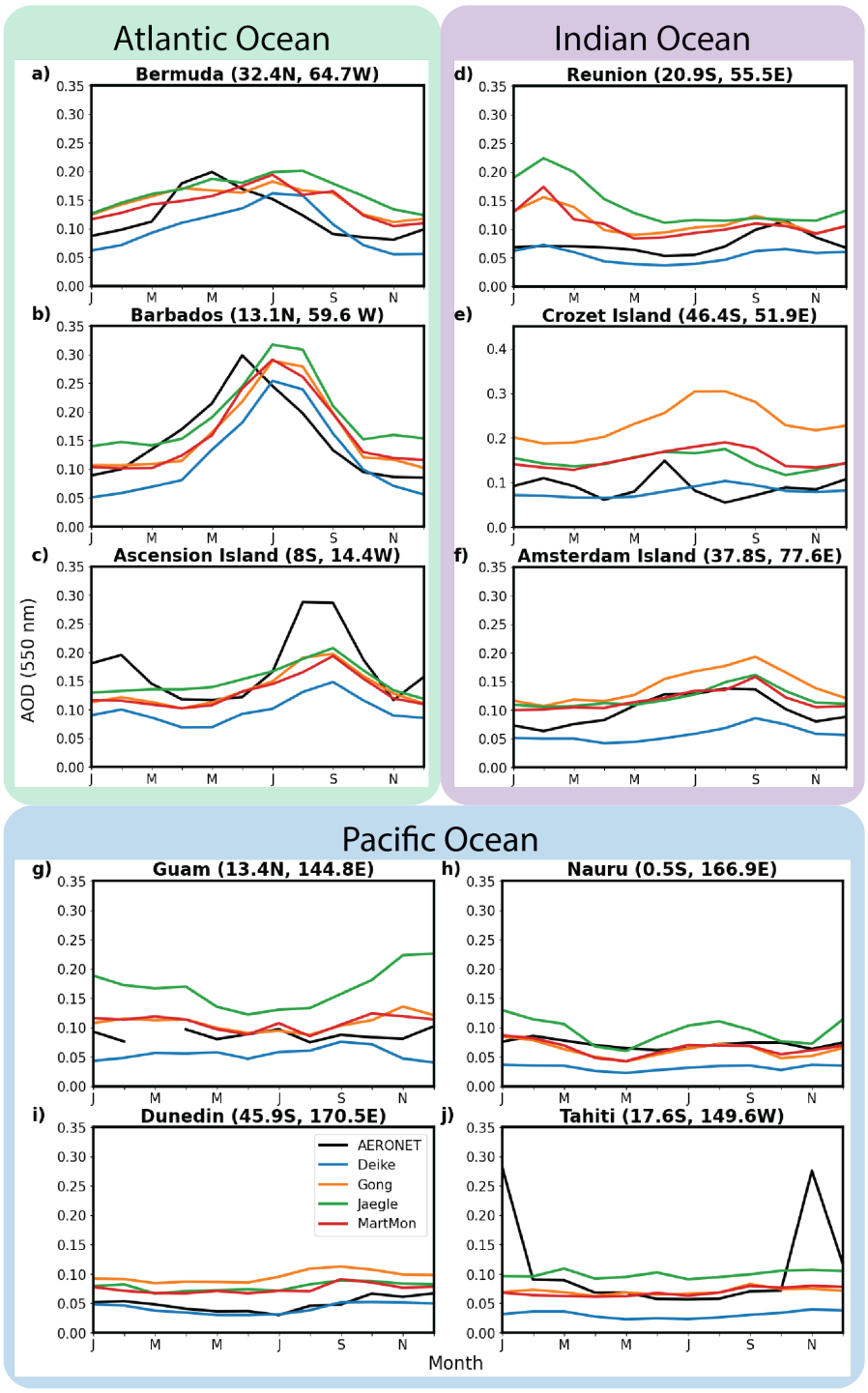


Figure 2.15: Comparison of AERONET observations and simulated AOD at the 10 sites where SSA accounts for more than 50% of the total AOD, grouped by geographical region.

grouped by geographic region (Atlantic Ocean, Pacific Ocean, and Indian Ocean). Unlike Figure 2.12, which averages all observations within each geographic region, Fig. 2.15 displays

the seasonal cycle for specific sites within each region. We find that seasonal variations in AOD differ for each site within a geographic region. In the Atlantic Ocean, AOD peaks in May in Bermuda (Fig. 2.15a), whereas it peaks in September on Ascension Island (Fig. 2.15c). In the Pacific Ocean, most sites (Fig. 2.15g, h, and i) show less pronounced AOD peaks, similar to the pattern observed in Fig. 2.12f, with Tahiti (Fig. 2.15j) being an exception. Model simulations generally capture seasonality well at most sites in the Atlantic Ocean, though their accuracy varies. However, the modeled AOD peaks for Barbados and Bermuda (Figs. 2.15a and b) are delayed by a few months, similar to what was observed in Fig. 2.12b. In contrast, the model significantly deviates for Reunion and Crozet Island in the Indian Ocean, failing to accurately represent the observed seasonal patterns.

Table 2.3 reinforces our previous findings by the region-specific performance of each simulation compared to observations. Deike exhibits the highest correlation with observations in Ascension Island, Crozet Island, Guam, Dunedin, and Tahiti. However, Deike has a negative bias throughout all of the AERONET sites, suggesting an underestimation of AOD observations. This is consistent with the comparison between Deike and the satellite-retrieved AOD observations in the preceding section. Similarly, this may be related to wind speed changes and/or the effects of a skewed size distribution, which can influence SSA lifetime and reduce AOD per unit mass due to faster settling of coarser particles. On the contrary, schemes like Jaegle and MartMon (temperature and wind speed dependent) and Gong (wind speed only) exhibit positive bias. MartMon has the lowest bias in Bermuda, Amsterdam Island, Guam, and Nauru, while Deike has the lowest bias for sites Reunion, Crozet Island, and Dunedin. This suggests that some blend of a weaker temperature and wind speed dependence between MartMon and Deike would minimize bias. However, errors in modeled-simulated winds, transport and removal processes may also contribute to discrepancies between the model and observations.

			Corrcoef	RMSE	Bias
Atlantic Ocean	Bermuda (32°N, 64.7°W)	Deike	0.670	0.039	−0.023
		Gong	*0.736*	0.038	0.026
		Jaegle	0.626	0.051	0.040
		Martmon	0.639	*0.037*	*0.021*
	Barbados (13.1°N, 59.6°W)	Deike	0.766	0.057	−0.033
		Gong	0.749	0.048	*0.006*
		Jaegle	0.735	0.063	0.039
		MartMon	*0.790*	*0.044*	0.008
	Ascension Island (8°S, 14.4°W)	Deike	*0.912*	0.084	−0.075
		Gong	0.849	0.052	−0.038
		Jaegle	0.768	*0.047*	*−0.023*
		MartMon	0.821	0.058	−0.043
Indian Ocean	Reunion (20.9°S, 55.5°E)	Deike	0.603	*0.024*	*−0.020*
		Gong	0.142	0.046	0.039
		Jaegle	−0.172	0.082	0.069
		MartMon	*0.086*	0.045	0.035
	Crozet Island (46.4°S, 51.9°E)	Deike	*−0.265*	*0.031*	*−0.010*
		Gong	−0.244	0.155	0.147
		Jaegle	0.074	0.064	0.058
		MartMon	−0.213	0.072	0.063
	Amsterdam Island (37.8°S, 77.6°E)	Deike	0.551	0.048	−0.042
		Gong	0.888	0.043	0.042
		Jaegle	0.785	0.026	0.021
		MartMon	*0.895*	*0.021*	*0.017*
Pacific Ocean	Guam (13.4°N, 144.8°E)	Deike	*−0.279*	0.036	−0.032
		Gong	0.102	0.025	*0.020*
		Jaegle	0.239	0.086	0.080
		MartMon	*0.279*	*0.024*	*0.020*
	Nauru (0.5°S, 166.9°E)	Deike	0.475	0.040	−0.040
		Gong	*0.626*	0.014	−0.010
		Jaegle	0.596	0.029	0.023
		MartMon	0.605	*0.012*	*−0.007*
	Dunedin (45.9°S, 170.5°E)	Deike	*0.877*	*0.009*	*−0.007*
		Gong	0.419	0.048	0.047
		Jaegle	0.668	0.031	0.030
		MartMon	0.541	0.028	0.026
	Tahiti (17.6°S, 149.6°W)	Deike	*0.523*	0.108	−0.078
		Gong	0.185	0.086	−0.039
		Jaegle	0.258	*0.077*	*−0.009*
		MartMon	0.352	0.086	−0.040

Table 2.3: The correlation coefficient, RMSE and bias calculated for each of the four model simulations and the AERONET observations of AOD for 10 sites. The schemes with the lowest RMSE, lowest absolute value of bias, and highest correlation coefficient are italicized.

2.5.3 Maritime (MAN) AERONET: 2004-2019

The maritime aerosol network (MAN) component of AERONET (2004–2019; Fig. 2.16a) provides AOD observations from cruises across various ocean regions, enabling a more focused analysis of SSA's impact on oceanic AOD. MAN AERONET shows a high correlation with both MISR and MODIS data, although slightly lower than the correlation observed between land-based AERONET sites and these satellite products. MISR demonstrates a marginally higher correlation coefficient, along with lower bias and RMSE, when matched with ocean-only MAN AERONET observations.

We proceed with a comparison of the observed AOD from the MAN AERONET stations with the model simulations. Figure 2.17a presents the zonal mean distribution of maritime AOD for MAN AERONET observations and AM4 simulations. Figures 2.17b, c, d, and e show the difference between the model simulations and MAN AERONET observations.

Overall, Deike shows the highest correlation coefficient and lowest RMSE when compared to MAN AERONET observations, while MartMon exhibits the lowest bias magnitude. Figure 2.17a illustrates that in the extratropics, the AOD simulated using the Deike SSA emission scheme aligns the most with MAN AERONET observations. However, in the tropics, the Deike-based simulation fails to capture the observed large increase in AOD. Instead, simulations using the Jaegle SSA emissions, which incorporate strong wind-speed and temperature dependencies, followed by MartMon, more accurately replicate the observed tropical AOD increase. It is important to note that most MAN network observations are concentrated in the tropical Atlantic Ocean, while data from extratropical regions are limited. This lack of extratropical observations may obscure the robustness of our comparison.

Our analysis suggests that Deike's simulation excels in matching observed AOD from MAN AERONET in the Southern Ocean (Fig. 2.17) and exhibits the highest correlation coefficient across all MISR satellite retrievals in this region (Table 2.2). However, its performance in the tropics, particularly in the Atlantic Ocean, is inconsistent. Although Deike's simulation matches (AERONET) site-specific observations well in the tropics, MartMon or

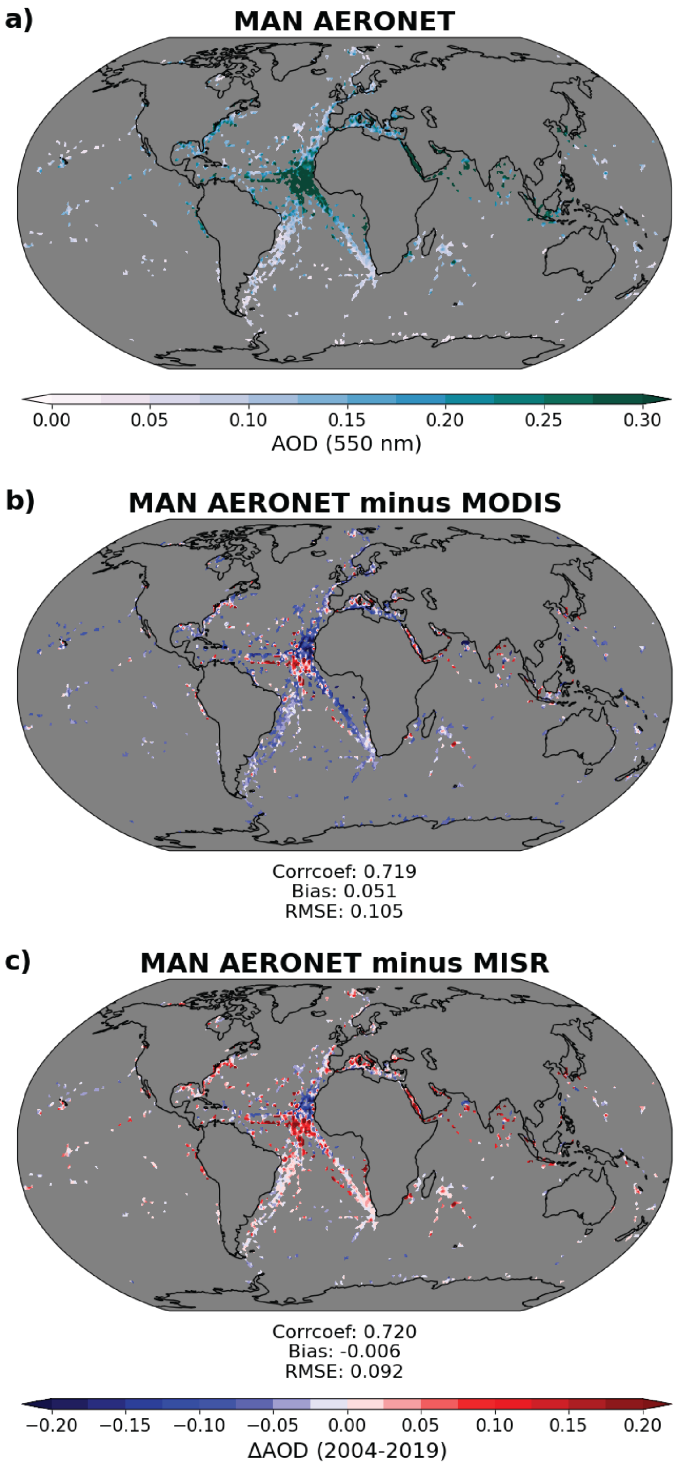


Figure 2.16: The 2004–2019 average AOD from the MAN component of AERONET. Panels b and c show the differences between MAN AERONET and MODIS/MISR, respectively. Correlation coefficients, bias, and RMSE are provided below figures b and c.

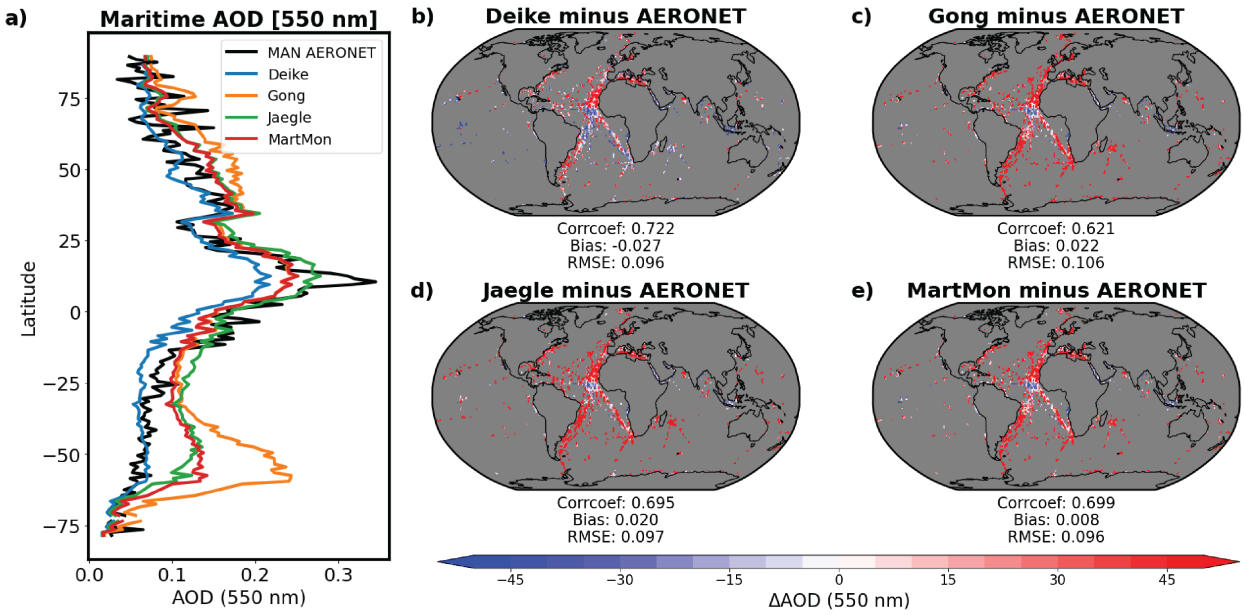


Figure 2.17: The zonal-mean AOD (2004-2019) for the MAN component of AERONET (black), Deike (blue), Gong (orange), Jaegle (green) and MartMon (red). The zonal means are calculated by sampling the model at the locations of the MAN AERONET observations. The AOD difference between the model and MAN AERONET is shown in b), c), d) and e).

Jaegle outperform it when validated against MAN AERONET and (MISR and MODIS) satellite-retrieved observations (Fig. 2.17).

The performance of a particular scheme may vary between regions because these schemes often apply the physical principles of SSA production to data from specific meteorological conditions or geographical settings. For example, the Martensson and Monahan schemes are based on laboratory experiments conducted under controlled meteorological conditions. In contrast, Gong's wind-speed-dependent formulation is tailored to fit observations from three distinct geographic regions: the Tropical Pacific, North Atlantic, and Southern Ocean. Notably, Jaegle's scheme deviates from a physically-based approach by empirically introducing a SST-dependency to Gong's wind-speed-dependent formulation. Meanwhile, the Deike sea-spray production function is grounded in a theoretical interpretation of bubble-bursting physics and has not been adjusted to match existing datasets. The varying performance of these simulations underscores the necessity of accurately representing SSA emission processes across diverse regions and meteorological conditions.

2.6 Conclusion

In this study, we run AM4 AMIP simulations focusing on years 2000–2019 using various SSA emission formulations to investigate how different sea-spray generation functions and their sensitivity to SST and wind speed impact SSA emission and concentration distributions, and subsequently AOD. We validate our model simulations by comparing the simulated AOD with observations from three groups of AOD products: satellite-retrieved observations (MISR and MODIS), ground-site observations (AERONET) and cruise observations (MAN component of AERONET).

We compare satellite-retrieved MODIS and MISR observations with data from AERONET sites and MAN AERONET, finding that MODIS and MISR provide comparable AOD estimates across AERONET sites. This result is consistent with previous studies (Mishchenko et al., 2010; Farahat, 2019; Bibi et al., 2015). Satellite retrievals such as MODIS and MISR are highly sensitive to landscape features, topography, and AOD ranges, affecting data accuracy but provide a global coverage. However, ground-based measurements such as AERONET provide a continuous time series of AOD with high temporal resolutions and high accuracy over a specific location. Thus, the consistency and precision of various datasets emerge as crucial considerations when comparing them with model simulations to analyze and interpret global and regional aerosol patterns (J. Li et al., 2014).

The SSA production flux in Deike et al. (2022) exhibits a negative temperature dependency unlike Jaegle and MartMon. In contrast to MartMon and Jaegle, the SSA emissions derived from Deike et al. (2022) suggest that SSA emissions are suppressed at higher temperatures, indicating a potential positive feedback in a warmer climate. This suppression is observed when considering a composite of particle sizes. However, as shown in Fig. 2 of Deike et al. (2022), the mechanisms of sea-spray production exhibit varying sensitivities to temperature.

Validation of modeled AOD against observations reveals varying levels of agreement across regions, metrics, and observational sources (Table 2.4). Globally, Deike consistently

	MODIS (ocean-only)	MISR (ocean-only)	AERONET (10 sites)	MAN AERONET
Highest Correlation Coefficient	Deike	Deike	Deike	Deike
Lowest Bias Magnitude	Gong	MartMon	MartMon	MartMon
Lowest RMSE	Jaegle	MartMon	MartMon	Deike/MartMon

Table 2.4: Summary of model performance in simulating aerosol optical depth (AOD) across different observational datasets: MODIS (ocean-only), MISR (ocean-only), AERONET (10 sites), and MAN AERONET. The table reports which sea spray aerosol (SSA) emission scheme yields the highest correlation coefficient, lowest bias magnitude, and lowest root-mean-square error (RMSE) for each dataset.

shows the highest correlation, while MartMon performs best in terms of bias and RMSE across most comparisons. However, significant geographical differences emerge in the agreement between model simulations and observations. Deike performs best in matching extra-tropical MAN AERONET observations, most AERONET sites in the Pacific Ocean, and MISR observations over most ocean basins. In contrast, Gong outperforms Deike in aligning with MODIS observations across the majority of ocean basins and most AERONET sites in the Indian Ocean. Meanwhile, Jaegle provides the best match for maritime (MAN) AERONET observations in the tropics. The varied performance of each scheme across various geographical regions stresses the importance of accurate representation of SSA emission across different meteorological conditions and geographical regions.

The evaluation of simulations employing various SSA emission formulas against multiple observational data sets facilitates a comprehensive assessment of the advantages and limitations of each validation data set. In particular, even among satellite-retrieved observations from MODIS and MISR, the AOD detection algorithm utilized by MODIS exhibits slightly greater sensitivity compared to MISR, precluding definitive conclusions regarding the accuracy of model AOD values in relation to these datasets. AERONET ground-based

measurements, focusing on 10 sites where SSA contributes more than 50% of total AOD, reveal varying performance of each simulation in capturing seasonal variations across each geographical region. Furthermore, AERONET's MAN component suggests that Deike's simulation best matches AOD observations in the Southern Ocean. However, Deike performs poorly in tropical regions, likely due to its negative temperature dependence at high temperatures.

It is important to note that AM4 is tuned for MartMon, not Deike. While key features such as wind-speed dependency and source size distribution are primarily governed by the emission parameterization itself, model-wide tuning parameters—such as those affecting aerosol lifetime, wet scavenging efficiency, cloud properties, or radiative balance—were optimized with MartMon's emission characteristics in mind. These tunings can inadvertently influence variables relevant for sea spray aerosol production, such as surface wind speed, thereby altering the resulting emissions even when using identical SSTs. Furthermore, the CMIP6 configuration of GFDL-CM4 increases both fine and coarse SSA emissions by 33% for MartMon, as well as for simulations using the Gong and Jaegle schemes, whereas no scaling is applied to the Deike simulation. As a result, the negative bias in AOD observed in simulations using the Deike scheme may partly reflect a mismatch between the model's underlying tuning and the emission characteristics of Deike, rather than limitations of the emission scheme itself. Nonetheless, Deike exhibits strong correlation with observations, comparable to – or in some cases better than – MartMon. However, an experiment with nudged wind speeds in addition to observed SST would be a relevant study to remove potential impacts on wind speed changes arising from land surface temperature changes on SSA emissions.

It is worth noting that, unlike in Chapter 1 – where no SSA emission scaling was applied – this chapter evaluates the SSA emission schemes within a configuration where MartMon-specific tuning factors are applied, which can influence comparative performance. The application of MartMon-specific tuning parameters to the Gong and Jaegle emission schemes

was inadvertent and likely suboptimal. As a result, the resulting AOD distributions from Gong and Jaegle may reflect an artificial enhancement in SSA emissions, rather than intrinsic differences in the emission schemes themselves. This limits the interpretability of their performance, especially when evaluating model–observation agreement. Nevertheless, this analysis of these sets of simulations remains a useful framework for evaluating the sensitivity of modeled AOD to emission parameterizations and for identifying the spatial patterns and magnitude of deviations relative to satellite and ground-based observations. If time permitted, a more rigorous approach would involve either retuning the model for each emission scheme to optimize performance or, alternatively, disabling emission-specific tunings altogether to isolate the raw behavior of each scheme.

When comparing simulations using various SSA emission formulas with multiple observational datasets, it is essential to acknowledge that discrepancies between simulated and observed AOD values may not arise solely from differences in SSA emission formulations. Model formulation errors, such as the inadequate representation of aerosol transport and removal mechanisms, can also contribute to these discrepancies. As highlighted in Chapter 1, uncertainties in model parameters and physical processes (e.g., vertical and horizontal transport mechanisms) may contribute to the emission formulation differences, complicating assessments of their accuracy against observations. However, this study examines the various treatments of SSA emission and validates simulated AOD against three different sets of observations, highlighting the limitations of refinements in the physical representation of SSA production processes. Moving forward, we recommend that integrating these refinements, combined with improvements in modeling aerosol transport and removal mechanisms, would improve the model's predictive capabilities and reliability.

Chapter 3

Circulation responses to Sea Salt Aerosol Engineering in a GFDL Coupled Model

3.1 Abstract

We employ simulations of enhanced emissions of sea salt aerosol (SSA) in the tropics following the G4sea-salt protocol using a NOAA GFDL climate model and examine the circulation response. Increasing SSA in the tropics locally cools the deployment region, reducing the Equator-minus-mid-latitude temperature difference. This triggers non-local changes on surface wind speeds and SSA emissions, including weakened westerlies and decreased sea salt emissions in the mid-latitudes. The combined effect of reduced extratropical and tropical SSA emissions offsets the global impact of tropical geoengineered SSA increase by 23%. Notably, our results show that a zonally uniform tropical SSA emission increase, like G4sea-salt, induces less cooling in the eastern equatorial Pacific compared to the central to western equatorial Pacific, contrary to regional SSA emission increases in other climate models. Our findings highlight that aerosol injection climate intervention strategies, such as marine cloud brightening via SSA emission increases, alter both aerosol distribution and circulation patterns, which must be considered when designing such protocols.

3.2 Introduction

Marine cloud brightening (MCB) is a proposed geoengineering approach to increase sea salt aerosol (SSA) emissions to cool the planet (Latham, 1990, 2002). It is hypothesized that increasing sea salt aerosol (SSA) emissions would lead to higher SSA concentrations, which in turn would increase cloud droplet number concentration (the first aerosol indirect effect; e.g., Twomey, 1977) as well as cloud cover and liquid water path (the second indirect effect; e.g., Albrecht, 1989). SSA also has considerable direct aerosol–radiation interactions (e.g., Jones & Haywood, 2012; Partanen et al., 2012; Hill & Ming, 2012; Mahfouz et al., 2023). The complex interactions between aerosols and the climate (e.g., uncertain rapid adjustments; Bellouin et al., 2020) make it difficult to predict the outcome of climate interventions such as sea salt emission increases, and the circulation and climate response to forcing from these interventions can attenuate the intended climate effect.

The oceanic regions between 30°S and 30°N contain most of the radiatively important stratocumulus cloud decks (Alterskjær et al., 2012; Jones & Haywood, 2012; Partanen et al., 2012). To study the radiative and climate response to brightening marine clouds by increasing SSA emissions, experiments have employed a regional (Jones & Haywood, 2012; Jones et al., 2009; Hill & Ming, 2012; C.-C. Chen et al., 2024) or zonally uniform increase in SSA emissions (i.e., G4sea-salt in Ahlm et al. (2017); Mahfouz et al. (2023)) within this latitude range. However, the climate, particularly global mean temperature change, is sensitive to the latitude, altitude, and nature of the forcing (Hansen et al., 1997). This study investigates circulation changes resulting from a zonally uniform increase in SSA emission following the G4sea-salt protocol (Kravitz et al., 2013) applied to the intermediate shared socioeconomic pathway scenario 4.5 (SSP2-4.5).

Mahfouz et al. (2023) employed the G4sea-salt protocol in a NOAA GFDL model to assess radiative and cloud responses to geoengineered zonally uniform increases in tropical SSA emission. They found that while increased tropical SSA has the potential to cool the planet by scattering solar radiation and (modestly) enhancing cloud formation, its impact

extends beyond the regions where SSA emissions are increased. Ahlm et al. (2017) applied G4sea-salt in three different Earth System Models (ESM) (NorESM1-M, GISS-E2-R and HADGEM2-ES) and suggested that direct radiative effects dominate in regions with less cloudy skies, while indirect effects dominate in regions with persistent stratocumulus.

This study extends the analysis of Mahfouz et al. (2023) and previous work by examining rapid adjustment and atmospheric circulation responses to G4sea-salt. We find that increasing tropical SSA emissions cools the region, reducing the temperature difference between the Equator and midlatitudes. This leads to a decrease in surface westerlies in the extratropics, leading to decreased SSA emission flux. The combined effects of changes in circulation, which encompasses changes in both wind speed and temperature, on SSA emissions in both the extratropics and the tropics offset 23% of the geoengineered SSA emission increase. Furthermore, we find the eastern equatorial Pacific cools less than the western equatorial Pacific. Thus, the temperature gradient from the eastern to the western equatorial Pacific is reduced. This contrasts with the strengthened temperature gradient from the eastern to western equatorial Pacific observed in previous studies where geoengineered emissions are applied regionally in the tropical Pacific and Atlantic Ocean (see, e.g., CESM2, C.-C. Chen et al. (2024); GFDL AM2.1, Hill and Ming (2012); UKESM1, Haywood et al. (2023)). This suggests significant differences in the climate and circulation response to zonally uniform versus regionally uniform increases in SSA emission, which must be considered in future studies of MCB.

3.3 Background

Effective radiative forcing (ERF), rapid adjustments, and feedbacks provide a comprehensive framework for understanding climate forcings and responses. Here, we discuss the concept and conventional methods for calculating ERF, rapid adjustments, and feedbacks, as well as their applications in geoengineering.

Radiative forcing (RF) quantifies the perturbation of Earth's energy balance caused by natural or anthropogenic agents such as greenhouse gases, aerosols, and land-use changes. ERF refers to the net change in the Earth's energy budget after rapid adjustments have taken place but before significant changes in sea surface temperatures occur.

There are two methods to calculate the ERF: 1) the fixed-SST method involves setting SSTs and sea ice cover to average climatological values, while allowing other parts of the system to respond until they reach a steady state (Hansen et al., 2005) and 2) the regression method analyzes the global mean surface temperature response to an instantaneous forcing and extrapolates the regression of the response to the start of the simulation (t=0) to derive the initial ERF (Gregory et al., 2004).

The fixed-SST method is particularly beneficial for understanding rapid adjustments because it removes the influence of sea surface temperature changes, providing a controlled environment to study short-term radiative effects. However, changes on the land surface can introduce artificial land-sea temperature gradients, potentially triggering small local climate responses. In contrast, the regression method excludes the global mean temperature response. However, analysis of both techniques shows that the fixed-SST method yields a smaller spread across models (Andrews et al., 2012). Furthermore, estimates of the ERF using the fixed-SST approach are available for a wider range of forcing agents in the current generation of climate models, compared to estimates diagnosed using the regression method (IPCC AR5, Chapter 8). In this chapter, we use fixed-SST simulations to analyze the ERF and the encompassing rapid adjustments. However, in Chapter 4, we use the regression method to quantify the ERF and compare with the ERF calculated using the fixed-SST method.

The abrupt-4xCO2 experiment, which involves instantaneous quadrupling of CO_2 concentrations, is widely used to diagnose the ERF of CO_2 in models. For abrupt-4xCO2, the ERF calculated using the fixed-SST counterparts from a multi-model analysis (Andrews et al., 2012) is 7% higher than the ERF calculated using the regression method (IPCC AR5,

Chapter 8). However, ERFs have also been diagnosed for short-lived climate forcers (SLCFs), which are time-varying and have shorter atmospheric residence times (IPCC AR6, Chapter 6). The ERF calculated for SLCF includes contributions from both direct aerosol-radiation interactions and indirect aerosol-cloud interactions. It is calculated as the difference in radiative fluxes between two simulations: a simulation with time-evolving aerosols and a control simulation with emissions held at their 1850 levels (W. J. Collins et al., 2017). Both simulations use time-evolving SSTs and sea ice data from the respective coupled model historical simulation (IPCC AR6, Chapter 6). This differs from the ERFs calculated using fixed pre-industrial SST and sea ice fields (Pincus et al., 2016). However, the effects of this difference are generally small (P. M. Forster et al., 2016).

With this precedent, we apply this framework to understanding ERF and rapid adjustment in response to geoengineering using a pair of fixed-SST atmosphere-only simulations (2020ssclimo and 2020climo). We compare these with the coupled simulations (G4sea-salt and SSP2-4.5), allowing us to assess the circulation feedbacks versus rapid adjustments to sea salt geoengineering.

Feedback describes the processes that amplify or dampen the climate response to an initial radiative forcing, typically mediated through changes in surface temperature. The main feedback mechanisms include water vapor feedback, lapse rate feedback, surface albedo feedback, and cloud feedback. Chapter 4 provides additional discussion and quantification concerning these feedback mechanisms, both for abrupt-4xCO2 scenarios and sea salt geoengineering. However, in this chapter, we focus on circulation feedbacks and rapid adjustments that are particularly relevant for geoengineering applications.

3.4 Methods

3.4.1 Model Description

The GFDL coupled model CM4 (Held et al., 2019) contributed to the sixth phase of the Coupled Model Intercomparison Project (CMIP6). It consists of atmosphere and land models (AM4 and LM4; M. Zhao et al., 2018) as well as ocean and sea ice models (OM4; Adcroft et al. (2019)). AM4 has a horizontal resolution of 100 km (1°) with 33 layers, and OM4 has a horizontal resolution of 0.25° with 75 layers.

As summarized by Mahfouz et al. (2023), the current emission and transport scheme for SSA in CM4 uses five sectional size bins ranging from particle radius sizes 0.1 to 10 microns. To approximate SSA emissions at the sea surface, two schemes are used: Mårtensson et al. (2003) for particles smaller than 1.4 μm and Monahan et al. (1986) for particles greater than 1.4 μm. The wind speed at 10 m drives emissions through a power-law dependence, where emissions $\propto U_{10}^{3.41}$. This relationship holds across particle sizes, with the exception that particles smaller than 1.4 μm, are also sensitive to sea surface temperature (SST; Mårtensson et al., 2003).

GFDL models utilize a cloud droplet activation scheme that redistributes the submicron mass of SSA to a prescribed size distribution (Ming et al., 2006, 2007). The prescribed size distribution consists of three modes, with a predefined total number concentration ratio of 340 to 60 to 0.75. The geometric mean diameters for these modes are 10, 150, and 620 nm, with geometric standard deviations of 1.6, 2.0, and 2.7, respectively. It should be noted that this fixed-modal representation, which employs three modes for liquid cloud droplet activation and indirect effects, is not consistent with the fixed sectional representation used for emissions and direct radiative effects that utilizes five sectional bins.

	Experiment Name	Description
Fixed-SST (2020)	2020climo	AM4 simulation using the annual mean SSTs from year 2020 of one of the SSP2-4.5 ensembles repeated for 30 years. All radiative forcing agents kept to their 2020 values.
	2020ssclimo	The 2020climo simulation with prescribed additional submicron SSA emissions of 7.66×10^{-11} kg m^{-2} s^{-1} (constant in time) for each of the first two bin sizes in each marine grid cell between 30°S and 30°N. This amount was chosen to offset an ERF of 2 W m^{-2} as specified in Kravitz et al. (2013).
Coupled (2020-2070; 3 ensemble members)	SSP2-4.5 (ssp)	CM4 simulation initialized from year 2015 of the historical simulation and run following the SSP-based Representative Concentration Pathway RCP4.5, which stabilizes radiative forcing at 4.5 W m^{-2} in 2100.
	G4sea-salt (g4ss)	The SSP2-4.5 simulation with prescribed additional submicron SSA emissions of 7.66×10^{-11} kg m^{-2} s^{-1} (constant in time) for each of the first two bin sizes in each marine grid cell between 30°S and 30°N.

Table 3.1: A summary of the experiments used in this work. The atmosphere-only simulations are run using sea-surface temperatures from year 2020 of one of the SSP2-4.5 ensembles. The coupled simulations are run using the SSP2-4.5 scenario, with interactive ocean and sea ice components.

3.4.2 Simulation Protocol

In total, eight simulations are used in this study: a pair of fixed-SST simulations and 3 ensemble pairs of coupled simulations, summarized in Table 3.1. We first conduct a pair of fixed-SST atmosphere-only cyclic AM4 simulations using the annual mean SSTs from year 2020 (repeated for 30 years) of one of the ensemble members from SSP2-4.5 simulations and keeping the radiative forcing agents in the AM4 simulations at their 2020 values. The reference simulation uses the present day aerosol emission scenario with all radiative forcing agents kept to their 2020 values, hereafter 2020climo. In 2020ssclimo, we prescribe an additional submicron SSA emission of 7.66×10^{-11} kg m^{-2} s^{-1} (constant in time) for each of the first two bin sizes in each marine grid cell between 30°S and 30°N. Both the reference and perturbed simulations feature interactive SSA emissions that respond to atmospheric conditions. The fixed-SST experiments were run to determine the added SSA emissions required to reduce the top-of-atmosphere (TOA) earth's energy imbalance by 2 W m^{-2}. This value was chosen to offset an ERF of 2 W m^{-2} as specified by Kravitz et al. (2013).

We used two three-member ensembles of transient 50-year CM4 coupled simulations (2020-2070) in our analysis of circulation response to geoengineering. The reference simulations follow the SSP2-4.5 projections. The initial conditions of the SSP2-4.5 at 2020 are obtained from historical simulations branched by CM4 in 2015 and run following the SSP-based Representative Concentration Pathway RCP4.5, which stabilizes radiative forcing at 4.5 W m^{-2} in 2100 (O'Neill et al., 2014; O'Neill et al., 2016). In the perturbed simulation, G4sea-salt, an additional emission of submicron SSA is prescribed for 2020-2070 as in 2020ss-climo (by 7.66×10^{-11} kg m^{-2} s^{-1} for the first two size bins (submicron) in each marine grid cell between 30°S and 30°N), providing a source of $E_{\text{geoeng}} = 1.532 \times 10^{-10}$ kg m^{-2} s^{-1} over tropical oceans. G4sea-salt will be denoted as subscript g4ss (e.g. emission is E_{g4ss}). SSP2-4.5 will be denoted as subscript ssp (e.g. emission is E_{ssp}).

3.5 Response to SSA emission increase

The ensemble mean difference in SSA emissions (ΔE), vertically integrated SSA concentration ($\Delta \int C \mathrm{d}z$), 10-m wind speed ($\Delta U$), and surface temperature (ΔT_{s}) for the fixed-SST (2020ssclimo minus 2020climo) and coupled (G4sea-salt minus SSP2-4.5) simulations are shown in Fig. 3.1. The globally averaged SSA emissions imposed in our tropical geoengineering experiment is 5.70×10^{-11} kg m^{-2} s^{-1}. Fig. 3.1a shows that the 30-year global average emission difference between 2020ssclimo minus 2020climo is 3% greater than the global geoengineered-only emissions, that is, the rapid adjustments to the geoengineered SSA emissions result in an additional increase in SSA emissions globally. In contrast, the averaged emissions from G4sea-salt minus SSP2-4.5 are 23% lower than the geoengineered-only emissions (Fig. 3.1e), that is, circulation feedbacks result in a decrease in SSA emissions, partially offsetting the increase in SSA emissions from geoengineering. The vertically integrated SSA concentration, representing the total atmospheric column burden, mirrors the

emission disparity. Specifically, higher emissions in the fixed-SST runs correspond to higher concentrations compared to the coupled runs.

Although the same SSTs are used in 2020ssclimo and 2020climo simulations, changes in land temperature are still observed (Fig. 3.1c). The land temperature changes drive wind speed and subsequent emission changes as rapid adjustments shown in Fig. 3.1a and d. In particular, increased wind speeds over the Southern Ocean (45°S to 65°S; Fig. 3.1d) lead to higher SSA emissions and concentrations in this region (Fig. 3.1a and b).

In contrast, the coupled run with feedbacks exhibits decreases in wind speeds and emissions in the Southern Ocean (Fig. 3.1e and g). The reduced SSA emissions in the Southern Ocean (Fig. 3.1e) spatially coincide with the regions of the largest reductions in wind speed in the Southern Hemisphere (SH) (Fig. 3.1h). These changes in wind speed are attributed to the cooling effect of the tropical SSA enhancement in G4sea-salt (Fig. 3.1g), which weakens the temperature gradient between the equator and the mid-latitudes. Consequently, the prevailing surface westerlies in the extratropics, particularly in the Southern Ocean, are dampened due to thermal wind balance (Deng et al., 2022). Thus, the rapid adjustments characterized by increased wind speeds, emissions, and concentrations in the fixed-SST simulations appear to be opposite in sign to their coupled counterparts.

Figure 3.2 shows the geographical distribution of SSA emissions for the fixed-SST and coupled simulations. To evaluate changes in emissions caused by rapid adjustments in the fixed-SST simulations, we subtract the 2020climo emissions and prescribed geoengineered SSA emissions (E_{geoeng}) from the 2020ssclimo emissions in the tropics (Fig. 3.2c). We find that rapid adjustments, primarily driven by changes in wind speed (Fig. 3.1d), result in global increases in emissions, with a slight reduction observed in the Northern Hemisphere (NH).

Fig. 3.2f further illustrates the impact of circulation changes–encompassing variations in wind speed and temperature–on ocean-wide emissions, particularly in the tropics. In addition to the non-local changes in SSA emissions observed in the Southern Ocean and NH

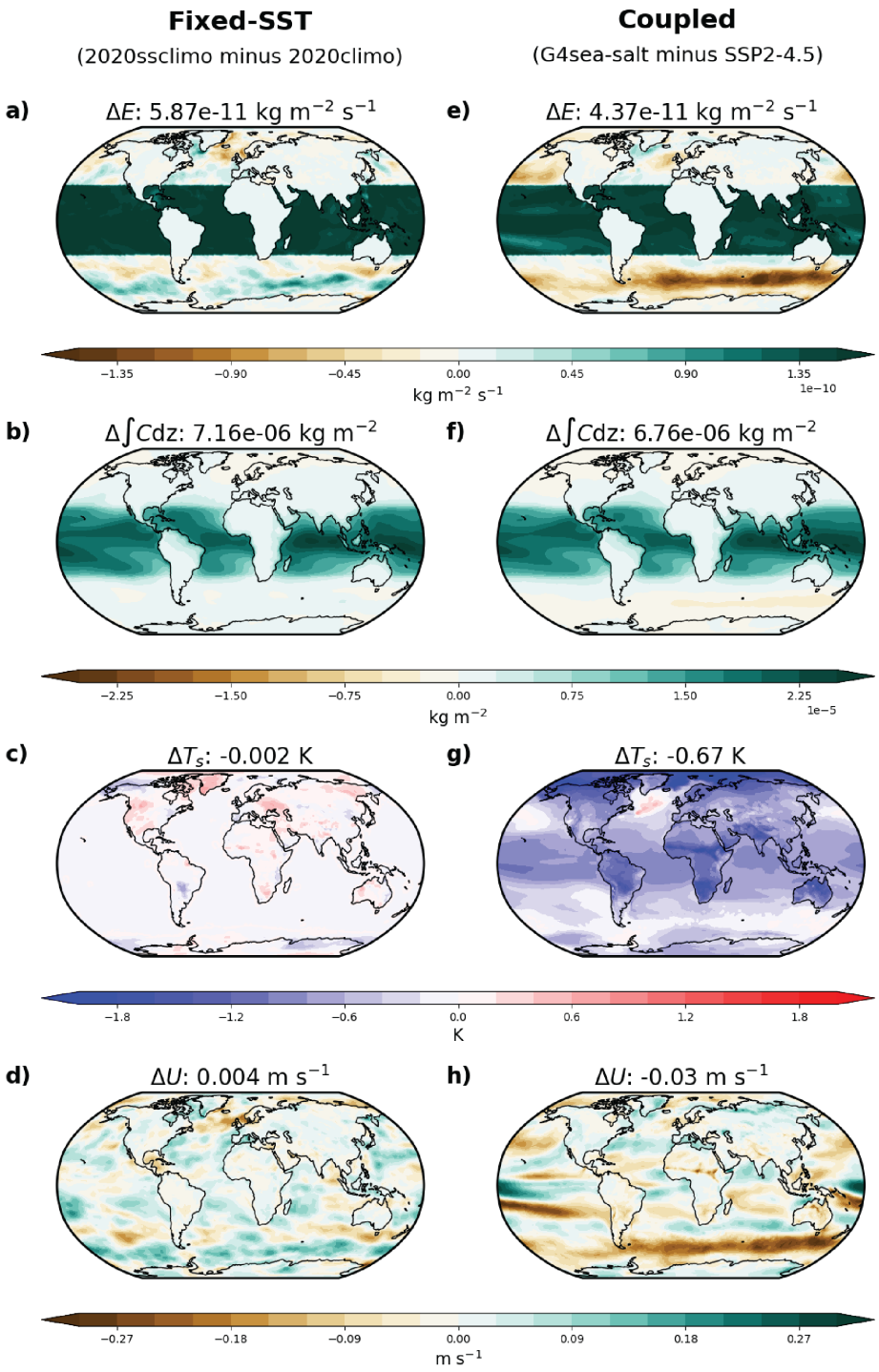


Figure 3.1: The global difference in SSA emissions (ΔE; e), vertically integrated SSA concentration ($\Delta \int C\mathrm{d}z$; f) surface temperature (ΔT_s; g), and 10-m wind speed (ΔU; h) for the ensemble-mean coupled simulations (G4sea-salt minus SSP2-4.5). The fixed-SST counterparts (2020ssclimo minus 2020climo) are presented in a, b, c and d. The global average values for each are displayed in the title.

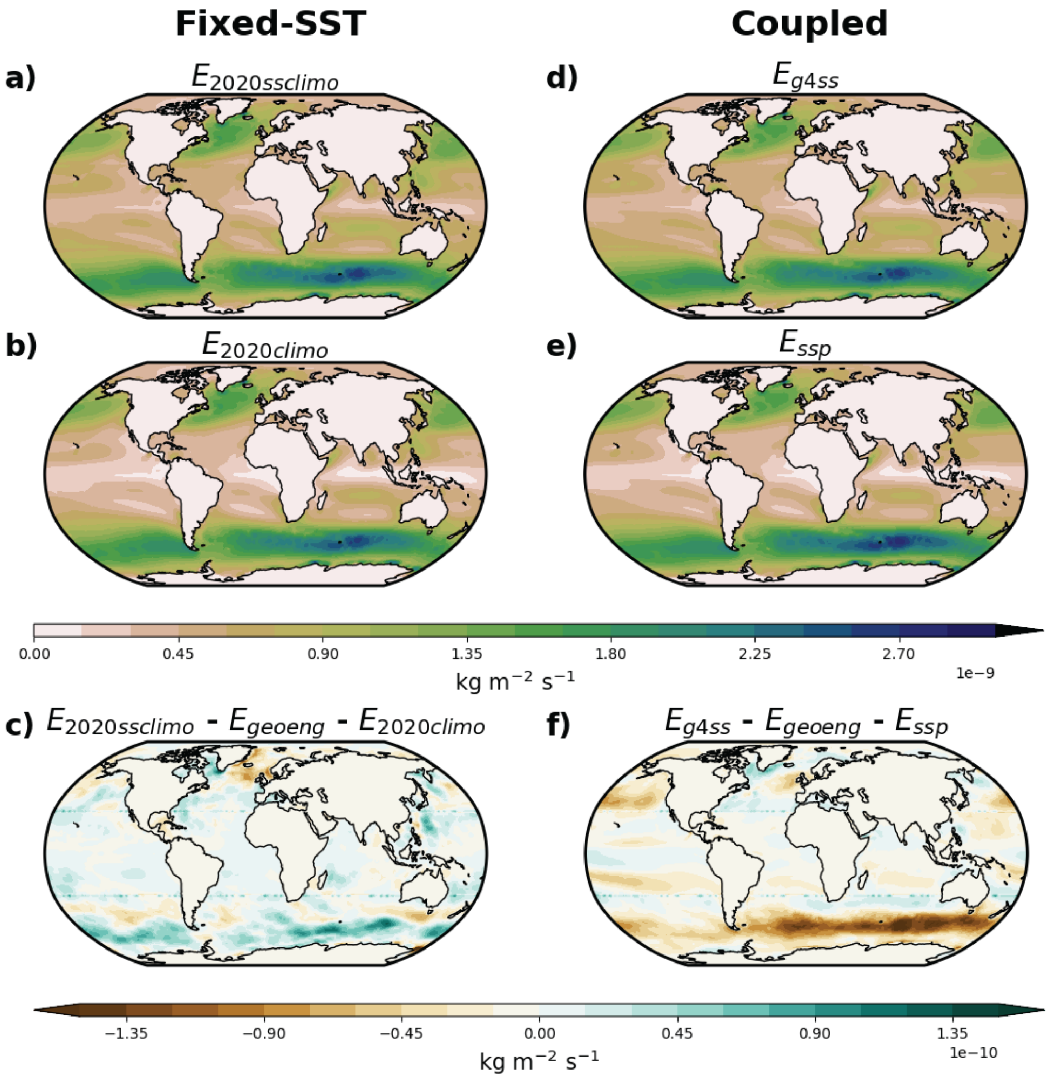


Figure 3.2: The ensemble-mean SSA emissions for d) G4sea-salt (E_{g4ss}), e) SSP2-4.5 (E_{ssp}), f) E_{g4ss}-E_{geoeng}- E_{ssp}. The fixed-SST counterparts are presented in a), b), and c).

(Fig. 3.2f), we identify circulation-induced reductions in tropical SSA emissions that offset 6% of the prescribed tropical geoengineered SSA emission increases. In contrast, emissions resulting from rapid adjustments in the fixed-SST simulations increase tropical emissions by 0.27% of the geoengineered increase (Fig. 3.2c and Table 3.2).

While wind speed influences SSA emissions in both the fixed-SST and coupled simulations, their effects lead to emission changes of opposite signs (Fig. 3.2f and Table 3.3). In the coupled run, the global emission increase from tropical geoengineered emissions is dampened

due to two main factors: lower-than-expected emissions in the tropics and significant reductions in the Southern Ocean. Conversely, in the fixed-SST run, the global emission increase from tropical geoengineered emissions is enhanced due to slightly higher emissions in both the tropics and the Southern Ocean. To better understand these changes in emissions, we examine the dependence of the emissions on the 10-m wind speeds and SST.

3.5.1 Sensitivity of SSA emissions to wind speed and temperature changes

To evaluate the impact of temperature and wind speed changes on SSA emissions, we calculate SSA emissions offline using parameterizations from Mårtensson et al. (2003) and Monahan et al. (1986), hereafter MartMon. The off-line calculations of SSA emissions emulate how emissions are calculated in the GFDL CM4 and AM4 model and are evaluated as the aggregate of the same five sectional size bins used in the model. MartMon is presented as a function of wind speed and SST, thus $E_{\mathrm{MM}}(\mathrm{U}, \mathrm{SST})$.

Fig. 3.3 illustrates the absolute and relative changes in MartMon emission in response to incremental changes in temperature and wind speed, confirming moderate temperature sensitivity and greater wind speed sensitivity. Figs. 3.3a and b show the magnitude of the emission changes in response to incremental changes in temperature and wind speed, while Figs. 3.3c and d illustrate the corresponding percentage changes in emission due to these changes in temperature and wind speed. Fig. 3.3a shows that at a given temperature, emission increases with wind speed, but the rate of this increase remains consistent across temperatures ranging from -15 to 25°C. Thus, the figure indicates that the functional dependence on wind speed is the dominant factor influencing emission changes, rather than the SST itself. In contrast, Fig. 3.3b illustrates the rate of change of emission with respect to wind speed, revealing substantial increases in emissions for wind speeds between 2.5 and 15 m/s. The functional dependence on SST becomes a secondary factor that influences the changes in emission within this wind speed range (see Appendix C.2).

When Fig. 3.3a is normalized by the emission, the wind speed dependency is decoupled. This is due to the specific form of the MartMon formulation (detailed in Appendix C.1), which enables us to isolate and retrieve the percentage change in emission per degree Celsius as a function of temperature (Fig. 3.3c). Similarly, normalizing Fig. 3.3b by the emission decouples the temperature dependence, isolating the percentage change in emission per m/s as a function of wind speed (Fig. 3.3d). Our analysis reveals that wind speed has a dominant impact on MartMon emissions, with a 0.1 m/s increase in wind speed leading to a substantial 20–120% increase in emissions at wind speeds ranging from 14 to 2 m/s, respectively. In contrast, temperature has a relatively modest effect, with a 0.5°C increase corresponding to a less than 1% increase in emissions over a wide temperature range of -15 to 25°C.

3.5.2 Relating emission changes to rapid adjustments and circulation changes

Since SSTs are the same in the 30-year 2020ssclimo and 2020climo simulations, we quantitatively evaluate rapid adjustments in wind speed and their affect on emissions. Emission values are presented as both ocean-averaged (e.g., $\overline{E}$) and ocean-integrated (e.g., $\langle E \rangle$). Specifically, ocean integration refers to the total accumulated emissions for a region, while ocean averaging refers to the average SSA emissions per unit of ocean area. We provide both averages and integrals to facilitate comparisons of the magnitude of emission changes between regions and the relative contribution of each region to the total emission increase.

In Table 3.2, we quantify the emission changes resulting from rapid adjustments in the fixed-SST simulations by evaluating the ocean-averaged and ocean-integrated difference between the prescribed amount of geoengineered SSA emissions in the tropics (E_{geoeng}) and the actual increase between 2020ssclimo and 2020climo. To assess how only the mean changes in wind speeds over the basins contribute to emission changes, we generate estimates of the rapid adjustments in emission for each ocean region by taking the difference between the

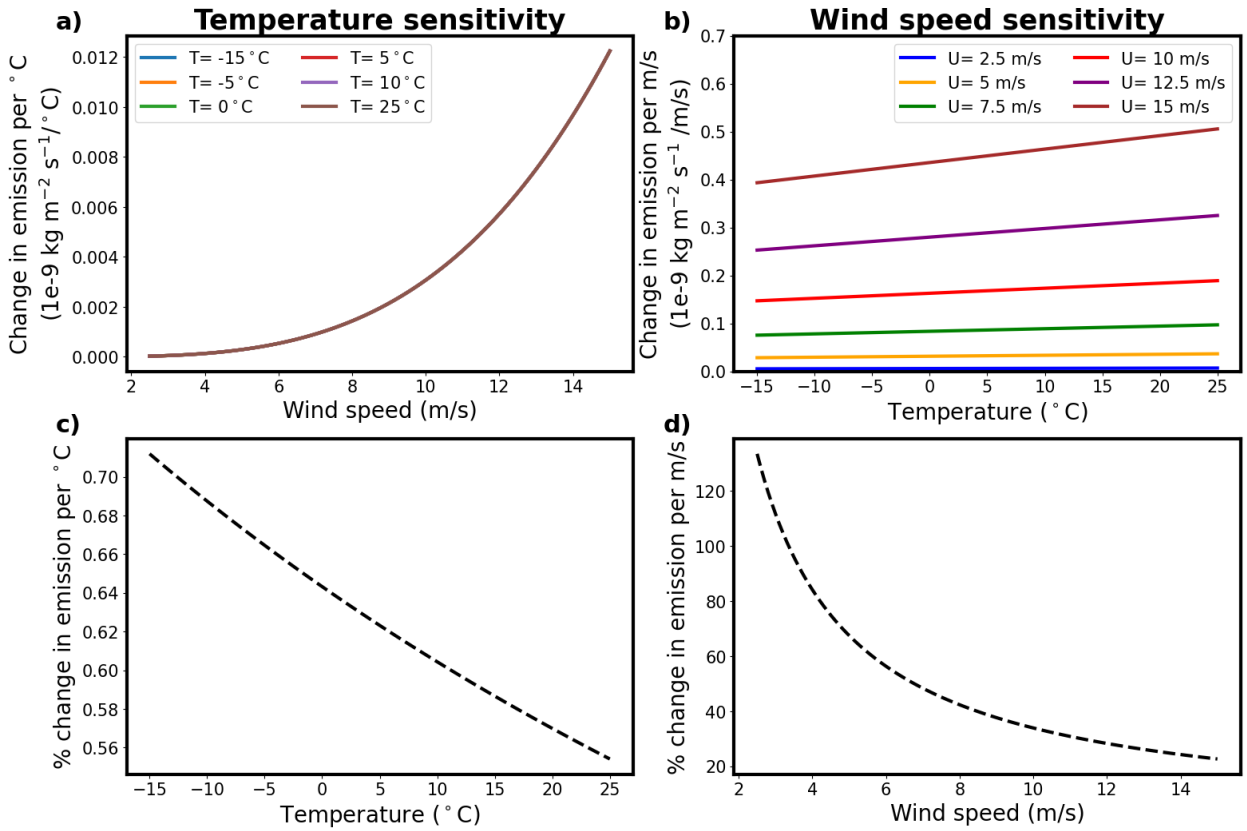


Figure 3.3: The sensitivity of MartMon emissions to wind speed and temperature are presented as the change in emission per unit change in a) temperature (°C) and b) wind speed (m/s). This is computed by calculating the emission when temperature is increased in increments of 0.5°C or when wind speed is increased by increments by 0.1 m/s. This specific increment were calculated using finite differences and verified to converge with smaller increments. The corresponding percent changes in emission due to incremental increases in temperature and wind speed are shown in c and d.

MartMon emissions calculating using ocean-averaged wind speeds and identical SSTs for 2020ssclimo and 2020climo ($E_{\mathrm{MM}}(\overline{\mathrm{U}}_{\mathrm{2020ssclimo}}, \overline{\mathrm{SST}}_{\mathrm{2020ssclimo}})$ - $E_{\mathrm{MM}}(\overline{\mathrm{U}}_{\mathrm{2020climo}}, \overline{\mathrm{SST}}_{\mathrm{2020climo}})$).

Compared to the changes in emission from rapid adjustments in AM4 ($\overline{E}_{\mathrm{2020ssclimo}}$ - $\overline{E}_{\mathrm{geoeng}}$ - $\overline{E}_{\mathrm{2020climo}}$) for different ocean regions, the MartMon emissions calculated using the temporal and geographical means of wind speeds and SST are consistently lower than the modeled emissions. This discrepancy arises from limitations in using temporally and spatially averaged wind speed and temperature values, which do not capture the inherent nonlinearities and variabilities. Specifically, the MartMon formula is highly nonlinear, and using long-term

		Global Oceans	Tropical Oceans	SH extratropical Oceans	NH extratropical Oceans
Ocean-averaged wind speed (m s^{-1})	$\overline{\mathrm{U}}_{\mathrm{2020climo}}$	7.64	6.64	9.41	7.64
	$\overline{\mathrm{U}}_{\mathrm{2020ssclimo}}$	7.65	6.65	9.42	7.63
	$\overline{\mathrm{U}}_{\mathrm{2020ssclimo}}$ - $\overline{\mathrm{U}}_{\mathrm{2020climo}}$	0.01	0.01	0.01	−0.01
Ocean-averaged SST (K)	$\overline{\mathrm{SST}}_{\mathrm{2020climo}}$	290.49	299.11	280.95	281.01
	$\overline{\mathrm{SST}}_{\mathrm{2020ssclimo}}$	290.49	299.11	280.95	281.01
	$\overline{\mathrm{SST}}_{\mathrm{2020ssclimo}}$ - $\overline{\mathrm{SST}}_{\mathrm{2020climo}}$	0.00	0.00	0.00	0.00
Ocean-integrated SSA emission (kg s^{-1})	$\langle E_{\mathrm{geoeng}} \rangle$	2.91e+4	2.91e+4	0.00	0.00
	$\langle E_{\mathrm{2020climo}} \rangle$	2.60e+5	6.91e+4	1.39e+5	5.14e+4
	$\langle E_{\mathrm{2020ssclimo}} \rangle$ - $\langle E_{\mathrm{geoeng}} \rangle$	2.61e+5	6.92e+4	1.41e+5	5.12e+4
	$\langle E_{\mathrm{2020ssclimo}} \rangle$ - $\langle E_{\mathrm{geoeng}} \rangle$ - $\langle E_{\mathrm{2020climo}} \rangle$	7.89e+2	1.90e+2	7.90e+2	−1.89e+2
Ocean-averaged SSA emission (kg m^{-2} s^{-1})	$\overline{E}_{\mathrm{geoeng}}$	8.05e-11	1.53e-10	0.00	0.00
	$\overline{E}_{\mathrm{2020climo}}$	7.29e-10	3.64e-10	1.29e-9	8.16e-10
	$\overline{E}_{\mathrm{2020ssclimo}}$ - $\overline{E}_{\mathrm{geoeng}}$	7.32e-10	3.65e-10	1.30e-9	8.13e-10
	$\overline{E}_{\mathrm{2020ssclimo}}$ - $\overline{E}_{\mathrm{geoeng}}$ - $\overline{E}_{\mathrm{2020climo}}$	2.21e-12	1.00e-12	7.30e-12	−3.00e-12
$E_{\mathrm{MM}}(\overline{\mathrm{U}}_{\mathrm{2020ssclimo}}, \overline{\mathrm{SST}}_{\mathrm{2020ssclimo}})$ - $E_{\mathrm{MM}}(\overline{\mathrm{U}}_{\mathrm{2020climo}}, \overline{\mathrm{SST}}_{\mathrm{2020climo}})$		5.04e-13	7.09e-13	1.00e-12	−1.00e-12

Table 3.2: We use Martensson and Monahan (MartMon) to compute emissions using 30-year global and regional ocean-averaged wind speed and SST alongside ocean-averaged (e.g., $\overline{E}$) and ocean-integrated (e.g., $\langle E \rangle$) SSA emissions from 2020ssclimo and 2020climo. For regional calculations, tropical oceans cover ocean areas between 30°S to 30°N, Southern Hemisphere (SH) extratropical oceans cover ocean areas between 90°S to 30°S and Northern Hemisphere (NH) extratropical oceans cover ocean areas between 30°N to 90°N. We compare our computed emissions with the ocean-averaged emissions for 2020ssclimo and 2020climo, and changes in SSA emissions from rapid adjustments ($\overline{E}_{\mathrm{2020ssclimo}}$ - $\overline{E}_{\mathrm{geoeng}}$ - $\overline{E}_{\mathrm{2020climo}}$). The SSTs are fixed in the AM4 simulations, so we assess the contribution of the mean wind speed to emission changes, by computing the difference in MartMon emissions calculated using 2020ssclimo and 2020climo wind speeds ($E_{\mathrm{MM}}(\overline{\mathrm{U}}_{\mathrm{2020ssclimo}}, \overline{\mathrm{SST}}_{\mathrm{2020ssclimo}})$ - $E_{\mathrm{MM}}(\overline{\mathrm{U}}_{\mathrm{2020climo}}, \overline{\mathrm{SST}}_{\mathrm{2020climo}})$).

spatial mean values instead of calculating emissions at high spatial and temporal resolution (every 30 minutes) and then averaging them geographically and temporally leads to an underestimation of emissions. To better understand MartMon's nonlinear behavior, calculating and analyzing its Probability Density Function using high-frequency data would be a relevant analysis.

Following the enhancement of geoengineered SSA emissions in the tropics, rapid adjustments increase ocean-averaged global emissions by 0.28% (calculated from Table 2). This change is driven by a 0.78% increase in emissions in the SH extratropical oceans (90°S to 30°S), along with a slight increase in the tropical oceans and decrease in the NH extratropical oceans (30°N to 90°N), consistent with the emission changes shown in Figs. 3.1a and

3.2c. Using MartMon and ocean-averaged wind speeds, we calculate rapid adjustments in emissions for 2020ssclimo and 2020climo (which share identical SSTs) and find qualitative agreement with the AM4-modeled rapid adjustments in emissions across all regions, albeit with lower magnitudes. Table 3.2 shows that the MartMon emissions estimated using the sign of changes in mean wind speeds yield the same sign as the modeled emission changes. Specifically, we obtain a global increase in emissions, accompanied by a decrease in emissions in the NH extratropical oceans when considering wind speed changes alone in our MartMon emission calculations. Thus, the adjustments are only driven by changes in wind speed, characterized by global increases and localized reductions in the NH extratropics (Fig. 3.1d).

Next, we assess the impact of circulation changes as the ocean is allowed to respond and fully coupled feedbacks operate following geoengineered SSA emission increases. In Table 3.3, we assess the impact of circulation changes, which encompass changes in wind speed and temperature, on ocean-wide SSA emissions by evaluating the difference between the prescribed amount of geoengineered SSA emissions in the tropics (E_{geoeng}) and the actual increase in the coupled model simulations (G4sea-salt minus SSP2-4.5).

We find that the circulation-induced changes in SSA emission decrease the global contribution of the tropical SSA emission enhancement by 23%. This reduction is primarily driven by a large decrease in ocean-integrated SSA emission in the SH extratropical oceans (90°S to 30°S), followed by the tropical oceans and then the NH extratropical oceans (30°N to 90°N). Upon examining the circulation-induced ocean-averaged SSA emission, we find that the largest circulation-induced emission reductions per unit of ocean area occur in the SH extratropical oceans, followed by the NH extratropical oceans and then the tropical oceans. Although the circulation-induced decrease in ocean-averaged SSA emissions is greater in the NH extratropical oceans than in the tropics, the tropics contribute more to the global ocean-integrated value of the circulation-induced SSA emission due to their vast ocean area compared to the NH extratropics.

		Global Oceans	Tropical Oceans	SH extratropical Oceans	NH extratropical Oceans
Ocean-averaged wind speed ($\overline{\mathrm{U}}$; m s^{-1})	$\overline{\mathrm{U}}_{\mathrm{ssp}}$	7.71	6.69	9.54	7.67
	$\overline{\mathrm{U}}_{\mathrm{g4ss}}$	7.68	6.67	9.47	7.65
	$\overline{\mathrm{U}}_{\mathrm{g4ss}}$ - $\overline{\mathrm{U}}_{\mathrm{ssp}}$	−0.03	−0.02	−0.07	−0.02
Ocean-averaged SST ($\overline{\mathrm{SST}}$; K)	$\overline{\mathrm{SST}}_{\mathrm{ssp}}$	291.22	299.66	281.83	282.67
	$\overline{\mathrm{SST}}_{\mathrm{g4ss}}$	290.67	298.93	281.56	282.06
	$\overline{\mathrm{SST}}_{\mathrm{g4ss}}$ - $\overline{\mathrm{SST}}_{\mathrm{ssp}}$	−0.57	−0.73	−0.27	−0.61
Ocean-integrated SSA emission (kg s^{-1})	$\langle E_{\mathrm{ssp}} \rangle$	2.70e+5	7.10e+4	1.47e+5	5.25e+4
	$\langle E_{\mathrm{g4ss}} \rangle$	2.92e+5	9.83e+4	1.43e+5	5.16e+4
	$\langle E_{\mathrm{g4ss}} \rangle$ - $\langle E_{\mathrm{ssp}} \rangle$	2.23e+4	2.73e+4	−4.22e+3	−8.44e+2
	$\langle E_{\mathrm{g4ss}} \rangle$ - $\langle E_{\mathrm{geoeng}} \rangle$	2.64e+5	6.94e+4	1.43e+5	5.16e+4
	$\langle E_{\mathrm{g4ss}} \rangle$ - $\langle E_{\mathrm{geoeng}} \rangle$ - $\langle E_{\mathrm{ssp}} \rangle$	−6.79e+3	−1.71e+3	−4.22e+3	−8.44e+2
Ocean-averaged SSA emission (kg m^{-2} s^{-1})	$\overline{E}_{\mathrm{ssp}}$	7.49e-10	3.74e-10	1.36e-9	8.33e-10
	$\overline{E}_{\mathrm{g4ss}}$	8.11e-10	5.18e-10	1.32e-9	8.20e-10
	$\overline{E}_{\mathrm{g4ss}}$ - $\overline{E}_{\mathrm{ssp}}$	6.17e-11	1.44e-10	−3.90e-11	−1.34e-11
	$\overline{E}_{\mathrm{g4ss}}$ - $\overline{E}_{\mathrm{geoeng}}$	7.30e-10	3.65e-10	1.32e-9	8.20e-10
	$\overline{E}_{\mathrm{g4ss}}$ - $\overline{E}_{\mathrm{geoeng}}$ - $\overline{E}_{\mathrm{ssp}}$	−1.88e-11	−9.00e-12	−3.90e-11	−1.34e-11
MartMon emissions calculated using ocean-averaged wind speed and SST (kg m^{-2}s^{-1})	$E_{\mathrm{MM}}(\overline{\mathrm{U}}_{\mathrm{ssp}}, \overline{\mathrm{SST}}_{\mathrm{ssp}})$	2.42e-10	1.42e-10	4.29e-10	2.05e-10
	$E_{\mathrm{MM}}(\overline{\mathrm{U}}_{\mathrm{g4ss}}, \overline{\mathrm{SST}}_{\mathrm{g4ss}})$	2.36e-10	1.39e-10	4.17e-10	2.02e-10
	$E_{\mathrm{MM}}(\overline{\mathrm{U}}_{\mathrm{g4ss}}, \overline{\mathrm{SST}}_{\mathrm{g4ss}})$ - $E_{\mathrm{MM}}(\overline{\mathrm{U}}_{\mathrm{ssp}}, \overline{\mathrm{SST}}_{\mathrm{ssp}})$	−5.25e-12	−2.04e-12	−1.20e-11	−3.00e-12
	$E_{\mathrm{MM}}(\overline{\mathrm{U}}_{\mathrm{g4ss}}, \overline{\mathrm{SST}}_{\mathrm{g4ss}})$ - $E_{\mathrm{MM}}(\overline{\mathrm{U}}_{\mathrm{ssp}}, \overline{\mathrm{SST}}_{\mathrm{g4ss}})$	−4.76e-12	−1.99e-12	−1.10e-11	−2.03e-12
	$E_{\mathrm{MM}}(\overline{\mathrm{U}}_{\mathrm{g4ss}}, \overline{\mathrm{SST}}_{\mathrm{g4ss}})$ - $E_{\mathrm{MM}}(\overline{\mathrm{U}}_{\mathrm{g4ss}}, \overline{\mathrm{SST}}_{\mathrm{ssp}})$	−5.09e-13	−5.80e-14	−1.00e-12	−1.02e-12
Contribution of wind speed to emission changes		90.33%	97.16%	91.67%	67.67%
Contribution of SST to emission changes		9.67%	2.84%	8.33%	32.33%

Table 3.3: The ocean-averaged wind speed and SST for SSP2-4.5, G4sea-salt and G4sea-salt minus SSP2-4.5 are presented here alongside ocean-averaged (Appendix B.3) and ocean-integrated (Appendix B.4) SSA emissions. The subscript g4ss and ssp refer to G4sea-salt and SSP2-4.5, respectively. Circulation-induced changes in ocean-integrated and ocean-averaged SSA emissions are calculated by taking the difference between the geoengineered SSA emission and the G4sea-salt minus SSP2-4.5 emission (Appendix B.5). We use MartMon to compute emissions using 50-year global and regional ocean-averaged wind speed and SST. The MartMon emissions for the global oceans are calculated using the weighted averages of the regions. Rows 3–5 from the bottom of the MartMon emissions sections are used to compute the contribution of wind speed and SST separately to emission changes.

Circulation feedbacks in the G4sea-salt simulation, particularly changes in wind speed and SST, lead to reduced natural emissions across all regions. This contrasts with the fixed-SST simulations, where rapid adjustments resulted in increased natural emissions globally. The largest SSA emission reductions from circulation changes occur in the SH extratropical oceans, where the wind speed decreases the most, while the SST decreases the least. In contrast, the tropics experience the largest reduction in SST but a smaller reduction in wind speed.

To evaluate the impact of mean changes in temperature and wind speed between G4sea-salt and SSP2-4.5 and their emissions, we generate estimates of MartMon emissions using 50-year ocean-averaged wind speeds and SSTs for G4sea-salt and SSP2-4.5 (Table 3.3). Taking the difference between MartMon emissions calculated using ocean-averaged wind speeds and SST from G4sea-salt and SSP2-4.5 ($E_{\mathrm{MM}}(\overline{\mathrm{U}}_{\mathrm{g4ss}}, \overline{\mathrm{SST}}_{\mathrm{g4ss}})$ - $E_{\mathrm{MM}}(\overline{\mathrm{U}}_{\mathrm{ssp}}, \overline{\mathrm{SST}}_{\mathrm{ssp}})$), we generate estimates of circulation-induced emissions for each ocean region.

To quantify the distinct influences of wind speed and SST on MartMon emissions, we employ a sequential adjustment method that involves systematically adjusting one variable at a time, while keeping others constant to analyze the impact of each variable. Initially, emissions are calculated for G4sea-salt using ocean-averaged wind speed and SST for each region ($E_{\mathrm{MM}}(\overline{\mathrm{U}}_{\mathrm{g4ss}},\overline{\mathrm{SST}}_{\mathrm{g4ss}})$). We conducted two sensitivity experiments: adjusting the wind speeds to match the wind speed of SSP2-4.5 while maintaining the original SSTs ($E_{\mathrm{MM}}(\overline{\mathrm{U}}_{\mathrm{ssp}},\overline{\mathrm{SST}}_{\mathrm{g4ss}})$) and adjusting the SSTs to match the SSP2-4.5 SST while retaining the original wind speeds ($E_{\mathrm{MM}}(\overline{\mathrm{U}}_{\mathrm{g4ss}},\overline{\mathrm{SST}}_{\mathrm{ssp}})$). We then subtract these sensitivity calculations from $E_{\mathrm{MM}}(\overline{\mathrm{U}}_{\mathrm{g4ss}},\overline{\mathrm{SST}}_{\mathrm{g4ss}})$ to quantify the individual contribution of wind speed and SST to the total emission changes. The last two rows of Table 3.3 summarize the influence of wind speed and SST on emissions, indicating that wind speed significantly impacts emissions more than SST changes, with effects ranging from 97.16% in tropical oceans to 67.67% in the NH extratropical oceans. These estimates are based on mean values and therefore do not account for the strong nonlinearities in the emission responses to wind speed and temperature. A more comprehensive evaluation using the full PDFs of wind speed and temperature differences could yield quantitatively different results.

In the fixed-SST simulations, rapid adjustments characterized by a global increase in natural emissions occur solely due to wind speed, as the SST are the same in 2020ssclimo and 2020climo. However, the fully coupled system, where feedbacks operate after the imposition of tropical geoengineered SSA emissions, shows a global reduction in natural emissions, opposite in sign to the rapid adjustments in emission. These emission changes are driven by

wind speed, with secondary contributions from SST. Although SST has a less direct impact on emissions compared to wind speed, it influences wind patterns, particularly by weakening westerlies in the Southern Ocean, through the thermal wind relationship.

3.5.3 The equatorial Pacific temperature gradient

This section examines the temperature gradient change in G4sea-salt minus SSP2-4.5, comparing it to abrupt-4xCO2. A key distinction between the two scenarios lies in their respective forcings: G4sea-salt experiences negative forcing from geoengineered SSA increases, whereas abrupt-4xCO2 experiences positive forcing from a quadrupling of CO_2. The geographic application of the forcing also differs, with the abrupt-4xCO2 scenario applying its forcing globally, whereas the G4sea-salt scenario applies its forcing exclusively over tropical ocean regions. Despite these differences in forcing type and application, our analysis reveals that the east–to–west equatorial Pacific temperature gradient is weakened in both cases.

Figure 3.4 presents a comparison of the ensemble-mean 50-year averaged surface temperature change, normalized by the magnitude of the global mean surface temperature change, for two forcing experiments: G4sea-salt minus SSP2-4.5 and the 50-year period following an instantaneous quadrupling of CO_2 starting from a pre-industrial CM4 run (abrupt-4xCO2) (Eyring et al., 2016; Guo et al., 2018). Fig. 3.4 shows the surface temperature change (ΔT_s) normalized by the magnitude of the global mean surface temperature change ($|\Delta T_{\mathrm{GMST}}|$) for abrupt-4xCO2 and G4sea-salt minus SSP2-4.5. Both G4sea-salt minus SSP2-4.5 and abrupt-4xCO2 exhibit Arctic amplified temperature changes between 65-90°N relative to the global mean temperature change, although this effect is more pronounced in the abrupt-4xCO2 scenario for the ensemble average and for two out of three of the members of the SSA geoengineered increase simulation (Fig. 3.4a). Arctic amplification (AA) is a robust change to various climate forcings such as CO_2 forcing, solar irradiance (Cai & Tung, 2012), aerosols and aerosol precursors (Lambert et al., 2013), and methane (Stjern et al., 2019). The occurrence of AA in response to these various climate forcings (Stuecker et al., 2018;

Serreze & Barry, 2011; A. Xie et al., 2022; Zhu et al., 2023) suggests that AA is primarily driven by feedbacks and internal mechanisms, rather than by the characteristics of the global mean forcing (Previdi et al., 2021; Russotto & Biasutti, 2020).

The global mean change in surface temperature is -0.67 K for G4sea-salt minus SSP2-4.5 and +4.01 K for abrupt-4xCO2. In the equatorial Pacific, the warming is strongest in the eastern Pacific compared to the western Pacific for abrupt-4xCO2 (Fig. 3.4b). Whereas, for G4sea-salt minus SSP2-4.5, the cooling is strongest in the western Pacific compared to the eastern Pacific (Fig. 3.4c). Despite differences in forcing and geographical application of the forcing, both experiments display a reduction in the east-to-west temperature gradient in the equatorial Pacific region. However, the extent of this weakening varies for each ensemble member with ensemble member 2 in Fig. 3.4e showing less weakening of the east–to–west SST gradient, highlighting the potential variability in how CM4 responds to the G4sea-salt scenario and its influence on the east-to-west equatorial Pacific SST gradient.

The SST gradient in the Pacific is critical for modulating the frequency of atmospheric rivers, tropical storms, and mesoscale convective systems (Zhao, 2024). Changes in the tropical Pacific SST gradient are an important characteristic of El Niño-Southern Oscillation (ENSO), including overall warming and spatial variability, by affecting atmospheric moisture and ENSO-related circulation (Jiang et al., 2024; X. Xie et al., 2021). Under abrupt-4xCO2, there is a more pronounced warming in the eastern equatorial Pacific relative to the western Pacific similar to El Niño-like conditions (Fig. 3.4b). This behavior is consistent in multiple models (Vecchi et al., 2008; Sun & Du, 2023; Kang et al., 2023); however how the tropical Pacific SST gradient responds to positive GHG forcing has generally been an active topic of debate for decades (Heede & Fedorov, 2023; Deser et al., 2010; Z. Liu et al., 2005; M. Collins, 2005).

This reduced east-to-west equatorial Pacific SST gradient weakens Walker circulation, reducing easterly trade winds and moisture transport across the tropics (Tokinaga et al., 2012). This has significant implications for regional hydroclimate, including intensified heat-

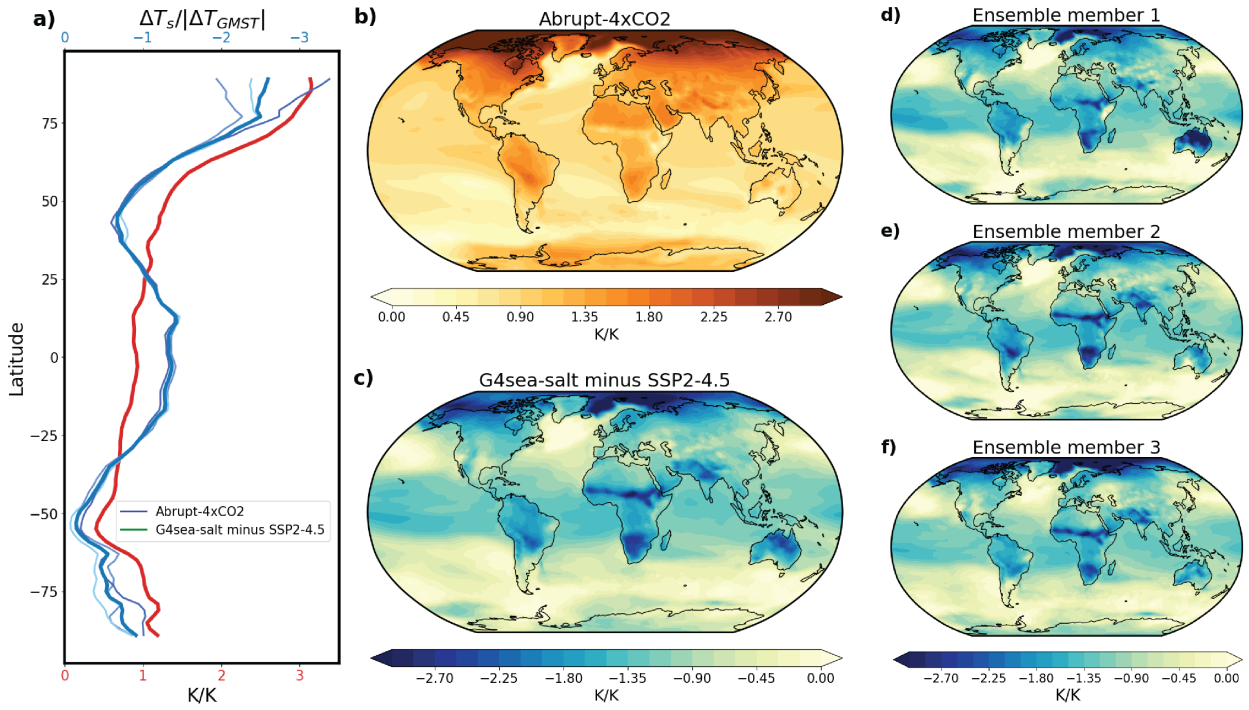


Figure 3.4: Surface temperature change (ΔT_s) normalized by the magnitude of the global mean surface temperature change ($|\Delta T_{\mathrm{GMST}}|$) are displayed for a) zonal mean abrupt-4xCO2 (red) and G4sea-salt minus SSP2-4.5 (blue), b) abrupt-4xCO2 and c) G4sea-salt minus SSP2-4.5. Panels d-f present the normalized surface temperature change for the three individual ensemble members of G4sea-salt minus SSP2-4.5.

waves in parts of the globe (Wu et al., 2024) and severe droughts in regions dependent on Walker circulation, such as Southeast Asia and Australia (Huang et al., 2020; Zhao & Cook, 2021) Fig. 3.4 shows the east-to-west equatorial Pacific SST gradient is similarly reduced in G4sea-salt minus SSP2-4.5, suggesting that a uniform negative forcing may yield comparable effects on the Walker circulation and regional hydroclimate. This highlights the importance of carefully considering how SSA emission increases are applied in geoengineering experiments and underscores the need for a detailed analysis to understand the potential impacts of geoengineering experiments on the Pacific SST gradient and regional hydroclimate.

3.6 Conclusion

In this study, we investigate and compare rapid adjustments and circulation changes (e.g, wind speed and temperature) that result from an increase in SSA emissions using the G4sea-salt protocol in a NOAA GFDL model. In the fixed-SST experiments, we observed rapid adjustments that involve changes in land temperature, intensifying the prevailing westerlies in the SH while weakening them in the NH. In the coupled simulations, the implementation of G4sea-salt not only produces the intended cooling effect, but also induces circulation responses. This includes a reduction in the equator-minus-mid-latitude temperature difference, which in turn leads to a weakening of the prevailing westerly winds in the mid-latitudes.

We quantify the changes in SSA emissions induced by rapid adjustments and circulation response to G4sea-salt by comparing the prescribed increase in SSA emissions in the tropics with the resulting emissions in the fixed-SST and coupled model simulations, respectively. Globally, we find that circulation-induced changes in SSA emissions reduce the overall increase from geoengineered SSA emissions by 23% in the coupled simulations. The circulation-induced reductions in global SSA emissions are primarily attributed to reductions in ocean-integrated SSA emissions in the SH extratropical oceans (14.3%), followed by the tropics (5.8%) and lastly, the NH extratropical oceans (2.9%). This represents a combination of ocean-averaged emission reductions and geographical extents. In contrast, the rapid adjustments in the fixed-SST simulations lead to globally increased natural emissions due to higher wind speeds. Natural emissions increase in nearly all ocean regions, with one exception: the NH extratropical oceans, where decreased wind speeds resulted in lower emissions.

To assess the impact of changes in temperature and wind speed on SSA emissions, we use MartMon to calculate SSA emissions offline. MartMon incorporates the temperature and wind speed dependent emission parameterization of Mårtensson et al. (2003) for particles smaller than 1.4 μm and the wind-speed-dependent emission formulation of Monahan et al. (1986) for larger particles. Our off-line SSA emission calculations mimic those in the GFDL

CM4 and AM4 models. Emissions are aggregated from the same five sectional-size bins used in the GFDL models, allowing for a direct comparison. Our analysis reveals that wind speed is the primary driver of MartMon emissions. A 0.1 m/s wind speed increase yields a significant 20-120% increase in emissions at wind speeds ranging from 2-14 m/s. In contrast, temperature has a modest impact, with a 0.5°C increase resulting in less than a 1% increase in emissions across a broad temperature range (-15° to 25°C).

A comparison of SSA emissions between the coupled G4sea-salt and SSP2-4.5 simulations reveals that wind speed fluctuations are the dominant factor driving emission changes, contributing 68-97% of the variations, while temperature changes have a minor impact, accounting for only 2.8-32% of the changes. However, the relative contributions of wind speed and temperature to circulation-induced changes in SSA emission, after geoengineered increases in SSA emission, are sensitive to the specific SSA emission configuration used in the model.

Although the two scenarios utilize different types and applications of forcing, both G4sea-salt minus SSP2-4.5 and abrupt-4xCO2 exhibit a reduction in the east-to-west equatorial Pacific temperature gradient. The geoengineered increase in SSA emissions through the G4sea-salt protocol generally produces stronger cooling in the central to western equatorial Pacific compared to the eastern equatorial Pacific. However, the extent of this cooling pattern and the associated weakening of the east-to-west SST gradient vary among ensemble members, with two out of three ensemble members showing a more pronounced gradient reduction. This finding contrasts with previous studies that applied regional increases in SSA emissions (Hill & Ming, 2012; C.-C. Chen et al., 2024; Haywood et al., 2023), and found that such changes induce stronger cooling in the eastern equatorial Pacific than in the western equatorial Pacific. These discrepancies may be attributed to intermodel differences and variations in the application of SSA emission increases. Specifically, the G4sea salt protocol increases SSA emissions throughout the tropical oceans, while other studies (Hill

& Ming, 2012; Haywood et al., 2023) target specific regions, such as the eastern equatorial Pacific.

This reduced temperature gradient has implications for hydroclimates and may alter precipitation patterns, drought occurrences, and severe weather events in regions like the western United States, South America, and Southeast Asia (Huang et al., 2020; Zhao & Cook, 2021; Wu et al., 2024). Thus, the application of increasing SSA emissions to brighten marine clouds has significant implications for the temperature gradient in the equatorial Pacific, which is closely linked to the Walker circulation and its associated impacts on regional hydroclimate.

This study highlights that uniform increases in SSA emission over the tropical oceans can trigger significant climatic responses, altering the geographic distribution of aerosols due to changes in the mean state of the climate system and circulation. Rapid adjustments (2020ssclimo minus 2020climo) to geoengineered tropical emission increase yield increases in SSA emission, changes that are opposite in sign to the circulation-induced changes in the coupled simulation. In the coupled G4sea-salt simulation, reductions in SSA emissions over the extratropical and tropical oceans, driven by decreased wind speed, counteract some of the geoengineered SSA emissions, thus attenuating the intended effects of such interventions. The resulting equatorial SST gradient in the Pacific exhibited in G4sea-salt minus SSP2-4.5 diverges from that observed in regional SSA emission increase experiments conducted with other climate models. This discrepancy highlights substantial differences in climate responses to regional versus zonally uniform SSA emission increases, emphasizing the need for further investigation and consideration during the development of model experimentation for MCB.

Chapter 4

The Radiative Feedback to Sea Salt Aerosol Engineering in a GFDL Coupled Model

4.1 Introduction

Climate geoengineering, particulary marine cloud brightening (MCB), has garnered significant attention as a potential strategy to mitigate global warming. Building on the analysis by Mahfouz et al. (2023) and the work presented in Chapter 3, this study investigates the radiative feedbacks to geoengineered increased sea salt aerosol (SSA) emissions in the tropics using simulations based on the G4sea-salt protocol (Kravitz et al., 2013) and the SSP2-4.5 base state with a NOAA GFDL climate model.

The traditional forcing-feedback paradigm provides a framework for understanding the Earth's climate response to external perturbations. Radiative forcing initiates a climate response that is then shaped by feedback mechanisms. Although this analysis is typically prescribed for understanding the climate response and feedbacks to anthropogenic (i.e., greenhouse gases) and natural (i.e., land surface, volcanic and tropospheric aerosols) forcing, this study attempts to apply this framework to geoengineering (i.e., increased SSA emissions).

This study assesses radiative forcing and climate feedback parameters in the context of geoengineering using G4sea-salt and SSP2-4.5 simulations. We isolate the effects of SSA geoengineering by considering the difference between the two coupled simulations (G4sea-

salt minus SSP2-4.5), assuming that the forcing and feedbacks from increased SSA emissions operate independently and do not interact significantly with those present in SSP2-4.5. The fixed-SST counterparts of G4sea-salt and SSP2-4.5 are used to diagnose the effective radiative forcing for the perturbations. We then apply a forcing analysis similar to that for a quadrupling carbon dioxide experiment (abrupt-4xCO2) in a pre-industrial (PI) climate to isolate feedbacks for an increase in geoengineered SSA emissions. Radiative kernels are also employed in this study because they offer a powerful tool for attributing components of the feedback.

This study aims to provide a comprehensive assessment of the potential impact of MCB on the Earth's climate system by examining the sensitivity of the GFDL model to radiative forcing and feedbacks attributed to geoengineered SSA emission changes. We investigate the differences in 50-year feedback between the G4sea-salt and abrupt-4xCO2 simulations, considering factors such as model variability, climate state differences (time-varying versus steady control state), and localized forcing from tropical SSA increases, all while acknowledging that this comparison is limited due to internal variability and time-varying forcing and feedback present in G4sea-salt minus SSP2-4.5.

4.2 Background

The Earth's energy budget describes the balance between incoming solar radiation and outgoing radiation, comprising reflected solar radiation and thermal radiation emitted by the climate system (P. Forster et al., 2021). In a steady-state climate, incoming and outgoing radiation are generally balanced over the long term, despite fluctuations driven by interannual variability (Brown et al., 2014). However, anthropogenic forcing can induce a global mean imbalance in TOA radiation, known as the Earth's energy imbalance (EEI; W m^{-2}) (Hansen et al., 2005; Raghuraman et al., 2021). EEI quantifies the change in the Earth's energy budget due to forcing and provides valuable insights into global climate change.

Let us consider an instantaneous quadrupling of CO_2 (abrupt-4xCO2; denoted as subscript 4xco2) that is applied to year 100 of a pre-industrial simulation (piControl) and then run for 150 years. The initial positive EEI is the effective radiative forcing (ERF) due to the imposition of 4xCO_2 and is gradually restored to equilibrium by feedbacks as the surface temperature increases (Fig. 4.1). For each year in an abrupt-4xCO2 experiment, there is a pair of $\Delta T_{\mathrm{s,4xco2}}(t_y) = T_{s,\mathrm{4xco2}}(t_y)$ - $\overline{T}_{s,\mathrm{picontrol}}$ and EEI_{4xco2}. $\overline{T}_{s,\mathrm{piControl}}$ is the 150 year averaged surface temperature of piControl (years 100-250 of piControl with no CO_2 forcing). These pairs are sorted by increasing $\Delta T_{s,\mathrm{4xco2}}$. The EEI_{4xco2} is plotted as a function of $\Delta T_{s,\mathrm{4xco2}}$ (see Fig. 4.2a). A linear regression is then applied to the plotted points, following the methodology of Gregory et al. (2004). The forcing and feedback framework follows Eq. 7.1 in Box 7.1 in the IPCC AR6 assessment (P. Forster et al., 2021) that is applied to abrupt-4xCO2:

$$EEI_{\mathrm{4xco2}}(\Delta T_{s,\mathrm{4xco2}}) = ERF + \lambda_{\mathrm{4xco2}} \cdot \Delta T_{s,\mathrm{4xco2}} \tag{4.1}$$

where EEI_{4xco2} (W m^{-2}) is the TOA net energy flux. λ_{4xco2} (W m^{-2} K^{-1}) is the climate feedback, and defined as the slope of the linear regression in Fig. 4.2a. ERF (W m^{-2}) is the effective radiative forcing, the intercept of the linear regression on the Gregory diagram at ΔT_s =0.

The ERF quantifies the change in net TOA energy flux due to an imposed perturbation (i.e. changes in GHG). As mentioned in Chapter 3, two methods have been used to estimate ERF. As shown in Figure 1 Box 7.1 in the IPCC AR6 assessment, one method for estimating ERF is to extrapolate from the regression of the EEI with changes in surface temperature at zero temperature change (that is, for abrupt-4xCO2: $EEI_{\mathrm{4xco2}}(\Delta T_{s,\mathrm{4xco2}} = 0)$). Another method of estimating ERF include subtracting the net TOA radiation fluxes between a perturbation experiment (i.e., abrupt-4xCO2) and a control experiment (i.e. piControl), with fixed sea surface temperatures (SST) in both simulations. Both methods yield different estimates of ERF (see Chapter 3). For abrupt-4xCO2, the multi-model mean ERF is 7.98 $\pm$ 0.38 W m^{-2} (C. J. Smith et al., 2020).

The climate feedback, λ_{4xco2}, is defined as the slope of the linear regression applied to the sorted pairs of $\Delta T_{s,4xco2}$, and EEI_{4xco2}. For the full 150-year abrupt-4xCO2 simulation, it is denoted as $\lambda_{4xco2}(0, 150)$. λ_{4xco2} depends on the number of years considered in the regression. We will consider other numbers of years for the regression later in the text. Climate feedbacks are processes that either intensify or weaken the initial surface temperature change (warming, in the case of abrupt-4xCO2) in response to external radiative forcing (RF). The net feedback is negative, primarily due to the Planck temperature response. The multimodel mean feedback for abrupt-4xCO2 is –1.16 (-1.81 to -0.51) W m^{-2} K^{-1} as reported in IPCC AR6 assessment (P. Forster et al., 2021).

The net climate feedback can be further decomposed into a sum of terms ($\lambda = \sum \lambda_X$) where X represents changes in temperature (T), water vapor (w) and surface albedo (α). The remaining feedback (i.e. residual) is ascribed to changes in the cloud if the feedback due to changes in aerosol is not large, such as that for abrupt-4xCO2. Contributions of the component feedbacks to the total feedback is computed using the "radiative kernel" method (Soden et al., 2008). The residual feedback (i.e cloud feedback for abrupt-4xCO2) is calculated as the difference between the total feedback calculated using the "Gregory" method and the sum of the temperature, water vapor and surface albedo feedback calculated using the "radiative kernel" method. This method of calculating the feedback and its components is hereafter referred to as the combined Gregory-kernel method (Block & Mauritsen, 2013).

Feedbacks are evaluated on long timescales (typically 150 years) because this is the timescale needed to bring the climate system to radiative equilibrium (Gregory et al., 2004). M. Zhao (2022) has shown that the climate feedback parameter varies depending on the time period to which the linear regressions are applied. Specifically, for an abrupt-4xCO2 simulation, λ_{4xco2}(0,50) versus λ_{4xco2}(0,150) yields different estimates, highlighting the effect of time-varying feedback. To account for this, we will express feedbacks as a function of start year, end year, and X (e.g., $\lambda(t_1, t_2, X)$ for feedback decomposition and $\lambda(t_1, t_2)$ for total feedback).

Although this traditional framework for quantifying the climate response to external perturbations is prescribed to understand radiative responses and feedbacks to changes in greenhouse gases (i.e., CO_2 increases), we attempt to apply this framework to understand the feedback to geoengineering using G4sea-salt and SSP2-4.5. The tropical increase in SSA emissions in G4sea-salt is interpreted as a large forcing that is imposed on the SSP2-4.5 simulation. However, this forcing is applied to a base state (SSP2-4.5) that is not at equilibrium and contains both time-varying forcing and feedbacks from greenhouse gases and aerosols in addition to interannual variability. Subsequently, we subtract the TOA energy imbalance in SSP2-4.5 from G4sea-salt (hereafter G4sea-salt minus SSP2-4.5; denoted by subscript g4ss-ssp) in an attempt to isolate the effects of increased SSA emission and the resulting radiative response and feedback, assuming they can be isolated from a background of time-varying forcing and feedbacks in the SSP2-4.5 simulation.

The study proposes using the Gregory-kernel methodology, previously applied to abrupt-4xCO2 scenarios, to quantify forcing and feedback from geoengineered SSA emissions in G4sea-salt minus SSP2-4.5. In this case, pairs of $\Delta EEI_{\text{g4ss-ssp}}$ and $\Delta T_{s,\text{g4ss-ssp}}$ are sorted by increasing $\Delta T_{s,\text{g4ss-ssp}}$ and plotted, with $\Delta EEI_{\text{g4ss-ssp}}$ as a function of $\Delta T_{s,\text{g4ss-ssp}}$ (see Fig. 4.2b). A linear regression is then applied to the plotted points. The slope of this regression line for G4sea-salt minus SSP2-4.5 is denoted as $\lambda_{\text{g4ss-ssp}}(2020, 2070)$.

We consider the temperature, water vapor and surface albedo feedback in this analysis. However, the residual feedback for G4sea-salt minus SSP2-4.5 encompasses changes in cloud, as well as aerosol-cloud interactions (ACI) and clear-sky aerosol-radiation interactions, and will be referred to as $\lambda_{\text{g4ss-ssp}}(2020, 2070, \text{cloud+aerosol})$.

We compare the feedbacks to geoengineered SSA emission increase to that for the first 50 years after quadrupling of CO_2 while acknowledging the differences in climate state, application of forcing and internal variability present between the simulations. In particular, the G4sea-salt and SSP2-4.5 experiments introduce time-varying components due to the evolv-

ing nature of the underlying forced state, unlike the abrupt-4xCO2 scenario. Nonetheless, we propose that comparing these simulations can still provide valuable insight.

The feedback calculated for the first 50 years after quadrupling of CO_2 for abrupt-4xCO2 will be referred to as $\lambda_{4xco2}(0, 50, X)$. The feedback calculated using the full 150 year abrupt-4xCO2 simulation by Zelinka et al. (2020) is presented here for comparison with our estimates of $\lambda_{4xco2}(0, 50, X)$ and $\lambda_{4xco2}(0, 150, X)$ calculated using the combined kernel-Gregory method.

4.3 Methods

4.3.1 Model Description

We use the GFDL coupled model CM4 which is part of the sixth phase of the Coupled Model Intercomparison Project (CMIP6). It consists of the atmosphere and land models (AM4 and LM4; M. Zhao et al., 2018) as well as ocean and sea ice models (OM4; Adcroft et al. (2019)). AM4 has a horizontal resolution of 1° (approximately 100 km) with 33 layers, and OM4 has a horizontal resolution of 0.25° with 75 layers.

As summarized by Mahfouz et al. (2023), the current emission and transport scheme for SSA in CM4 uses five sectional size bins ranging from 0.1 to 10 microns. To represent SSA emissions at the sea surface, two schemes are used: Mårtensson et al. (2003) for particles smaller than 1.4 μm and Monahan et al. (1986) for particles larger than 1.4 μm. In both cases, emission depends on the wind speed at 10 m which holds across particle sizes, however smaller particles less than 1.4 μm are also sensitive to sea surface temperature (SST; Mårtensson et al., 2003).

4.3.2 Simulation Protocol

In total, eight simulations are used in this study. We first conduct a pair of fixed-SST atmosphere-only cyclic AM4 simulations using the annual-mean SSTs from year 2020 (re-

peated for 30 years) of the CM4 SSP2-4.5 simulation and keeping the radiative forcing agents in the AM4 simulations at their 2020 values. The reference simulation uses the present-day aerosol emission scenario with all radiative forcing agents kept to their 2020 values. In AM4 G4sea-salt, we prescribe an additional submicron SSA emission of 7.66×10^{-11} kg m^{-2} s^{-1} (constant in time) for each of the first two size bins in each marine grid cell between 30°S and 30°N (Kravitz et al., 2013). The fixed-SST experiments were run to determine the added SSA emissions required to reduce the top-of-atmosphere (TOA) earth's energy imbalance by 2 W m^{-2}. This value was chosen to offset an ERF of 2 W m^{-2} as specified by Kravitz et al. (2013).

We also conduct two three-member ensembles of 50-year CM4 coupled simulations (2020-2070). The reference coupled simulations follow the SSP2-4.5 projections. The initial conditions of the CM4 SSP2-4.5 at 2020 are obtained from CM4 historical simulations branched at year 2015 and run following the SSP-based Representative Concentration Pathway RCP4.5, which stabilizes radiative forcing at 4.5 W m^{-2} in 2100 (O'Neill et al., 2014; O'Neill et al., 2016). In the perturbed simulation, CM4 G4sea-salt, the emission of submicron SSA is increased for 2020-2070 by the same amount as in AM4 G4sea-salt (by 7.66×10^{-11} kg m^{-2} s^{-1} for the first two bins (submicron) in each marine grid cell between 30° S and 30° N).

We use the 50-year (2020-2070) G4sea-salt and SSP2-4.5 CM4 simulations for the feedback and forcing calculations in Section 4.41. We compare the 2020-2070 feedback to the negative forcing from the increased SSA with the feedback to the positive forcing from the first 50 years after an instantaneous quadrupling of CO_2 in a pre-industrial CM4 run. We also present the feedback over 50 and 150 years following the quadrupling to show the sensitivity of the feedback over time and to allow comparison to estimates of the feedback presented in Zelinka et al. (2020) and M. Zhao (2022).

4.4 Comparing Earth's Energy Imbalance (EEI) in Geoengineering and Abrupt-4xCO2 Scenarios

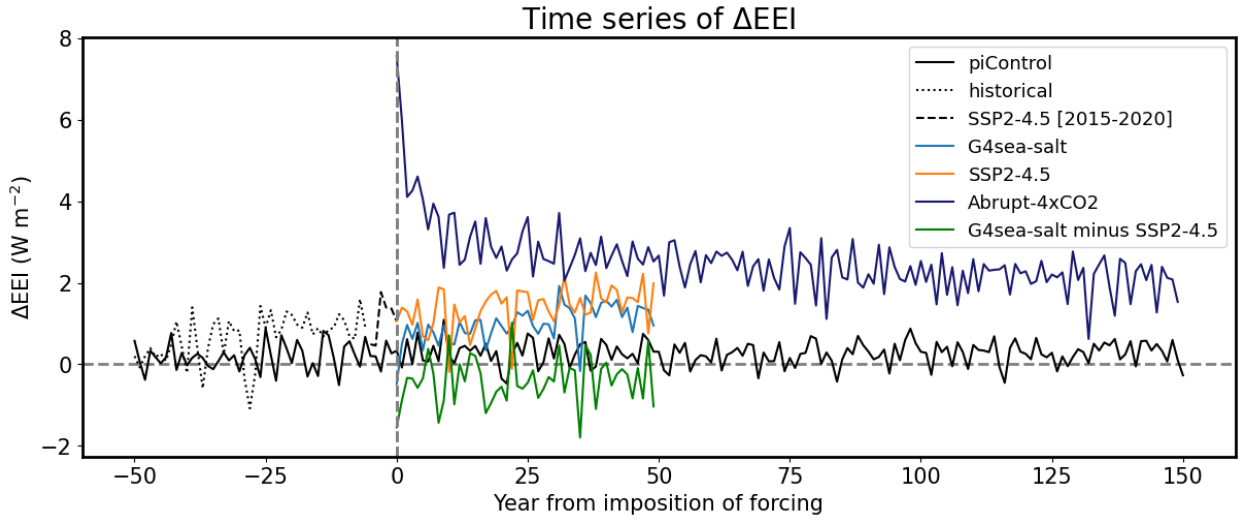


Figure 4.1: The time series of EEI as a function of year from imposition of forcing for abrupt-4xCO2, G4sea-salt and SSP2-4.5 and the base states (piControl, historical and SSP2-4.5 (2015-2020)).

Figure 4.1 presents a comparison of the Earth's energy imbalance (EEI) for various simulations: abrupt-4xCO2, G4sea-salt, SSP2-4.5, and the unforced base states (piControl and historical). The abrupt-4xCO2 simulation is initiated from year 100 of piControl (Eyring et al., 2016), therefore years 50-100 of piControl correspond to years -50 to 0 relative to the imposition of forcing. Similarly, years 100–150 of piControl represent years 0 to 50 after the imposition of forcing. To isolate the EEI change due to the increase in geoengineered tropical SSA emissions, we calculate the difference between G4sea-salt and SSP2-4.5 (G4sea-salt minus SSP2-4.5) and compare it with the EEI for abrupt-4xCO2. The two forcing experiments differ in magnitude and sign, leading to distinct EEI time series for G4sea-salt minus SSP2-4.5 and abrupt-4xCO2, with the former exhibiting greater variability.

Despite the noisiness in EEI for G4sea-salt, the EEI responds to the imposition of forcing (at t_y=2020) by decreasing for G4sea-salt minus SSP2-4.5 and increasing for abrupt-4xCO2. This suggests that the radiative response to the increase in geoengineered tropical SSA

emissions (G4sea-salt minus SSP2-4.5) is amenable to forcing analysis, similar to that applied to abrupt-4xCO2. However, we acknowledge that the noisiness in EEI for G4sea-salt minus SSP2-4.5 may confound the interpretation of our analysis.

	EEI Standard Deviation (W m^{-2})
historical (1970-2015)	0.57
SSP2-4.5 (2020-2070)	0.51
G4sea-salt (2020-2070)	0.45
piControl (yr -50 to 0)	0.33

Table 4.1: The standard deviation of EEI for historical, SSP2-4.5, G4sea-salt, and piControl (year -50 to 0 from imposition of forcing).

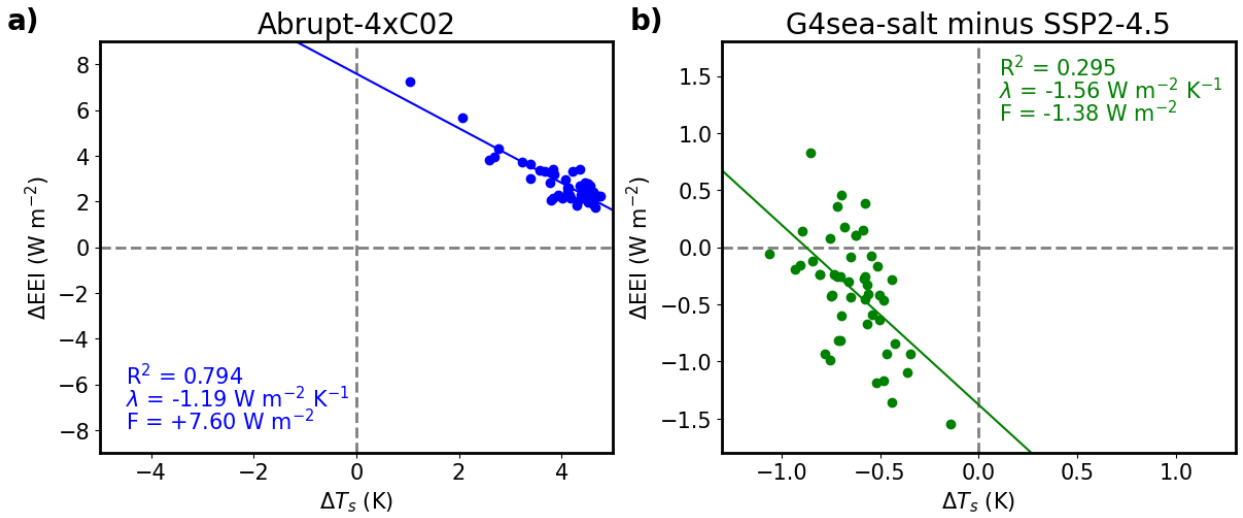


Figure 4.2: EEI and ΔEEI plotted as a function of global average surface temperature (ΔT_s) for a) abrupt-4xCO2 and b) G4sea-salt minus SSP2-4.5, respectively. For abrupt-4xCO2, EEI and ΔT_s are calculated as the difference between abrupt-4xCO2 (first 50-years) and piControl (averaged from 100-250 year of piControl). For G4sea-salt minus SSP2-4.5, ΔEEI, and ΔT_s are calculated as the year-by-year differences between G4sea-salt and SSP2-4.5 over the period 2020-2070. The slope of the regression line (λ; W m^{-2} K^{-1}) is calculated for the 50-year period and the forcing (F; W m^{-2}) is determined as the y-intercept of the regression line.

In Fig. 4.2, we evaluate the 50-year climate feedback by regressing changes in EEI (ΔEEI) against the change in surface temperature (ΔT_s) following Gregory et al. (2004) for two scenarios: a) abrupt-4xCO2 ($\lambda_{4xco2}(0, 50)$) and b) G4sea-salt minus SSP2-4.5

($\lambda_{\text{g4ss-ssp}}(2020, 2070)$). We calculate ΔT_{s} as the differences between the respective simulations and their control runs.

At the instantaneous quadrupling of CO_2, EEI rises as outgoing longwave radiation (OLR) decreases due to absorption of infrared radiation by the higher CO_2 concentration in the atmosphere (Fig. 4.1). However, over time, feedbacks (i.e., water vapor, Planck, cloud and albedo) act to counteract the radiative forcing from quadrupling of CO2 as temperature increases until EEI reaches equilibrium. Thus, the initial positive energy imbalance is gradually restored towards equilibrium as surface temperature increases for abrupt-4xCO2 in Fig. 4.2a. In contrast, at the imposition of a negative forcing such as an increase in SSA emissions, the EEI changes in response to this forcing and decreases due to reduced absorbed short-wave radiation (Fig. 4.1). In the absence of internal variability and time-varying forcing, EEI is expected to increase quite uniformly due to the presence of feedbacks as the temperature decreases over time until EEI reaches equilibrium. However, the EEI for G4sea-salt minus SSP2-4.5 with respect to the surface temperature change in Fig. 4.2b is quite noisy, which is attributed to either SSA variability or internal variability from forcing and response.

The 2020-2070 total climate feedback from increased tropical sea salt emissions in G4sea-salt is 31% more negative than the feedback for years 0-50 of quadrupling CO_2 (-1.56 versus -1.19 W m^{-2} K^{-1}). Furthermore, the difference in EEI between G4sea-salt and SSP2-4.5 along the regression line when $\Delta T_{s,\text{g4ss-ssp}}$=0 (e.g., y-intercept) is -1.38 W m^{-2}, which is 31% less than the ERF of -2.00 W m^{-2} calculated using the fixed-SST counterparts. Fixed-SST ERF values are consistently 11–32% higher than those obtained through linear regression across various forcing agents and models (Tang et al., 2019). This discrepancy arises due to the inclusion of land adjustments in the fixed-SST approach (IPCC AR6, Chapter 7).

To quantify the observed variability in EEI for G4sea-salt and SSP2-4.5, we calculate their standard deviations and compare them with those of the base states (historical and piControl) in Table 4.1. The standard deviation of EEI for SSP2-4.5 and G4sea-salt is

	Standard Deviation					
	SSA emission ($\times$1e-12 kg m$-$2 s^{-1})			**$\int$ SSA concentration dz** ($\times$1e-7 kg m$-$2)		
	Global	Tropics	Southern Ocean	Global	Tropics	Southern Ocean
SSP2-4.5 (2020-2070)	4.71	3.06	15.82	1.57	1.62	4.01
G4sea-salt (2020-2070)	4.09	2.52	13.82	1.19	1.08	3.10
G4sea-salt minus SSP2-4.5	5.74	3.57	20.31	1.74	1.83	4.90
piControl (yr 50-100)	5.96	4.15	20.58	1.73	2.15	4.59
Abrupt-4xCO2 (yr 0-50)	6.75	4.08	27.02	2.24	1.90	7.84
Abrupt-4xCO2 minus piControl	8.94	5.42	32.98	2.87	2.63	9.66

Table 4.2: The standard deviation of SSA emission and vertically integrated SSA concentration globally, in the tropics and Southern Ocean (60°S to 30°S). The abrupt-4xCO2, SSP2-4.5 and G4sea-salt are evaluated from years 0-50 from the onset of forcing while piControl is evaluated from years -50 to 0 from the onset of forcing.

similar magnitude to that of the historical (1970-2015) and greater than that of piControl. A comparison of the standard deviation of year-to-year SSA emission and vertically integrated SSA concentration in Table 4.2 reveals that the standard deviation of SSA emission and vertically integrated concentration for piControl, abrupt-4xCO2, and abrupt-4xCO2 minus piControl all exhibit year-to-year variations in SSA that are equal to or greater than those present in the geoengineered SSA experiments. This suggests that SSA variability is not the primary cause of EEI variability in the geoengineering experiments. Instead, the EEI variability for SSP2-4.5 and G4sea-salt can be attributed to contributions from time-evolving forcing and feedbacks.

To further understand the difference between the 50-year feedbacks for G4sea-salt minus SSP2-4.5 and abrupt-4xCO2, we analyze the differences between the base states for the two forcing experiments. Fig 4.3 presents the EEI anomaly, along with its long-wave (LW) and short-wave (SW) components, as functions of the surface temperature anomaly for the two

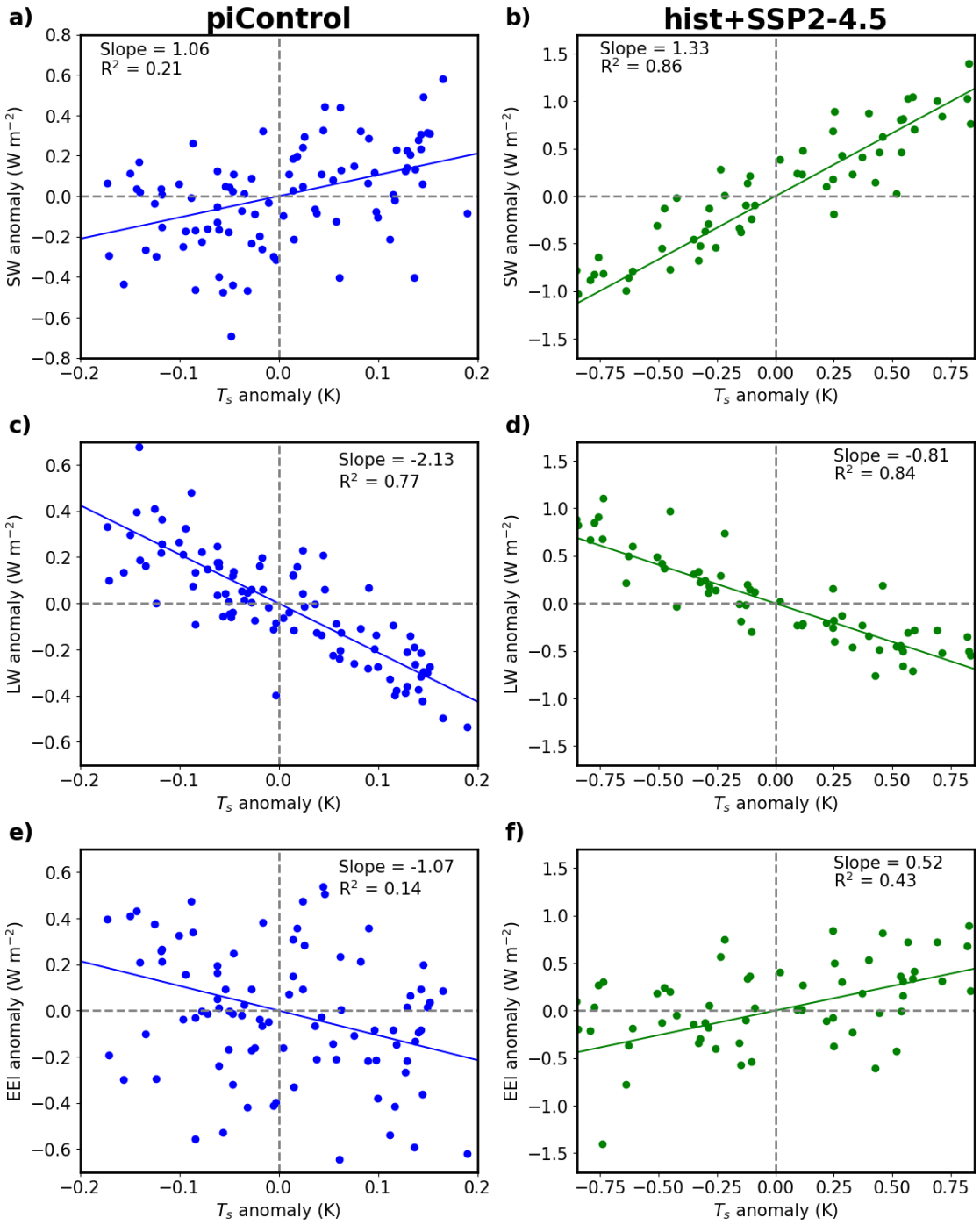


Figure 4.3: The longwave radiation (LW) and shortwave radiation (SW) and EEI calculated as the anomaly from the 100-year SW, LW, and EEI means (respectively) subtracted for each (i.e, LW anomaly = LW - $\overline{\text{LW}}$) plotted as a function of global surface temperature anomaly (T_s anomaly =T_s - $\overline{T_s}$) for piControl (year 100-250; a, c and e) and historical (1970-2014) + SSP2-4.5 (2015-2070) (hereafter hist+SSP2-4.5; b, d and f).

base states: piControl and hist+SSP2-4.5. The EEI anomaly is calculated as the difference between the annual EEI and the global 100-year-averaged EEI. The LW and SW components are defined as positive when directed into the system.

In piControl, changes in SW and LW radiation are driven by internal climate variability (e.g., El Niño–Southern Oscillation (ENSO) and other modes of variability such as Pacific Decadal Oscillation (PDO), Madden-Julian Oscillation (MJO), etc) and model-specific factors (e.g., radiative scheme limitations or model drift). To obtain some insights on the variability, let us consider ocean-driven SST variability in the absence of SW responses. Then warmer SSTs increase OLR, while cooler SSTs decrease OLR. Thus the negative correlation between LW radiation and surface temperature change is expected (Fig. 4.3c). In addition to changes in LW radiation, SW radiation also varies with SST. In piControl, SW radiation exhibits a positive correlation with changes in surface temperature (Fig. 4.3a). This relationship arises from cloud and surface albedo responses to SST changes. For instance, as SST increases, sea ice loss and modifications in cloud properties (e.g., cloud cover, thickness, or optical depth) enhance SW absorption. This SW response aligns with SW feedbacks that occur when SST increases in a forced run (Ceppi et al., 2017; Gettelman et al., 2016; Zelinka & Hartmann, 2010).

The 100-year average EEI for piControl, which is subtracted from the EEI anomalies, is 0.24 W m^{-2}. The radiative response to surface temperature change (ΔEEI/ΔT_s) is -1.05 W m^{-2} K^{-1} (Fig. 4.3e). However, there is a large amount of scatter present in the LW anomaly, SW anomaly and EEI anomaly with respect to surface temperature change.

In contrast to piControl, hist+SSP2-4.5 contains the emergence of anthropogenic climate drivers and aerosol changes in addition to interannual variability (M. Zhao et al., 2018). Aerosols decline over this period, leading to less reflected SW radiation and this coincides with increasing SSTs. Additionally, cloud and surface albedo feedback play a role in modulating SW radiation. Furthermore, transient GHG forcing muddies the system's attempts to equilibrate the original radiative forcing by emitting OLR, which dampens the amount of

OLR emitted as the Earth warms. Subsequently, the combination of a 25.5% more positive slope in SW and a 62% less negative slope in LW results in a positive slope in the EEI anomaly with respect to surface temperature for hist+SSP2-4.5 (Fig. 4.3f).

Comparison of the base states (piControl vs. hist+SSP2-4.5) in Fig. 4.3 indicates that the base states are intrinsically very different in the evolution of the EEI and their SW and LW component with respect to surface temperature change. The piControl base state contains interannual variability, while hist+SSP2-4.5c contains time-varying forcing in addition to interannual variability. This has implications for the behavior of the SW and LW components with respect to changes in surface temperature, as shown in Fig. 4.3. More studies are needed to understand these differences, but we proceed with the limited analysis of the forcing analysis on sea salt as a forcing on the base state, acknowledging these limitations.

To further decompose the total 50-year climate feedback into contributions from temperature, water vapor, and surface albedo, we use radiative kernels, which will be discussed in the subsequent section.

4.4.1 Decomposing the total feedback

We use radiative kernel method to calculate components of the total feedback; see Appendix D for a general description. We attempt to isolate the forcing and feedback due to sea salt geoengineering on SSP2-4.5 by considering the imposition of increased SSA emission as forcing. While customarily used with equilibrium climate simulations, such as coupled pre-industrial control (piControl) and quadrupling carbon dioxide, (4xCO2) (e.g., Wang et al. (2021)), we argue it is possible to apply this method to SSA forcing, even though it is a transient coupled simulation, following Gettelman et al. (2016), and references therein. Furthermore, examining the ERF and climate response to other short-lived, time-varying climate forcers has been described in Chapter 6 AR6 (P. Forster et al., 2021).

In our case, both simulations extend the historical GFDL CM4 simulation from 2015 onwards. We use the average of the 1985-2015 CM4 historical simulation as the reference

with respect to which we calculate EEI using the kernels. The kernels can then be used to calculate $\delta\text{EEI}_X(t_y)$ in succeeding years, relative to the 1985-2015 EEI mean, by multiplying the kernels by changes in X. Note that δEEI includes forcings and feedbacks in SSP2-4.5 and G4sea-salt.

For SSP2-4.5, we calculate the $\delta\text{EEI}_{X,\text{SSP2}-4.5}(t_y)$, following Eq. D.3, by multiplying the corresponding monthly-mean kernel by the difference in monthly-mean climate state X between SSP2-4.5 (2020-2070) and the corresponding monthly-mean climate state from 1985-2015 CM4 historical:

$$\delta EEI_{\text{X,SSP2}-4.5}(t_y) = \sum_{i,j,k,m} \kappa_X(i,j,k,t_m) \cdot \Delta X_{\text{SSP2}-4.5}(i,j,k,t) \tag{4.2}$$

where $\Delta X_{\text{SSP2-4.5}}(i,j,k,t) = X_{\text{SSP2-4.5}}(i,j,k,t) - X_{\text{historical}}(i,j,k,t,t_{y=1985-2015})$.

We do a similar calculation using $\Delta X_{\text{G4sea}-\text{salt}}(i,j,k,t)$ to obtain $\delta\text{EEI}_{\text{X,G4sea}-\text{salt}}(t_y)$. The first column of Fig 4.4 shows $\delta\text{EEI}_X(t_y)$ for G4sea-salt and SSP2-4.5.

We take the difference in TOA energy imbalance between the two transient simulations, assuming that SSA forcing and feedbacks can be isolated from a background of time-varying forcing and feedbacks in the SSP2-4.5 simulation. Furthermore, this implicitly assumes that the forcing and feedbacks from increased SSA emissions are independent of those from time-varying forcing in SSP2-4.5. Thus:

$$\Delta\text{EEI}_{X,\text{SSA}}(t_y) = \delta\text{EEI}_{X,\text{G4sea}-\text{salt}}(t_y) - \delta\text{EEI}_{X,\text{SSP2}-4.5}(t_y) \tag{4.3}$$

where $\Delta\text{EEI}_{X,\text{SSA}}(t_y)$ is shown in the second column of Fig. 4.4.

To calculate the 2020-2070 feedback for G4sea-salt minus SSP2-4.5, we first sort pairs of $\Delta\text{EEI}_{X,\text{SSA}}$ and ΔT_s in order of increasing ΔT_s. $\Delta\text{EEI}_{X,\text{SSA}}$ is then plotted as a function of ΔT_s (Fig. 4.5d, e and f). The slope of the linear regression fitted to these points is the feedback for X, $\lambda_{\text{g4ss-ssp}}(2020, 2070, X)$ (column 3 of Fig. 4.5).

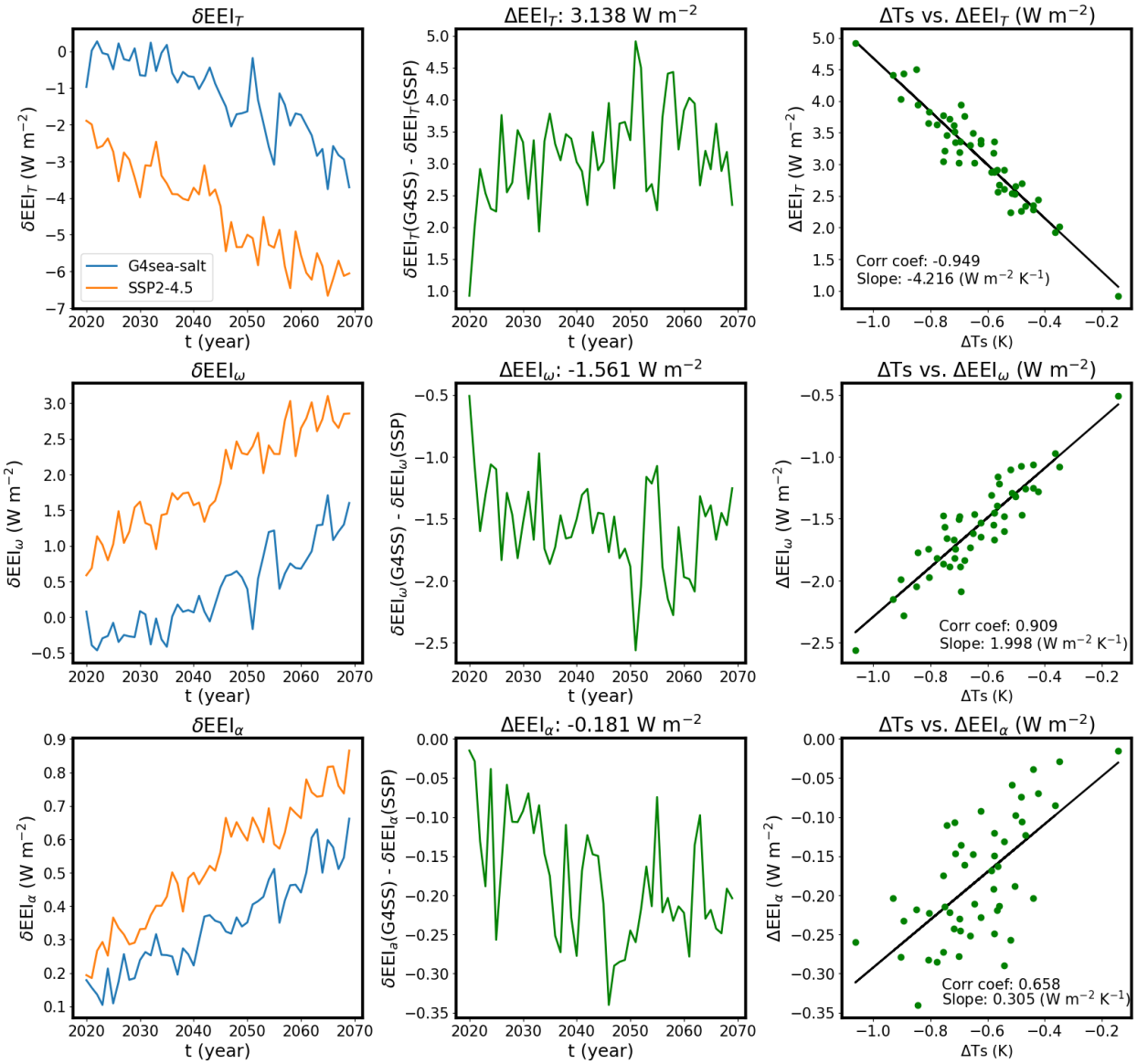


Figure 4.4: The decomposition of the feedback due to contributions from temperature (first row), water vapor (second row) and surface albedo (third row). The first column shows the change in EEI calculated due to changes in climate state X for G4sea-salt and SSP2-4.5 separately (relative to historical) using the radiative kernels, as in Eq. 4.2. The second column shows the difference in EEI between the two transient experiments, i.e. $\Delta\text{EEI}_{X,\text{SSA}}(t_y) = \delta\text{EEI}_{X,\text{G4sea-salt}}(t_y) - \delta\text{EEI}_{X,\text{SSP2-4.5}}(t_y)$. The third column shows the regression line fit to $\Delta\text{EEI}_{X,\text{SSA}}$ plotted as a function of surface temperature change, ΔT_s.

We present the results of the decomposition of the total feedback for G4sea-salt minus SSP2-4.5 (i.e., last column of Fig. 4.4) compared to the abrupt-4xCO2 experiment in Fig. 4.5. Fig. 4.5d, e and f indicate that the relationship between ΔEEI_X and surface temperature

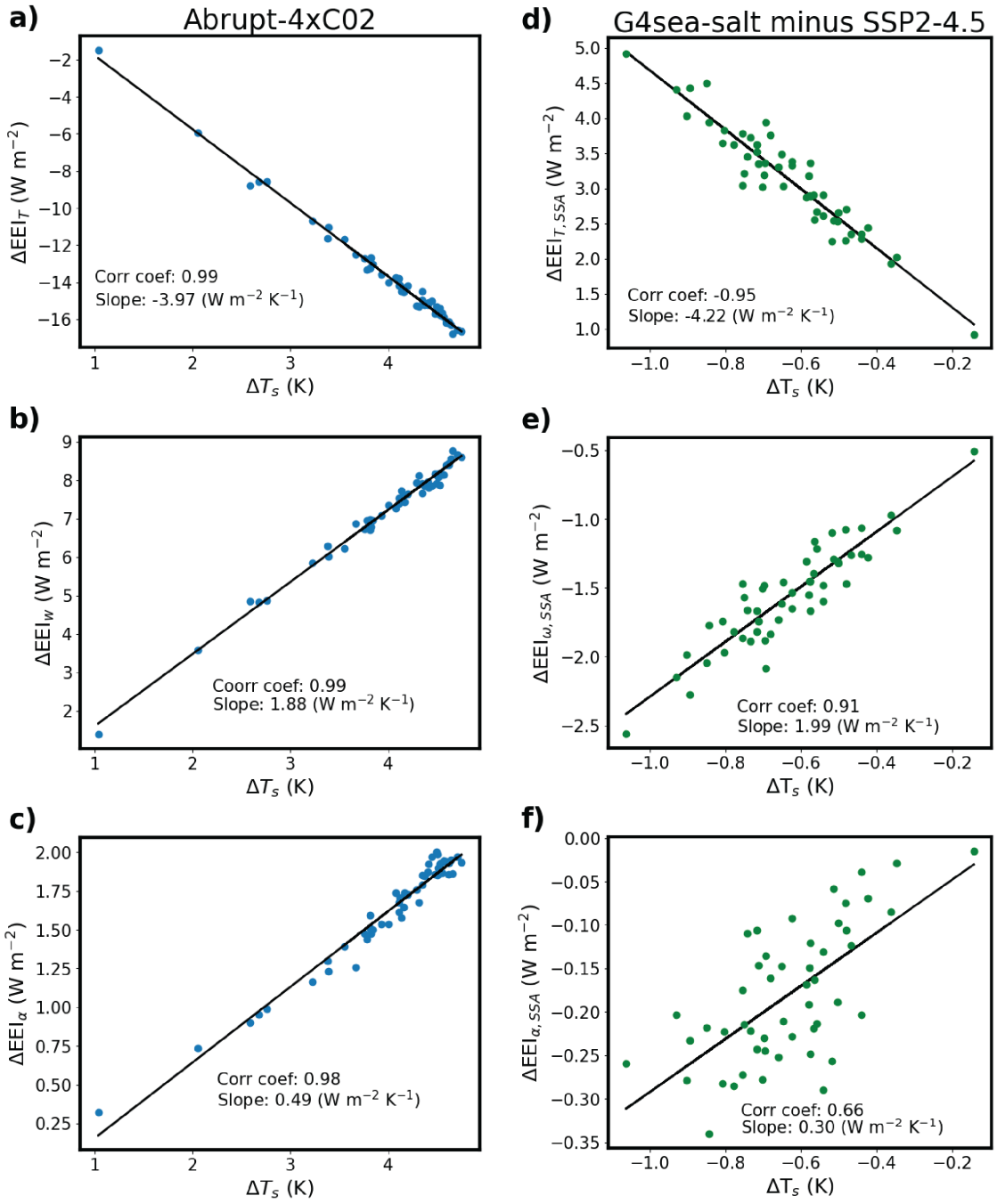


Figure 4.5: The change in EEI due to changes in temperature, water vapor and surface albedo relative to changes in surface temperature for abrupt-4xCO2 (a, b, and c) and G4sea-salt minus SSP2-4.5 (d, e, and f).

change is noisier and less correlated in G4sea-salt minus SSP2-4.5 compared to the abrupt-4xCO2 experiment. Although interannual variability is present in piControl, the noisiness of the EEI evolution for G4sea-salt minus SSP2-4.5 with respect to temperature change suggests

that the presence of the complex mixture of time-varying forcing and feedback contributing to variability is greater than the variability from SSA emissions. Since variability in SSA emission and concentration cannot explain the large variabilities in EEI, it is unclear how much the year 2020-2070 feedback from G4sea-salt minus SSP2-4.5 is picking up variability versus a discernible response to tropical SSA emission increase.

In addition to the decomposition of the total feedback calculated for 150-years of abrupt-4xCO2, 50-years of abrupt-4xCO2 and (2020-2070) G4sea-salt minus SSP2-4.5 using the combined kernel-Gregory method, we present the feedback calculated by Zelinka et al. (2020) using the 150-year abrupt-4xCO2 CM4 simulation in Table 4.3 for comparison with our estimates. The sensitivity of the approximations to feedback for different time periods in prognostic abrupt-4xCO2 simulation is referred to as the time-varying feedback (e.g., see Fig 1 in M. Zhao (2022)). The total feedback for the first 50 years after imposition of the forcing is 40% more than the feedback calculated using 150 years, demonstrating the effect of the time-varying negative response (e.g, Winton et al. (2010); M. Zhao (2022)).

Decomposing the total feedback into its components, we see that the temperature feedback contributes the most to the more negative total feedback for G4sea-salt minus SSP2-4.5 compared to abrupt-4xCO2 (Table 4.3). However, there is also an increase in positive feedback due to changes in water vapor and reductions in positive feedback due to changes in surface albedo and cloud+aerosol (residual) for G4sea-salt minus SSP2-4.5 compared to abrupt-4xCO2 (Table 4.3).

The negative and positive forcing, if uniformly distributed, results in stronger negative feedback to the negative forcing compared to a positive forcing. However the relative magnitudes are model dependent (i.e, CCSM3.5 in (Schaller et al., 2014), SPEAR-LO in (Zhang et al., 2023) and CESM1 in (Stolpe et al., 2019)). The spatial pattern of the forcing has been explored by (Zhang et al., 2023), who suggested that the magnitude of the pattern response is stronger than the climate response to the sign of the forcing for the total feedback and lapse rate + Planck (temperature) feedback. Lastly, whether the climate response to

forcing is independent of the simulated base state climate has been largely debated, and the magnitude of the climate response varies amongst climate models (i.e., CESM1 (Stolpe et al., 2019) suggests a weak base state dependency while HadCM3 (Brierley et al., 2009) and FLOR (He et al., 2017) suggest a strong base state dependency).

Ultimately, the differences in feedback between G4sea-salt minus SSP2-4.5 and abrupt-4xCO2 arise from a combination of factors, including: 1) climate response to negative vs. positive forcing (Schaller et al., 2014; Zhang et al., 2023; Stolpe et al., 2019), 2) localization of sea salt forcing in the tropics vs. uniform CO_2 forcing (Zhang et al., 2023), 3) imposition of forcing on a warmer base state (Stolpe et al., 2019; Brierley et al., 2009; He et al., 2017), and 4) type of forcing (quadrupling of CO_2 vs. increase SSA).

	Abrupt-4xCO2 [150 years] Zelinka et al., (2020)		**Abrupt-4xCO2 [50 years]**	**G4sea-salt minus SSP2-4.5**
Temperature	−3.77	−3.75	−3.97	−4.21
Surface Albedo	0.55	0.48	0.49	0.31
Water Vapor	1.84	1.75	1.88	2.00
Cloud(+Aerosol)	0.56	0.70	0.41	0.34
Total feedback	−0.82	−0.82	−1.19	−1.56

Table 4.3: The decomposition of the total feedback (W m^{-2} K^{-1}) for abrupt-4xCO2 and G4sea-salt minus SSP2-4.5. Values of the feedback decomposition using 150 years of the CM4 abrupt-4xCO2 simulation from Zelinka et al. (2020) are presented in comparison to our estimates retrieved using the radiative kernels from Soden et al. (2008) and the residual method using Gregory et al. (2004). The cloud+aerosol feedback refers to the residual feedback calculated for G4sea-salt minus SSP2-4.5, whereas the residual feedback is ascribed to the cloud feedback for abrupt-4xCO2.

We use a bootstrap method to test the robustness of our estimates and calculate the confidence interval [2.5%, 97.5%]. This involves randomly selecting 10 values to remove from both datasets (abrupt-4xCO2 and G4sea-salt minus SSP2-4.5), fitting a linear regression line to the remaining data, and storing the slope (e.g., feedback). We iterate this process for 100 times for the total feedback and its decomposition for both datasets (Table 4.4). The averaged total feedbacks and decompositions from the bootstrap method are similar to estimates obtained when all points in the 50 years are used for both G4sea-salt and

abrupt-4xCO2. The confidence intervals for the cloud (+aerosol) feedback overlap between G4sea-salt and abrupt-4xCO2, indicating that these estimates are sensitive to sampling to the extent that differences between the experiments are not clearly detectable. This is because G4sea-salt is very sensitive to sampling. In contrast, the confidence intervals for water vapor feedback, surface albedo feedback, and temperature feedback show minimal to no overlap, confirming that the differences in these feedbacks between the experiments are robust, detectable, and unlikely to result from sampling alone. The confidence intervals for the total feedback in the two experiments slightly overlap, primarily due to the substantial overlap in the cloud (+aerosol) feedback confidence intervals.

	Abrupt-4xCO2 [50 years]		**G4sea-salt minus SSP2-4.5**	
	Bootstrap mean	Confidence interval [2.5%, 97.5%]	Bootstrap mean	Confidence interval [2.5%, 97.5%]
Temperature	−3.97	[−4.03, −3.83]	−4.21	[−4.39, −4.06]
Surface Albedo	0.49	[0.48, 0.52]	0.31	[0.26, 0.35]
Water Vapor	1.87	[1.81, 1.91]	2.00	[1.89, 2.09]
Residual: Cloud(+Aerosol)	0.42	[0.34, 0.61]	0.34	[0.12, 0.64]
Total feedback	−1.18	[−1.29, −0.91]	−1.56	[−1.93, −1.17]

Table 4.4: Estimates of the total feedback and its decomposition and the confidence interval range (2.5-97.5%) calculated using a bootstrapping method.

4.5 Conclusion

In this analysis, we interpret the geoengineered SSA emissions in G4sea-salt as a forcing imposed on the SSP2-4.5 simulation and thus analyze the differences in the TOA energy imbalance between the two simulations (G4sea-salt minus SSP2-4.5) as forcing and feedback from geoengineered SSA emissions. We then compare it to a quadrupling carbon dioxide experiment (abrupt-4xCO2) applied on a pre-industrial (PI) climate.

We begin by comparing the base state for abrupt-4xCO2 and G4sea-salt. We find that hist+SSP2-4.5 contains internal variability and time-varying and increasing forcing and response in addition to interannual variability, while piControl contains interannual variability. As a result, the 2020-2070 feedback for G4sea-salt minus SSP2-4.5 exhibits less linearity between EEI and surface temperature change compared to the feedback for the first 50 years of abrupt-4xCO2 due to the presence of interannual variability and the increasing forcing and feedback present in SSP2-4.5.

The EEI decreases in response to the imposition of forcing in G4sea-salt minus SSP2-4.5, mirroring the EEI increase observed in response to a quadrupling of CO_2 in abrupt-4xCO2. This suggests that forcing and feedback can arise from tropial geoengineered SSA emission increases, making G4sea-salt minus SSP2-4.5 amenable to a forcing and feedback analysis. The forcing analysis employed herein, analogous to that in the abrupt-4xCO2 scenario, captures the aggregated effects of historical aerosol fluctuations and interannual variability on TOA radation. We conduct our analysis comparing the forcing and feedback mechanisms in G4sea-salt minus SSP2-4.5 with those in abrupt-4xCO2, while accounting for key differences between the two scenarios: 1) the sign of the forcing, 2) the spatial distribution of the forcing, 3) the nature of the forcing and 4) the base climate state. The 2020-2070 feedback for G4sea-salt minus SSP2-4.5 is 31% more negative than the feedback for the first 50 years of abrupt-4xCO2. This difference is primarily due to a more negative temperature feedback and less positive surface albedo and cloud(+aerosol) feedback in G4sea-salt minus SSP2-4.5.

The surface albedo feedback in abrupt-4xCO2 remains similar whether considered during the first 50 or full 150 years after the imposition of forcing. However, the surface albedo feedback for the first 50 years of abrupt-4xCO2 is 58% greater than that the surface albedo feedback observed in sea salt geoengineering. The reduced surface albedo feedback in G4sea-salt minus SSP2-4.5 aligns with the lower sea ice extent in the SSP2-4.5 base state, which likely limits the potential for surface albedo feedback. However, it remains unclear whether

this difference in surface albedo can be attributed solely to changes in sea ice within the G4sea-salt minus SSP2-4.5 scenario, suggesting that further investigation may be warranted. A bootstrap method shows that the confidence intervals for the surface albedo feedback, the water vapor albedo and temperature feedbacks, between G4sea-salt minus SSP2-4.5 and abrupt-4xCO2 have minimal to little overlap. This confirms that the differences in these feedbacks between the experiments are robust, detectable, and unlikely to result from sampling alone.

The difference in the cloud (+aerosol) feedback between G4sea-salt minus SSP2-4.5 and abrupt-4xCO2 is quite large (20.6%). However, the differences in the cloud(+aerosol) feedback between G4sea-salt minus SSP2-4.5 and abrupt-4xCO2 are dwarfed by the differences between cloud feedback calculated for 150 and 50 years of abrupt-4xCO2 (which is 70.73%). Thus, it is unclear how the cloud (+aerosol) feedback in G4sea-salt minus SSP2-4.5 would change if evaluated on a longer time scale. Using the bootstrap method, we find that the confidence intervals for cloud (+aerosol) feedback in G4sea-salt minus SSP2-4.5 are wide and overlap with those of abrupt-4xCO2, indicating high variability and a lack of statistically clear differences between the experiments.

A central assumption of this analysis is that subtracting SSP2-4.5 from G4sea-salt isolates the effects of geoengineered SSA emissions, disregarding potential interactions with SSP2-4.5's time-varying forcing and feedbacks. However, the nonlinearity of the EEI response arising from time-varying forcing and feedbacks complicates the attribution of simulated changes solely to tropical geoengineered SSA emissions. Despite these limitations, this study is the first to attempt to quantify and analyze feedbacks resulting from geoengineering. The findings suggest that forcings and feedbacks arise from geoengineering and thus are amenable to a forcing analysis similar to that for abrupt-4xCO2, while highlighting the need to account for the dynamic nature of the SSP2-4.5 baseline when interpreting the results. One potential approach for future research is to investigate the effects of increased tropical SSA emissions within a piControl base state, thus avoiding the confounding influence of time-

varying forcings in SSP2-4.5. However, it is essential to note that real-world geoengineering applications will likely occur in a warming climate. Therefore, alternative approaches may be needed to isolate geoengineered radiative feedbacks in a non-stationary climate.

Conclusions

This thesis investigates the processes governing sea salt aerosol (SSA) production, their representation in climate models, and the climatic consequences of regionally enhanced SSA emissions within a geoengineering framework. We begin with a theoretical framework to examine three limiting cases and compare model outputs with observations of SSA concentration to identify the physical mechanisms driving discrepancies between modeled and observed values. We then assess how the sensitivity of sea-spray generation functions to temperature and wind speed influences the geographical distribution of modeled SSA emissions and concentrations, while using aerosol optical depth (AOD) observations to validate and evaluate the performance of each formulation. Lastly, we explore the climate impacts of enhanced SSA emissions by analyzing circulation responses and radiative feedbacks resulting from regionally applied SSA geoengineering, following a GeoMIP protocol.

In Chapter 1, we develop a framework to investigate discrepancies between modeled and observed SSA concentrations by evaluating three limiting cases: (1) errors in SSA emissions, (2) errors in vertical transport, and (3) subgrid variability, sampling discrepancies, and unresolved horizontal transport. By evaluating GEOS-Chem simulations against PMEL cruise data within a simplified 1-D model framework, we examine how each mechanism contributes to the addressing the mismatch between modeled and observed SSA concentrations. While each case individually offers a plausible explanation for the model-observation discrepancies, the discrepancies are likely driven by a combination of all three explanations. In particular, the coarse spatial and temporal resolution of global models limits their ability to resolve

subgrid-scale convection and gustiness–processes that may be especially important for SSA production in warm, low-wind regimes.

We also assess the performance of the Deike et al. (2022) sea spray generation function–designed to incorporate physical processes of bubble-bursting–under the assumptions of no horizontal transport and idealized vertical mixing. Despite its physically grounded formulation, the Deike scheme does not reproduce observed SSA concentrations well under these constraints, underscoring the need to improve both emission parameterizations and transport representations in models. This chapter sets the stage for evaluating the Deike scheme alongside three other emission schemes–MartMon (a combination of Mårtensson et al. (2003) and Monahan et al. (1986)), Gong (Gong, 2003), and Jaegle (Jaeglé et al., 2011)–in Chapter 2, and highlights the importance of developing physically consistent, observation-constrained approaches for representing SSA emissions in climate models.

Building on these insights, Chapter 2 evaluates how different sea spray generation functions–and their sensitivities to SST and wind speed–affect simulated SSA emission, concentration distributions and AOD. We conduct AMIP-style simulations using the GFDL AM4 model for four formulations: MartMon, Gong, Jaegle and Deike. Notably, Deike exhibits an opposite-sign temperature dependence compared to MartMon and Jaegle. Model outputs are evaluated against three observational datasets: satellite retrievals (MODIS and MISR), ground-based measurements (AERONET), and cruise-based observations (MAN AERONET). Deike shows the highest global correlation with observations. Regionally, it performs best in matching MISR and MAN AERONET observations, particularly in the extratropics. In contrast, Gong aligns well with MODIS across the majority of the ocean basins and with AERONET sites in the Indian Ocean, while Jaegle provides the best match for tropical MAN AERONET observations. These spatially distinct performance patterns highlight the importance of using multiple observational datasets when evaluating SSA emission schemes.

However, interpretations of these results is complicated by the use of MartMon-specific model tunings applied across all simulations. A 33% increase in both fine and coarse SSA emissions–originally calibrated for MartMon–was applied to Gong and Jaegle, while no scaling was applied to Deike. This tuning likely enhances MartMon's performance and may partly explain the underestimation (e.g. negative bias) of AOD in the Deike simulation. Moreover, tuning can indirectly influence other variables such as wind speed, further confounding inter-scheme comparisons. As a result, this limits the extent to which performance differences can be attributed solely to the intrinsic properties of the emission formulations. Despite these limitations, Chapter 2 shows that the choice of SSA parameterization affects modeled AOD and its agreement with observations. However, as emphasized in Chapter 1, improving SSA emission schemes alone is insufficient. Improvements in the representation of aerosol transport, removal processes, and model tuning practices are also critical for resolving the discrepancies between models and observations.

Chapters 3 and 4 shift focus to the climatic impacts of SSA under idealized geoengineering experiments, using the G4sea-salt protocol to uniformly increase SSA emissions in the tropics. In Chapter 3, we analyze the rapid adjustments and circulation responses to this perturbation. In fixed-SST experiments, tropical SSA increases lead to stronger wind speeds and enhanced natural SSA emissions across most ocean regions. However, in the fully coupled simulations, the same intervention cools the tropics, reducing the Equator-to-midlatitude temperature gradient. This weakens the extratropical westerlies, resulting in a reduction in SSA emissions outside the injection region. Circulation-induced changes offset approximately 23% of the intended global increase in SSA emissions, with the largest reductions occurring over the Southern Hemisphere extratropics, followed by smaller decreases in the tropics and Northern Hemisphere. Wind speed changes account for the majority (68–100%) of circulation-induced emission changes, while temperature plays a secondary role, contributing less than one-third.

The coupled simulations also reveal less cooling in the eastern equatorial Pacific compared to the central and western regions, leading to a reduced east–west SST gradient–similar to the pattern observed in abrupt-4xCO2 experiments. This contrasts with regional SSA geoengineering studies, which tend to produce stronger cooling in the eastern Pacific. Changes in this temperature gradient have implications for the Walker circulation and downstream hydroclimate impacts, potentially influencing precipitation, drought, and extreme weather patterns in regions such as the western United States, South America, and Southeast Asia. Overall, Chapter 3 highlights that uniformly applied tropical SSA emission increases can trigger non-local and unintended responses in circulation and aerosol distributions. The differing outcomes between fixed-SST and coupled simulations underscore the need to account for both rapid adjustments and circulation feedbacks in assessing the impacts of SSA-based geoengineering.

Chapter 4 complements this by applying a radiative forcing and feedback framework to assess the climate response to SSA geoengineering under the G4sea-salt protocol. Using a Gregory-regression framework and radiative kernel decomposition, we isolate the feedback components associated with G4sea-salt and compare them to those from an abrupt-4xCO2 experiment. Although both scenarios involve imposed forcings, they differ in sign, spatial distribution, and base climate state. We find that the feedback structure under SSA geoengineering diverges notably from that of abrupt-4xCO2: the temperature feedback is 31% more negative and surface albedo feedback is 58% weaker–likely due to reduced sea ice in the SSP2-4.5 baseline. Despite challenges posed by variability and the non-stationary nature of SSP2-4.5, the SSA geoengineering simulations produces some detectable and robust feedback (i.e., surface albedo, water vapor and temperature feedback) signals distinct from those associated with greenhouse gas forcing. However, wide confidence intervals–especially for cloud+aerosol feedback–highlight the difficulty of isolating aerosol-induced responses in a transient climate. These findings suggest that traditional forcing–feedback paradigms may not be directly applicable to aerosol-based interventions and that future evaluations must

account for the evolving background climate and potential nonlinearities in the Earth system response.

Taken together, these chapters contribute to our understanding of both the production mechanisms and climate impacts of sea salt aerosols. Chapter 1 identifies critical physical processes–such as vertical and horizontal transport and subgrid variability–that are often misrepresented in current models and contribute to mismatches between observed and modeled SSA concentrations. These discrepancies are multi-faceted and cannot be resolved through emission adjustments alone. Chapter 2 assess how changes in SSA emission formulations affect global aerosol distributions. Physically based emission schemes like Deike show improvements in certain regions but require careful integration and tuning within complex models. Chapter 3 demonstrates that geoengineering strategies involving uniform increases in tropical SSA emissions can trigger non-local consequences, with circulation feedbacks that offset a significant portion of the intended increase in global aerosol loading. Chapter 4 reveals that radiative feedbacks from SSA geoengineering differ fundamentally from those associated with greenhouse gas forcing, highlighting the need for diagnostic tools that can account for transient climate states, spatial heterogeneity, and nonlinear responses within the Earth system.

The diagnostic and evaluative work in Chapters 1 and 2 directly informs the geoengineering experiments in Chapters 3 and 4 by identifying key uncertainties in SSA emission representation and aerosol transport. These uncertainties shape the applied forcings, the modeled circulation responses, and the diagnosed radiative feedbacks. Consequently, the climate impacts of SSA geoengineering cannot be fully understood–or reliably projected–without addressing the emission, transport, and tuning issues raised in the first half of this thesis. Together, these chapters underscore the critical need for physically grounded, observationally constrained approaches when evaluating the feasibility and implications of SSA-based climate interventions.

Future work should build on these findings by incorporating observational constraints into model tuning strategies, testing SSA emission schemes in fully coupled model configurations, and further disentangling the complex interplay between radiative forcing, circulation responses, and aerosol–cloud interactions. As emphasized in Chapters 1 and 2, improving SSA emission schemes alone is insufficient to resolve the persistent discrepancies between models and observations. Addressing these gaps requires concurrent advances in the representation of aerosol transport and removal processes, as well as careful reexamination of model tuning practices. In particular, the analysis in Chapter 2 underscores that tuning calibrated for one emission scheme–such as MartMon–can bias intercomparisons and obscure the intrinsic behavior of other formulations.

Moreover, either returning the model for each emission scheme or disabling emission-specific tunings altogether should be applied consistently across schemes to avoid confounding the evaluation of each scheme. The benefits of using consistent meteorological fields, such as through nudging to reanalysis wind data, should also be explored to reduce variability in simulated emissions and transport patterns. A similar framework applied across the suite of emission schemes evaluated in this thesis would likely yield more robust diagnostics than the current experimental design, where shifts in emissions are entangled with circulation and tuning differences.

The results presented in this chapter are based on fully coupled simulations, in which changes to the sea spray emission formulation also influence and are influenced by circulation, aerosol transport, and removal processes. This complexity limits our ability to attribute differences in SSA burden or AOD exclusively to the emission parameterization. A more constrained experimental design, such as that used by Grythe, Ström, Krejci, Quinn, and Stohl (2014), would offer a complementary perspective. Grythe's study used a Lagrangian trajectory model with analyzed wind fields to isolate the performance of different emission schemes, and found that the Jaeglé et al. (2011) scheme outperformed Gong (2003), in line with some of our findings. Future work could apply a similar offline or nudged modeling

approach to the full suite of emission schemes considered here to more clearly disentangle the role of the emission parameterization from that of the broader model environment.

Given the increasing interest in marine cloud brightening for climate intervention, it is essential that modeling frameworks and analyses move beyond idealized representations and account for the full spectrum of dynamic, radiative, and microphysical feedbacks associated with SSA. Such efforts will be critical for assessing the feasibility, effectiveness, and risks of using SSA-based geoengineering as a component of future climate strategies.

Appendix A

Integrating density flux

Here we calculate the mass density flux of a production flux $\frac{dF_{\mathrm{X}}}{dr_{80}}$. We start by assuming that SSA particles are spherical and convert from droplet to mass density flux by multiplying by density (ρ_{SSA}) and volume ($\frac{4}{3}\pi r^3$). Doing so yields:

$$\frac{dF_{\mathrm{mass}}}{dr_{80}} = \frac{dF_{\mathrm{X}}}{dr_{80}} * [\frac{4}{3}\pi r^3 \rho_{SSA}] \tag{A.1}$$

This now gives us the mass density flux of the production flux X, which is in units of kg m^{-2} s^{-1}. For dry particles, we assume a density (ρ_{SSA}) of 2200 kg m^{-3} (2.2e-15 kg $\mu\mathrm{m}^{-3}$), which is the density of pure NaCl (Hess et al., 1998). To obtain SSA emission, we integrate the particle number flux (Eq. A.1) across the particle range [r_1, r_2] of each cruise observation to recover:

$$F_{\mathrm{mass}} = \frac{4}{3}\pi\rho_{\mathrm{SSA}} \int_{r_1}^{r_2} \frac{dF_0}{dr_{80}} r^3 dr \tag{A.2}$$

We approximate the integration of Eq. A.2 by using the quadrature midpoint method and assume equally spaced quadrature intervals. We construct a rectangle for every subinterval and evaluate the function at the midpoint of the subinterval. This results in the equation:

$$\int_{r_1}^{r_2} \frac{dF_{\mathrm{mass}}}{dr_{80}} dr = (r_{\max} - r_{\min}) \sum F_{\mathrm{mass}}(\frac{r_1 + r_2}{2}) \tag{A.3}$$

where the quadrature point $((r_2 + r_1)/2)$ is the midpoint of $[r_1, r_2]$. The interval $[r_1, r_2]$ is a finite interval, while the interval $[r_{\min}, r_{\max}]$ refers to the overall range of the particle radius size measured for the PMEL cruise.

Integrating the density flux to get the emission flux requires careful consideration of the aerosol size distribution. Applying a sensitivity test, we assess what resolution of particle radius size will not compromise the accuracy of the model results while minimizing the computational run time. Since we are conducting manual calculations, we use the finest resolution appropriate for the radius size distribution ($\Delta r = 0.0001$ μm). This method is applied for the four emission configurations to calculate the emission for the PMEL cruises.

Appendix B

Calculations for global and regional averages

For SSA, e refers to local emissions (kg/m^2/s) while $\overline{E}$ refers to area averaged SSA emissions (kg/m^2/s). Meanwhile $\langle E \rangle$ refers to area-integrated SSA emissions (kg/s). X refers to SSA mixing ratio (kg(salt)/kg(air)). b refers to the vertically integrated SSA concentration (kg/m^2) and B refers to the SSA mass (burden) (kg). SSA emissions vary in space (i,j) where i (ψ) = latitude and j (λ) = longitude. SSA concentration vary in space (i,j,k).

B.1 Geoengineered ocean-averaged SSA emission

In the G4sea-salt protocol, the emission of submicron SSA is increased by 7.66×10^{-11} kg m^{-2} s^{-1} (constant in time) for each of the first two bin sizes in each marine grid cell in the tropics (30°S to 30°N). Therefore the geoengineered emission averaged over all tropical marine grid cells is:

$$\overline{E}_{\text{geoeng,tropics,ocean}} = 7.66 \times 10^{-11} \times 2 = 1.53 \times 10^{-10} \text{ kg m}^{-2} \text{ s}^{-1}$$

B.1.1 Geoengineered global averaged SSA emission

The area of the globe (A_{global}) is $5.1{\times}10^{14}$ m^2 and is calculated as 4πr^2. The fractional area of the tropics is 0.5 of the total area of the globe. Lastly, using the ocean mask (fractional amount of land) output from the model, we calculate the fractional area of the ocean in the tropics which is 0.744. Thus the area of the tropics ($A_{\text{tropics,marine}}$) is calculated as $5.1{\times}10^{14}$ m$^2 \times 4\pi r^2 \times 0.5$.

$$\begin{aligned}
\overline{E}_{\text{geoeng,global,ocean}} &= \frac{7.66 \times 10^{-11} \times 2 \times A_{\text{tropics,marine}}}{A_{\text{global}}} \\
&= \frac{7.66 \times 10^{-11} \times 2 \times 5.1 \times 10^{14} \times 0.5 \times 0.744}{5.1 \times 10^{14}} \\
&= 7.66 \times 10^{-11} \times 2 \times 0.5 \times 0.744 \\
&= 5.70 \times 10^{-11} \text{ kg m}^{-2} \text{ s}^{-1}
\end{aligned}$$

B.1.2 Geoengineered SSA emissions averaged over the global oceans

Now, we calculate the geoengineered emissions ocean-averaged over the globe using the geoengineered ocean-averaged emission in the tropical ocean, the NH ocean and the SH ocean. The geoengineered ocean-averaged emission in the NH and SH ocean is zero, so the expression simplifies to:

$$\overline{E}_{\text{geoeng,global,ocean}} = \left(\overline{E}_{\text{geoeng,tropics,ocean}} \cdot \frac{A_{\text{tropics,ocean}}}{A_{\text{global,ocean}}} \right)$$

Using the ocean mask (fractional amount of land) output from the model, we calculate the ratio of $A_{\text{tropics,ocean}}/A_{\text{global,ocean}}$ which is (0.5×0.744)/0.708.

$$\begin{aligned}\overline{E}_{\text{geoeng,global,ocean}} &= \left(1.53 \times 10^{-10} \times \frac{0.744 \times 0.5}{0.708}\right) \\ &= 8.05 \times 10^{-11} \text{ kg m}^{-2} \text{ s}^{-1}\end{aligned}$$

B.2 Globally and regionally averaged SSA emissions (land+ocean)

We calculate global and regionally averaged SSA emissions over land and ocean in this section. However, it is important to note that SSA emissions are naturally zero over land.

B.2.1 Global averaged SSA emission

For the global average, the bounds are $\psi = [-\frac{\pi}{2}, \frac{\pi}{2}]$ and $\lambda = [0, 2\pi]$. The equation for the globally averaged emissions is:

$$\begin{aligned}\overline{E}_{\text{global}} &= \frac{1}{2\pi r^2(\sin(\frac{\pi}{2}) - \sin(-\frac{\pi}{2}))} \int_0^{2\pi} \int_{-\frac{\pi}{2}}^{\frac{\pi}{2}} e(\psi, \lambda) \cdot r^2 \cos(\psi) d\psi d\lambda \\ &= \frac{1}{4\pi r^2} \int_0^{2\pi} \int_{-\frac{\pi}{2}}^{\frac{\pi}{2}} e(\psi, \lambda) \cdot r^2 \cos(\psi) d\psi d\lambda \\ &= \frac{1}{4\pi} \int_0^{2\pi} \int_{-\frac{\pi}{2}}^{\frac{\pi}{2}} e(\psi, \lambda) \cdot \cos(\psi) d\psi d\lambda\end{aligned}$$

The discrete form of this is:

$$\overline{E}_{\text{global}} = \frac{1}{4\pi} \sum_{0}^{2\pi} \sum_{-\frac{\pi}{2}}^{\frac{\pi}{2}} e(\psi, \lambda) \cdot \cos(\psi) \Delta\psi \Delta\lambda$$

For the model outputs, the indexes in the 1° lat x 1.25° model output ranges from i = [0:nlat-1], where nlat is the total number of latitude points (180) and j =[0:nlon-1], where

nlon is the total number of longitude points (288). The discrete form becomes:

$$\begin{aligned}\overline{E}_{\text{global}} &= \frac{1}{4\pi}\sum_{j=0}^{nlon-1}\sum_{i=0}^{nlat-1} e(i,j)\cdot\cos(\psi_{i,j})\Delta\psi_{i,j}\Delta\lambda_{i,j} \\ &= \frac{\pi}{2\cdot nlon\cdot nlat}\sum_{j=0}^{nlon-1}\sum_{i=0}^{nlat-1} e(i,j)\cdot\cos(\psi_{i,j})\end{aligned}$$

Where $\psi_{i,j}$ refers to the radian form of latitude, $\Delta\lambda_{i,j} = \frac{2\pi}{nlon}$ and $\Delta\psi_{i,j} = \frac{\pi}{nlat}$ and $\frac{2\pi^2}{4\pi}$ simplifies to $\frac{\pi}{2}$.

B.2.2 Tropical average SSA emission

For averaging SSA emissions over the tropics, the bounds are $\psi = [-\frac{\pi}{6},\frac{\pi}{6}]$ and $\lambda = [0,2\pi]$. The equation for the tropical average SSA emissions is:

$$\begin{aligned}\overline{E}_{\text{tropics}} &= \frac{1}{2\pi r^2(\sin(\frac{\pi}{6})-\sin(-\frac{\pi}{6}))}\int_0^{2\pi}\int_{-\frac{\pi}{6}}^{\frac{\pi}{6}} e(\psi,\lambda)\cdot r^2\cos(\psi)d\psi d\lambda \\ &= \frac{1}{2\pi r^2}\int_0^{2\pi}\int_{-\frac{\pi}{6}}^{\frac{\pi}{6}} e(\psi,\lambda)\cdot r^2\cos(\psi)d\psi d\lambda \\ &= \frac{1}{2\pi}\int_0^{2\pi}\int_{-\frac{\pi}{6}}^{\frac{\pi}{6}} e(\psi,\lambda)\cdot\cos(\psi)d\psi d\lambda\end{aligned}$$

The discrete form of this is:

$$\overline{E}_{\text{tropics}} = \frac{1}{2\pi}\sum_{0}^{2\pi}\sum_{-\frac{\pi}{6}}^{\frac{\pi}{6}} e(\psi,\lambda)\cdot\cos(\psi)\Delta\psi\Delta\lambda$$

For model outputs, the indexes in the model output ranges from i = [60:119] and j = [0:nlon-1], where nlon is 288. The discrete form becomes

$$\overline{E}_{\text{tropics}}(i,j) = \frac{1}{2\pi} \sum_{j=0}^{nlon-1} \sum_{i=60}^{119} e(i,j) \cdot \cos(\psi_{i,j}) \Delta\psi_{i,j} \Delta\lambda_{i,j}$$
$$= \frac{\pi}{nlat \cdot nlon} \sum_{j=0}^{nlon-1} \sum_{i=60}^{119} e(i,j) \cdot \cos(\psi_{i,j})$$

Where $\psi_{i,j}$ refers to the radian form of latitude, $\Delta\lambda_{i,j} = \frac{2\pi}{nlon}$ and $\Delta\psi_{i,j} = \frac{\pi}{nlat}$ and $\frac{2\pi^2}{2\pi}$ simplifies to π. The bounds of the summation change, but the grid spacing for $\Delta\psi_{i,j}$ remains consistent and depends on the resolution of the model grid.

B.2.3 NH extratropics average SSA emission

For averaging SSA emissions over the NH, the bounds are $\psi = [\frac{\pi}{6}, \frac{\pi}{2}]$ and $\lambda = [0, 2\pi]$. The equation for the NH average SSA emissions is:

$$\overline{E}_{\text{NH}} = \frac{1}{2\pi r^2(\sin(\frac{\pi}{2}) - \sin(\frac{\pi}{6}))} \int_0^{2\pi} \int_{\frac{\pi}{6}}^{\frac{\pi}{2}} e(\psi,\lambda) \cdot r^2 \cos(\psi) d\psi d\lambda$$
$$= \frac{1}{\pi r^2} \int_0^{2\pi} \int_{\frac{\pi}{6}}^{\frac{\pi}{2}} e(\psi,\lambda) \cdot r^2 \cos(\psi) d\psi d\lambda$$
$$= \frac{1}{\pi} \int_0^{2\pi} \int_{\frac{\pi}{6}}^{\frac{\pi}{2}} e(\psi,\lambda) \cdot \cos(\psi) d\psi d\lambda$$

The discrete form for this is:

$$\overline{E}_{\text{NH}} = \frac{1}{\pi} \sum_{0}^{2\pi} \sum_{\frac{\pi}{6}}^{\frac{\pi}{2}} e(\psi,\lambda) \cdot \cos(\psi) \Delta\psi \Delta\lambda$$

For model outputs, the indexes in the model output ranges from i = [120:179] and j = [0:nlon-1], where nlon is 288. The discrete form becomes:

$$\begin{aligned}\overline{E}_{\mathrm{NH}}(i,j) &= \frac{1}{\pi}\sum_{j=0}^{nlon-1}\sum_{i=120}^{179} e(i,j)\cdot\cos(\psi_{i,j})\Delta\psi_{i,j}\Delta\lambda_{i,j} \\ &= \frac{2\pi}{nlat\cdot nlon}\sum_{j=0}^{nlon-1}\sum_{i=120}^{nlat-1} e(i,j)\cdot\cos(\psi_{i,j})\end{aligned}$$

Where $\psi_{i,j}$ refers to the radian form of latitude, $\Delta\lambda_{i,j} = \frac{2\pi}{nlon}$ and $\Delta\psi_{i,j} = \frac{\pi}{nlat}$.

B.2.4 SH extratropics average SSA emission

For averaging SSA emissions over the SH, the bounds are $\psi = [-\frac{\pi}{2}, -\frac{\pi}{6}]$ and $\lambda = [0, 2\pi]$. The equation for the SH average SSA emissions is:

$$\begin{aligned}\overline{E}_{\mathrm{SH}} &= \frac{1}{2\pi r^2(\sin(-\frac{\pi}{6}) - \sin(-\frac{\pi}{2}))}\int_0^{2\pi}\int_{-\frac{\pi}{2}}^{-\frac{\pi}{6}} e(\psi,\lambda)\cdot r^2\cos(\psi)d\psi d\lambda \\ &= \frac{1}{\pi r^2}\int_0^{2\pi}\int_{-\frac{\pi}{2}}^{-\frac{\pi}{6}} e(\psi,\lambda)\cdot r^2\cos(\psi)d\psi d\lambda \\ &= \frac{1}{\pi}\int_0^{2\pi}\int_{-\frac{\pi}{2}}^{-\frac{\pi}{6}} e(\psi,\lambda)\cdot\cos(\psi)d\psi d\lambda\end{aligned}$$

The discrete form for this is:

$$\overline{E}_{\mathrm{SH}} = \frac{1}{\pi}\sum_{0}^{2\pi}\sum_{-\frac{\pi}{2}}^{-\frac{\pi}{6}} e(\psi,\lambda)\cdot\cos(\psi)\Delta\psi\Delta\lambda$$

For model outputs, the indexes in the model output ranges from i = [0:59] and j = [0:nlon-1], where nlon is 288. The discrete form becomes:

$$\begin{aligned}\overline{E}_{\mathrm{SH}}(i,j) &= \frac{1}{\pi}\sum_{j=1}^{nlon-1}\sum_{i=0}^{59} e(i,j)\cdot\cos(\psi_{i,j})\Delta\psi_{i,j}\Delta\lambda_{i,j} \\ &= \frac{2\pi}{nlat\cdot nlon}\sum_{j=1}^{nlon-1}\sum_{i=0}^{59} e(i,j)\cdot\cos(\psi_{i,j})\end{aligned}$$

Where $\psi_{i,j}$ refers to the radian form of latitude, $\Delta\lambda_{i,j} = \frac{2\pi}{nlon}$ and $\Delta\psi_{i,j} = \frac{\pi}{nlat}$.

B.2.5 Globally averaged SSA emission from regional components

The globally averaged SSA emission is just the sum of the regional averages multiplied by the ratio of the area of the region over the global area:

$$\overline{E}_{\mathrm{global}} = \left(\overline{E}_{\mathrm{tropics}}\cdot\frac{A_{\mathrm{tropics}}}{A_{\mathrm{global}}}\right) + \left(\overline{E}_{\mathrm{NH}}\cdot\frac{A_{\mathrm{NH}}}{A_{\mathrm{global}}}\right) + \left(\overline{E}_{\mathrm{SH}}\cdot\frac{A_{\mathrm{SH}}}{A_{\mathrm{global}}}\right)$$

where:

$$\begin{aligned}\frac{A_{\mathrm{tropics}}}{A_{\mathrm{global}}} &= \frac{2\pi r^2(\sin(\frac{\pi}{6}) - \sin(-\frac{\pi}{6}))}{4\pi r^2} = 0.5 \\ \frac{A_{\mathrm{NH}}}{A_{\mathrm{global}}} &= \frac{2\pi r^2(\sin(-\frac{\pi}{6}) - \sin(-\frac{\pi}{2}))}{4\pi r^2} = 0.25 \\ \frac{A_{\mathrm{SH}}}{A_{\mathrm{global}}} &= \frac{2\pi r^2(\sin(\frac{\pi}{2}) - \sin(\frac{\pi}{6}))}{4\pi r^2} = 0.25\end{aligned}$$

B.3 Globally and regionally averaged SSA emissions (ocean-only)

Prepare the land-sea mask ($M_{\psi,\lambda}$) where the ocean values have a value of 1 and the land cells have a value of 0. For grid boxes between 0 and 1, grid boxes that are less than 0.5 are rounded down to the nearest digit and grid boxes that are greater than 0.5 are rounded up

to the nearest digit. This is consistent with how sea salt emissions are increased over marine grid cells in G4sea-salt. Note that emissions (e) are zero over land and thus do not require application of the land-sea mask. However, calculations involving properties with nonzero land values will require multiplying the properties by the land-sea mask.

B.3.1 Global ocean-averaged SSA emission

The ocean-only global average is the weighted sum divided by the total area of the global ocean.

$$\overline{E}_{\text{global,ocean}} = \frac{1}{A_{\text{global,ocean}}} \int_0^{2\pi} \int_{-\frac{\pi}{2}}^{\frac{\pi}{2}} e(\psi, \lambda) \cdot r^2 \cos(\psi) d\psi d\lambda$$

Calculate the total global ocean area ($A_{\text{global,ocean}}$) using the mask and the area weight for each grid cell based on its latitude.

$$\begin{aligned} A_{\text{global,ocean}} &= \int_0^{2\pi} \int_{-\frac{\pi}{2}}^{\frac{\pi}{2}} M_{\psi,\lambda} \cdot r^2 \cos(\psi) d\psi d\lambda \\ &= r^2 \int_0^{2\pi} \int_{-\frac{\pi}{2}}^{\frac{\pi}{2}} M_{\psi,\lambda} \cdot \cos(\psi) d\psi d\lambda \end{aligned}$$

The ocean-only global average simplifies to:

$$\overline{E}_{\text{global,ocean}} = \frac{1}{\int_0^{2\pi} \int_{-\frac{\pi}{2}}^{\frac{\pi}{2}} M_{\psi,\lambda} \cdot \cos(\psi) d\psi d\lambda} \int_0^{2\pi} \int_{-\frac{\pi}{2}}^{\frac{\pi}{2}} e(\psi, \lambda) \cdot \cos(\psi) d\psi d\lambda$$

For the model outputs, the indexes in the model output ranges from i = [0:nlat-1], where nlat is the total number of latitude points (180) and j =[0:nlon-1], where nlon is the total number of longitude points (288). The discrete form becomes:

$$\begin{aligned} \overline{E}_{\text{global,ocean}} &= \frac{\sum_{j=0}^{nlon-1} \sum_{i=0}^{nlat-1} e(i,j) \cdot \cos(\psi_i) \Delta\psi_{i,j} \Delta\lambda_j}{\sum_{j=0}^{nlon-1} \sum_{i=0}^{nlat-1} M_{i,j} \cdot \cos(\psi_i) \Delta\psi_{i,j} \Delta\lambda_j} \\ &= \frac{\sum_{j=0}^{nlon-1} \sum_{i=0}^{nlat-1} e(i,j) \cdot \cos(\psi_i)}{\sum_{j=0}^{nlon-1} \sum_{i=0}^{nlat-1} M_{i,j} \cdot \cos(\psi_i)} \end{aligned}$$

We next calculate the fractional area of the global ocean to the global surface area of the Earth:

$$\begin{aligned}\frac{A_{\text{global,ocean}}}{A_{\text{global}}} &= \frac{\sum_{j=0}^{nlon-1}\sum_{i=0}^{nlat-1} M_{i,j}\cdot\cos(\psi_i)}{nlon\sum_{i=0}^{nlat-1}\cos(\psi_i)} \\ &= \frac{23369.53}{33002.787} \\ &= 0.708\end{aligned}$$

B.3.2 Ocean-averaged SSA emissions over the tropics

The ocean-only tropical average is the weighted sum divided by the total area of the ocean in the tropics.

$$\overline{E}_{\text{tropics,ocean}} = \frac{1}{A_{\text{tropics,ocean}}}\int_0^{2\pi}\int_{-\frac{\pi}{6}}^{\frac{\pi}{6}} e(\psi,\lambda)\cdot r^2\cos(\psi)d\psi d\lambda$$

Calculate the ocean area in the tropics ($A_{\text{tropics,ocean}}$) using the land-sea mask and the area weight for each grid cell based on its latitude.

$$A_{\text{tropics,ocean}} = \int_0^{2\pi}\int_{-\frac{\pi}{6}}^{\frac{\pi}{6}} M_{\psi,\lambda}\cdot r^2\cos(\psi)d\psi d\lambda$$

The ocean-only average in the tropics simplifies to:

$$\overline{E}_{\text{tropics,ocean}} = \frac{1}{\int_0^{2\pi}\int_{-\frac{\pi}{6}}^{\frac{\pi}{6}} M_{\psi,\lambda}\cdot\cos(\psi)d\psi d\lambda}\int_0^{2\pi}\int_{-\frac{\pi}{6}}^{\frac{\pi}{6}} e(\psi,\lambda)\cdot\cos(\psi)d\psi d\lambda$$

The discrete form is:

$$\begin{aligned}\overline{E}_{\text{tropics,ocean}} &= \frac{\sum_{j=0}^{nlon-1}\sum_{i=60}^{119} e(i,j)\cdot\cos(\psi_i)\Delta\psi_i\Delta\lambda_j}{\sum_{j=0}^{nlon-1}\sum_{i=60}^{119} M_{i,j}\cdot\cos(\psi_i)\Delta\psi_i\Delta\lambda_j} \\ &= \frac{\sum_{j=0}^{nlon-1}\sum_{i=60}^{119} e(i,j)\cdot\cos(\psi_i)}{\sum_{j=0}^{nlon-1}\sum_{i=60}^{119} M_{i,j}\cdot\cos(\psi_i)}\end{aligned}$$

We calculate the fractional area of the tropics that is ocean relative to the global area:

$$\begin{aligned}\frac{A_{\text{tropics,ocean}}}{A_{\text{tropics}}} &= \frac{\sum_{j=0}^{nlon-1}\sum_{i=60}^{119} M_{i,j}\cdot\cos(\psi_i)}{nlon\sum_{i=60}^{119}\cos(\psi_i)} \\ &= \frac{12280}{16501} \\ &= 0.744\end{aligned}$$

B.3.3 Ocean-only averaged SSA emissions over the NH extratropics

The ocean-only average in the NH is the weighted sum divided by the total area of the ocean in the NH.

$$\overline{E}_{\text{NH, ocean}} = \frac{1}{A_{\text{NH,ocean}}}\int_0^{2\pi}\int_{\frac{\pi}{6}}^{\frac{\pi}{2}} e(\psi,\lambda)\cdot r^2\cos(\psi)d\psi d\lambda$$

Calculate the ocean area in the NH ($A_{\text{NH,ocean}}$) using the land-sea mask and the area weight for each grid cell based on its latitude.

$$A_{\text{NH,ocean}} = \int_0^{2\pi}\int_{\frac{\pi}{6}}^{\frac{\pi}{2}} M_{\psi,\lambda}\cdot r^2\cos(\psi)d\psi d\lambda$$

The ocean-only average in the NH simplifies to:

$$\overline{E}_{\text{NH, ocean}} = \frac{1}{\int_0^{2\pi}\int_{\frac{\pi}{6}}^{\frac{\pi}{2}} M_{\psi,\lambda}\cdot\cos(\psi)d\psi d\lambda}\int_0^{2\pi}\int_{\frac{\pi}{6}}^{\frac{\pi}{2}} e(\psi,\lambda)\cdot\cos(\psi)d\psi d\lambda$$

The discrete form is:

$$\begin{aligned}\overline{E}_{\text{NH, ocean}} &= \frac{\sum_{j=0}^{nlon-1}\sum_{i=120}^{nlat-1} e(i,j)\cdot\cos(\psi_i)\Delta\psi_i\Delta\lambda_j}{\sum_{j=0}^{nlon-1}\sum_{i=120}^{nlat-1} M_{i,j}\cdot\cos(\psi_i)\Delta\psi_i\Delta\lambda_j} \\ &= \frac{\sum_{j=0}^{nlon-1}\sum_{i=120}^{nlat-1} e(i,j)\cdot\cos(\psi_i)}{\sum_{j=0}^{nlon-1}\sum_{i=120}^{nlat-1} M_{i,j}\cdot\cos(\psi_i)}\end{aligned}$$

We next calculate the fractional area of the NH that is ocean:

$$\begin{aligned}\frac{A_{\text{NH,ocean}}}{A_{\text{NH}}} &= \frac{\sum_{j=0}^{nlon-1}\sum_{i=120}^{nlat-1} M(i,j)\cdot\cos(\psi_i)}{nlon\sum_{i=120}^{nlat-1}\cos(\psi_i)} \\ &= \frac{4075.83}{8250.69} \\ &= 0.494\end{aligned}$$

B.3.4 Ocean-only averaged SSA emissions over the SH extratropics

The ocean-only average in the SH is the weighted sum divided by the total area of the ocean in the SH.

$$\overline{E}_{\text{SH,ocean}} = \frac{1}{A_{\text{SH,ocean}}}\int_0^{2\pi}\int_{-\frac{\pi}{2}}^{-\frac{\pi}{6}} e(\psi,\lambda)\cdot r^2\cos(\psi)d\psi d\lambda$$

Calculate the ocean area in the SH ($A_{\text{SH,ocean}}$) using the land-sea mask and the area weight for each grid cell based on its latitude.

$$A_{\text{SH,ocean}} = \int_0^{2\pi}\int_{-\frac{\pi}{2}}^{-\frac{\pi}{6}} M_{\psi,\lambda}\cdot r^2\cos(\psi)d\psi d\lambda$$

The ocean-only average in the SH simplifies to:

$$\overline{E}_{\text{SH,ocean}} = \frac{1}{\int_0^{2\pi}\int_{-\frac{\pi}{2}}^{-\frac{\pi}{6}} M_{\psi,\lambda}\cdot\cos(\psi)d\psi d\lambda}\int_0^{2\pi}\int_{-\frac{\pi}{2}}^{-\frac{\pi}{6}} e(\psi,\lambda)\cdot\cos(\psi)d\psi d\lambda$$

The discrete form is:

$$\begin{aligned}\overline{E}_{\text{SH,ocean}} &= \frac{\sum_{j=1}^{nlon-1}\sum_{i=0}^{59} e(i,j)\cdot\cos(\psi_i)\Delta\psi_i\Delta\lambda_j}{\sum_{j=1}^{nlon-1}\sum_{i=0}^{59} M_{i,j}\cdot\cos(\psi_i)\Delta\psi_i\Delta\lambda_j} \\ &= \frac{\sum_{j=1}^{nlon-1}\sum_{i=0}^{59} e(i,j)\cdot\cos(\psi_i)}{\sum_{j=1}^{nlon-1}\sum_{i=0}^{59} M_{i,j}\cdot\cos(\psi_i)}\end{aligned}$$

We calculate the fractional area of the SH that is ocean:

$$\begin{aligned}\frac{A_{\mathrm{SH,ocean}}}{A_{\mathrm{SH}}} &= \frac{\sum_{j=1}^{nlon-1}\sum_{i=0}^{59} M(i,j)\cdot\cos(\psi_i)}{nlon\sum_{i=0}^{59}\cos(\psi_i)} \\ &= \frac{7012.742}{8250.69} \\ &= 0.849\end{aligned}$$

B.3.5 Global ocean-averaged SSA emission using the regional ocean-averages

Ocean-only global emissions is the sum of the regional ocean-averages multiplied by the ratio of the regions respective ocean-only fractional area to the total global ocean area:

$$\begin{aligned}\overline{E}_{\mathrm{global,ocean}} = \left(\overline{E}_{\mathrm{tropics,ocean}}\cdot\frac{A_{\mathrm{tropics,ocean}}}{A_{\mathrm{global,ocean}}}\right) + \left(\overline{E}_{\mathrm{NH,ocean}}\cdot\frac{A_{\mathrm{NH,ocean}}}{A_{\mathrm{global,ocean}}}\right) \\ + \left(\overline{E}_{\mathrm{SH,ocean}}\cdot\frac{A_{\mathrm{SH,ocean}}}{A_{\mathrm{global,ocean}}}\right)\end{aligned}$$

B.4 Converting from ocean-averaged to ocean-integrated values

Ocean-averaged values (i.e., emission, wind speed, and SST) refer to the average value for each marine grid cell globally and regionally; thus amount per unit of ocean area. For instance ocean-averaged emission values will have units of kg m^{-2} s^{-1}. Ocean-integrated values refers to the total accumulated emissions for a region. For instance, ocean-integrated emissions will have units of kg s^{-1}.

To retrieve the ocean-integrated values from the ocean-averaged values, simply multiply the ocean-averaged values by the ocean area of the region. For example, let us calculate the area-integrated geoengineered emission, over areas where applied (marine tropics).

Recall that the ocean-averaged geoengineered emissions ($\overline{E}_{\text{geoeng,tropics,ocean}}$) over the marine tropics is given in Appendix B.1 as 1.53×10^{-10} kg m^{-2} s^{-1}. The area-integrated geoengineered emissions ($\langle E_{\text{geoeng,tropics,ocean}} \rangle$) is written as:

$$\langle E_{\text{geoeng,tropics,ocean}} \rangle = \overline{E}_{\text{geoeng,tropics,ocean}} \times A_{\text{tropics,ocean}}$$

where

$$\begin{aligned} A_{\text{tropics,ocean}} &= \text{area of globe} \times \text{frac area of tropics} \times \text{frac area of ocean in tropics} \\ &= 5.1 \times 10^{14} \times 0.5 \times 0.744 \\ &= 1.90 \times 10^{14} \end{aligned}$$

B.5 Circulation-induced changes in SSA emission

Circulation-induced changes in SSA emissions are calculated by taking the difference between the prescribed amount of geoengineered SSA emissions in the tropics and the actual increase in the coupled model simulations (G4sea-salt minus SSP2-4.5), as shown in Table 3.3.

B.5.1 Circulation-induced changes in ocean-integrated SSA emission

For the global oceans, the circulation-induced changes in ocean-integrated SSA emission is calculated by taking the difference in the geoengineered ocean-integrated SSA emission and the G4sea-salt minus SSP2-4.5 ocean-integrated SSA emission. The computation is as follows:

$$\underbrace{2.24 \times 10^4}_{\substack{\text{G4sea-salt minus SSP2-4.5} \\ \text{ocean-integrated SSA emission}}} - \underbrace{2.91 \times 10^4}_{\substack{\text{geoengineered} \\ \text{ocean-integrated SSA emission}}} = -6.79 \times 10^3 \text{ kg s}^{-1} \qquad \text{(B.1)}$$

B.5.2 Circulation-induced changes in ocean-averaged SSA emission

For the global oceans, the circulation-induced changes in ocean-averaged SSA emission is calculated by taking the difference in the geoengineered ocean-averaged SSA emission and the G4sea-salt minus SSP2-4.5 ocean-averaged SSA emission. The computation is as follows:

$$\underbrace{6.17 \times 10^{-11}}_{\substack{\text{G4sea-salt minus SSP2-4.5} \\ \text{ocean-averaged SSA emission}}} - \underbrace{8.05 \times 10^{-11}}_{\substack{\text{geoengineered} \\ \text{ocean-averaged SSA emission}}} = -1.88 \times 10^{-11} \text{ kg m}^2 \text{ s}^{-1} \tag{B.2}$$

Appendix C

The sensitivity of MartMon emissions

Within the standard AM4 configuration, Mårtensson et al. (2003) is applied to particles with radii less than 1.4 μm, whereas Monahan et al. (1986) is applied to particles with radii greater than 1.4 μm.

The functional form of Mårtensson et al. (2003) can be written as:

$$E_{\text{Mart}} = f_1(\text{U}) \times g(\text{SST}) \tag{C.1}$$

where g(SST) refers to the functional temperature dependency (see Chapter 1 for more details) and f_1(U) refers to the area covered by the white cap presented as a function of wind speed (m/s). g(SST) and f_1(U) are functions independent of each other.

Separately, the functional form of Monahan et al. (1986) can be written as

$$E_{\text{Mon}} = f_2(\text{U}) \tag{C.2}$$

where f_2(U) refers to the functional dependence on the wind speed in Monahan et al. (1986).

However, the dependence of wind speed on emissions present in both f_1(U) and f_2(U) are differentiated by their particle size-dependent coefficient and share the form of wind speed

dependency calculated as $U^{3.41}$, and so the relationship between $f_1(U)$ and $f_2(U)$ can be written as:

$$\alpha \times f_1(U) = f_2(U) \tag{C.3}$$

where α is a coefficient that is size-dependent and nonchanging.

As a result, MartMon can be written as a combination of E_{Mon} and E_{Mart}, hereafter E_{MM}:

$$E_{\text{MM}} = E_{\text{Mon}} + E_{\text{Mart}} \tag{C.4}$$

$$= f_1(U) \times g(\text{SST}) + \underbrace{f_2(U)}_{\alpha \times f_1(U)} \tag{C.5}$$

$$= f_1(U) \times g(\text{SST}) + \alpha \times f_1(U) \tag{C.6}$$

$$= \big(g(\text{SST}) + \alpha\big) \times f_1(U) \tag{C.7}$$

C.1 Temperature sensitivity

Taking Eq. C.7, we calculate the derivative of E_{MM} with respect to SST that corresponds to the rate of change of the functional temperature dependence multiplied by the functional wind speed dependency.

$$\frac{\partial E_{\text{MM}}}{\partial \text{SST}} = f_1(U) \frac{\partial g}{\partial \text{SST}} \tag{C.8}$$

This is what is presented in Figure 3.3a and shows that the functional dependence of the wind speed dominates $\frac{\partial E_{\text{MM}}}{\partial \text{SST}}$.

Next, we normalize $\frac{\partial E_{\text{MM}}}{\partial \text{SST}}$ by the emission E_{MM} to get the following:

$$\frac{1}{E_{\text{MM}}} \frac{\partial E_{\text{MM}}}{\partial \text{SST}} = \frac{f_1(U)}{(g(\text{SST}) + \alpha) \times f_1(U)} \tag{C.9}$$

$$= \frac{\partial g}{\partial \text{SST}} \times \frac{1}{g(\text{SST}) + \alpha} \tag{C.10}$$

We see that normalizing the derivative of MartMon emissions with respect to the SST by the emission yields Eq. C.10 where the function for wind speed cancels out, and we are left with just the function for temperature dependence. Figure 3.3c shows $\frac{1}{E_{\mathrm{MM}}}\frac{\partial E_{\mathrm{MM}}}{\partial \mathrm{SST}} \times 100$.

C.2 Wind speed sensitivity

Taking Eq. C.7, we calculate the derivative of E_{MM} with respect to wind speed (U) as follows:

$$\frac{\partial E_{\mathrm{MM}}}{\partial \mathrm{U}} = g(\mathrm{SST})\frac{\partial f_1}{\partial \mathrm{U}} + \frac{\partial f_2}{\partial \mathrm{U}} \tag{C.11}$$

$$= \frac{\partial f_1}{\partial \mathrm{U}} \times \big(g(\mathrm{SST}) + \alpha\big) \tag{C.12}$$

This is what is presented in Figure 3.3b and shows that the functional dependences for temperature and wind speed are present there in $\frac{\partial E_{\mathrm{MM}}}{\partial \mathrm{U}}$.

We normalize $\frac{\partial E_{\mathrm{MM}}}{\partial \mathrm{U}}$ by the emission E_{MM} to get the following:

$$\frac{1}{E_{\mathrm{MM}}}\frac{\partial E_{\mathrm{MM}}}{\partial \mathrm{U}} = \left[\frac{\partial f_1}{\partial \mathrm{U}} \times \big(g(\mathrm{SST}) + \alpha\big)\right] \times \frac{1}{g(\mathrm{SST}) + \alpha) \times f_1(\mathrm{U})} \tag{C.13}$$

$$= \frac{\partial f_1}{\partial \mathrm{U}} \times \frac{1}{f_1(\mathrm{U})} \tag{C.14}$$

Normalizing the derivative of MartMon emissions with respect to wind speed by the emission yields Eq. C.14 where the function for SST cancels out, leaving only the function for the wind speed dependency. The % form of $\frac{1}{E_{\mathrm{MM}}}\frac{\partial E_{\mathrm{MM}}}{\partial \mathrm{U}}$ is shown in Fig. 3.3d.

Appendix D

Calculating components of the total feedback

To further analyze the components of the feedback in the coupled simulations in this study, we use the radiative kernel method (Soden et al., 2008; Wang et al., 2021; Gettelman et al., 2016). In particular, we use the radiative kernel developed by Soden et al. (2008) and used recently by Wang et al. (2021). Radiative kernels can be used to quantify the contributions of component feedbacks to the total feedback discussed in the preceding section.

As developed by Soden et al. (2008), the radiative kernel method uses offline kernels corresponding to $\partial R(t)/\partial X(\lambda, \psi, p, t)$, denoting a change in the top-of-atmosphere global mean radiation flux R in response to a change in atmospheric state (X) at a specific latitude (λ), longitude (ψ), pressure (p) and time (t) (Gettelman et al., 2016). Our goal is to use radiative kernels to understand climate feedbacks. Let R be the TOA flux in some climate state, as a function of geographical position (i, j, p for all except albedo) and time (t). The net TOA flux (R) in some climate state is the difference between the absorbed shortwave component (Q) and the outgoing longwave component (F), i.e $Q - F$. R is a function of climate variables X including temperature, trace gas concentrations, cloud ice, cloud liquid, cloud area, etc.

We focus on the feedback related to 3D water vapor (w), 3D temperature (T), and 2D surface albedo (a). The remaining feedback can be calculated as a residual between the total feedback estimated from the "Gregory" regression method and the sum of the temperature, water vapor and surface albedo feedback. The residual feedback is ascribed to changes in cloud for abrupt-4xCO2 (i.e. $\lambda_{\text{4xco2}}(0, 50, \text{cloud})$), whereas it is ascribed to changes in cloud as well as aerosol-cloud interactions (ACI) and clear-sky aerosol-radiation interactions in G4sea-salt minus SSP2-4.5 (i.e. $\lambda_{\text{g4ss-ssp}}(2020, 2070, \text{cloud} + \text{aerosol})$).

We use temperature, water vapor and surface albedo kernels from Soden et al. (2008) obtained from an integration of the Geophysical Fluid Dynamics Laboratory (GFDL) atmospheric model (version AM2p12b) (Team et al., 2004) with climatological, seasonally varying sea surface temperature and sea ice distributions. The 3-hourly instantaneous TOA fluxes and all variables required to calculate the TOA fluxes, as functions of lat (i), lon (j), and height (k), are retrieved from a 1-year simulation.

Soden et al. (2008) then construct state changes for each feedback. For temperature kernels, they impose a 1 K uniform increase in temperatures. Specific humidities are increased such that the relative humidity would remain constant for a saturation specific humidity increase for 1 K warming. The surface albedo kernel is constructed by applying a 1% additive increase in surface albedo.

For 3D climate states (i.e. water vapor and temperature), the perturbation in the climate state X is uniformly applied layer by layer throughout the column of the atmosphere at a point i, j. For the temperature kernel, the change in the top-of-atmosphere global mean radiative flux R in response to a unit perturbation in the temperature (T) for layer k and geographical position (i, j), can be written as:

$$\frac{\partial R}{\partial T_{i,j,k,t}} \tag{D.1}$$

where k for temperature goes up to $N + 1$, where N is the number of model layers (24 in AM2p12b) and +1 accounts for the surface. For water vapor (which follows a similar form of the above equation), k goes up to N and for surface albedo (which follows a similar form of the above equation but is 2D), $k = 1$. The full vertical radiation computation is run 2N+2 times for each latitude and longitude (i,j). In total the full radiation computation is run $I \cdot J \cdot (2N + 2)$, where I is the number of latitudes (90) and J is the number of longitudes (144) in AM2p12b. The radiative flux computation is performed eight times daily for a one year simulation (Soden et al., 2008).

After discretizing longitude, latitude and height, there is a kernel for every latitude (i), longitude (j), height (k, for 3D properties), and month (t_m), therefore $\kappa_X(i, j, k, t_m) = \frac{\partial R(t_m)}{\partial X(i,j,k,t_m)}$. The kernels are provided as monthly means (averaged from the eight times daily one-year simulation), which will subsequently be used with longer model runs to evaluate feedbacks:

$$\kappa_T(i, j, k, t_m) = \overline{\left(\frac{\partial R}{\partial T_{i,j,k,t}}\right)} \tag{D.2}$$

where t_m refers to month of year, and κ_X refers to the radiative kernel for the climate variable X.

The N pressure layers are then interpolated to the 19 standard CMIP6 pressure levels (e.g., $k = 19$; Smith et al., 2020). Thus, there are IxJx20 temperature and IxJx19 water vapor kernels, and IxJ surface albedo kernels for each of 12 months.

D.0.1 Decomposing EEI due to feedback-related state changes

When a climate forcing is applied, the Earth has an energy imbalance due to the forcing. This imbalance triggers a climate response, modulated by feedback mechanisms. The Earth's Energy Imbalance (EEI) is used to evaluate feedbacks, using kernels to decompose the EEI into feedback-related components.

For a forcing/feedback climate simulation, such as abruptly quadrupling carbon dioxide (abrupt-4xCO2) (e.g., Wang et al. (2021)) in a CM4 piControl simulation, we must first ensure that the latitude, longitude, and pressure grid is consistent with that of the kernel (90,144,19). If this is not the case, grid interpolation must be applied for consistency.

The ΔEEI attributable to a change in a climate property $X_{4\text{xco2}}(i,j,k,t)$ for a given month in the forced 4xCO2 simulation is the product of the corresponding monthly-mean kernel $\kappa_X(i,j,k,t_m)$ and the difference in climate state ($\Delta X_{4\text{xco2}}(i,j,k,t)$) between the control (i.e piControl) and the perturbed climate state (i.e abrupt-4xCO2). The contributions described above are then summed over grid cells and months to obtain ΔEEI due to global annual changes in X. For 3D climate properties X (i.e, temperature and water vapor) for year t_y:

$$\Delta\text{EEI}_{X,4\text{xco2}}(t_y) = \sum_{i,j,k,t_m} \kappa_X(i,j,k,t_m) \cdot \Delta X_{4\text{xco2}}(i,j,k,t) \tag{D.3}$$

where i goes up to I (90), j up to J (144), k up to K (19), and m (months) ranges from 1 to 12. The resulting $\Delta\text{EEI}_{X,4\text{xco2}}$ is a function of t_y (50 or 150 years). This expression can also be applied for surface albedo but only latitude, longitude, and monthly contributions are summed. Fig. D.1 displays the $\Delta\text{EEI}_{X,4\text{xco2}}(t_y)$ for temperature, water vapor and surface albedo for the CM4 abrupt-4xCO2 experiment relative to the piControl.

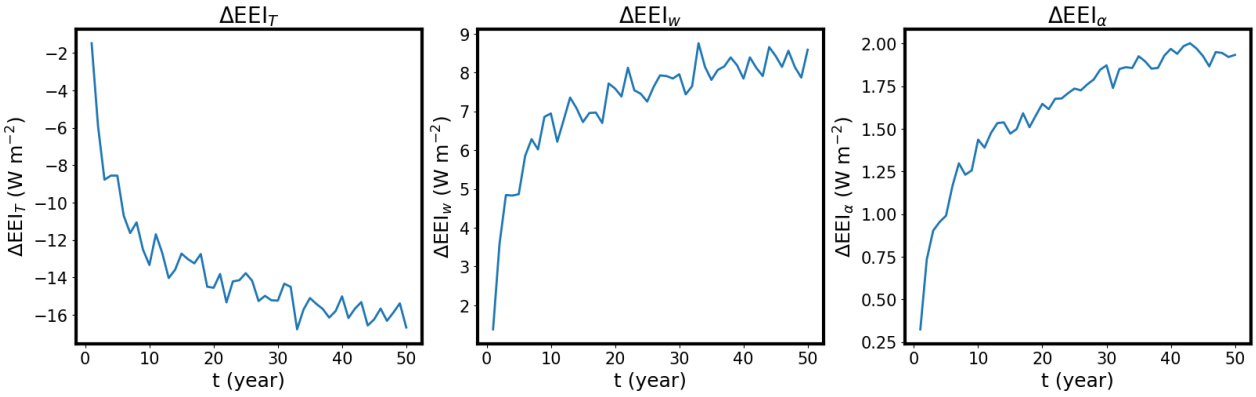


Figure D.1: Time series of the globally averaged change in TOA radiation imbalance due to a change in climate property X (temperature (T), water vapor (w) and surface albedo (α)) for the first 50-years of abrupt-4xCO2.

To calculate the feedback for the first 50 years after imposition of forcing for abrupt-4xCO2, we sort pairs of $\Delta\text{EEI}_{X,4\text{xco2}}$ and the corresponding change in surface temperature ($\Delta T_{s,4\text{xco2}}$; calculated as the difference between the first 50 years of abrupt-4xCO2 and pi-Control (averaged over the 100-250 year period)) by increasing $\Delta T_{s,4\text{xco2}}$. We then plot $\Delta\text{EEI}_{X,4\text{xco2}}$ as a function of $\Delta T_{s,4\text{xco2}}$ and apply linear regression to the plotted points. Then $\lambda_{4\text{xco2}}(0, 50, X)$ is defined as the regression slope of this line ($\lambda_{4\text{xco2}}(0, 50, X)$; Fig D.2):

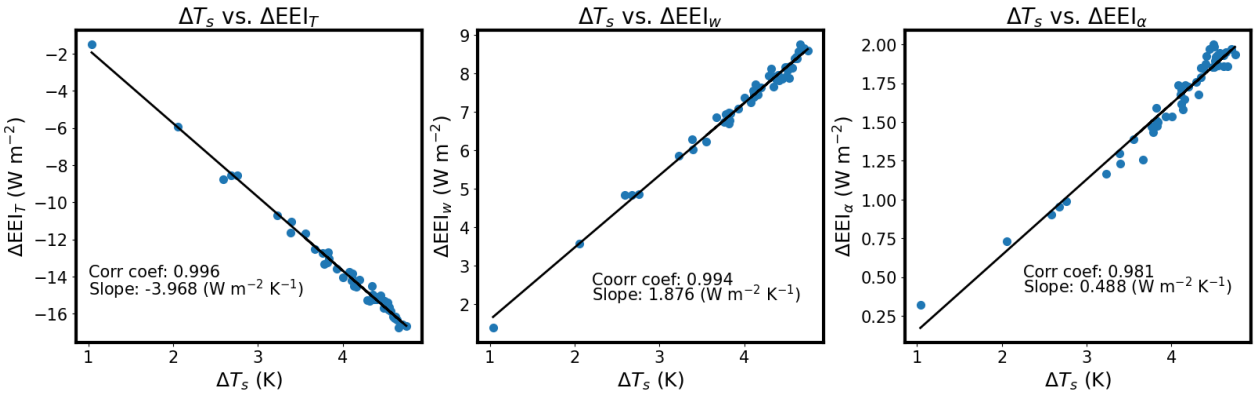


Figure D.2: The regression of globally averaged change in TOA radiation imbalance due to change in climate property X (temperature (T), water vapor (w) and surface albedo (α)) to the change in surface temperature calculated as the difference between the first 50-years of abrupt-4xCO2 and piControl (averaged over year 100-250 of the simulation).

References

Adachi, K., & Buseck, P. R. (2015). Changes in shape and composition of sea-salt particles upon aging in an urban atmosphere. *Atmospheric Environment*, *100*, 1–9.

Adcroft, A., Anderson, W., Balaji, V., Blanton, C., Bushuk, M., Dufour, C. O., ... others (2019). The gfdl global ocean and sea ice model om4. 0: Model description and simulation features. *Journal of Advances in Modeling Earth Systems*, *11*(10), 3167–3211.

Ahlm, L., Jones, A., Stjern, C. W., Muri, H., Kravitz, B., & Kristjánsson, J. E. (2017). Marine cloud brightening–as effective without clouds. *Atmospheric Chemistry and Physics*, *17*(21), 13071–13087.

Albert, M. F., Anguelova, M. D., Manders, A. M., Schaap, M., & Leeuw, G. d. (2016). Parameterization of oceanic whitecap fraction based on satellite observations. *Atmospheric Chemistry and Physics*, *16*(21), 13725–13751.

Albrecht, B. A. (1989). Aerosols, cloud microphysics, and fractional cloudiness. *Science*, *245*(4923), 1227–1230.

Alterskjær, K., Kristjánsson, J., & Seland, Ø. (2012). Sensitivity to deliberate sea salt seeding of marine clouds–observations and model simulations. *Atmospheric Chemistry and Physics*, *12*(5), 2795–2807.

Andreas, E. L. (1998). A new sea spray generation function for wind speeds up to 32 ms- 1. *Journal of Physical Oceanography*, *28*(11), 2175–2184.

Andreas, E. L., Edson, J. B., Monahan, E. C., Rouault, M. P., & Smith, S. D. (1995). The spray contribution to net evaporation from the sea: A review of recent progress. *Boundary-Layer Meteorology*, *72*(1), 3–52.

Andrews, T., Gregory, J. M., Webb, M. J., & Taylor, K. E. (2012). Forcing, feedbacks and climate sensitivity in cmip5 coupled atmosphere-ocean climate models. *Geophysical research letters*, *39*(9).

Anguelova, M. D., & Webster, F. (2006). Whitecap coverage from satellite measurements: A first step toward modeling the variability of oceanic whitecaps. *Journal of Geophysical Research: Oceans*, *111*(C3).

Athanasopoulou, E., Tombrou, M., Pandis, S., & Russell, A. (2008). The role of sea-salt emissions and heterogeneous chemistry in the air quality of polluted coastal areas. *Atmospheric Chemistry and Physics*, *8*(19), 5755–5769.

Ayash, T., Gong, S., & Jia, C. Q. (2008). Direct and indirect shortwave radiative effects of sea salt aerosols. *Journal of climate*, *21*(13), 3207–3220.

Ban-Weiss, G. A., Jin, L., Bauer, S. E., Bennartz, R., Liu, X., Zhang, K., ... Jiang, J. H. (2014). Evaluating clouds, aerosols, and their interactions in three global climate

models using satellite simulators and observations. *Journal of Geophysical Research: Atmospheres*, *119*(18), 10–876.

Barthel, S., Tegen, I., & Wolke, R. (2019). Do new sea spray aerosol source functions improve the results of a regional aerosol model? *Atmospheric Environment*, *198*, 265–278.

Bellouin, N., Quaas, J., Gryspeerdt, E., Kinne, S., Stier, P., Watson-Parris, D., ... others (2020). Bounding global aerosol radiative forcing of climate change. *Reviews of Geophysics*, *58*(1), e2019RG000660.

Bertram, T. H., Cochran, R. E., Grassian, V. H., & Stone, E. A. (2018). Sea spray aerosol chemical composition: elemental and molecular mimics for laboratory studies of heterogeneous and multiphase reactions. *Chemical Society Reviews*, *47*(7), 2374–2400.

Bibi, H., Alam, K., Chishtie, F., Bibi, S., Shahid, I., & Blaschke, T. (2015). Intercomparison of modis, misr, omi, and calipso aerosol optical depth retrievals for four locations on the indo-gangetic plains and validation against aeronet data. *Atmospheric Environment*, *111*, 113–126.

Bilal, M., Qiu, Z., Campbell, J. R., Spak, S. N., Shen, X., & Nazeer, M. (2018). A new modis c6 dark target and deep blue merged aerosol product on a 3 km spatial grid. *Remote Sensing*, *10*(3), 463.

Block, K., & Mauritsen, T. (2013). Forcing and feedback in the mpi-esm-lr coupled model under abruptly quadrupled co2. *Journal of Advances in Modeling Earth Systems*, *5*(4), 676–691.

Brierley, C. M., Thorpe, A. J., & Collins, M. (2009). An example of the dependence of the transient climate response on the temperature of the modelled climate state. *Atmospheric Science Letters*, *10*(1), 23–28.

Brown, P. T., Li, W., Li, L., & Ming, Y. (2014). Top-of-atmosphere radiative contribution to unforced decadal global temperature variability in climate models. *Geophysical Research Letters*, *41*(14), 5175–5183.

Cai, M., & Tung, K.-K. (2012). Robustness of dynamical feedbacks from radiative forcing: 2% solar versus 2× co2 experiments in an idealized gcm. *Journal of the atmospheric sciences*, *69*(7), 2256–2271.

Callaghan, A. H. (2013). An improved whitecap timescale for sea spray aerosol production flux modeling using the discrete whitecap method. *Journal of Geophysical Research: Atmospheres*, *118*(17), 9997–10.

Ceppi, P., Brient, F., Zelinka, M. D., & Hartmann, D. L. (2017). Cloud feedback mechanisms and their representation in global climate models. *Wiley Interdisciplinary Reviews: Climate Change*, *8*(4), e465.

Chen, Cheng, Y., Ma, N., Wei, C., Ran, L., Wolke, R., ... others (2020). Natural sea-salt emissions moderate the climate forcing of anthropogenic nitrate. *Atmospheric Chemistry and Physics*, *20*(2), 771–786.

Chen, C.-C., Richter, J. H., Lee, W. R., MacMartin, D. G., & Kravitz, B. (2024). Rethinking the susceptibility-based strategy for marine cloud brightening climate intervention: Experiment with cesm2 and its implications. *Geophysical Research Letters*, *51*(10), e2024GL108860.

Cheng, C. S., Li, G., Li, Q., Auld, H., & Fu, C. (2012). Possible impacts of climate change on wind gusts under downscaled future climate conditions over ontario, canada. *Journal of climate*, *25*(9), 3390–3408.

Christiansen, S., Salter, M. E., Gorokhova, E., Nguyen, Q. T., & Bilde, M. (2019). Sea spray aerosol formation: Laboratory results on the role of air entrainment, water temperature, and phytoplankton biomass. *Environmental science & technology*, *53*(22), 13107–13116.

Clarke, A. D., Owens, S. R., & Zhou, J. (2006). An ultrafine sea-salt flux from breaking waves: Implications for cloud condensation nuclei in the remote marine atmosphere. *Journal of Geophysical Research: Atmospheres*, *111*(D6).

Collins, M. (2005). El niño-or la niña-like climate change? *Climate Dynamics*, *24*, 89–104.

Collins, W. J., Lamarque, J.-F., Schulz, M., Boucher, O., Eyring, V., Hegglin, M. I., ... others (2017). Aerchemmip: Quantifying the effects of chemistry and aerosols in cmip6. *Geoscientific Model Development*, *10*(2), 585–607.

Davidson, C., Harrington, J., Stephenson, M., Small, M., Boscoe, F. P., & Gandley, R. (1989). Seasonal variations in sulfate, nitrate and chloride in the greenland ice sheet: relation to atmospheric concentrations. *Atmospheric Environment (1967)*, *23*(11), 2483–2493.

Deike, L., Reichl, B., & Paulot, F. (2022). A mechanistic sea spray generation function based on the sea state and the physics of bubble bursting. *AGU Advances*, *3*(6), e2022AV000750.

De Leeuw, G., Andreas, E. L., Anguelova, M. D., Fairall, C., Lewis, E. R., O'Dowd, C., ... Schwartz, S. E. (2011). Production flux of sea spray aerosol. *Reviews of Geophysics*, *49*(2).

Deng, K., Azorin-Molina, C., Yang, S., Hu, C., Zhang, G., Minola, L., & Chen, D. (2022). Changes of southern hemisphere westerlies in the future warming climate. *Atmospheric Research*, *270*, 106040.

Derkani, M. H., Alberello, A., Nelli, F., Bennetts, L. G., Hessner, K. G., MacHutchon, K., ... Toffoli, A. (2020). Wind, waves, and surface currents in the southern ocean: observations from the antarctic circumnavigation expedition. *Earth System Science Data Discussions*, *2020*, 1–22.

Deser, C., Alexander, M. A., Xie, S.-P., & Phillips, A. S. (2010). Sea surface temperature variability: Patterns and mechanisms. *Annual review of marine science*, *2*(1), 115–143.

Dunne, J., Horowitz, L., Adcroft, A., Ginoux, P., Held, I., John, J., ... others (2020). The gfdl earth system model version 4.1 (gfdl-esm 4.1): Overall coupled model description and simulation characteristics. *Journal of Advances in Modeling Earth Systems*, *12*(11), e2019MS002015.

Eichelberger, S., McCaa, J., Nijssen, B., & Wood, A. (2008). Climate change effects on wind speed. *North American Windpower*, *7*, 68–72.

Eyring, V., Bony, S., Meehl, G. A., Senior, C. A., Stevens, B., Stouffer, R. J., & Taylor, K. E. (2016). Overview of the coupled model intercomparison project phase 6 (cmip6) experimental design and organization. *Geoscientific Model Development*, *9*(5), 1937–1958.

Farahat, A. (2019). Comparative analysis of modis, misr, and aeronet climatology over the middle east and north africa. In *Annales geophysicae* (Vol. 37, pp. 49–64).

Fei, K.-c., Wu, L., & Zeng, Q.-c. (2019). Aerosol optical depth and burden from large sea salt particles. *Journal of Geophysical Research: Atmospheres*, *124*(3), 1680–1696.

Forestieri, S., Moore, K., Martinez Borrero, R., Wang, A., Stokes, M., & Cappa, C. (2018). Temperature and composition dependence of sea spray aerosol production. *Geophysical Research Letters*, *45*(14), 7218–7225.

Forster, P., Storelvmo, T., Armour, K., Collins, W., Dufresne, J.-L., Frame, D., ... others (2021). The earth's energy budget, climate feedbacks, and climate sensitivity.

Forster, P. M., Richardson, T., Maycock, A. C., Smith, C. J., Samset, B. H., Myhre, G., ... Schulz, M. (2016). Recommendations for diagnosing effective radiative forcing from climate models for cmip6. *Journal of Geophysical Research: Atmospheres*, *121*(20), 12–460.

Gettelman, A., Lin, L., Medeiros, B., & Olson, J. (2016). Climate feedback variance and the interaction of aerosol forcing and feedbacks. *Journal of Climate*, *29*(18), 6659–6675.

Ginoux, P. (2003). Effects of nonsphericity on mineral dust modeling. *Journal of Geophysical Research: Atmospheres*, *108*(D2).

Ginoux, P., Horowitz, L. W., Ramaswamy, V., Geogdzhayev, I. V., Holben, B. N., Stenchikov, G., & Tie, X. (2006). Evaluation of aerosol distribution and optical depth in the geophysical fluid dynamics laboratory coupled model cm2. 1 for present climate. *Journal of Geophysical Research: Atmospheres*, *111*(D22).

Gong, S. (2003). A parameterization of sea-salt aerosol source function for sub-and super-micron particles. *Global biogeochemical cycles*, *17*(4).

Gong, S., Barrie, L., & Blanchet, J.-P. (1997). Modeling sea-salt aerosols in the atmosphere: 1. model development. *Journal of Geophysical Research: Atmospheres*, *102*(D3), 3805–3818.

Gregory, J. M., Ingram, W. J., Palmer, M., Jones, G. S., Stott, P., Thorpe, R., ... Williams, K. (2004). A new method for diagnosing radiative forcing and climate sensitivity. *Geophysical research letters*, *31*(3).

Grini, A., Myhre, G., Sundet, J. K., & Isaksen, I. S. (2002). Modeling the annual cycle of sea salt in the global 3d model oslo ctm2: Concentrations, fluxes, and radiative impact. *Journal of Climate*, *15*(13), 1717–1730.

Grythe, H., Ström, J., Krejci, R., Quinn, P., & Stohl, A. (2014). A review of sea-spray aerosol source functions using a large global set of sea salt aerosol concentration measurements. *Atmospheric Chemistry and Physics*, *14*(3), 1277–1297.

Guo, H., John, J. G., Blanton, C., McHugh, C., Nikonov, S., Radhakrishnan, A., ... Zhang, R. (2018). Noaa-gfdl gfdl-cm4 model output abrupt-4xco2.
doi: 10.22033/ESGF/CMIP6.8486

Hansen, J., Nazarenko, L., Ruedy, R., Sato, M., Willis, J., Del Genio, A., ... others (2005). Earth's energy imbalance: Confirmation and implications. *science*, *308*(5727), 1431–1435.

Hansen, J., Sato, M., & Ruedy, R. (1997). Radiative forcing and climate response. *Journal of Geophysical Research: Atmospheres*, *102*(D6), 6831–6864.

Haywood, J. M., Jones, A., Jones, A. C., Halloran, P., & Rasch, P. J. (2023). Climate intervention using marine cloud brightening (mcb) compared with stratospheric aerosol injection (sai) in the ukesm1 climate model. *Atmospheric Chemistry and Physics*, *23*(24), 15305–15324.

He, J., Winton, M., Vecchi, G., Jia, L., & Rugenstein, M. (2017). Transient climate sensitivity depends on base climate ocean circulation. *Journal of Climate*, *30*(4), 1493–1504.

Heald, C., Ridley, D., Kroll, J., Barrett, S., Cady-Pereira, K., Alvarado, M., & Holmes, C. (2014a). Contrasting the direct radiative effect and direct radiative forcing of aerosols. *Atmospheric Chemistry and Physics*, *14*(11), 5513–5527.

Heald, C., Ridley, D., Kroll, J., Barrett, S., Cady-Pereira, K., Alvarado, M., & Holmes, C. (2014b). Contrasting the direct radiative effect and direct radiative forcing of aerosols. *Atmospheric Chemistry and Physics*, *14*(11), 5513–5527.

Heede, U. K., & Fedorov, A. V. (2023). Colder eastern equatorial pacific and stronger walker circulation in the early 21st century: Separating the forced response to global warming from natural variability. *Geophysical Research Letters*, *50*(3), e2022GL101020.

Held, I., Guo, H., Adcroft, A., Dunne, J., Horowitz, L., Krasting, J., ... others (2019). Structure and performance of gfdl's cm4. 0 climate model. *Journal of Advances in Modeling Earth Systems*, *11*(11), 3691–3727.

Hersbach, H., Bell, B., Berrisford, P., Biavati, G., Horányi, A., Muñoz Sabater, J., ... others (2018). Era5 hourly data on single levels from 1979 to present. *Copernicus climate change service (c3s) climate data store (cds)*, *10*(10.24381).

Hess, M., Koepke, P., & Schult, I. (1998). Optical properties of aerosols and clouds: The software package opac. *Bulletin of the American meteorological society*, *79*(5), 831–844.

Hill, S., & Ming, Y. (2012). Nonlinear climate response to regional brightening of tropical marine stratocumulus. *Geophysical Research Letters*, *39*(15).

Holben, B. N., Eck, T. F., Slutsker, I. a., Tanré, D., Buis, J., Setzer, A., ... others (1998). Aeronet—a federated instrument network and data archive for aerosol characterization. *Remote sensing of environment*, *66*(1), 1–16.

Holland, H. D. (2020). *The chemical evolution of the atmosphere and oceans*. Princeton University Press.

Horowitz, H. M., Holmes, C., Wright, A., Sherwen, T., Wang, X., Evans, M., ... others (2020). Effects of sea salt aerosol emissions for marine cloud brightening on atmospheric chemistry: Implications for radiative forcing. *Geophysical research letters*, *47*(4), e2019GL085838.

Horowitz, L. W., Naik, V., Paulot, F., Ginoux, P. A., Dunne, J. P., Mao, J., ... others (2020). The gfdl global atmospheric chemistry-climate model am4. 1: Model description and simulation characteristics. *Journal of Advances in Modeling Earth Systems*, *12*(10), e2019MS002032.

Hsu, S., Meindl, E. A., & Gilhousen, D. B. (1994). Determining the power-law wind-profile exponent under near-neutral stability conditions at sea. *Journal of Applied Meteorology and Climatology*, *33*(6), 757–765.

Huang, X., Zhou, T., Turner, A., Dai, A., Chen, X., Clark, R., ... others (2020). The recent decline and recovery of indian summer monsoon rainfall: relative roles of external forcing and internal variability. *Journal of Climate*, *33*(12), 5035–5060.

Ikegami, M., Okada, K., Zaizen, Y., & Makino, Y. (1994). Sea-salt particles in the upper tropical troposphere. *Tellus B*, *46*(2), 142–151.

Jaeglé, L., Quinn, P., Bates, T., Alexander, B., & Lin, J.-T. (2011). Global distribution of sea salt aerosols: new constraints from in situ and remote sensing observations. *Atmospheric Chemistry and Physics*, *11*(7), 3137–3157.

Jeong, D. I., & Sushama, L. (2019). Projected changes to mean and extreme surface wind speeds for north america based on regional climate model simulations. *Atmosphere*, *10*(9), 497.

Jiang, S., Zhu, C., & Jiang, N. (2024). Impacts of the annual cycle of background sst in the tropical pacific on the phase and amplitude of enso. *Atmospheric and Oceanic Science Letters*, 100496.

Jones, A., & Haywood, J. (2012). Sea-spray geoengineering in the hadgem2-es earth-system model: radiative impact and climate response. *Atmospheric Chemistry and Physics*, *12*(22), 10887–10898.

Jones, A., Haywood, J., & Boucher, O. (2009). Climate impacts of geoengineering marine stratocumulus clouds. *Journal of Geophysical Research: Atmospheres*, *114*(D10).

Junge, C. E. (1972). Our knowledge of the physico-chemistry of aerosols in the undisturbed marine environment. *Journal of Geophysical Research*, *77*(27), 5183–5200.

Junge, C. E., & Gustafson, P. E. (1956). Precipitation sampling for chemical analysis. *Bulletin of the American Meteorological Society*, *37*(5), 244–244.

Kahn, R. A., Nelson, D. L., Garay, M. J., Levy, R. C., Bull, M. A., Diner, D. J., ... Remer, L. A. (2009). Misr aerosol product attributes and statistical comparisons with modis. *IEEE Transactions on Geoscience and Remote Sensing*, *47*(12), 4095–4114.

Kalashnikova, O., Garay, M., Martonchik, J., & Diner, D. (2013). Misr dark water aerosol retrievals: operational algorithm sensitivity to particle non-sphericity. *Atmospheric Measurement Techniques*, *6*(8), 2131–2154.

Kang, S. M., Shin, Y., Kim, H., Xie, S.-P., & Hu, S. (2023). Disentangling the mechanisms of equatorial pacific climate change. *Science advances*, *9*(19), eadf5059.

Kawakami, N., Osada, K., Nishita, C., Yabuki, M., Kobayashi, H., Hara, K., & Shiobara, M. (2008). Factors controlling sea salt modification and dry deposition of nonsea-salt components to the ocean. *Journal of Geophysical Research: Atmospheres*, *113*(D14).

Kelly, J., Bhave, P., Nolte, C., Shankar, U., & Foley, K. (2009). Simulating emission and chemical evolution of coarse sea-salt particles in the community multiscale air quality (cmaq) model. *Geoscientific Model Development Discussions*, *2*(2), 1335–1374.

Kim, P. S., Jacob, D. J., Fisher, J. A., Travis, K., Yu, K., Zhu, L., ... others (2015). Sources, seasonality, and trends of southeast us aerosol: an integrated analysis of surface, aircraft, and satellite observations with the geos-chem chemical transport model. *Atmospheric Chemistry and Physics*, *15*(18), 10411–10433.

Kinne, S., Lohmann, U., Feichter, J., Schulz, M., Timmreck, C., Ghan, S., ... others (2003). Monthly averages of aerosol properties: A global comparison among models, satellite data, and aeronet ground data. *Journal of Geophysical Research: Atmospheres*, *108*(D20).

Kinne, S., Schulz, M., Textor, C., Guibert, S., Balkanski, Y., Bauer, S. E., ... others (2006). An aerocom initial assessment–optical properties in aerosol component modules of global models. *Atmospheric Chemistry and Physics*, *6*(7), 1815–1834.

Kravitz, B., Forster, P. M., Jones, A., Robock, A., Alterskjær, K., Boucher, O., ... others (2013). Sea spray geoengineering experiments in the geoengineering model intercomparison project (geomip): Experimental design and preliminary results. *Journal of Geophysical Research: Atmospheres*, *118*(19), 11–175.

Lambert, F., Kug, J., Park, R., Mahowald, N., Winckler, G., Abe-Ouchi, A., ... Lee, J. (2013). The role of mineral-dust aerosols in polar temperature amplification. *Nature Climate Change*, *3*(5), 487–491.

Latham, J. (1990). Control of global warming? *Nature*, *347*(6291), 339–340.

Latham, J. (2002). Amelioration of global warming by controlled enhancement of the albedo and longevity of low-level maritime clouds. *Atmospheric Science Letters*, *3*(2-4), 52–58.

Levy, R. C., Remer, L. A., Mattoo, S., Vermote, E. F., & Kaufman, Y. J. (2007). Second-generation operational algorithm: Retrieval of aerosol properties over land from inversion of moderate resolution imaging spectroradiometer spectral reflectance. *Journal of Geophysical Research: Atmospheres*, *112*(D13).

Lewis, E. R., Lewis, R., Karlstrom, K. E., Lewis, E. R., & Schwartz, S. E. (2004). *Sea salt aerosol production: mechanisms, methods, measurements, and models* (Vol. 152). American Geophysical Union.

Li, J., Carlson, B. E., & Lacis, A. A. (2014). Application of spectral analysis techniques in the intercomparison of aerosol data. part ii: Using maximum covariance analysis to effectively compare spatiotemporal variability of satellite and aeronet measured aerosol optical depth. *Journal of Geophysical Research: Atmospheres*, *119*(1), 153–166.

Li, Q., Cheng, Y., & Gentine, P. (2021). Connection between mass flux transport and eddy diffusivity in convective atmospheric boundary layers. *Geophysical Research Letters*, *48*(8), e2020GL092073.

Li, S., Garay, M. J., Chen, L., Rees, E., & Liu, Y. (2013). Comparison of geos-chem aerosol optical depth with aeronet and misr data over the contiguous united states. *Journal of Geophysical Research: Atmospheres*, *118*(19), 11–228.

Liu, Lacis, A. A., Carlson, B. E., Mishchenko, M. I., & Cairns, B. (2006). Assessing goddard institute for space studies modele aerosol climatology using satellite and ground-based measurements: A comparison study. *Journal of Geophysical Research: Atmospheres*, *111*(D20).

Liu, H., Jacob, D. J., Bey, I., & Yantosca, R. M. (2001). Constraints from 210pb and 7be on wet deposition and transport in a global three-dimensional chemical tracer model driven by assimilated meteorological fields. *Journal of Geophysical Research: Atmospheres*, *106*(D11), 12109–12128.

Liu, S., Liu, C.-C., Froyd, K. D., Schill, G. P., Murphy, D. M., Bui, T. P., ... others (2021). Sea spray aerosol concentration modulated by sea surface temperature. *Proceedings of the National Academy of Sciences*, *118*(9).

Liu, X., Penner, J. E., Das, B., Bergmann, D., Rodriguez, J. M., Strahan, S., ... Feng, Y. (2007). Uncertainties in global aerosol simulations: Assessment using three meteorological data sets. *Journal of Geophysical Research: Atmospheres*, *112*(D11).

Liu, Z., Vavrus, S., He, F., Wen, N., & Zhong, Y. (2005). Rethinking tropical ocean response to global warming: The enhanced equatorial warming. *Journal of Climate*, *18*(22), 4684–4700.

Ma, J., Foltz, G. R., Soden, B. J., Huang, G., He, J., & Dong, C. (2016). Will surface winds weaken in response to global warming? *Environmental Research Letters*, *11*(12), 124012.

Ma, X., von Salzen, K., & Li, J. (2008). Modelling sea salt aerosol and its direct and indirect effects on climate. *Atmospheric Chemistry and Physics*, *8*(5), 1311–1327.

Mahfouz, N. G., Hill, S. A., Guo, H., & Ming, Y. (2023). The radiative and cloud responses to sea salt aerosol engineering in gfdl models. *Geophysical Research Letters*, *50*(2), e2022GL102340.

Mårtensson, E., Nilsson, E., de Leeuw, G., Cohen, L., & Hansson, H.-C. (2003). Laboratory simulations and parameterization of the primary marine aerosol production. *Journal of Geophysical Research: Atmospheres*, *108*(D9).

McInnes, K. L., Erwin, T. A., & Bathols, J. M. (2011). Global climate model projected changes in 10 m wind speed and direction due to anthropogenic climate change. *Atmospheric Science Letters*, *12*(4), 325–333.

Ming, Y., Ramaswamy, V., Donner, L. J., & Phillips, V. T. (2006). A new parameterization of cloud droplet activation applicable to general circulation models. *Journal of the atmospheric sciences*, *63*(4), 1348–1356.

Ming, Y., Ramaswamy, V., Donner, L. J., Phillips, V. T., Klein, S. A., Ginoux, P. A., & Horowitz, L. W. (2007). Modeling the interactions between aerosols and liquid water clouds with a self-consistent cloud scheme in a general circulation model. *Journal of the Atmospheric Sciences*, *64*(4), 1189–1209.

Mishchenko, M. I., Liu, L., Geogdzhayev, I. V., Travis, L. D., Cairns, B., & Lacis, A. A. (2010). Toward unified satellite climatology of aerosol properties.: 3. modis versus misr versus aeronet. *Journal of Quantitative Spectroscopy and Radiative Transfer*, *111*(4), 540–552.

Monahan, E. C., Spiel, D. E., & Davidson, K. L. (1986). A model of marine aerosol generation via whitecaps and wave disruption. In *Oceanic whitecaps* (pp. 167–174). Springer.

Murphy, D. M., Froyd, K. D., Bian, H., Brock, C. A., Dibb, J. E., DiGangi, J. P., ... others (2019). The distribution of sea-salt aerosol in the global troposphere. *Atmospheric Chemistry and Physics*, *19*(6), 4093–4104.

Nair, P. R., Parameswaran, K., Abraham, A., & Jacob, S. (2005). Wind-dependence of sea-salt and non-sea-salt aerosols over the oceanic environment. *Journal of atmospheric and solar-terrestrial physics*, *67*(10), 884–898.

Norris, S., Brooks, I., Leeuw, G. d., Smith, M., Moerman, M., & Lingard, J. (2008). Eddy covariance measurements of sea spray particles over the atlantic ocean. *Atmospheric Chemistry and Physics*, *8*(3), 555–563.

Norris, S. J., Brooks, I. M., & Salisbury, D. J. (2013). A wave roughness reynolds number parameterization of the sea spray source flux. *Geophysical Research Letters*, *40*(16), 4415–4419.

O'Dowd, C. D., & Smith, M. H. (1993). Physicochemical properties of aerosols over the northeast atlantic: Evidence for wind-speed-related submicron sea-salt aerosol production. *Journal of Geophysical Research: Atmospheres*, *98*(D1), 1137–1149.

O'Dowd, C. D., Smith, M. H., Consterdine, I. E., & Lowe, J. A. (1997). Marine aerosol, sea-salt, and the marine sulphur cycle: A short review. *Atmospheric Environment*, *31*(1), 73–80.

O'Gorman, P. A., & Schneider, T. (2009). The physical basis for increases in precipitation extremes in simulations of 21st-century climate change. *Proceedings of the National Academy of Sciences*, *106*(35), 14773–14777.

O'Neill, B. C., Tebaldi, C., Van Vuuren, D. P., Eyring, V., Friedlingstein, P., Hurtt, G., ... others (2016). The scenario model intercomparison project (scenariomip) for cmip6. *Geoscientific Model Development*, *9*(9), 3461–3482.

O'Neill, B. C., Kriegler, E., Riahi, K., Ebi, K. L., Hallegatte, S., Carter, T. R., ... Van Vuuren, D. P. (2014). A new scenario framework for climate change research: the concept of shared socioeconomic pathways. *Climatic change*, *122*, 387–400.

Pachauri, R. K., Allen, M. R., Barros, V. R., Broome, J., Cramer, W., Christ, R., ... others (2014). *Climate change 2014: synthesis report. contribution of working groups i, ii and iii to the fifth assessment report of the intergovernmental panel on climate change*. Ipcc.

Parajuli, S. P., Stenchikov, G. L., Ukhov, A., Shevchenko, I., Dubovik, O., & Lopatin, A. (2020). Aerosol vertical distribution and interactions with land/sea breezes over the eastern coast of the red sea from lidar data and high-resolution wrf-chem simulations. *Atmospheric Chemistry and Physics*, *20*(24), 16089–16116.

Parameswaran, K., Vijayakumar, G., Krishna Murthy, B., & Krishna Moorthy, K. (1995). Effect of wind speed on mixing region aerosol concentrations at a tropical coastal station. *Journal of Applied Meteorology and Climatology*, *34*(6), 1392–1397.

Partanen, A.-I., Kokkola, H., Romakkaniemi, S., Kerminen, V.-M., Lehtinen, K. E., Bergman, T., ... Korhonen, H. (2012). Direct and indirect effects of sea spray geoengineering and the role of injected particle size. *Journal of Geophysical Research: Atmospheres*, *117*(D2).

Patterson, E., Kiang, C., Delany, A., Wartburg, A., Leslie, A., & Huebert, B. (1980). Global measurements of aerosols in remote continental and marine regions: Concentrations, size distributions, and optical properties. *Journal of Geophysical Research: Oceans*, *85*(C12), 7361–7376.

Paulot, F., Paynter, D., Winton, M., Ginoux, P., Zhao, M., & Horowitz, L. W. (2020). Revisiting the impact of sea salt on climate sensitivity. *Geophysical Research Letters*, *47*(3), e2019GL085601.

Pierce, J. R., & Adams, P. J. (2006). Global evaluation of ccn formation by direct emission of sea salt and growth of ultrafine sea salt. *Journal of Geophysical Research: Atmospheres*, *111*(D6).

Pincus, R., Forster, P. M., & Stevens, B. (2016). The radiative forcing model intercomparison project (rfmip): Experimental protocol for cmip6. *Geoscientific Model Development*, *9*(9), 3447–3460.

Previdi, M., Smith, K. L., & Polvani, L. M. (2021). Arctic amplification of climate change: a review of underlying mechanisms. *Environmental Research Letters*, *16*(9), 093003.

Pu, B., Ginoux, P., Guo, H., Hsu, N. C., Kimball, J., Marticorena, B., ... others (2020). Retrieving the global distribution of the threshold of wind erosion from satellite data and implementing it into the geophysical fluid dynamics laboratory land–atmosphere model (gfdl am4. 0/lm4. 0). *Atmospheric Chemistry and Physics*, *20*(1), 55–81.

Quinn, P., Bates, T., Coffman, D., Miller, T., Johnson, J., Covert, D., ... Novakov, T. (2000). A comparison of aerosol chemical and optical properties from the 1st and 2nd aerosol characterization experiments. *Tellus B: Chemical and Physical Meteorology*, *52*(2), 239–257.

Quinn, P. K., & Bates, T. S. (2005). Regional aerosol properties: Comparisons of boundary layer measurements from ace 1, ace 2, aerosols99, indoex, ace asia, tarfox, and neaqs. *Journal of Geophysical Research: Atmospheres*, *110*(D14).

Raghuraman, S. P., Paynter, D., & Ramaswamy, V. (2021). Anthropogenic forcing and response yield observed positive trend in earth's energy imbalance. *Nature communications*, *12*(1), 4577.

Righi, M., Hendricks, J., & Sausen, R. (2013). The global impact of the transport sectors on atmospheric aerosol: simulations for year 2000 emissions. *Atmospheric Chemistry and Physics*, *13*(19), 9939–9970.

Russotto, R. D., & Biasutti, M. (2020). Polar amplification as an inherent response of a circulating atmosphere: Results from the tracmip aquaplanets. *Geophysical Research Letters*, *47*(6), e2019GL086771.

Salter, M. E., Nilsson, E. D., Butcher, A., & Bilde, M. (2014). On the seawater temperature dependence of the sea spray aerosol generated by a continuous plunging jet. *Journal of Geophysical Research: Atmospheres*, *119*(14), 9052–9072.

Satheesh, S., & Moorthy, K. K. (2005). Radiative effects of natural aerosols: A review. *Atmospheric Environment*, *39*(11), 2089–2110.

Sayer, A., Munchak, L., Hsu, N., Levy, R., Bettenhausen, C., & Jeong, M.-J. (2014). Modis collection 6 aerosol products: Comparison between aqua's e-deep blue, dark target, and "merged" data sets, and usage recommendations. *Journal of Geophysical Research: Atmospheres*, *119*(24), 13–965.

Schaller, N., Sedláček, J., & Knutti, R. (2014). The asymmetry of the climate system's response to solar forcing changes and its implications for geoengineering scenarios. *Journal of Geophysical Research: Atmospheres*, *119*(9), 5171–5184.

Schmidt, G. A., Bader, D., Donner, L. J., Elsaesser, G. S., Golaz, J.-C., Hannay, C., ... Saha, S. (2017). Practice and philosophy of climate model tuning across six us modeling centers. *Geoscientific Model Development*, *10*(9), 3207–3223.

Schulz, M., de Leeuw, G., & Balkanski, Y. (2004). Sea-salt aerosol source functions and emissions. In *Emissions of atmospheric trace compounds* (pp. 333–359). Springer.

Seinfeld, J. H., & Pandis, S. N. (2016). *Atmospheric chemistry and physics: from air pollution to climate change*. John Wiley & Sons.

Sellegri, K., O'Dowd, C., Yoon, Y., Jennings, S., & de Leeuw, G. (2006). Surfactants and submicron sea spray generation. *Journal of Geophysical Research: Atmospheres*, *111*(D22).

Serreze, M. C., & Barry, R. G. (2011). Processes and impacts of arctic amplification: A research synthesis. *Global and planetary change*, *77*(1-2), 85–96.

Shi, J., Zhao, D.-l., Li, X.-Q., & Zhong, Z. (2009). New wave-dependent formulae for sea spray flux at air-sea interface. *Journal of Hydrodynamics*, *21*(4), 573–581.

Slinn, S., & Slinn, W. (1980). Predictions for particle deposition on natural waters. *Atmospheric Environment (1967)*, *14*(9), 1013–1016.

Smirnov, A., Holben, B., Giles, D., Slutsker, I., O'Neill, N., Eck, T., ... others (2011). Maritime aerosol network as a component of aeronet–first results and comparison with global aerosol models and satellite retrievals. *Atmospheric Measurement Techniques*, *4*(3), 583–597.

Smith, C. J., Kramer, R. J., Myhre, G., Alterskjær, K., Collins, W., Sima, A., ... others (2020). Effective radiative forcing and adjustments in cmip6 models. *Atmospheric Chemistry and Physics*, *20*(16), 9591–9618.

Smith, M., Park, P., & Consterdine, I. (1993). Marine aerosol concentrations and estimated fluxes over the sea. *Quarterly Journal of the Royal Meteorological Society*, *119*(512), 809–824.

Soden, B. J., Held, I. M., Colman, R., Shell, K. M., Kiehl, J. T., & Shields, C. A. (2008). Quantifying climate feedbacks using radiative kernels. *Journal of Climate*, *21*(14), 3504–3520.

Solomon, S. (2007). The physical science basis: Contribution of working group i to the fourth assessment report of the intergovernmental panel on climate change. *Intergovernmental Panel on Climate Change (IPCC), Climate change 2007*, *996*.

Stjern, C. W., Lund, M. T., Samset, B. H., Myhre, G., Forster, P. M., Andrews, T., ... others (2019). Arctic amplification response to individual climate drivers. *Journal of Geophysical Research: Atmospheres*, *124*(13), 6698–6717.

Stocker, T. (2014). *Climate change 2013: the physical science basis: Working group i contribution to the fifth assessment report of the intergovernmental panel on climate change*. Cambridge university press.

Stolpe, M. B., Medhaug, I., Beyerle, U., & Knutti, R. (2019). Weak dependence of future global mean warming on the background climate state. *Climate Dynamics*, *53*, 5079–5099.

Struthers, H., Ekman, A., Glantz, P., Iversen, T., Kirkevåg, A., Seland, Ø., ... Nilsson, E. (2013). Climate-induced changes in sea salt aerosol number emissions: 1870 to 2100. *Journal of Geophysical Research: Atmospheres*, *118*(2), 670–682.

Stuecker, M. F., Bitz, C. M., Armour, K. C., Proistosescu, C., Kang, S. M., Xie, S.-P., ... others (2018). Polar amplification dominated by local forcing and feedbacks. *Nature Climate Change*, *8*(12), 1076–1081.

Sun, Q., & Du, Y. (2023). Sea surface salinity changes and trans-basin water vapor transport between the atlantic and pacific under cmip6 abrupt-4xco2 scenario. *Climate Dynamics*, *60*(5), 1907–1924.

Talbot, R., Andreae, M., Berresheim, H., Artaxo, P., Garstang, M., Harriss, R., ... Li, S. (1990). Aerosol chemistry during the wet season in central amazonia: The influence of long-range transport. *Journal of Geophysical Research: Atmospheres*, *95*(D10), 16955–16969.

Tang, T., Shindell, D., Faluvegi, G., Myhre, G., Olivié, D., Voulgarakis, A., ... others (2019). Comparison of effective radiative forcing calculations using multiple methods, drivers, and models. *Journal of Geophysical Research: Atmospheres*, *124*(8), 4382–4394.

Team, G. G. A. M. D., Anderson, J. L., Balaji, V., Broccoli, A. J., Cooke, W. F., Delworth, T. L., ... others (2004). The new gfdl global atmosphere and land model am2–lm2: Evaluation with prescribed sst simulations. *Journal of Climate*, *17*(24), 4641–4673.

Tebaldi, C., Hayhoe, K., Arblaster, J. M., & Meehl, G. A. (2006). Going to the extremes. *Climatic change*, *79*(3), 185–211.

Tegen, I., & Schepanski, K. (2018). Climate feedback on aerosol emission and atmospheric concentrations. *Current Climate Change Reports*, *4*(1), 1–10.

Tokinaga, H., Xie, S.-P., Timmermann, A., McGregor, S., Ogata, T., Kubota, H., & Okumura, Y. M. (2012). Regional patterns of tropical indo-pacific climate change: Evidence of the walker circulation weakening. *Journal of Climate*, *25*(5), 1689–1710.

Twomey, S. (1977). The influence of pollution on the shortwave albedo of clouds. *J. atmos. Sci*, *34*, 1149–1152.

van den Berg, A., Dentener, F., & Lelieveld, J. (2000). Modeling the chemistry of the marine boundary layer: Sulphate formation and the role of sea-salt aerosol particles. *Journal of Geophysical Research: Atmospheres*, *105*(D9), 11671–11698.

Vecchi, G. A., Clement, A., & Soden, B. J. (2008). Examining the tropical pacific's response to global warming. *Eos, Transactions American Geophysical Union*, *89*(9), 81–83.

Vignati, E., De Leeuw, G., & Berkowicz, R. (2001). Modeling coastal aerosol transport and effects of surf-produced aerosols on processes in the marine atmospheric boundary layer. *Journal of Geophysical Research: Atmospheres*, *106*(D17), 20225–20238.

Wang, C., Soden, B. J., Yang, W., & Vecchi, G. A. (2021). Compensation between cloud feedback and aerosol-cloud interaction in cmip6 models. *Geophysical Research Letters*, *48*(4), e2020GL091024.

Waples, J. T., & Klump, J. V. (2013). Vertical and horizontal particle transport in the coastal waters of a large lake: An assessment by sediment trap and thorium-234 measurements. *Journal of Geophysical Research: Oceans*, *118*(10), 5376–5397.

Winton, M., Takahashi, K., & Held, I. M. (2010). Importance of ocean heat uptake efficacy to transient climate change. *Journal of Climate*, *23*(9), 2333–2344.

Witek, M. L., Teixeira, J., & Matheou, G. (2011). An eddy diffusivity–mass flux approach to the vertical transport of turbulent kinetic energy in convective boundary layers. *Journal of the Atmospheric Sciences*, *68*(10), 2385–2394.

Woodcock, A. H. (1953). Salt nuclei in marine air as a function of altitude and wind force. *Journal of Atmospheric Sciences*, *10*(5), 362–371.

Wu, S., Luo, M., Liu, Z., Wang, X., Huang, Z., & Li, X. (2024). Longer-and slower-moving contiguous heatwaves linked to el niño. *Geophysical Research Letters*, *51*(11), e2024GL109067.

Xie, A., Zhu, J., Kang, S., Qin, X., Xu, B., & Wang, Y. (2022). Polar amplification comparison among earth's three poles under different socioeconomic scenarios from cmip6 surface air temperature. *Scientific Reports*, *12*(1), 16548.

Xie, X., Zhou, S., Zhang, J., & Huang, P. (2021). The role of background sst changes in the enso-driven rainfall variability revealed from the atmospheric model experiments in cmip5/6. *Atmospheric Research*, *261*, 105732.

Xu, X., Wang, J., Henze, D. K., Qu, W., & Kopacz, M. (2013). Constraints on aerosol sources using geos-chem adjoint and modis radiances, and evaluation with multisensor (omi, misr) data. *Journal of Geophysical Research: Atmospheres*, *118*(12), 6396–6413.

Yu, P., Froyd, K. D., Portmann, R. W., Toon, O. B., Freitas, S. R., Bardeen, C. G., ... others (2019). Efficient in-cloud removal of aerosols by deep convection. *Geophysical Research Letters*, *46*(2), 1061–1069.

Yue, X., Wang, H., Liao, H., & Jiang, D. (2011). Simulation of the direct radiative effect of mineral dust aerosol on the climate at the last glacial maximum. *Journal of Climate*, *24*(3), 843–858.

Zelinka, M. D., & Hartmann, D. L. (2010). Why is longwave cloud feedback positive? *Journal of Geophysical Research: Atmospheres*, *115*(D16).

Zelinka, M. D., Myers, T. A., McCoy, D. T., Po-Chedley, S., Caldwell, P. M., Ceppi, P., ... Taylor, K. E. (2020). Causes of higher climate sensitivity in cmip6 models. *Geophysical Research Letters*, *47*(1), e2019GL085782.

Zhang, B., Zhao, M., He, H., Soden, B. J., Tan, Z., Xiang, B., & Wang, C. (2023). The dependence of climate sensitivity on the meridional distribution of radiative forcing. *Geophysical Research Letters*, *50*(18), e2023GL105492.

Zhao. (2024). Crucial role of sea surface temperature warming patterns in near-term high-impact weather and climate projection. *npj Clim Atmos Sci 7, 130*.

Zhao, & Cook, K. H. (2021). Influence of walker circulations on east african rainfall. *Climate Dynamics*, *56*(7), 2127–2147.

Zhao, M. (2022). An investigation of the effective climate sensitivity in gfdl's new climate models cm4. 0 and spear. *Journal of Climate*, *35*(17), 5637–5660.

Zhao, M., Golaz, J.-C., Held, I., Guo, H., Balaji, V., Benson, R., ... others (2018). The gfdl global atmosphere and land model am4. 0/lm4. 0: 1. simulation characteristics with prescribed ssts. *Journal of Advances in Modeling Earth Systems*, *10*(3), 691–734.

Zhu, J., Xie, A., Qin, X., Xu, B., & Wang, Y. (2023). Assessment of antarctic amplification based on a reconstruction of near-surface air temperature. *Atmosphere*, *14*(2), 218.